Quantum Dynamics of van der Waals Molecular Clusters with MCTDH: Potential Energy Surface Representation, Rovibrational States Calculations, and Collisional Dynamics

by

HERVE TAJOUO TELA

Supervisor

Dr. Steve Alexandre Ndengué

Department of Physics and Astronomy, Haverford College, Haverford, PA, USA

Co-Supervisor

Dr. Ali Hassanali

The Abdus Salam International Centre for Theoretical Physics, Trieste, Italy

Thesis

Submitted in partial fulfilment of the requirements for the degree of

Ph.D. Degree by research in Physics

At

ICTP - East African Institute for Fundamental Research, University of Rwanda,

Kigali, Rwanda

November 18, 2024

Acknowledgement

I extend my heartfelt thanks to the ICTP's External Activities Office for funding most of the years of this project and supporting a significant amount of my travel.

My gratitude also goes to my ICTP advisor, Dr. Ali Hassanali for our discussions about this thesis. I also appreciate EAIFR for allowing me to participate in conferences, professional training, and the exchange of ideas with scientists in my field.

Special thanks to Prof. Fabien Gatti for his warm welcome at ISMO and to the DIRAM team, whose discussions have greatly benefited me.

I am deeply grateful to my supervisor, Dr. Steve Alexandre Ndengué, for his invaluable support and guidance throughout this project. His support extended beyond scientific advice to human and social encouragement. Completing this work in meticulous detail would have been impossible without his continuous support and belief in me; he challenged me to go beyond my limits, as well as the ample time he allowed for calculations and discussions.

I extend my appreciation to the EAIFR staff, including Prof. Cathérine Meriaux, Dr. Omololu Akin Ojo, Dr. Shoaib Munir, Dr. Obodo Kingsley, and Dr. Marcello Muso, for their scientific discussions.

I am also grateful to my fellow PhD students for the moments we shared, including lunches, coffee breaks, and numerous scientific discussions. A special mention goes to Sunday Joseph, Irambona Sosthène, Murad Ali, and Wala.

A special thank you to Mrs. Sylvane for the time you dedicate to us every day for the administrative processes.

I am profoundly grateful to God for my family: my mother, Rose, and my late father, Lucas Tela, for their enduring love and trust. To my brothers and sisters—Frédéric, Laurette, Angèle, Marinette, Sédrigue, Régine, Abigael, Trésor, Mégane, Latifa, Luclaire,

and Océane—your support has been immeasurable. I love you all dearly.

Abstract

This research aims to advance the quantum dynamics simulation of van der Waals molecular clusters, including H_2O-H_2O, H_2O-HCN, and N_2O-CO, which are formed with abundant molecules in the interstellar medium (ISM) such H_2O and CO. While these systems have traditionally been studied through classical methods, the full quantum approach using the Multi-Configuration Time-Dependent Hartree (MCTDH) method was chosen to address challenges related to dimensionality. A critical first step in this approach is the accurate representation of the Potential Energy Surface (PES), as it underpins all subsequent calculations. Although previous studies have characterized some properties of these clusters, this work provides comprehensive rovibrational state calculations and initiates collision simulations for the water dimer. Achieving convergence, however, has proven challenging, as it is highly sensitive to the size of the primitive basis set and the number of single-particle functions (SPFs) utilized in flux calculations for computing inelastic cross sections and rate coefficients. Spectroscopic calculations were performed using the Block Improved Relaxation procedure from the Heidelberg MCTDH package, allowing extraction of transition frequencies and rotational constants. The zero-point energy (ZPE) and intermolecular vibrational frequencies obtained from these simulations align well with prior *ab initio* studies, while the transition frequencies and rotational constants show good agreement with experimental data.

Contents

List of Tables

List of Figures

List of Abbreviations and Symbols

Abbreviations

ISM Interstellar Medium

vdW van der Waals

PES Potential Energy Surface

MCTDH MultiConfiguration Time-Dependent Hartree

BOA Born-Oppenheimer Approximation

DVR Discrete Variable Representation

FBR Finite Basis Representation

TDSE Time Dependent Schrödinger equation

DOF Degrees Of Freedom

BF Body-Fixed

SF Space-Fixed

TDH Time-Dependent Hartree

MCSCF MultiConfiguration Self-Consistent Field

ZPE Zero-Point Energy

KEO Kinetic Energy Operator

SOP Sum-Of-Products

CAP Complex Absorbing Potential

CC Close Coupling

MQCT Mixed Quantum/Classical Theory

QCT Quasi-Classical Theory

1. Introduction

This thesis focuses on the theoretical study of the spectroscopy and dynamics of van der Waals molecular clusters. I will begin with the astrochemistry background and the current status of the research on spectroscopy and collision processes.

1.1 Background

1.1.1 General context

It is well-established that the formation, destruction, and excitation of molecules are useful for describing and investigating atmospheric chemical phenomena [6, 7, 8]. A deep understanding of these chemical processes will require exploring the main application of the molecular clusters simulated in this thesis, which is astrochemistry. Astrochemistry is a science that includes the exploration of molecular systems for astrophysical studies, and investigates the chemical processes in space related to the formation, decomposition, and excitation of molecules in various environments [9]. It integrates chemistry, physics, and astrophysics to investigate the chemical composition and interaction of molecular clusters throughout the universe. To provide more details about astrochemistry, Michael De Becker defined astrochemistry as the science devoted to the study of chemical processes in astrophysical environments, including the Interstellar Medium (ISM), comets, circumstellar, and circumplanetary regions where molecules are generally subject to excitations due to temperature variations and can therefore interact [10].

Estimating molecular abundances is essential in observational astrochemistry. Modeling the physical conditions requires molecular and spectroscopic data for the observed species, which can be obtained through experimental or theoretical studies. In addition to spectroscopic data, radiative transfer is used to determine molecular abundances from line spectra. This requires precise knowledge of rotational state-to-state excitation (or de-excitation) rate constants [11] and astronomers require these data on the observed molecules to interpret the observations and model the physical conditions of the observed

environments [12].

Molecules in the astrochemical environment are primarily formed on dust grain surfaces in interstellar clouds or through gas-phase reactions. The formation processes are related the adsorption, diffusion, and chemical reactions on the grain surfaces [13]. Before delving into the heart of the subject, I will start by describing the astrochemical environments in which molecular clusters, as well as the physical quantities we will study, play an essential role.

1.1.1.1 The Interstellar Medium (ISM):

The interstellar medium refers to the matter that exists between star systems in a galaxy—sometimes referred to as interstellar space [14]. This matter is composed of gas and dust, such as molecular clouds and nebulae. Most molecules are found in the gas phase, with hydrogen and helium making up over 98% of the composition as shown in Figure 1.1 [13, 15], where there is a small amount of dust containing carbon, oxygen, and various other chemical elements. Figure 1.2 illustrates the molecular diversity present throughout the life cycle of the interstellar medium. This cycle begins in the diffuse interstellar medium, continues in dense molecular clouds where stars and planets form, and ends with their return to the interstellar medium following the explosion of stars [5]. This process then gives rise to a new cycle. During these stages, heavy elements are synthesized and gradually become more abundant [5].

1.1.1.2 The Comets:

comets are another relevant laboratory in astrochemistry. Comets are easier to study than the ISM because when they come close to the sun, they release gases and dust that provide clues about how our solar system formed long ago [16, 17]. We can sometimes spot them with our own eyes at night. However, just seeing them is not enough; to truly understand what is happening with them physically or chemically, detailed observations are required.

Comets mostly contain water along with various volatile compounds [18] such as carbon dioxide (CO_2), carbon monoxide (CO), methanol (CH_3OH), and some complex organic

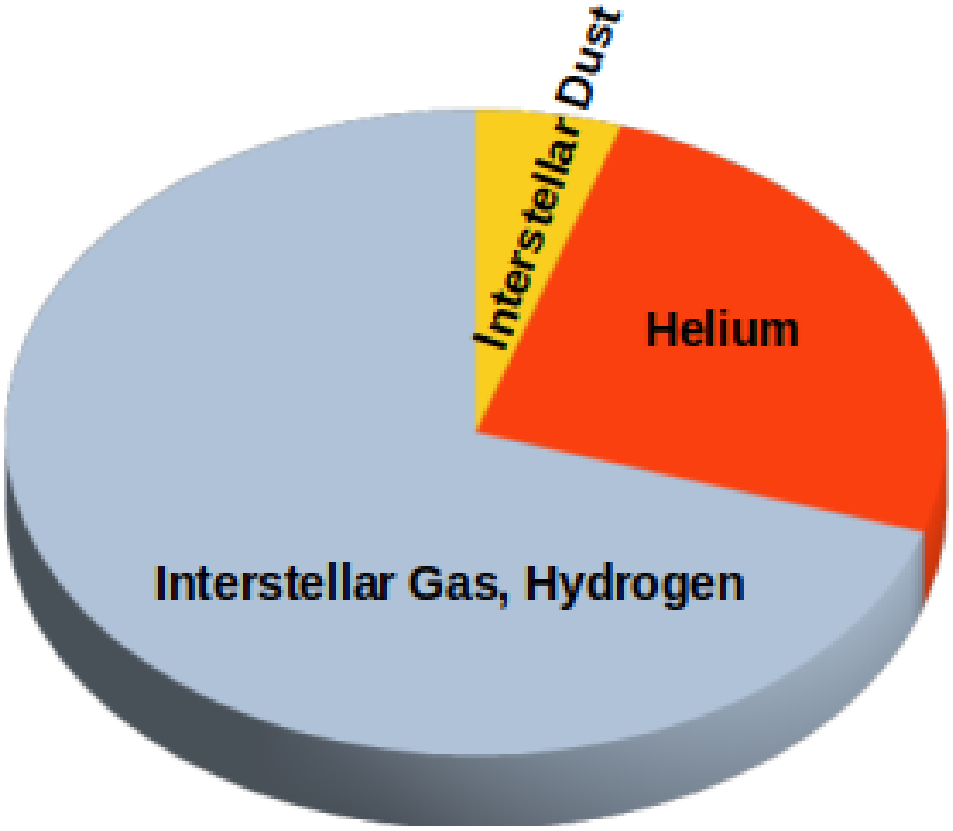

Figure 1.1: An illustration of the interstellar medium. The figure has been modified and taken from reference [4].

molecules like aldehydes and alcohols [1]. Therefore, detailed observations are important when studying their chemistry. Unlike the interstellar medium, comets provide scientists with opportunity to make measurements up close.

Unlike the interstellar medium, comets are more accessible, allowing in situ measurements. Comets are remnants of the planet formation process around our sun. As time capsules, they have spent most of their existence far from the sun without undergoing significant thermal changes since their formation. This makes them unique sources of information about the conditions of planet formation [19, 20]. Comets have two main parts: their nucleus which is a mix of ice and rock, preserving old molecules since our solar system's formation, and their atmosphere called a coma formed by gas and dust when they heat up near the sun. By studying what comes from this coma, we learn valuable details about

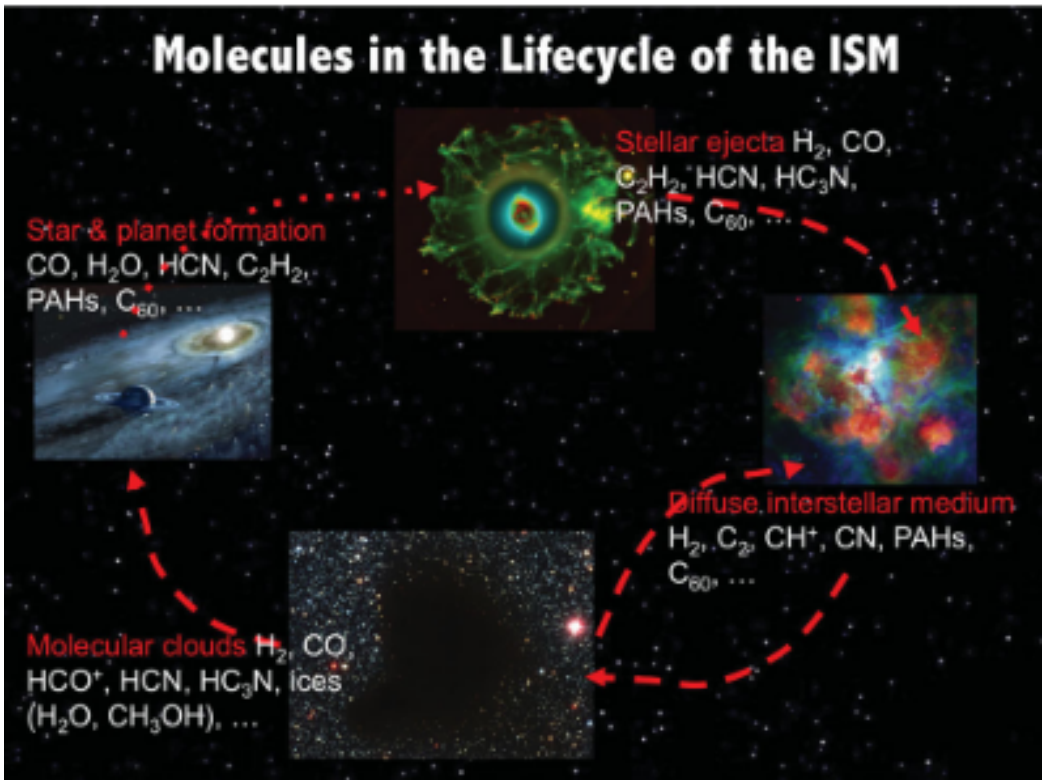

Figure 1.2: An illustration of the life cycle of the interstellar medium. The figure was taken from reference [5] with Tielens (author) and Reviews of Modern Physics (journal) permissions.

early solar systems - even ideas about how life could have started on Earth [21, 22].

The abundance of different molecules relative to water in comets is reported in Table 1.1. The presence of certain organic molecules in comets has been a basic hypothesis [23] for their contribution to the development of living beings on the terrestrial planet. This hypothesis suggests that comets, made up of ice, dust, rock, and frozen gases, might have brought organic molecules to Earth in its early stages. These organic substances could have been the subject of the development of life. This concept is known as panspermia [24, 25], proposing that life, or its essential components, could have come from space.

Table 1.1: Abundance ratios of detected molecules relative to water in comets. This table has been modified and taken from reference [1].

Compound	Chemical formula	Molar mass	Proportion relative to water
Water	H_2O	18	100
Methane	CH_4	16	0.5
Hydrogen cyanide	HCN	27	0.9
Carbon monoxyde	CO	28	1.2
Methylamine	CH_3NH_2	31	0.6
Ethanenitrile	CH_3CN	41	0.3
Isocyanic acid	HNCO	43	0.3
Ethanal	CH_3CHO	44	0.5
Methanamide	$HCONH_2$	45	1.8
Ethylamine	C_2H_3CHO	45	0.3
Isocyanatomethane	CH_3NCO	57	1.3
Propanone	CH_3COCH_3	58	0.3
Propanal	C_2H_5CHO	58	0.1
Ethanamide	CH_3CONH_2	59	0.7
2-Hydroxyethanal	CH_2OHCHO	60	0.4
1,2-Ethanediol	$CH_2(OH)CH_2(OH)$	62	0.2

1.1.2 Molecular detection and analysis in Astrochemistry

In the previous section, I discussed the environments where molecules can be observed. I will now focus on the types of molecules detected in the interstellar medium. The first identified molecules, such as Hydrocarbon gas (CH), Cyanogen gas (CN), and methylidyne cation CH^+ [26, 27, 28], were discovered over 80 years ago. However, they were initially overlooked as scientists considered them to be simple fragments of larger molecules. In the late 1950s and during the 1960s, the development of radio astronomy significantly

accelerated the discovery of new molecules [29], with OH being the first to be detected using this technique [30]. In 1968, the discovery of ammonia NH_3 [31] marked a major breakthrough, drawing attention to the presence of heavy molecules formed during nucleosynthesis and released into the interstellar medium [13]. Since then, over 270 molecules have been discovered in the ISM, ranging from simple two-atom molecules to complex organic compounds [32]. Many of these molecules cannot be produced on Earth due to the unique conditions in space, making the interstellar medium a fascinating research area.

To analyze the detected molecules, experimental and theoretical data on molecular interactions, particularly spectra and collisional data, are essential for interpreting the observations [33]. This data can also be used to simulate astrochemical environments [34]. The combination of state-to-state art spectroscopic observations and advanced atmospheric modeling and statistical inference methods is also used to explore and analyze the detected spectra of molecular complexes in the ISM [35]. These spectroscopic observations make a major contribution to our understanding of the greenhouse effect and ozone depletion. Experimental studies can replicate interstellar medium conditions to gather spectroscopic and collisional data but have limitations, such as laboratory costs and sometimes no experimental data. In fact, to offset the cost of laboratory studies, theoretical studies have been considered as a way to pave to these molecular spectra analyses [36].

Molecular observations are not limited to the identification of the molecules themselves. They also provide more information about the physical and chemical conditions of the environment where these molecules are found. To obtain these details, researchers try to reproduce the spectra of the observed molecules. An accurate modeling of these spectra requires a good understanding of the distribution of molecules in their different energy levels [37]. If we consider a local thermodynamic equilibrium (LTE) state, this distribution can be easily calculated, as it means that molecules reach their energy levels through collisions in a dense medium [38].

However, this equilibrium state is rarely present in environments like the interstellar medium (ISM) due to its low density and low temperature [39]. This complicates the

interpretation of spectra because energy transfer depends on an interaction between radiative and collisional processes. Radiative processes include absorption, stimulated emission, and spontaneous emission, while collisional processes involve the excitation and relaxation of molecules. To properly model the spectra, it is essential to take into account these two types of mechanisms [39].

1.1.3 Motivations of the study

As discussed earlier, following the discovery of various molecules in the interstellar medium, our first focus has been to understand the chemical and physical processes responsible for creating these species. Experimental studies aim to replicate the physical conditions of the ISM to interpret and analyze spectroscopic and collisional data. However, these experiments face limitations, such as the range of temperatures and pressures achievable in the lab, or the size and complexity of molecules that can be synthesized. This makes theoretical studies can be considered, as they can overcome these restrictions and provide spectroscopic and collisional data that complement experimental findings—or even serve as the primary source of information when experiments are not feasible. Nevertheless, theoretical calculations also come with challenges, often requiring significant computational resources and complex methodologies.

In recent years, many computational simulations have been conducted using the coupled equation method, also known as the Close Coupling (CC) approach [40, 41], to solve the time independent nuclear Schrödinger equation. The coupled state (CS) is based on the simplification of the CC method with some Coriolis couplings and it is valid only at high energy [42]. The infinite -order approximation is valid even at larger energies and for molecules with small rotational constants [43]. Other relevant methods such as such as Quasi-Classical Theory (QCT) [44] and Mixed Quantum/Classical Theory (MQCT) [45] are also employed in studying reaction dynamics across various systems, such as diatom and atom [46, 47], diatom and diatom [48, 49], triatom and atom [50, 51], triatom and diatom [52], and triatom and triatom [53], etc. However, these calculations encounter several difficulties, such as:

Spectroscopic and inelastic collision studies involving molecular systems using time independent CC methods are often limited due to the computational time and memory required to store the wave functions for large systems. Van der Avoird $et\ al.$ [54] used Davidson's algorithm to compute the rovibrational states of H_2O-H_2, Stoecklin $et\ al.$ [55] employed a rigid-bend CC to treat the inelastic collisions of H_2O with para-H_2, and then the CC bending relaxation of H_2O by He. With the same CC method, the bound state rovibrational energy and inelastic cross-sections of other systems have been widely studied, such as H_2O-CO and its isotopologues [56, 57, 58], and H_2O-HF [59].

The Quasiclassical Trajectory (QCT) method is most effective in high-temperature conditions where quantum effects are less likely to play a significant role. However, at low temperatures, its reliability may be uncertain, especially when strong resonances are present [60]. These assumptions underscore the limitations of current methodologies and emphasize the necessity for alternative approaches that are more efficient and adaptable across various temperature and energy ranges. For instance, the MultiConfiguration Time-Dependent Hartree (MCTDH) method [61] is well-suited for managing large systems efficiently, providing significant advantages in terms of computational time and memory utilization for wave function storage. Furthermore, it is a quantum method that demonstrates particular effectiveness at high collisional energies, in contrast to time-independent approaches.

In this project, the MCTDH method is employed to address the challenges associated with molecular clusters, accommodating a wide range of degrees of freedom (DOF). This capability enhances the feasibility of calculations and reduces resource demands, enabling a comprehensive investigation of the spectroscopy and dynamics of various molecular clusters. While MCTDH excels at managing large-dimensional systems compared to alternative methods, expanding the calculation basis can lead to even greater performance improvements.

1.2 Objectives

The aim of this thesis is twofold: the first objective is to represent the multipolar potential energy surface (PES) and utilize this potential in conjunction with the kinetic energy operator (KEO) to compute the rovibrational states of selected van der Waals molecular clusters. The second objective is to investigate the inelastic collisions of various molecular clusters that are pertinent to astrophysics and atmospheric studies. To achieve these goals, the nuclear Schrödinger equation is solved using the MultiConfiguration Time-Dependent Hartree (MCTDH) method, which has proven to be highly effective.

1.2.1 Rovibrational Spectroscopy

In recent years, advances in rovibrational spectroscopy techniques of molecular clusters have been widely studied theoretical [62, 63] and experimentally [64]. For example, the use of tunable lasers in the far infrared (FIR) [65, 66] allows for the measurement of intermolecular vibrations. In parallel, to better understand these clusters, it is essential to improve the description of the interactions that govern them. Experimentally the obtained spectra provide valuable data for theorists to refine potential energy surfaces. Theoretical modeling of a system like a van der Waals complex presents several challenges, including the large basis dimension required for calculations to achieve accurate convergence. Furthermore, calculating spectra of such systems is becoming increasingly complex, especially when aiming to go beyond the rigid rotor approximation. This requires highly efficient numerical methods to perform the calculations. Rovibrational states play a key role in the physicochemical processes of the atmosphere [64, 67].

These calculations are based on the application of the Born-Oppenheimer Approximation (BOA) [68], which assumes that the movements of electrons and nuclei can be treated separately, given the large difference in their masses. This approach allows solving the Schrödinger equation in two distinct steps. First, the electronic part of the equation is solved, which requires determining the Potential Energy Surface (PES) of the system for different fixed positions of the nuclei, representing the electronic interaction. Then,

this PES is used to solve the nuclear Schrödinger equation, thereby obtaining the rovibrational states. The MCTDH method has been favored to solve the Schrödinger equation in this type of system due to the large number of Degrees Of Freedom (DOF) involved. Numerous rovibrational calculations were performed using the rigid-rotor monomer approximations for various systems, such as H_2O-H_2 [54, 62, 69], H_2O-CO [56, 57], H_2O-HF [59, 70], H_2O/D_2O–CO_2 [71], H_2O-HCl [72, 73, 74], CH_4-H_2O [75, 76], and H_2O-H_2O [63, 77, 78]. I only named the water-containing clusters as examples of the molecular clusters because it was the main goal of my thesis project. Some recent approaches developed for the computational simulations, such as the use of compact contracted bases of intermolecular and low-energy rigid-monomer intermolecular eigenstates [79, 80], and the combination of Discrete Variable Representation (DVR) and Finite Basis Representation (FBR) with Lanczos diagonalization [62, 63], have enabled full-dimensional and coupled quantum calculations of the rovibrational states of water-containing clusters with flexible monomers. This includes systems like H_2O-HCl [72] and its isotopologues [81, 73], H_2O/D_2O–CO [82], HDO–CO [83], benzene-H_2O [84], and the water dimer [63, 85]. Lanczos diagonalization is an iterative method particularly effective for finding eigenvalues and eigenvectors of large, sparse matrices, enabling the computation of a few eigenstates without fully diagonalizing the matrix [86]. This technique is frequently applied when only a limited number of low-energy rovibrational states, such as the ground and low-lying excited states, are required. By focusing on these specific states rather than the entire spectrum, Lanczos diagonalization offers computational efficiency for large systems. In contrast, coupled quantum calculations explicitly solve the coupled equations governing all degrees of freedom within the system, encompassing both rotational and vibrational interactions [87]. These calculations typically use a basis set that incorporates both rotational and vibrational states, necessitating a complete treatment of the Hamiltonian. This approach is essential when obtaining the full set of rovibrational states or when accounting for significant interactions between rotational and vibrational modes, especially in systems where mode coupling strongly influences the dynamics. However, coupled quantum calculations are more computationally demanding than Lanczos diagonalization, as they require a comprehensive solution of the Hamiltonian matrix, mak-

ing them preferable for smaller systems or situations demanding high accuracy across the entire spectrum of states.

1.2.2 Dynamical Collision

In this section, I will begin by detailing the various types of scattering processes, providing a foundation for understanding the underlying mechanisms and distinctions between them. Subsequently, I will present an overview of prior scattering calculations and notable limitations encountered in earlier approaches. We consider a non-reactive diffusion process between two systems A and B.

$$A(i) + B(j) \longrightarrow A(i') + B(j') \tag{1.2.1}$$

A and B, characterized by sets of quantum numbers i and j for the initial state, and i' and j' for the final state after the process. The values i and j describe the configurations of systems A and B before the interaction, while i' and j' provide information about their respective states after the interaction. There are two main categories of non-reactive scattering processes. The first type, known as elastic scattering, is characterized by the fact that the internal states of the systems remain unchanged during the collision. In other words, this means that $i = i'$ and $j = j'$. The second type, called inelastic collision, is distinguished by changes in the internal states of the systems after the collision. In this case, we have $i \neq i'$ and/or $j \neq j'$. In the inelastic process, one may also observe excitation and/or de-excitation of the system [88, 89].

Quantum scattering between molecule-molecule, molecule-atom, and atom-atom interactions is significant in various fields such as chemical processes in Earth's atmosphere, industrial and aeronautic combustion chemistry, and environments beyond Earth, such as the interstellar medium and the atmospheres of stars and planets [90, 91, 41, 92]. For example, determining the molecular abundances in protostellar clouds can be achieved by solving radiative transfer equations, which require an understanding of state-to-state collisional rate coefficients. One can note that for collisional calculations, the Born-

Oppenheimer approximation [68] is also used, which facilitates the determination of cross sections. These cross sections are then used to calculate collisional rate coefficients, essential parameters for estimating the abundance of a species in the interstellar medium. The close-coupling method, introduced by Arthus and Dalgarno in 1960 [93], is commonly employed to obtain accurate collision data by simplifying the problem into a set of coupled second-order differential equations that need to be numerically solved. Scientists at that time were limited in performing calculations for a few and small collisional systems (in terms of numbers of atoms) due to their small computational resources. Since then, with the enormous growth in computational technology, several methods have been proposed to study the collision of large molecules, including the time-dependent MCTDH method. We have been able to study more complex systems, necessary for the chemical modeling of astrophysical media. Time-independent CC calculations have been widely used for atom-atom or molecule-atom inelastic collisions [94, 95]. Several works in the literature have focused on the time-independent CC approach, dealing with van der Waals complexes in the rigid rotor or full-dimensional approximation [96, 97, 98, 99, 100, 101]. As molecules become larger and heavier, the density of internal states increases, making the problem unfeasible using the CC method at higher collision energies when the number of accessible rovibrational states increases [102]. Some methods have been proposed as alternative approaches to the CC method, such as the QCT method, used to solve classical Hamilton's equations and is numerically efficient, especially at higher collision energies. The MQCT method developed by Semenov and Babikov [103] is used for inelastic scattering, providing computational gain for larger molecules at higher collision energies, such as $CO + He$ [104], $H_2O + He$ [51, 47], and the statistical adiabatic channel model (SACM) [100, 101]. While those methods show promising results, their accuracy and domain of validity require further investigation, especially in extending the SACM calculations to obtain collisional data for the highest transitions between two partners [101].

Additionally, collisional data for molecular clusters, such as rate coefficients, is essential. Estimating molecular abundances in the interstellar medium (ISM) from spectral line observations relies heavily on accurate collisional rate coefficients. Numerical modifications

will be made to the potential energy surface for long-distance interactions. This work focuses on performing quantum calculations on selected molecular clusters using both existing and newly developed PESs. While this study is theoretical, significant computational challenges arose when employing the Multi-Configuration Time-Dependent Hartree (MCTDH) method, as many of the simulations required specialized external tools and methodologies that were still under development for the systems investigated in this thesis.

1.3 Relevance of molecular clusters

In this thesis, I investigate specific van der Waals (vdW) complexes, which can be easily used to understand the chemical reaction intermediates and phase transitions between gas and condensed phases. These complexes provide essential insights into a wide range of chemical phenomena, with applications across fundamental chemistry, astrophysics, atmospheric physics, and biochemistry [105]. Thus, I will present four molecules: water (H_2O), hydrogen cyanide (HCN), carbon monoxide (CO), and nitrous oxide (N_2O). These molecules were selected because of their importance in astrochemical environments. Here, I explain the reasons for choosing each of these molecules.

1.3.1 Water (H_2O)

Water (H_2O) molecule is one of the most abundant polyatomic systems in the Universe. In 1969, Cheung $et\ al.$ [106], observed water in space, and it is a prevalent component in Earth's environment, playing a significant role in the composition of many planets, moons, and also comets [107]. The study of molecule detection has been greatly enhanced by new technologies such as the Submillimeter Wave Astronomy Satellite (SWAS) [108] and the Infrared Space Observatory (ISO) [109], to name only a few. Water is essential everywhere on Earth's surface for biological, chemical (as a key factor in the chemical reactivity of the ISM), and physical processes [110]. Without it, the Earth would be radically different. It is a versatile molecule that can exist in a wide range of environments, making it a valuable tool for studying different environmental conditions beyond the earth [111]. With its

numerous rovibrational levels, water plays an essential role in cooling processes during the processes of star formation. Given water's importance in sustaining life, its presence in the ISM and on planets has sparked interest in the possibility of extraterrestrial life [112, 113].

Water in the ISM is the third most abundant molecule after CO and H_2 [114, 5, 115, 69, 39] and can interact with other relevant complexes, including water itself. That is one of the main reasons for the extensive studies of the water dimer [63, 116, 117]. The initial calculations of the rovibrational states, based on an accurate representation of the PES, were straightforwardly feasible. To address this issue, we developed a new methodology. We utilized the most accurate PES of H_2O-H_2O system available in the literature [118] and transformed it into a more user-friendly analytical form [119]. My projects for this thesis began with an in-depth study of the H_2O-H_2O system, which formed the cornerstone of my doctoral work. This theoretical investigation centered on understanding the van der Waals (vdW) interactions within this system and expanded to include interactions with other molecular complexes, such as HCN.

1.3.2 Hydrogen Cyanide (HCN)

Hydrogen cyanide is one of the most observed molecules in the ISM, and its large dipole moment is also a parameter used to consider HCN as a good tracer of high-density regions [120]. Its initial observation was by Snyder and Buhl in 1971 [121], where they recorded the transition from the ground state with $J = 1$ to $J = 0$ at a frequency of 88.6 GHz. It was initially detected in comet Kohoutek [122] and later in comet Halley [123, 124] but its formation path is not well known. Furthermore, HCN can be considered a potential reactant nitrogen during the formative stages of Earth's biosphere [125, 126]. Beyond our planet, HCN has been avidly studied due to its wide-ranging presence in extraterrestrial contexts, including comets [127], rigid molecular clouds [128, 129], circumstellar envelopes [130], and even active galaxies [131]. Additionally, HCN can interact with a selected few molecules in high-redshift galaxies, such as CO, CN, and HCO^+ [132] as it is cosmic. Recent advancements in observational technology, handled by the Atacama Large Millimeter/Submillimeter Array (ALMA) interferometer and the Herschel Space Observa-

tory, have provided a large amount of HCN emission spectra data [133]. These data extend through a large cosmic space, including molecular clouds such as Sgr A* [134] within our own galaxy, circumstellar envelopes such as IRC+10216 [135], and extending to the far reaches of the cosmos, where external galaxies come into focus [136, 137]. The non-local-thermal equilibrium (N-LTE) models [138] are very useful to determine the abundance of HCN with the requirement of radiative and collisional properties of the molecule. The studies of the interaction between HCN and H_2O are then of high interest.

1.3.3 Carbon monoxide (CO) and nitrous oxide N_2O

The weak intermolecular interactions and rovibrational spectra of VdW complexes involving CO and N_2O have been a subject of sustained interest [139, 140, 141]. CO is the second most abundant molecule in the Universe after H_2. Its abundance, relative to hydrogen, stands at 4×10^{-4} for carbon and 7.4×10^{-4} for oxygen [142]. CO also acts as one of the major by-products of combustion processes; it has been shown in many occurrences in the Earth's atmosphere, hydrocarbons, and also interstellar clouds [143]. Therefore, CO is of great importance and interest in atmospheric research, combustion chemistry, and environmental monitoring [144]. In astrophysical studies, the CO emission spectrum is used to detect H_2 and this detection is due to its absence of a dipole moment, making carbon monoxide (CO) the most frequently observed molecule across a diverse array of cosmic environments [143]. N_2O and CO play significant roles in the atmospheric environment as they are two major greenhouse gases that contribute to the Earth's heat retention [145]. Their atmospheric concentrations have been shown to be increasing. Additionally, N_2O is a precursor to the production of stratospheric NOx, which is responsible for the natural depletion of stratospheric ozone [3]. The accurate CO fundamental band has proven to be a good quantitative tracer of molecular gas [146], but the initial detection of carbon monoxide only dates back to the year 1970 [147].

1.4 Outline of this thesis

The theoretical study of the spectroscopy and inelastic collisions of molecular clusters is especially important when the dimensionality of the two partners is increasing. This thesis aims to investigate the interaction of two molecular complexes using the MCTDH method. In particular, the work described herein illustrates a theoretical method that can be used to break down unfeasible spectroscopy and collisional studies of molecular clusters with a large number of degrees of freedom.

The present thesis is structured in the following way:

In Chapter 2, I present the theoretical frameworks employed in performing quantum dynamics calculations, starting with the Born-Oppenheimer approximation and extending to the computation of rovibrational states and rate coefficients using the Multi-Configuration Time-Dependent Hartree (MCTDH) approach [148, 149].

In Chapter 3, I present the rovibrational states calculations of the H_2O-HCN in the rigid rotor approximation using a 5D-dimensional PES. In this part, the research aims to investigate the spectroscopic properties of the H_2O-HCN heterodimer utilizing the MCTDH method.The rovibrational states will be calculated and analyzed by external scripts, and their weights predicted. The analysis involves investigating hydrogen bonding characteristics, geometric arrangement, and vibrational couplings within the complex in the rigid rotor approximation.

In Chapter 4, I calculate the rovibrational states and preliminary steps for the inelastic collision of the water dimer in the rigid rotor approximation. This chapter focuses on analyzing the spectroscopic characteristics, cross sections, and rate coefficients of the water dimer using the MCTDH method. These tasks require accurately transforming the potential energy surface (PES) and implementing it within the MCTDH framework. Following the approach in Chapter 3, the HCN molecule is replaced by H_2O to assess the complexities involved in describing this system. This substitution facilitates a comparison between the challenges associated with HCN and H_2O, particularly regarding convergence

behavior and low-energy dynamics. The objective is to determine whether the complexity of calculations increases or decreases based on H_2O's unique properties, including its molecular structure and symmetries inherent to Wigner functions, which may influence wave function accuracy.

In Chapter 5, I computed the spectroscopic properties: the rovibrational states, transition frequencies, and rotational constants of the N_2O-CO molecule in the rigid rotor approximation. This work complements my thesis project, which primarily focused on water molecules within clusters. The main task is to demonstrate to the reader how to represent the PES of such systems without using the multipolar form or performing multiple integrations to obtain the expansion coefficients. The approach (not new) aims to provide a more direct and accurate representation of the potentials of linear-linear systems, especially in calculations of rovibrational states and collisional dynamics. Additionally, the N_2O-CO system has a notably larger reduced mass, making the calculations much more difficult to converge. This highlights the connection to the overall thesis project and specifies the objective of a new method for representing the PES.

Finally, in Chapter 6, I summarize all the work done in this thesis and present some perspectives for future work.

2. Theoretical framework

In this chapter, I provide an overview of the quantum chemical methods used for spectroscopy and collisions. I will provide more details about the molecular system and the Born-Oppenheimer approximation (BOA) derivation process. Electronic structure methods are widely used to calculate the *ab initio* PESs, but precision depends on the chosen methodologies or levels of theory. Next, I will introduce the theoretical methods used for quantum dynamics calculations. Finally, I will present the MCTDH method I used to solve the nuclear Schrödinger equation.

2.1 The Molecular Schrödinger Equation

the treatment of a quantum dynamics problem requires calculating the PES, typically derived using the Born-Oppenheimer approximation (BOA). Considering a molecular system with N electrons and M nuclei, each position of nuclei is labeled by R, and r corresponds to the electrons. Interactions other than Coulombic interactions (such as spin-orbit and spin-spin interactions) are neglected initially, as are relativistic effects [150]. The nuclear Schrödinger equation in its time independent form for the complete solution of this problem is:

$$\hat{H}\psi(r,R) = E\psi(r,R) \tag{2.1.1}$$

where $\hat{H}$ stands for the molecular Hamiltonian, the molecular wave function $\psi(r,R)$, *R* and *r*, are the coordinates of the nuclei and electrons respectively, and *E* is the molecular eigenergy function. One can express the total Hamiltonian $\hat{H}$ as follows:

$$\hat{H}(r,R) = \hat{T}_n(R) + \hat{T}_e(r) + \hat{V}_{ee}(r) + \hat{V}_{nn}(R) + \hat{V}_{en}(r,R), \tag{2.1.2}$$

where:

- $\hat{H}(r,R)$ represents the total Hamiltonian of the system.

- $\hat{T}_n(R)$ is the kinetic energy operator for the nuclei.
- $\hat{T}_e(r)$ is the kinetic energy operator for the electrons.
- $\hat{V}_{ee}(r)$ represents the electron-electron interaction energy, accounting for Coulombic repulsion between electrons.
- $\hat{V}_{nn}(R)$ represents the nuclear-nuclear interaction energy, which accounts for Coulombic repulsion between nuclei.
- $\hat{V}_{en}(r, R)$ represents the electron-nuclear interaction energy, accounting for the attraction between electrons and nuclei.

To solve equation 2.1.2 directly is not practical because it is computationally expensive [151].

Now, looking at equation 2.1.2, each term can be rewritten as:

$$\hat{T}_n(R) = -\sum_{i=1}^{N} \frac{1}{2M_i} \nabla^2_{\boldsymbol{R}_i} \tag{2.1.3}$$

$$\hat{T}_e(r) = -\sum_{i=1}^{N} \frac{1}{2m_e} \nabla^2_{\boldsymbol{r}_i} \tag{2.1.4}$$

$$\hat{V}_{ee}(r) = \sum_{i=1}^{N} \sum_{j>i}^{M} \frac{1}{|\boldsymbol{r}_i - \boldsymbol{r}_j|} \tag{2.1.5}$$

$$\hat{V}_{nn}(R) = \sum_{i}^{M} \sum_{j>i}^{M} \frac{Z_i Z_j}{|\boldsymbol{R}_i - \boldsymbol{R}_j|} \tag{2.1.6}$$

$$\hat{V}_{ne}(r, R) = -\sum_{i=1}^{N} \sum_{j=1}^{M} \frac{Z_j}{|\boldsymbol{r}_i - \boldsymbol{R}_j|} \tag{2.1.7}$$

The mass of a given nucleus is M_i at position R_i and M is the total number of nuclei; m_e is the mass of the electrons, N is the number of electrons at position r_i. In atomic units $m_e = \hbar = 1$. The $|r_i - r_j|$ are the distances between electrons i and j and $|R_i - R_j|$ are the distances between nuclei i and j with the nuclear charge Z. Equation 2.1.2

does not account for any relativistic effects [150]. The Schrödinger equation can be solved analytically for simple two-particle systems, such as hydrogen, which consists of one electron and one nucleus. However, for multi-atomic systems, the equation becomes analytically unsolvable due to the complexity of the electron-nucleus interaction term, $\hat{V}_{en}(r, R)$. We must introduce approximations to obtain a solution to the Schrödinger equation.

2.2 The Born-Oppenheimer approximation

In simple words, Born-Oppenheimer approximation has been introduced in 1927 [68] by Born and Oppenheimer allowing one to solve the Schrödinger equation of systems with more than one nucleus and one electron. An assumed aspect of this approximation is the mass ratio between the electron and nucleus, where the proton's mass is approximately 1836 times that of the electron. Due to this significant difference in mass, the nuclei move more slowly than electrons. In other words, the nuclei distance R becomes a parameter, and the term $\hat{V}_{en}(r, R)$ becomes $\hat{V}_{en}(r; R)$.

One can consider the electrons to adjust almost instantaneously and adiabatically to the motion of the nuclei. This adiabatic adaptation forms the basis for separating the total Hamiltonian, which defines the energy in the system, into two parts. The total wave function can be written as a product of the electronic and nuclear wave fuction as follows

$$\psi(R; r) = \psi_{el}(r; R)\psi_N(R) \tag{2.2.1}$$

As a result, the molecular Hamiltonian can be written as follows

$$\hat{H} = \hat{T}_n + \hat{H}_{el} + \hat{V}_{nn} \tag{2.2.2}$$

$\hat{H}_{el}$ is the electronic Hamiltonian, which can be written as follows

$$\hat{H}_{el}(r, R) = \hat{T}_e + \hat{V}_{en} + \hat{V}_{ee} = -\frac{1}{2}\sum_{i=1}^{N} \nabla^2_{\boldsymbol{r}_i} - \sum_{i=1}^{N}\sum_{j=1}^{M} \frac{Z_j}{|\boldsymbol{r}_i - \boldsymbol{R}_j|} + \sum_{i=1}^{N}\sum_{j>i}^{M} \frac{1}{|\boldsymbol{r}_i - \boldsymbol{r}_j|} \tag{2.2.3}$$

And the electronic shrödinger equation is

$$\hat{H}_{el}\psi_{el}(r;R) = E_{el}(R)\psi_{el}(r;R) \tag{2.2.4}$$

where E$_e l$ is the electronic energy of the system associated with the electronic wave function $\psi_{el}(r;R)$, and the nuclear coordinate R is a parameter for the electronic wave function. This approach is treated in two procedures: first, the electronic energy levels are determined for specific nuclear arrangements, then the motion of the nuclei is analyzed within the influence of the electronic potential energy configuration [152]. The total electronic energy of the system can thus be obtained by adding the $\hat{V}_{nn}$ term

$$E_{el}^{\text{tot}} = E_{el} + \sum_{i=1}^{M}\sum_{j>i}^{M}\frac{Z_i Z_j}{|\boldsymbol{R}_i - \boldsymbol{R}_j|} \tag{2.2.5}$$

By calculating the total electronic energy E_{el}^{tot} for various nucleus positions, we obtain a potential energy surface (PES).

One can separate the problem into two parts, one can solve the nuclear problem while considering that the nuclei evolve within an electronic potential, a potential that is the solution to the electronic problem. The Nuclear Schrödinger equation can be written as follows

$$\hat{H}_n(R)\psi_N(R) = E\psi_N(R), \tag{2.2.6}$$

where $\psi_N(R)$ is the nuclear wave function independent of the electronic coordinate r.

$\hat{H}_n$ is the nuclear Hamiltonian written as follows

$$\hat{H}_n = \hat{T}_n(R_j) + E_{el}^{\text{tot}}(R_j) = -\sum_{j=1}^{N}\frac{1}{2M_j}\nabla_{\boldsymbol{R}_j}^2 + E_{el}^{\text{tot}}(R_j), \tag{2.2.7}$$

where E in equation 2.2.6 is the total energy of the system for each nuclear position

j. The electronic coordinate is considered as a parameter for the nuclear Schrödinger equation.

In this Hamiltonian setup, the BOA says that the nuclear kinetic energy operator, $\hat{T}_n(R)$, does not depend on the electronic wave function. In other words, the electrons move rapidly according to the positions taken by the nuclei, not according to the speed at which they move. The first correction to this is looking at the diagonal elements of this operator. So with BOA, we totally separate electronic motion from nuclear motion. We first get the electronic eigenvalues at given nuclear shapes and then track how the nuclei behave in that electronic potential [152]. In this thesis, I have limited the discussion to electronic structure methods and the corresponding equations used in potential energy surface (PES) calculations. Instead, the primary focus here is on representing the PES for applications within the Multiconfigurational Time-Dependent Hartree (MCTDH) framework. The objective is not to delve into the computational details of electronic structure theory but rather to emphasize the accuracy and suitability of the PES representation for enabling high-quality MCTDH calculations. This approach aligns with the main goal of efficiently modeling rovibrational states and inelastic collisional dynamics for van der Waals molecular clusters.

2.3 Reference frame and coordinates system

Before diving into any calculations, one has to set up our coordinate system. This system helps describe positions in our setup and how molecules interact with one another.

2.3.1 Reference frame

Any molecular system consisting of N atoms can be described by $3N$ Cartesian coordinates in space. In order to reduce the number of variables on which the system depends, a mobile frame is used to separate the coordinates associated with the translation and rotation movements of the molecule. In the laboratory frame $\left(G_1, X_1, Y_1, Z_1\right)$, the center of mass of any isolated system will perform a rectilinear uniform motion. By subtracting this

global translational motion, a new reference frame is introduced, called Space-Fixed (SF) frame to the molecule, where $\left(G_0, X, Y, Z\right)$ represents the center of mass, and X, Y, Z corresponds to a moving trihedron, whose axes remain parallel to those of the laboratory fixed frame (LF). The Hamiltonian of the system can be expanded as follows

$$H = T_{LF} + V = T_{G_0} + T_{SF} + V, \tag{2.3.1}$$

where T_{LF} is the kinetic energy of the system in the laboratory reference frame (LF), T_{SP} is the kinetic energy of the system in the Space-Fixed reference frame, T_{G_0} is the kinetic energy associated with the translational movement of the system, and V is the PES. The change of reference frame allows us to go from a problem in $3N$ dimensions to a problem in $3N-3$ dimensions by removing the three degrees of freedom associated with the translational motion of the center of mass.

To describe the overall rotation in the coordinate representation, a third reference frame (G, x, y, z), called the Body-Fixed (BF) frame, is introduced. The orientation of this frame is defined by three Euler angles $\left(\alpha, \beta, \gamma\right)$, which parameterize the overall rotation of the molecule. Once the Euler angles are defined, we then have a $3N-6$ dimensional problem for N atoms [153].

2.3.2 Coordinates system

Once the reference frame is established for the study of molecular systems, we can choose a suitable coordinate system to describe them. This choice of the suitable coordinate system is not only useful for formulating the molecular system's Hamiltonian but also for describing the primitive basis used for the calculations.

Various coordinate systems can be used to describe a molecular system, including **rectilinear internal coordinates** based on the number of atoms constituting the molecular system. These coordinate systems are linear combinations of Cartesian coordinates and have the advantage of simplifying the expression of the kinetic energy operator. They are particularly useful for describing low-amplitude movements of molecular systems. We can

also have **curvilinear internal coordinates**, which are not linear combinations of Cartesian coordinates. Among these, we find for example valence coordinates [154], suitable for describing anharmonic systems, Jacobi coordinates [155], useful for systems undergoing large amplitude motions, and finally hyperspherical coordinates [156, 157], widely used in the study of collisional systems. The choice of coordinates generally depends on several criteria, such as obtaining the most compact expression possible of the Hamiltonian with respect to the system under study, the convergence of calculations, as a complex formulation of the Hamiltonian often slows down convergence, and taking into account the symmetries of the system. Since the systems studied in this thesis are molecular systems with large amplitudes, I used Jacobi coordinates.

2.3.2.1 Polyspherical coordinates:

In this part, many equations are taken from refs. [158, 159], and reference therein.

Euler angles can be defined as follows to be placed in the body-fixed frame. We start by choosing a system of orthogonal vectors, such as the Jacobi vectors connecting two atoms, in order to reduce the dimension of the problem. To do this, we place ourselves in the Body-Fixed frame, defined using two intermediate reference frames denoted E_1 and E_2.

The E_1, X_{E_1} and Y_{E_1} reference frame is obtained from the Space-Fixed by a rotation of an angle α around the Z_{SF}. We obtain $\vec{R} \in (X_{E_1} G Z_{SF})$ and $Z_{SF} = Z_{E_1}$. At this stage, we choose the Jacobi vectors with the largest reduced mass to minimize Coriolis coupling. Then, the E_2,X_{E_2} and Z_{E_2} reference frame is obtained from E_1 by a rotation of an angle β around the Y_{E_1} axis and $Y_{E_2} = Y_{E_1}$. In this stage Z_{E_2} and $\vec{R}$ are equivalent and define the quantification axis Finally, the final reference frame is obtained from E_2 by a rotation of an angle γ around the Y_{E_2} axis. This reference frame corresponds to the mobile BF frame defined by X_{BF} and Y_{BF} as described in the previous section, with the same z-axis as E_2. It is appropriate to say that the rest of the work I did was in the E_2 reference frame. In practice, the relationship between the coordinates of a vector $\vec{R}(X^{SF}, Y^{SF}, Z^{SF})$ in the Space-Fixed frame and the coordinates $\vec{R}(x^{BF}, y^{BF}, z^{BF})$ of

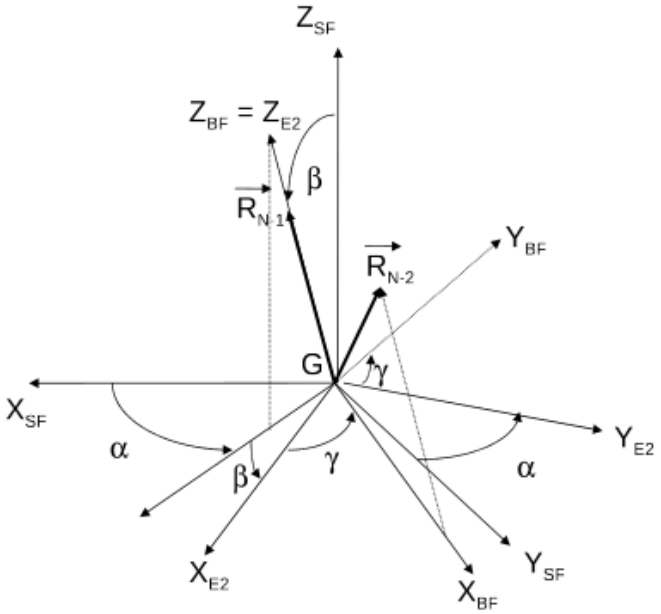

Figure 2.1: Representation of the Body-Fixed (BF) frame with respect to the Space-Fixed (SF) frame and Euler angles.

the same vector in the Body-Fixed is established by the following transformation:

$$\begin{pmatrix} X^{SF} \\ Y^{SF} \\ Z^{SF} \end{pmatrix} = R(\alpha, \beta, \gamma) \begin{pmatrix} x^{BF} \\ y^{BF} \\ z^{BF} \end{pmatrix} \tag{2.3.2}$$

With $R(\alpha, \beta, \gamma)$ the Euler rotation matrix [160].

2.3.3 Formalism of the Hamiltonian for a molecular system.

In this section, I will present the complete formulations of kinetic energy for two rigid systems.

2.3.3.1 Classical Hamiltonian:

The classical Kinetic Energy Operator (KEO) using the Jacobi vector can be written as follows [157]

$$2T = \sum_{i=1}^{n} \frac{\vec{P}_i^2}{\mu_i}, \tag{2.3.3}$$

where μ_i is the reduced mass associated with the i^{th} vector of Jacobi. Using the quasi-momentum decomposition, $\vec{P}_i$ can be expressed as follows [161, 162, 157, 159]

$$\vec{P}_i = P_i^R \vec{e_{Ri}} - \frac{\vec{e_{Ri}} \wedge \vec{L}_i}{R_i} \tag{2.3.4}$$

$$\vec{e}_{R_i} = \frac{\vec{R}_i}{R_i}, \tag{2.3.5}$$

where $\vec{e_{Ri}}$ is the unit vector collinear with $\vec{R}_i$. $\vec{P}_i^R$ is the radial momentum and the kinetic momentum is $\vec{L}_i = \vec{R}_i \wedge \vec{P}_i^2$. From there, the kinetic energy is written as follows

$$2T = \sum_{i=1}^{n} \left(\frac{P_i^{R^2}}{\mu_i} + \frac{\vec{L}_i^2}{\mu_i R_i} \right) \tag{2.3.6}$$

2.3.3.2 From classical Hamiltonian to quantum Hamiltonian:

One can decompose the last vector of Jacobi as $\vec{L}_n = \vec{J} - \sum_{i=1}^{n-1} \vec{L}_i = \vec{J} - \vec{L}$. For this, we use the rules of direct quantification, which allow us to go from $\hat{L}_i^\dagger \hat{L}_i$ to L_i^2 and from $\hat{P_i^R}^\dagger \hat{P}_i^R$ to $P_i^{R^2}$. We then obtain the following relationships [163, 161, 162, 157, 159]:

$$\hat{P}_i^R = -\mathrm{i}\hbar \frac{\partial}{\partial R_i} \tag{2.3.7}$$

$$\hat{P_i^R}^\dagger = -\mathrm{i}\hbar \frac{\partial}{\partial R_i} - \frac{2\mathrm{i}\hbar^2}{R_i} \tag{2.3.8}$$

We can obtain the quantum vectorial expansion of the kinetic energy as follows

$$2\hat{T} = \sum_{i=1}^{n} -\frac{\hbar^2}{\mu_i} \frac{1}{R_i} \frac{\partial^2}{\partial R_i^2} R_i + \sum_{i=1}^{n-1} \frac{\hat{L}_i^\dagger \hat{L}_i}{\mu_i R_i^2} + \frac{\hat{J}^\dagger \hat{J} + \hat{L}^\dagger \hat{L} - 2\hat{J}^\dagger \hat{L}}{\mu_i R_n^2} \tag{2.3.9}$$

As discussed in reference [157], the general expression can be derived in cases where the states are not orthogonal. The angular momenta involved in the kinetic energy operator are calculated in the space-fixed (SF) reference frame but projected onto the axes of the body-fixed (BF) frame. The kinetic energy operator can be expressed by substituting the projections of the angular momenta $\hat{L}_i$ with their corresponding formulation in terms

of the conjugate momentum operator $\hat{P}_i = -\mathrm{i}\partial/\partial q_i$ associated with the polyspherical coordinates q_i. This approach has been extensively detailed in these reviews [157, 164] discussing the formulation of the kinetic energy operator. The general expression of the operator is given as follows

$$\hat{T} = \underbrace{\sum_{l,m=1}^{3N-6} \frac{\hat{P}_l^\dagger G_{lm} \hat{P}_m}{2}}_{\hat{T}_{vib}} + \underbrace{\sum_{l=1}^{3N-6} \sum_{\alpha=x,y,z} \frac{\hat{P}_l^\dagger C_{l\alpha} \hat{J}_\alpha + \hat{J}_\alpha C_{\alpha l} \hat{P}_l}{2}}_{\hat{T}_{cor}} + \underbrace{\sum_{\alpha=x,y,z} \sum_{\beta=x,y,z} \frac{\hat{J}_\alpha \Gamma_{\alpha\beta} \hat{J}_\beta}{2}}_{\hat{T}_{rot}} \tag{2.3.10}$$

In this context, $\hat{T}_{vib}$, $\hat{T}_{cor}$, and $\hat{T}_{rot}$ represent the vibrational kinetic energy operator, Coriolis coupling term, and rotational kinetic energy operator, respectively. This result is universal and applies to any set of vectors, whether orthogonal or not. As shown in equation 2.3.10, the terms G, C, and Γ are defined by three matrices: G of dimension $(3N-6) \times (3N-6)$, C of dimension $(3N-6) \times 3$, and Γ of dimension 3×3.

This vectorial approach has been successfully utilized by Gatti in the study of the ammonia molecule (NH_3) [157, 165] and has proven to be very effective. This formalism has also been employed by Yohann Scribano [163] in his studies of the water dimer.

2.4 The rigid rotor ro-vibrational energy levels

In this section, I describe the method for obtaining rovibrational energies, which correspond to the combined rotational and vibrational energy levels of molecular systems. One can mention that Coriolis coupling, a phenomenon where rotational and vibrational states interact, can also influence these energies. These rovibrational energy levels are calculated by diagonalizing the Hamiltonian operator of the system'[163]. *Ab initio* simulations are generally costly for very large numbers of electrons. A limited number of ab initio points can be calculated in many situations to avoid computational costs by reducing the number of degrees of freedom. For this reason, we consider the computational cost and memory needed to store the wave function. Since intramolecular coordinates are more prone to high-amplitude motions than intermolecular coordinates, leading to intense vibrational

movements in molecular dynamics, we can make a simplifying assumption: by freezing the internal geometries of molecules, we reduce the number of degrees of freedom and treat the system as a $\boldsymbol{rigid\ rotor}$.

Commonly employed to perform simulations in the quantum chemical community and theoretical spectroscopy, the rigid rotor approximation is mainly used to describe the rotation of complex molecules [166]. In this approximation, the molecular complex is considered connected by rigid bonds with the intramolecular distances held constant when the system rotates. For further details regarding the equations presented in this section, the reader can refer to references [167, 166].

The full rovibrational Hamiltonian of a molecular system can be expressed as follows

$$\hat{H}_{\text{rov}} = \hat{H}_r + \hat{H}_v + \hat{H}_c \tag{2.4.1}$$

$$\hat{H}_{\text{rov}}|\psi_{\text{rov}}\rangle = E_{\text{rov}}|\psi_{\text{rov}}\rangle \tag{2.4.2}$$

where $\hat{H}_r$ is the rotational Hamiltonian, $\hat{H}_v$, the vibrational Hamiltonian, and $\hat{H}_c = \frac{1}{2\mu R^2}\left\{\hat{J}^2 + \hat{j}^2 - 2\hat{j}.\hat{J}\right\}$ the coupling term called Coriolis coupling or vibration-rotational interaction and the system is treated so that this Coriolis interaction minimal. In this section, I will briefly present the characteristics of the rotational and vibrational states of different types of molecular systems. The calculations of the rovibrational states for each system studied in this thesis will then be described in detail in each chapter.

2.4.1 The rigid rotor rotational energy levels

Before continuing, I will start by defining angular momentum. The rotational energy levels in the rigid rotor approximation can be calculated from the rotational Hamiltonian in terms of the angular momentum component in the molecular fixed frame $\left(e_1, e_2, e_3\right)$ by solving the Schrödinger equation expressed as follows [168]:

$$\hat{H}_r = \frac{\hat{J}_{e_1}^2}{2I_{e_1}} + \frac{\hat{J}_{e_2}^2}{2I_{e_2}} + \frac{\hat{J}_{e_3}^2}{2I_{e_3}} \tag{2.4.3}$$

where I_{e_1}, I_{e_2}, I_{e_3} are the principal moments of inertia. Instead of solving the Schrödinger equation directly, rotational energy levels can be determined by utilizing the commutation properties of the relevant operators.

$$\hat{J}^2 = \hat{J}^2_{e_1} + \hat{J}^2_{e_2} + \hat{J}^2_{e_3} = \hat{J}^2_{E_1} + \hat{J}^2_{E_2} + \hat{J}^2_{E_3} \tag{2.4.4}$$

where E_1, E_2, and E_3 stand for the components along the SF axis. Those components can be commutated as follows [169]:

$$\begin{aligned} \left[\hat{J}_i, \hat{J}_j\right] &= +\mathrm{i}\sum_k \epsilon_{ijk}\hat{J}_k \\ \left[\hat{J}_l, \hat{J}_m\right] &= -\mathrm{i}\sum_n \epsilon_{lmn}\hat{J}_n \end{aligned} \tag{2.4.5}$$

$$\epsilon_{ijk} = \begin{cases} +1 & \text{if } ijk \text{ is an even permutation of } ijk, \\ -1 & \text{if } ijk \text{ ijk is an odd permutation of } ijk, \\ 0 & \text{if if two or more indices are equal.} \end{cases} \tag{2.4.6}$$

With $i, j, k = E_1, E_2, E_3$, $l, m, n = e_1, e_2, e_3$, and ϵ_{ijk} the Levi-Civita symbol. Each component of angular momentum in the SF frame commutes with every component in the molecular fixed frame as follows

$$\left[\hat{J}_i, \hat{J}_l\right] = 0 \tag{2.4.7}$$

With $i = E_1, E_2, E_3$ and $l = e_1, e_2, e_3$. We can then deduce these commutation relation-

ships on angular momentum.

$$\begin{aligned}\left[\hat{J}^2, \hat{J}_{e_1}\right] &= \left[\hat{J}^2, \hat{J}_{E_1}\right] = 0 \\ \left[\hat{J}^2, \hat{J}_{e_2}\right] &= \left[\hat{J}^2, \hat{J}_{E_2}\right] = 0 \\ \left[\hat{J}^2, \hat{J}_{e_3}\right] &= \left[\hat{J}^2, \hat{J}_{E_3}\right] = 0\end{aligned} \tag{2.4.8}$$

The rotational Hamiltonian can commute with the total angular momentum operator as well as with one of the components of angular momentum in the space-fixed frame as follows

$$\left[\hat{H}_r, \hat{J}_{e_3}\right] = +\mathrm{i}\Big(\frac{1}{2I_{e_1}} - \frac{1}{2I_{e_2}}\Big)\Big(\hat{J}_{e_1}\hat{J}_{e_2} + \hat{J}_{e_2}\hat{J}_{e_1}\Big) \tag{2.4.9}$$

We can then deduce the operators commuting with the same set of eigenfunctions as follows

$$\begin{aligned}\left[\hat{H}_r, \hat{J}^2\right] &= 0 \\ \left[\hat{H}_r, \hat{J}_{E_3}\right] &= 0 \\ \left[\hat{J}^2, \hat{J}_{E_3}\right] &= 0\end{aligned} \tag{2.4.10}$$

where $J = 0, 1, 2, \cdots$, represents the total angular momentum, and m represents the projection of the total angular momentum. The values range from $J = 0, 1, 2, 3, \cdots$ and $m = -J, -J+1, \cdots, J-1, J$.

The moment of inertia of a rigid rotor is represented by a 3×3 matrix characterizing the rotation of the three-dimensional rigid body system. In this case, one can designate the three axes as a, b, and c. It is worth noting that in this convention, the a-axis has the smallest moment of inertia, and the c-axis has the highest value, as shown in Figure 2.2.

$$I_a \leq I_b \leq I_c \tag{2.4.11}$$

One can express the rigid rotor Hamiltonian in the body-fixed frame as a function of the

moments of inertia as follows

$$\hat{H}(A,B,C) = A\hat{J}_a^2 + B\hat{J}_b^2 + C\hat{J}_a^2 \tag{2.4.12}$$

and

$$A = (2I_a)^{-1}, B = (2I_b)^{-1}, C = (2I_c)^{-1} \tag{2.4.13}$$

To calculate the energy of a molecular cluster, one has to know its symmetry group. Five groups are characterized based on the moments of inertia [170]. We can name a few of them.

- The linear molecules are characterized by the rotational constants $B = C$ and a small value of A. In this case, we can assume that $A = 0$. For example, HCl. Thus, $B = C, A = 0$
- Prolate symmetric top: $A > B = C$, for example C_2H_6.
- Oblate symmetric top: $A = B > C$, for example C_6H_6.
- Spherical top: $A = B = C$, for example CH_4.
- Asymmetric top: $A > B > C$, for example H_2O.

2.4.2 Symmetric tops

In the case of rigid rotor symmetric tops, two moments of inertia are equal, and the third value is not zero and different from the first two values. The z-axis is defined along the symmetry axis of the molecule. We characterize them as prolate (the symmetry axis is aligned with the a-axis) and oblate (aligned with the c-axis) as shown in Figure 2.2. We can show that from the principal axes (a, b, c), the commutation relation between the rotational Hamiltonian and the angular momentum in the prolate case is expressed as follows

$$\left[\hat{H}_r, \hat{J}_a\right] = +\mathrm{i}\left(\frac{1}{2I_b} - \frac{1}{2I_c}\right)\left(\hat{J}_b\hat{J}_c + \hat{J}_c\hat{J}_b\right) = 0 \tag{2.4.14}$$

And in the oblate

$$\left[\hat{H}_r, \hat{J}_c\right] = +\mathrm{i}\left(\frac{1}{2I_a} - \frac{1}{2I_b}\right)\left(\hat{J}_b\hat{J}_a + \hat{J}_a\hat{J}_b\right) = 0 \tag{2.4.15}$$

From the above demonstrations, one can see that $\hat{H}_r$, $\hat{J}^2$, $\hat{J}_{z=E_3}$, and $\hat{J}_a$ share the same set of eigenfunctions $|Jk_am\rangle$. We can then deduce the following equations in the prolate case.

$$\begin{aligned}
\hat{H}_r = |Jk_ama\rangle &= E_r|Jk_am\rangle \\
\hat{J}^2|Jk_am\rangle &= J(J+1)|Jk_am\rangle \\
\hat{J}_{Z=E_3}|Jk_am\rangle &= m|Jk_am\rangle \\
\hat{J}_a|Jk_am\rangle &= k_a|Jk_am\rangle
\end{aligned} \tag{2.4.16}$$

We can then express the rotational Hamiltonian for the rotational energy in the prolate form as follows

$$\begin{aligned}
\hat{H}_r|Jk_am\rangle &= \left(A\hat{J}_a^2 + B\hat{J}_b^2 + C\hat{J}_c^2\right)|Jk_am\rangle \\
&= \left[B\hat{J}^2 + \left(A-B\right)\hat{J}_a^2\right]|Jk_am\rangle
\end{aligned} \tag{2.4.17}$$

In the prolate case, the energy level is expanded as:

$$E_{rot}(J, k_a) = BJ(J+1) + (A-B)k_a^2 \tag{2.4.18}$$

and for oblate top

$$E_{rot}(J, k_c) = BJ(J+1) + (C-B)k_c^2 \tag{2.4.19}$$

Here, k_a stands for the projection of the total angular momentum J onto the symmetry axis of the body-fixed frame with value $k_a = -J, -J+1, \cdots, J-1, J$. The same applied for k_c. The wave function in this case is expressed as a function of the Wigner matrix [171].

$$D^J_{m,k_a}(\alpha, \beta, \gamma) = \langle Jm|R(\alpha, \beta, \gamma)|Jk_a\rangle \tag{2.4.20}$$

And

$$|Jk_am\rangle = (-1)^{m-k_a}\sqrt{\frac{2J+1}{8\pi^2}}D^J_{-m,-k_a}(\alpha,\beta,\gamma) \tag{2.4.21}$$

Where

$$D^J_{m,k}(\alpha,\beta,\gamma) = e^{\mathrm{i}m\alpha}d^J_{m,k}(\beta)e^{\mathrm{i}k\gamma}, \tag{2.4.22}$$

where $d^J_{m,k}(\beta)$ is the Wigner-d function and can be expressed in terms of hypergeometric functions.

2.4.3 Asymmetric top

In the case where the rotational constants that characterize its energy levels are distinct, signifying a lack of symmetry that prevents the simplification of its Hamiltonian, unlike the case of a symmetric top. Consequently, it is not feasible to decompose the Hamiltonian into components solely dependent on $\hat{J}^2$ and $\hat{J}_{e_1}$, as no preferred axis exists within the molecule's fixed frame.

For an asymmetric top, explicit expressions of the energy levels are not readily available. Instead, the Schrödinger equation for such a system is typically solved by constructing the Hamiltonian matrix using the basis of symmetric top wave functions. Diagonalizing this matrix allows for the determination of energy eigenvalues and corresponding wave functions. These wave functions emerge as linear combinations of symmetric top wave functions, with coefficients dependent on the specific values of the rotational constants A, B, and C.

For an asymmetric top with rotational constants A, B, and C, the asymmetric parameter k can be written as follows:

$$k = \frac{2B - A - C}{A - C} \tag{2.4.23}$$

where k is from -1 to 1 $(-1 \leq k \leq 1)$. For $k = -1$, the system corresponds to a prolate symmetric top, $i.e$, $A = B$, and a value $k = 1$ corresponds to the oblate symmetric

top, $i.e,\ B = C$. A value $k = 0$ corresponds to the most asymmetric top, for which $B = \frac{(A+C)}{2}$.

The Hamiltonian of an asymmetric top can be expressed as follows [171]:

$$\hat{H}_{rot} = (\frac{B+C}{2})\hat{J}^2 + (A - \frac{B+C}{2})\hat{J}^2_{e_3} + (\frac{B+C}{4})\Big[(\hat{J}_{+,m})^2 + (\hat{J}_{-,m})^2\Big] \tag{2.4.24}$$

where $\hat{J}_{+,m}$ and $\hat{J}_{-,m}$ stand for the angular momentum corresponding to the operators in the molecular-fixed frame.

$$\Big[\hat{J}_{e_3}, J_{\pm,m}\Big] = \pm J_{\pm,m}, \tag{2.4.25}$$

and,

$$J_{\pm,m}|J, k_a, m\rangle = \sqrt{J(J+1) - k_a(k_a \pm 1)}|J, k_a \pm 1, m\rangle \tag{2.4.26}$$

From equation 2.4.26, the non-zero matrix elements that one can require to construct the Hamiltonian matrix are:

$$\langle J, k_a, m|\hat{J}^2|J, k_a, m\rangle = J(J+1), \tag{2.4.27}$$

and,

$$\langle J, k_a, m|\hat{J}^2_{e_3}|J, k_a, m\rangle = k_a^2 \tag{2.4.28}$$

$$\langle J, k_a \pm 2, m|(\hat{J}_{\pm,m})^2|J, k_a, m\rangle = \sqrt{\big[J(J+1) - k_a(k_a \pm 1)\big]\big[J(J+1) - (k_a \pm 1)(k_a \pm 2)\big]} \tag{2.4.29}$$

The eigenvalues of the Hamiltonian obtained by diagonalization correspond to states with the same total angular momentum J and the same quantum number m. Likewise for states with the same k_a with $k_a \neq 2$. The eigenvalues formed from these eigenstates are expressed in terms of $|J, k_a, m\rangle$ and $|J, -k_a, m\rangle$, and the energy levels of a top asymmetric are also expressed as $J_{K_a K_c}$, where $K_a = |k_a|$ and $K_c = |k_c|$.

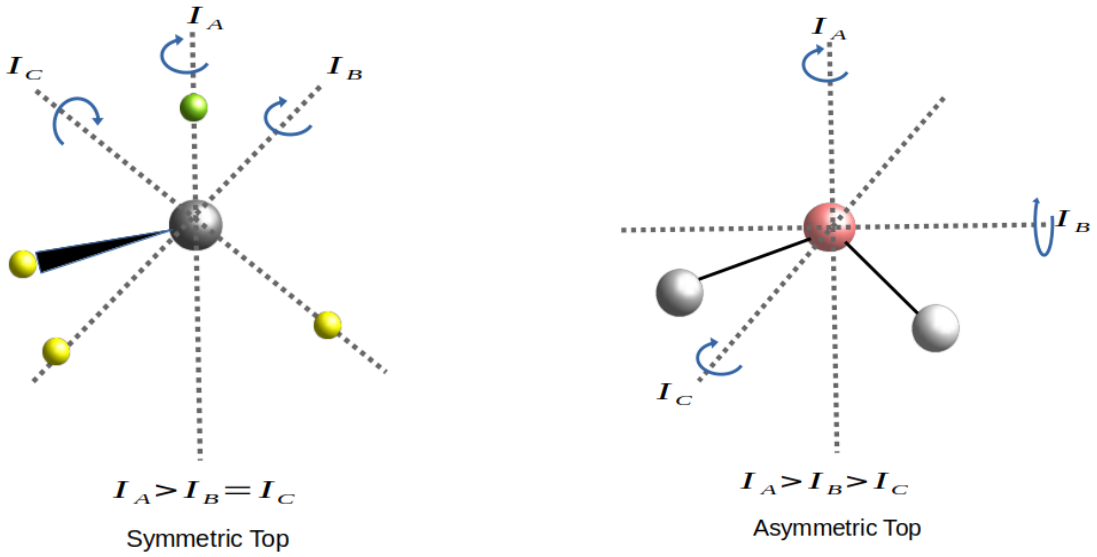

Figure 2.2: Representation of the symmmetric and asymmetric tops molecules.

From this classification scheme, the energy levels of the asymmetric vertex can be classified as even-even (ee), odd-odd (oo), even-odd (eo), and odd-even (oe) based on the parity of the quantum numbers K_a and K_c; in some cases, the system's *para* and *ortho* characters. Another labeling method involves the difference $\tau = K_a - K_c$, which is particularly useful because it reflects the decreasing order of energy levels within a given J state, with the levels ordered by decreasing values of τ. The value of τ is positive for the *para* character and negative for the *ortho* character. Table 2.1 presents the energy levels of asymmetric rotors for $J = 0, 1, 2, 3$ according to this classification.

2.4.3.1 The vibrational energy levels:Harmonic Oscillator:

The vibrational motion of molecules is generally modeled by a harmonic oscillator. In the case of a molecule composed of N atoms, $3N - 6$ vibrational modes can be identified (or 3N-5 for a linear molecule), and each of these modes can be approximated by a harmonic oscillator. However, in reality, molecular vibrations exhibit anharmonic behavior, leading to a dissociation limit. The model of the harmonic oscillator remains relevant for describing the lowest energy levels, such as the vibrational ground state. The Schrödinger equation

Table 2.1: The expressions used to determine the first energy levels of rigid rotor as a function of the rotational constants with the total angular momentum $J = 0, 1, 2, 3$ [2].

τ	$J_{k_a k_b}$	E_r
0_0	0_{00}	0
1_1	1_{10}	$A + B$
1_0	1_{11}	$A + C$
1_{-1}	1_{01}	$B + C$
2_2	2_{20}	$2A + 2B + 2C + 2\sqrt{(B-C)^2 + (A-C)(A-B)}$
2_1	2_{21}	$4A + B + C$
2_0	2_{11}	$A_x + 4B + C$
2_{-1}	2_{12}	$A + B + 4C$
2_{-2}	2_{02}	$2A + 2B + 2C - 2\sqrt{(B-C)^2 + (A-C)(A-B)}$
3_3	3_{30}	$5A + 5B + 2C + 2\sqrt{4(A-B)^2 + (A-C)(B-C)}$
3_2	3_{31}	$5A + 2B + 5C + 2\sqrt{4(A-C)^2 - (A-B)(B-C)}$
3_1	3_{21}	$2A + 5B + 5C + 2\sqrt{4(B-C)^2 + (A-B)(A-C)}$
3_0	3_{22}	$4A + 4B + 4C$
3_{-1}	3_{12}	$5A + 5B + 2C - 2\sqrt{4(A-B)^2 - (A-C)(B-C)}$
3_{-2}	3_{13}	$5A + 2B + 5C - 2\sqrt{4(A-C)^2 - (A-B)(B-C)}$
3_{-3}	3_{03}	$2A + 5B + 5C - 2\sqrt{4(B-C)^2 + (A-B)(A-C)}$

for a one-dimensional harmonic oscillator is expressed as

$$\hat{H}_v\psi_v = \frac{1}{2}(\hat{P}^2 + \omega^2 Q^2)\psi = E_v\psi_v \tag{2.4.30}$$

where Q represents the coordinate weighted by mass, and $\hat{P} = -\mathrm{i}\hbar\frac{\partial}{\partial\omega}$ is the conjugate momentum. The harmonic vibrational frequency ω is given by $\omega = \sqrt{\frac{k}{m}}$, where k is the harmonic-oscillator force constant associated to the reduced mass m. By solving equation 2.4.30, the eigenvalues are obtained as $E_v = (v + \frac{1}{2})\hbar\omega$, with v being the vibrational quantum number that can take values $0, 1, 2, \cdots$. The minimum energy at $v = 0$ is not located at the bottom of the potential well but is equal to $\frac{\hbar\omega}{2}$, a quantity known as the zero-point energy. For a multidimensional system with N atoms, the harmonic

oscillator Shrödinger equation and eigenvalues can be written as follows

$$\hat{H}_v|\psi_v\rangle = \frac{1}{2}\sum_{i=1}^{3N-6}(\hat{P}_i^2 + \omega_i^2 Q_i^2)|\psi\rangle = E_v|\psi_v\rangle \tag{2.4.31}$$

$$E_v = \sum_{i=1}^{3N-6}\left(v_i + \frac{1}{2}\right)\hbar\omega \tag{2.4.32}$$

2.5 Quantum dynamics simulation with the MCTDH method

2.5.1 Fundamentals of Time-Dependent Computational Methods

The MCTDH, which stands for the MultiConfiguration Time-Dependent [172, 173, 174, 148], is a method used to solve the Time Dependent Schrödinger equation (TDSE).

$$\mathrm{i}\hbar\frac{\partial}{\partial t}|\Psi\rangle = \hat{H}|\Psi\rangle \tag{2.5.1}$$

where $|\Psi\rangle$ is the wave function and $\hat{H}$ is the Hamiltonian operator of the system.

This approach relies on the Dirac-Frenkel variational principle, allowing for the identification of fundamental functions and optimal coefficients that yield the most compact basis set possible. Essentially, it operates as a contraction method. This technique integrates key concepts from both the standard method [175, 176] and the time-dependent Hartree method [177], bringing together elements from these two approaches to enhance its overall efficacy. The subsequent two sections offer a review of the standard method and Time-Dependent Hartree (TDH), serving as background information for MCTDH. Both methods are identified as limits to MCTDH, and the distinct foundational principles of these two theories contribute to a good understanding of MCTDH.

The best way to solve the TDSE is to use the expression of the wave function on a direct-product basis and solve the resulting equation of motion. Here, the total time-dependent wave function can be written as a function of time-independent basis sets.

The uni-dimensional wave function is expressed as follows [178]:

$$\Psi(q_1,\ldots,q_f,t)=\sum_{j_1=1}^{N_1}\cdots\sum_{j_p=1}^{N_f}C_{j_1,\cdots,j_f}(t)\chi_{j_1}^{(1)}(q_1)\ldots\chi_{j_f}^{(f)}(q_f)\ , \tag{2.5.2}$$

In equation 2.5.2, f is the total number of Degrees Of Freedom (DOF), $q_1,\ldots,q_f$ are nuclear coordinates or nuclear degree of freedom, $C_{j_1,\cdots,j_f}$ stands for time-dependent expansion coefficients; $\chi_{j_1}^{(1)}(q_1)\ldots\chi_{j_f}^{(f)}(q_f)$ functions are the orthonormal time-independent basis functions for degrees of freedom k, and N_k is the number of basis functions employed for the kth DOF. In the pursuit of an efficient and accurate assessment of the Hamiltonian operator $\hat{H}$ acting on the wave function Ψ, a strategic selection of basis functions becomes imperative. To facilitate this, the use of Discrete Variable Representation (DVR) [179, 180, 181, 182] or Finite Basis Representation (FBR) [183] functions within a collocation method emerges as the best choice. Employing such basis functions not only ensures computational efficiency but also allows for a finite representation that adapts to the intricacies of the quantum system under consideration. The N_k basis functions are $\chi_{j_1}^{(1)}(q_1)\ldots\chi_{j_f}^{(f)}(q_f)$ and can be systematically chosen in the DVR/FBR, facilitating a seamless integration with the collocation method. This approach not only enhances the accuracy of the calculations but also streamlines the numerical evaluation of the Hamiltonian's action on the wave function, thereby contributing to the overall success of the quantum mechanical analysis. The dynamics of the expansion coefficients of the Ansatz wave fuction $C_{j_1,\cdots,j_f}(t)$ governing the time evolution of a quantum system can be derived systematically through the application of the Dirac-Frenkel variational principle [184]. This principle, to be elaborated upon in subsequent sections, forms the foundation for obtaining equations of motion that govern the evolution of the system's wave function. By employing the Dirac-Frenkel variational principle, one seeks the optimal set of coefficients by minimizing the action integral and obtaining the equations of motion that can be interplayed between the system's Hamiltonian and the wave function's coefficients, providing a comprehensive framework for understanding the quantum mechanical evolution of the system under consideration. The Dirac-Frenkel variational principle is expressed as:

$$\langle \delta\Psi | \hat{H} - \mathrm{i}\partial_t | \psi \rangle = 0, \tag{2.5.3}$$

where $\delta\Psi$ can be expressed with respect to variations in the wave function caused by changes in multiple parameters λ of the wave function defined as follows:

$$\delta\Psi = \sum_{\lambda} \frac{\partial \Psi}{\partial \lambda} \delta\lambda \tag{2.5.4}$$

Applying this formulation to the wave function equation 2.5.2, we obtain the following equations [185]:

$$\begin{aligned} \delta\Psi &= \sum_{j_1=1}^{N_1} \cdots \sum_{j_f=1}^{j_f} \delta C_{j_1 \cdots j_f}(t) \prod_{k=1}^{f} \chi_{i_\kappa}^{(k)}(q_k) \\ \dot{\Psi} &= \sum_{j_1}^{N_1} \cdots \sum_{j_f=1}^{N_f} \dot{C}_{j_1 \cdots j_f}(t) \prod_{k=1}^{f} \chi_{i_\kappa}^{(k)}(q_k) \end{aligned} \tag{2.5.5}$$

Applying the variational principle, we obtain the following equations:

$$\begin{aligned} &\langle \chi_{j_1}^{(1)} \cdots \chi_{j_f}^{(f)} | \sum_{j_1=1}^{N_1} \cdots \sum_{j_f=1}^{N_f} C_{l_1 \cdots l_f} H | \chi_{j_1}^{(1)} \cdots \chi_{j_f}^{(1)} \rangle \\ &= \mathrm{i} \langle \chi_{j_1}^{(1)} \cdots \chi_{j_f}^{(f)} | \sum_{j_1=1}^{N_1} \cdots \sum_{j_f=1}^{N_f} \dot{C}_{l_1 \cdots l_f} | \chi_{j_1}^{(1)} \cdots \chi_{j_f}^{(1)} \rangle \end{aligned} \tag{2.5.6}$$

We can then obtain the dependent equation of motion for the expansion coefficients as follows.

$$\mathrm{i}\dot{C}_{j_1 \cdots j_f} = \sum_{p_1=1}^{N_1=1} \cdots \sum_{p_f}^{N_f} \langle \chi_{(j_1)}^{(1)} \cdots \chi_{j_f}^{(f)} | H | \chi_{(l_1)}^{(1)} \cdots \chi_{l_f}^{(f)} \rangle C_{l_1 \cdots l_f} \tag{2.5.7}$$

2.5.2 The MCTDH Approach

2.5.2.1 Equations of motion:

MCTDH is a time-dependent method where the degrees of freedom are associated with a small number of orbitals (or SPFs), which, through their time dependence, allow an efficient description of the molecular dynamical processes. The wave function is defined using coefficients and time-dependent functions. To develop the equations of motion in the context of the MCTDH method comprehensively, I mainly consulted references [173, 149]. These sources provide essential theoretical foundations and practical examples that have helped me better understand and analyze molecular dynamics within this approach. and most equations for this method are also taken from reference [186]. It is discretized into a set of configurations, and following the TDH method, the total MCTDH wave function is expanded in Hartree products, that is, products of SPFs:

$$\begin{aligned}\Psi(Q_1,\ldots,Q_f,t) &= \sum_{j_1=1}^{n_1}\cdots\sum_{j_f=1}^{n_f} A_{j_1\cdots j_f}(t)\prod_{\kappa=1}^{f}\phi_{j_\kappa}^{(\kappa)}(Q_\kappa,t)\\ &= \sum_{J} A_J\Phi_J\\ &= \sum_{j=1}^{n_k}\varphi_j^{(k)}\Psi_j^{(k)}\ ,\end{aligned} \tag{2.5.8}$$

With $1 \leq k \leq f$

where f is the number of DOF of the system, $Q_1,\ldots,Q_f$ are the combined nuclear coordinates, $A_\Lambda \equiv A_{j_1\cdots j_f}$ denotes the expansion coefficients for the MCTDH, and $\phi_{j_\kappa}^{(\kappa)}(Q_\kappa,t)$ are the n_κ SPFs associated with each degree of freedom κ (*i.e.*, they form a time dependent variable basis along κ).

The following equations of motion for the expansion coefficients and SPFs are then derived after substituting the wave function $ansatz$ into the time-dependent Schrödinger equation.

To solve the equations of motion, the κ SPFs are represented on a (fixed) primitive basis or discrete variable representation (DVR)-grid [181] of N_κ points:

$$\varphi_{j_\kappa}^{(\kappa)}(Q_\kappa,t) = \sum_{i_\kappa=1}^{N_\kappa} c_{i_\kappa j_\kappa}^{(\kappa)}(t)\chi_{i_\kappa}^{(\kappa)}(Q_\kappa)\ , \tag{2.5.9}$$

where ideally the n_κ of equation 2.5.8 is such that $n_\kappa << N_\kappa$.

Constraints must be applied to prevent the phases and norms of the SPFS from becoming degenerated.

$$\langle \varphi_j^k(q_j,0)|\varphi_l^k(q_l,0)\rangle = \delta_{jl}, \tag{2.5.10}$$

and

$$\langle \varphi_j^k(q_j,t)|\dot{\varphi}_l^k(q_l,t)\rangle = -\mathrm{i}\langle \varphi_j^k(q_j,t)|g^{(k)}|\varphi_l^k(q_j,t)\rangle, \tag{2.5.11}$$

where $g^{(k)}$ is a Hermitian constraint operator that acts solely on the k_{th} DOF.

Constraints in equations 2.5.10 and 2.5.11 ensure that the single-particle functions, initially orthonormal, remain so throughout the propagation. The last two formulations of equation 2.5.8 under a new reformulation, lead us to choose a phi function $\psi_l^{(k)}$. It is special because it is composed of various parts, excluding a particular type of part known as single-particle functions associated with a specific aspect known as the kth degree of freedom. This ψ_j is expressed as follows

$$\psi_l^{(k)} = \sum_{j_1}\cdots\sum_{j_{k-1}}\sum_{j_{k+1}}\cdots\sum_{j_f} A_{j_1\cdots j_{k-1}l j_{k+1}\cdots j_f}\,\varphi_{j_1}^{(1)}\cdots\varphi_{j_{k-1}}^{(k-1)}\varphi_{j_{k+1}}^{(k+1)}\cdots\varphi_{j_f}^{(f)} \tag{2.5.12}$$

When we differentiate equation 2.5.12 above stated the wave function in its time-dependent form equation 2.5.12 with respect to the expansion coefficient A_J and the SPFs, we obtain:

$$\frac{\delta\psi}{\delta A_J} = \phi_J, \tag{2.5.13}$$

and,

$$\frac{\delta\psi}{\delta\varphi_j^{(k)}} = \psi_j^{(k)}, \tag{2.5.14}$$

We can then obtain the differentiation equation for the wave function:

$$\dot{\psi} = \sum_j \dot{A}_J \Phi_J + \sum_{k=1}^{n}\sum_{j=1}^{n_k} \dot{\varphi}_j^{(k)} \psi_j^{(k)}, \tag{2.5.15}$$

The equation for δA is then obtained by considering the variation with respect to the expansion coefficients A:

$$\langle \delta\psi | H | \rangle = \langle \Phi_J | H | \psi \rangle = \sum_L \langle \Phi_J | H | \Phi_L \rangle A_L, \tag{2.5.16}$$

and,

$$\begin{aligned} \mathrm{i}\langle \delta\psi | \dot{\psi} \rangle \quad &= \mathrm{i}\langle \Phi_J | \dot{\psi} \rangle = \langle \Phi_J | H | \psi \rangle \\ &= \mathrm{i}\dot{A}_J + \mathrm{i}\sum_k \sum_l \big(-\mathrm{i} g_{j_k l}^{(k)} \big) A_{J_l^k}, \end{aligned} \tag{2.5.17}$$

From the Dirac-Frenkel variational principle using the constraint above, one can obtain the following equations by varying the coefficients:

$$\langle \Phi_J | \psi \rangle - \mathrm{i}\langle \Phi_J | H | \dot{\psi} \rangle = 0, \tag{2.5.18}$$

We get the following expression

$$\mathrm{i}\dot{A}_J = \sum_L \langle \Phi_J | H | \Phi \rangle A_L - \sum_{k=1}^{f}\sum_{l=1}^{n_k} \langle \varphi_j^{(k)} | g^{(k)} | \varphi_l^{(k)} \rangle A_{j_1 \cdots j_{k-1} l_{j_{k+1} \cdots j_f}}, \tag{2.5.19}$$

Variation with respect to the SPFs induced the following equations:

$$\langle\psi_j^{(k)}|H|\psi\rangle = \mathrm{i}\langle\psi_j^{(k)}|\sum_{m=1}^{f}\sum_{j=1}^{n'_k}\dot{\varphi}_j^{(m)}\varphi_j^{(m)}\rangle + \mathrm{i}\sum_J\langle\psi_j^{(k)}|\Phi_J\rangle\dot{A}_J, \tag{2.5.20}$$

The constraint $g_{jl}^{(k)} = \langle\varphi^{(k)}|g^{(k)}|\varphi_l^{(k)}\rangle$ has been chosen for simplifications. This gives the new expression of equation 2.5.20 as follows

$$\mathrm{i}\sum_{l=1}^{n_k}\rho_{jl}^{(k)}\dot{\varphi}_l^{(k)} = \langle\psi_j^{(k)}|H|\psi\rangle - \sum_J\langle\psi_J^{(k)}|\Phi_J\rangle\langle\Phi_J|H|\psi\rangle + \sum_{k,l=1}^{n_k}\rho_{jl}^{(k)}g_{lk}^{(k)}\phi_l^{(k)}, \tag{2.5.21}$$

where the matrix density is given by:

$$\rho_{jl}^{(k)} = \langle\psi_j^{(k)}|\psi_l^{(k)}\rangle, \tag{2.5.22}$$

From the following equations:

$$\sum_J\langle\varphi_j^{(k)}|\Phi_J\rangle\langle\Phi_J| = P^{(k)}\langle\psi_j^{(k)}| \tag{2.5.23}$$

and

$$\langle\psi_j^{(k)}|H|\psi\rangle = \sum_{l=1}^{n_k}\langle H\rangle_{jl}^{(k)}\phi_l^{(k)}, \tag{2.5.24}$$

The projector for the MCTDH is given as follows

$$P^{(k)} = \sum_{j=1}^{n_k}|\psi_j^{(k)}\rangle\langle\psi_j^{(k)}|, \tag{2.5.25}$$

The equations of motion for the expansion coefficients and the SPFs are given by:

$$\mathrm{i}\dot{A}_J = \langle\Phi_J|H|\psi\rangle - \sum_{k=1}^{f}\sum_{l=1}^{n_k}\langle\varphi_j^{(k)}|g^{(k)}|\varphi_l^{(k)}\rangle A_{j_1\cdots j_{k-1}l_{j_{k+1}\cdots j_f}} \tag{2.5.26}$$

$$\mathrm{i}\dot{\varphi}^{(k)} = g^{(k)}\varphi^{(k)} + \left(1 + P^{(k)}\right)\left[\rho^{(k)^{-1}}\langle H\rangle^{(k)} - g^{(k)}\right]\varphi^{(k)} \tag{2.5.27}$$

Equations 2.5.26 and 2.5.27 are obtained using vectorial simplifications for SPFs, such that $\varphi^k = \left(\varphi^{(1)}, \cdots, \varphi^{(k)}_{n_k}\right)$. By fixing the constraint $g^{(k)} = 0$ for a better simplification, we obtain the following equations of motion

$$\mathrm{i}\dot{\mathbf{A}}_{\mathbf{J}} = \sum_{\mathbf{L}} \langle \mathbf{\Phi_J}|\mathbf{H}|\mathbf{\Psi}\rangle \mathbf{A_L}, \tag{2.5.28}$$

Equation 2.5.28 can be written in a compact form as follows

$$\mathrm{i}\dot{\mathbf{A}}_{\mathbf{J}} = \sum_{\mathbf{L}} \mathbf{K_{JL}}\mathbf{A_L}, \tag{2.5.29}$$

where $K_{JL} = \langle \Phi_J|H|\Psi\rangle$.

$$\mathrm{i}\dot{\varphi}^{(\mathbf{k})} = \left(\mathbf{1} - \mathbf{P}^{(\mathbf{k})}\right)\left(\rho^{(\mathbf{k})}\right)^{-\mathbf{1}}\langle \mathbf{H}\rangle^{(k)}\varphi^{(k)}, \tag{2.5.30}$$

To conclude this section, employing MCTDH enables us to achieve precise results with relatively short computational times. This method's effectiveness lies in its use of a multi-configuration approach, which represents the wave function compactly through time-dependent basis vectors. However, the wave function expansion in MCTDH relies on a sum-of-products form, which is also required for the system Hamiltonian. This means that the Hamiltonian must be rewritten as a sum of operator products acting on individual modes. The kinetic energy operator generally fits well in this format, whereas the potential term's adaptability depends on the problem's complexity. If an analytic form for the potential isn't possible, MCTDH offers a program called potfit, which uses a numerical approach similar to MCTDH to convert the potential into the necessary form. In Section 2.6.2, In the following section, I will discuss the numerical methods used to solve the time-dependent Schrödinger equation before providing a general discussion of this method.

2.5.3 Discussion about the block improved relaxation method

Various methods are available for solving the time-independent Schrödinger equation. The most straightforward approach involves diagonalizing the Hamiltonian matrix within a chosen basis. The basis size is determined by the system's degrees of freedom (DOFs) and the desired number of eigenstates. However, direct diagonalization for large matrices is computationally demanding and may even become impractical, making it less suitable for multi-dimensional systems. Several methods, such as iterative approaches like Davidson [187] and Lanczos [188], are widely used to compute eigenvalues and eigenvectors of large matrices. In this thesis, I have employed an approach integrated into the MCTDH framework known as Improved Relaxation, which incorporates these iterative techniques with the relaxation method. The following section presents an introduction to the relaxation method and highlights enhancements introduced by MCTDH.

2.5.3.1 Relaxation method:

The relaxation method, introduced by R. Kosloff $et\ al.$ [189], provides a way to solve the time-independent Schrödinger equation by employing a time-dependent approach. The core concept is that propagating a state under a Hamiltonian in negative imaginary time will cause it to converge to the Hamiltonian's lowest-energy eigenstates. This principle is easily demonstrated by examining the time evolution of any given state within the eigenstate basis. The eigenstates wave function in this case with the negative imaginary time $\tau = -\mathrm{i} \times t$ is expressed as follows [186]:

$$\varphi(t) = \sum_n a_n e^{-E_n t \varphi_n}, \tag{2.5.31}$$

Equation 2.5.31 above shows that the final wave function includes a term that decays exponentially at a rate proportional to its energy E_n. This implies that components associated with higher-energy eigenstates will decay much faster over time compared to those of lower-energy states. By propagating for a sufficiently long period and renormalizing, only the ground state remains. The system thus relaxes into its lowest energy configuration. To obtain excited states, we project the Hamiltonian onto a Hilbert space that

excludes previously calculated states, then allow the system to relax to the new lowest state within this space, now representing the first excited state, and so forth. We can select an appropriate initial wave function for accurate convergence, as the calculation will always yield the lowest-energy state contained within the chosen initial state. Therefore, the initial state should be chosen to encompass the energy range of interest.

2.5.3.2 Improved relaxation method:

As its name implies, the MCTDH method is developed to solve the time-dependent Schrödinger equation. However, it can also compute stationary states through its improved relaxation program, which leverages the time-dependent Schrödinger framework. This program enhances the traditional relaxation approach by incorporating diagonalization steps throughout the relaxation process. Through this approach, one can accurately determine the eigenstates and resonances [185, 190]. This stands in contrast to using the evolution operator, which typically yields excited states. This method is an MultiConfiguration Self-Consistent Field (MCSCF), an approach where the SPFs are optimized by relaxation [189, 191] and the coefficient vector (A-vector) is calculated by diagonalization of the Hamiltonian matrix evaluated in the set of SPFs. Improved relaxation method implemented in the block improved relaxation is employed to compute the rovibrational energy levels. This approach involves integrating relaxation techniques with the diagonalization of the Hamiltonian operator, mainly on the A-vector.

The algorithm can be derived from the so-called standard time-independent variational principle:

$$\delta\Big\{\langle\psi|\hat{H}|\psi\rangle - E\big(\sum_{J} A_J^* A_J - 1\big)\sum_{k=1}^{p}\sum_{j,l=1}^{n_k}\varepsilon_{jl}^{(k)}\big(\langle\phi_j^{(k)}|\phi_l^{(k)}\rangle - \delta_{ij}\big)\Big\} = 0, \qquad (2.5.32)$$

The approach used associates this restriction with the Lagrange parameter and is generally used to improve the parameters. Interestingly, for a few number of factors, the Lagrange parameter used in this approach is larger than that typically employed by standard meth-

ods. Here, E is the major Lagrange parameter in such an equation which was introduced earlier to ensure that A-vectors are normalized, and $\varepsilon_{jl}^{(k)}$ serves to ensure that SPFs applied herein are orthonormal.

The Hamiltonian corresponding to the particles j and k of the system can be written as follows

$$H_{jk} = \langle \Phi_j | H | \Phi_k \rangle, \tag{2.5.33}$$

Varying A_J^*, we obtain the following equation:

$$\sum_L H_{JL} A_k = E A_J, \tag{2.5.34}$$

From equation2.5.33, A is the eigenvector of the Hamiltonian matrix H_{JL}. To obtain the relation for the SPFs, one can follow the formula:

$$\langle \varphi | H | \varphi \rangle = \langle \sum_j \Psi_j^{(k)} \varphi_j^{(k)} | H | \sum_l \Psi_l^{(k)} \varphi_l^{(k)} = \sum_{j,l} \langle \varphi_j^{(k)} | \langle H \rangle_{jl}^{(k)} | \varphi^{(k)} \rangle, \tag{2.5.35}$$

with the total wave function expressed as follows

$$\Psi = \sum_{l=1}^{n_k} \varphi_l^{(k)} \Psi_l^{(k)}, \tag{2.5.36}$$

and varying $\langle \varphi_l^{(k)} |$, we obtain:

$$\sum_{l=1}^{n_k} \langle H \rangle_{jl}^{(k)} \varphi_l^{(k)} = \sum_{l=1}^{n_k} \varepsilon_{jl}^{(k)} \varphi_l^{(k)}, \tag{2.5.37}$$

Projecting equation 2.5.37 onto $\langle \varphi_k^{(k)} |$, we arrive at:

$$\varepsilon_{jk}^{(k)} = \sum_l \langle \varphi_k^{(k)} | \langle H \rangle_{jl}^{(k)} | \varphi_l^{(k)} \rangle, \tag{2.5.38}$$

From equations 2.5.37 and 2.5.38, it follows:

$$\left(1 - P^{(k)}\right) \sum_{l=1}^{n_k} \langle H \rangle_{jl}^{(k)} \varphi_l^{(k)} = 0, \tag{2.5.39}$$

Equation 2.5.39 is a compact expansion that is applicable to any number j. Similarly, it remains valid for any linear combination of j as well. Upon derivation of the aforementioned expression, we obtain the expression of motion governing the MCTDH method. When we insert the inverse of the matrix density, we arrive at:

$$\dot{\varphi}_j^{(k)} = -(1 - P^{(k)}) \sum_{kl}^{n_k} (\rho^{(k)})^{-1} \langle H \rangle_{jl}^{(k)} \varphi_l^{(k)}, \tag{2.5.40}$$

where $\dot{\varphi}$ stands for the time derivative in negative imaginary time

$$\dot{\varphi} = \frac{\partial \varphi}{\partial \tau}, \qquad \tau = -it \tag{2.5.41}$$

Equations 2.5.39 and 2.5.40 are considered equivalent under the condition that the inverse of the matrix density ρ^{-1} is nonsingular. Consequently, the variational solution is obtained only when the time derivatives of the SPFs become zero. This observation presents a practical approach to solving equation 2.5.39 variationally: by relaxing the SPFs (propagating them in negative imaginary time) until their time derivative reaches a sufficiently small value.

In order to find the best solution for calculating eigenstates, we need to satisfy equations 2.5.34 and 2.5.39 simultaneously. This leads us to equations 2.5.34 and 2.5.40 as the working equations in the MCTDH code. By choosing the right eigenstate, we can guide the algorithm to converge either to the ground state or to an excited state.

Since both equations 2.5.34 and 2.5.40 must be satisfied together, we use an iterative process. We start with a guess for the wave function and then diagonalize the Hamiltonian using the current SPFs as a basis to update the coefficients A_J according to equation 2.5.34. Next, we improve the SPFs while keeping the coefficient vector A_J con-

stant through short-time relaxation based on equation 2.5.40. This cycle continues until we achieve self-consistency.

The improved relaxation method involves propagating a block of initial vectors together to collectively converge towards a set of eigenstates.

The Heidelberg MCTDH package serves as a comprehensive suite of programs and routines within the realm of theoretical chemistry, specifically quantum dynamics calculations. This versatile package offers a range of functionalities essential for various computational tasks. Among these features are tools for fitting the PESs, which are appropriate for accurately describing chemical systems and reactions. Additionally, the package enables the propagation of wave packets, facilitating the simulation of quantum mechanical dynamics. Furthermore, it provides capabilities for the precise calculation of spectral lines, aiding in the analysis and interpretation of experimental spectroscopic data. Moreover, the package includes tools for propagation analysis.

2.6 Representation of the Potential Energy Surface

In this section, I will present the advantages of representing the potential energy surface for quantum dynamics calculations. To do this, I will start by defining the potential energy operator. The potential energy operator $\hat{V}(R)$ is generally expressed as a function of the coordinates of all particles involved in the system. For a system with multiple dimensions, the potential operator can be expressed in terms of generalized coordinates $q_1, q_2, \cdots, q_N$, where N is the number of degrees of freedom: $\hat{V}(R) = \hat{V}(q_1, q_2, \cdots, q_N)$. In systems with high degrees of freedom, it is often useful to exploit the physical symmetries of the system to further simplify the representation of the potential. For example, in symmetric molecules, the potential can be expressed in terms of symmetric combinations of coordinates (internal coordinates, angles, distances, etc.). The representation of the potential energy operator in MCTDH is a key step in reducing the complexity of quantum dynamics calculations. The decomposition into a sum of products allows for a simpler expression of the potential, thereby facilitating the numerical solution of the system equations using

the POTFIT algorithm implemented in the MCTDH code. However, when the number of degrees of freedom is too high for the POTFIT method to be applicable, it becomes necessary to represent the operator $\hat{V}(R)$ term by term, analytically. This means that each term of the potential is explicitly defined and implemented in the calculation. The general form of the potential operator could then be represented as a sum of analytically produced product terms:

$$\hat{V}(R) = \sum_{l} f_1^l(q_1) f_2^l(q_2) \cdots f_N^l(q_N), \tag{2.6.1}$$

where each function $f_j^(l)(q_j)$ is analytically defined for each coordinate q_j. This approach allows for the treatment of complex potentials that cannot be represented using the POTFIT algorithm.

2.6.1 Potential energy surface for MCTDH

We demonstrated previously how to obtain a potential energy surface from the Born-Oppenheimer approximation. The PES obtained, usually from *ab initio* calculations, are not immediately usable in the context of an MCTDH calculation. It is necessary to transform them into a suitable product form in order to make the calculations feasible. I also remind you that representation of the PES in the MCTDH code is the first step in any dynamics calculation.

In this dissertation, I use the MCTDH to solve equations that describe how systems move over time. When dealing with quantum dynamics, we need to break down the system's possible configurations into a grid. Each point on this grid represents a different way the system can be arranged. To understand how the system evolves, we often need to calculate a lot of complex mathematical quantities called matrix elements. This procedure would take a very long time if it had to be done for one grid point at a time.

The simplest approach to achieving a product form potential is by expanding it using a

product basis:

$$V^{app}(q_1, \cdots, q_f) = \sum_{j_1=1}^{n_1} \cdots \sum_{j_f=1}^{n_f} C_{j_1 \cdots j_f} v_{i_1}^{(1)}(q_1) \cdots v_{i_f}^{(f)}(q_f), \tag{2.6.2}$$

where $q_i^{(k)}$ stands for the position of the i-th grid point of the k-th grid. So, we can define:

$$V_{i_i, \cdots, i_f} = V(q_{i_1}^{(1)}, \cdots, q_{i_f}^{(f)}), \tag{2.6.3}$$

where $V_{i_i, \cdots, i_f}$ is the value of the potential at the grid points. One important solution we can use is called the Tucker form. This method helps us simplify the calculations by organizing the data in a more efficient way, so we do not have to compute every single matrix element individually. It is like finding a simple way to make our calculations faster and more manageable.

The approximate potential using the Tucker form is written as follows:

$$V_{i_1 \cdots i_f}^{app} = \sum_{j_1=1}^{n_1} \cdots \sum_{j_f=1}^{n_f} C_{j_1 \cdots j_f} v_{i_1 j_1}^{(1)} \cdots v_{i_f j_f}^{(f)}, \tag{2.6.4}$$

With $v_{i_m j_m}^{(m)}$ representing the SPFs and $C_{j_1 \cdots j_f}$ the coefficients, we use the traditional POTFIT algorithm [192, 193] to rewrite the potential energy as a sum-of -products of SPFs.

Among the MCTDH packages developed, the Heidelberg MCTDH package [61] is the most accessible one used in this thesis. It is a complete set of theoretical chemistry programs and routines useful for quantum dynamics simulations.

2.6.2 The POTFIT algorithm

In this thesis, every calculation begins with the representation of the PES, which, like the KEO operator, has to be represented in the Sum-Of-Products (SOP) form. Sometimes,

especially for systems with less than six dimensions, the PES is not already in this form. In such cases, we use a handy tool called POTFIT [192, 193] implemented in the MCTDH package [61]. This tool, which is part of the MCTDH package we are using, helps us efficiently convert the PES into the right format for our calculations. As mentioned in the previous paragraph, to avoid multi-dimensional integral calculations, we need to put the potential into Tucker form using the POTFIT algorithm. The single particle functions can be optimized and obtained through the optimization expression given by:

$$\Delta^2 = \sum_{i_1=1}^{N_1} \cdots \sum_{i_f=1}^{N_f} \left(V_{i_1 \cdots i_f} - V^{app}_{i_1 \cdots i_f} \right)^2 = \sum_{I} \left(V_I - V^{app}_I \right)^2, \tag{2.6.5}$$

where index I runs through all grid points, Δ^2 is also minimized by employing the variation of the expansion coefficients, according to the following equation:

$$C_{j_1 \cdots j_f} = \sum_{i_1=1}^{N_1} \cdots \sum_{i_f=1}^{N_f} V_{i_1 \cdots i_f} v^{(1)}_{i_1 j_1} \cdots v^{(f)}_{i_f j_f}, \tag{2.6.6}$$

We need to find the optimal single-particle potentials (SPPs), and this can be done using the density matrices of the potential energy surface corresponding to each degree of freedom:

$$\rho^{(k)}_{kk'} = \sum_{I^k} V_{I^k_k} V_{I^k_{k'}}, \tag{2.6.7}$$

We use indices I^k to iterate through all grid points except for the k-th one, and I^k_k replaces the k-th index with k. Afterwards, we diagonalize the density matrices $\rho^{(k)}$, where the eigenvectors represent the SPFs, also known as natural potentials, and the eigenvalues represent the natural weights. Employing all eigenvectors yields the exact potential. However, the POTFIT algorithm selectively ignores eigenvectors based on their natural weights; those with small weights are disregarded. This selective process allows

us to transition from the exact potential.

$$V^{exact}_{i_1\cdots i_f} = \sum_{j_1=1}^{N_1} \cdots \sum_{j_f=1}^{N_f} C_{j_1\cdots j_f} v^{(1)}_{i_1 j_1} \cdots v^{(f)}_{i_f j_f}, \tag{2.6.8}$$

The approximate potential is then written as:

$$V^{app}_{i_1\cdots i_f} = \sum_{j_1=1}^{m_1} \cdots \sum_{j_f=1}^{m_f} C_{j_1\cdots j_f} v^{(1)}_{i_1 j_1} \cdots v^{(f)}_{i_f j_f}, \tag{2.6.9}$$

2.6.2.1 Application of the POTFIT method:

In this section, I present the performance of the POTFIT algorithm. I used the recently constructed 4D-PES to study the PO^+-H_2 system. However, for this application, I used its 2D representation to make it possible to use the POTFIT algorithm. One can that this potential is used here only for testing purposes with the POTFIT algorithm. The potential was expressed as $V(R, \theta_1)$. Figure 2.3b shows the 2D contour plot of the two-dimensional PES for the description of the PO^+-H_2 system. Figure 2.3a presents the PES approximated using the POTFIT algorithm, while Figure 2.3c shows the absolute error $|V^{app}_{i_1\cdots i_f} - V^{exact}_{i_1\cdots i_f}|$ between the two. The channels visible in Figure 2.3c correspond to areas where the error is highest, as these are regions where the PES is less smooth. For this approximation of the PES, the maximum observed error is around 10^{-7} cm^{-1}, confirming the accuracy of the PES representation.

2.6.2.2 Contraction Scheme:

To make the calculations more efficient, one has to simplify the basis for the DOF with the highest natural weight. This can be done by finding a contraction coefficient that reduces the overall number of terms in the expansion. This coefficient is given by:

$$D^{(k)}_{j_1\cdots j_{k-1} j_{k+1}\cdots j_f} = \sum_{j_k=1}^{m_k} C_{j_1\cdots j_f} v^{(k)}_{i_k j_k}, \tag{2.6.10}$$

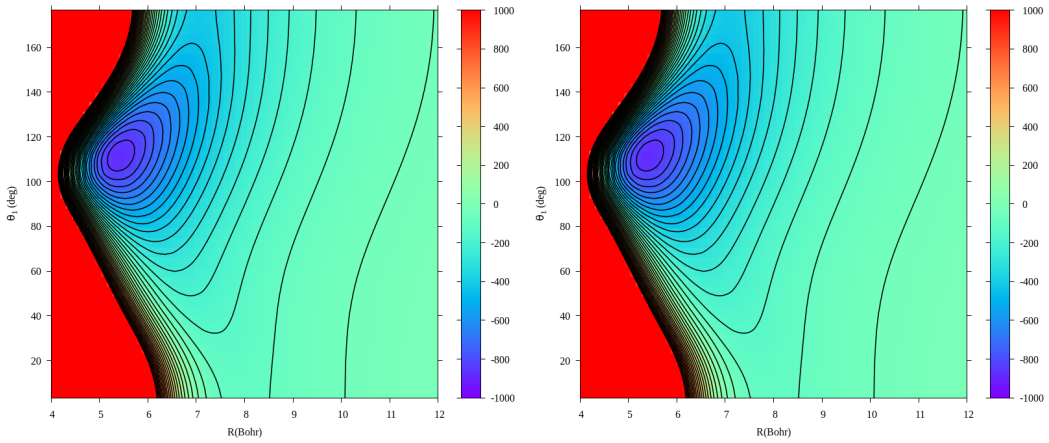

(a) (b)

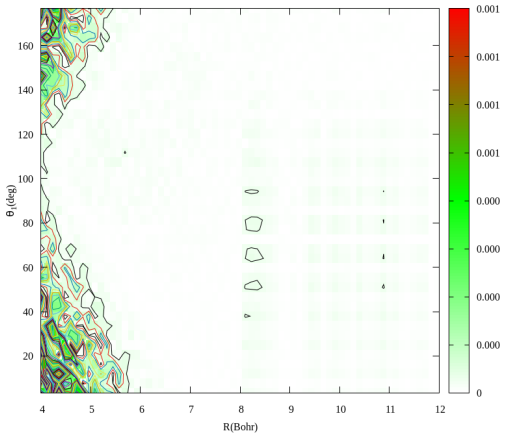

(c)

Figure 2.3: The first Figure 2.3b represents the exact potential used for the study of the PO^+-H_2 system. The second Figure 2.3a shows the potential adjusted by the POTFIT algorithm. Finally, the third Figure 2.3c illustrates the contour of the difference between the potential adjusted by POTFIT and the exact potential for the PO^+-H_2 system. The maximum observed error is 10^{-7} cm^{-1}.

We can then express our contracted potential as follows

$$V^{app}_{i_1\cdots i_f} = \sum_{j_1=1}^{m_1} \cdots \sum_{j_{k-1}}^{m_{k-1}} \sum_{j_{k+1}}^{m_{k+1}} \cdots \sum_{j_f}^{m_f} D^{(k)}_{j_1\cdots j_{k-1}j_{k+1}\cdots j_f} v^{(1)}_{i_1 j_1} \cdots v^{(k-1)}_{i_{k-1}j_{k-1}} v^{(k+1)}_{i_{k+1}j_{k+1}} v^{(f)}_{i_f j_f} \quad (2.6.11)$$

We can simplify any degree of freedom by using contractions, but typically, we choose

the one with the most terms to reduce complexity. When we contract, we do not need to calculate the coefficient vector C or the single-particle potentials for that specific mode. Currently, this traditional POTFIT method is not entirely valid for systems with more than four degrees of freedom. In this case, a method can be used that integrates the analytical potentials in the form of sums of products. This is the work we have carried out in this thesis, putting a lot of time into the transformation of potential energy surfaces for robust systems.

In this section, I have demonstrated all the theoretical methods used to represent a PES for MCTDH calculation.

Now, I will proceed to show step-by-step the results obtained through the application of these theoretical tools.

2.6.2.3 Study of the accuracy and the convergence of an MCTDH calculation:

The accuracy and convergence of an MCTDH calculation can be tested with respect to various parameters.

- The primitive basis,
- The SPF basis,
- The integrator.

The primitive basis test examines two main factors: the grid size and point density. To perform the calculations, a grid of maximum size is required to prevent wave packets from reflecting back and interfering with each other. This can be verified by analyzing the average center and width of the wave function and ensuring that the first and last grid points do not contain an excessive number of points. Additionally, there should be a sufficient number of points to accurately represent the basic functions. This process was previously referred to as fitting with interpolation. In this study, splines were utilized.

When the primitive basis and SPF are the same, the MCTDH calculation is exact. Therefore, if we want a good SPF, we need to increase the basis size until the property we are

calculating stops changing. The MCTDH code uses something called the density matrix to check the behavior of the SPFs. Eigenvectors and eigenvalues can also be parameters to show us whether the SPF has good values. If the smallest eigenvector's effect is small, the SPF is considered good for the calculation. However, it is better to choose the highest number of SPFs because, in the case of improved relaxation, when the values of the energies are non-negligible, the SPFs can affect the convergence.

We should avoid long simulations because they can lead to errors. To avoid this, the MCTDH code uses strong integration methods. But the best way to check if the integration is good is to make sure the total energy and the wave's size remain the same throughout the calculation. However, if we increase the size of the primitive base and add more SPFs, the calculation takes longer. This can be very difficult by taking a long time propagation when using the projection method to describe the PES.

2.6.3 Propagation of the Wave Packet

The inelastic collision study is very well performed. once a suitable form of the system Hamiltonian has been obtained, the initial wave packet must be constructed.

2.6.3.1 Wave Packet Flux Analysis in Molecular Collisions:

Employing the MCTDH method to propagate the wave packet on the potential energy surface (PES) by solving the Schrödinger equation is necessary to generate the initial wave packet before any calculation. This wave packet must have the required Hartree product form with a Gaussian energy distribution written as

$$\phi(R) = \frac{1}{\sqrt{2\pi\omega}} \exp\Big[-(\frac{R-R_0}{2\omega})^2 \Big] \exp^{\mathrm{i}p_0(r-R_0)}, \tag{2.6.12}$$

With R_0, p_0, and ω representing its center in coordinate and momentum space, and its width, respectively. The initial distribution is arranged so that the wave packet can initially move in any direction of the interaction zone, i.e., with negative or positive momentum

space values.

The wave packet propagation occurs on a grid that defines the potential, and the grid size has to be chosen to avoid some convergence issues. The wave packet is characterized by a Gaussian distribution function over a range of energies, not by a single energy. This results in different parts of the wave packet propagating at different speeds, with some parts already interacting and leaving the interaction zone while others are still present.

If the grid is too small, the front part of the wave packet may reach the edge of the grid before the whole wave packet has finished propagating. This leads to reflections at the grid's edge that return to the interaction zone, distorting the results. The simplest solution is to use a sufficiently large grid to avoid these issues, but this incurs high numerical calculation costs.

To reduce reflections when using a small grid size, Complex Absorbing Potential (CAP) [194] can be added to the nuclear Hamiltonian in the time-dependent Schrödinger equation. Placed near the grid ends, these CAPs absorb wave packet flux before it reaches the edge. However, introducing CAPs can cause reflections, so careful optimization is needed to minimize their impact. The CAPs can be written as

$$-\mathrm{i}W(x) = -\mathrm{i}\eta|x - x_c|^a\theta(x - x_c), \tag{2.6.13}$$

where η is the strength of the CAP, x_c is the starting point, a is its order, and θ is its Heaviside step function. One can also notice that the order a can influence the reflections produced by the CAP. The parameters of the CAP need to be fine-tuned to ensure complete absorption of the wave packet before reaching the grid's edge, while minimizing reflections. This optimization is done to enhance the effectiveness of the CAP in these calculations.

The optimal energy domain for a choice of CAP parameters imposes a strict restriction on the value of collision energy. If this energy is too large, some negligible reflections at

the ends of the Gaussian will occur. The CAP, placed at the end of the grid, can also be used to calculate the flux entering a specific channel, instead of measuring the flux through a surface positioned far into a channel.

2.6.3.2 Flux Analysis:

We recall our collisional process between two systems A and B.

$$A(i) + B(j) \longrightarrow A(i') + B(j'), \tag{2.6.14}$$

where $\lambda = (i, j)$ represents the initial state and $\lambda' = (i', j')$ represents the final state.

To calculate collision transitions and probabilities from the wave packet, it is essential to determine the elements of the scattering S-matrix element. Ideally, the wave packet should be propagated deep into the asymptotic regions from the $\lambda = (i, j)$ initial state to λ' final state. We consider a coordinate system where R denotes the distance between the two scattering fragments, A and B, and ω encompasses all other internal coordinates. The Hamiltonian for the scattering system is given by [173, 195, 196]

$$H = H_0 + V_K, \tag{2.6.15}$$

$$V_K = V_K(R, \omega), \tag{2.6.16}$$

where V_K represents the interaction potential, which may include a centrifugal term and approaches zero as R becomes large.

The free Hamiltonian can be written as follows

$$H_0 = T_R + H_{\text{int}}, \tag{2.6.17}$$

$$T_R = -\frac{1}{2\mu_R}\frac{\partial^2}{\partial R^2} \tag{2.6.18}$$

The internal Hamiltonian is assumed to have a discrete eigenvalues E_λ, such that

$$H_{\text{int}}\zeta_\lambda(\omega) = E_\lambda\zeta_\lambda(\omega) \tag{2.6.19}$$

Subsequently, energy-normalized free scattering wave functions are introduced. These wave functions, which are eigenfunctions of H_0, are expressed as the product of incoming or outgoing waves $\pm$ and L^2-normalized eigenfunctions of H_{int}. The next step is to project this wave packet $\Phi^{\pm}_{\zeta_\lambda}$ with eigenvalues $\xi^{\pm}_{\zeta_\lambda}$.

$$\Phi^{\pm}_{\zeta_\lambda}(R,\omega) = \xi^{\pm}_{\zeta_\lambda}(R)\zeta_\lambda(\omega), \tag{2.6.20}$$

$$\xi^{\pm}_{\zeta_\lambda}(R) = \sqrt{\frac{\mu_R}{2\pi p_\lambda}} exp^{\pm} \mathrm{i} p_\lambda R, \tag{2.6.21}$$

$$p_\lambda = \sqrt{2\mu_R(E_c - E_\lambda)} \tag{2.6.22}$$

where p_λ is the momentum space. By restricting the initial wave function $\Psi^{+}_{E_\lambda}$ to a single motion towards the interaction zone, the normalized energy of the collision wave function is expressed as follows.

$$\Psi^{+}_{E_\lambda}(R,\omega) \overset{R\to+\infty}{\to} \Phi^{-}_{E_\lambda}(R,\omega) - \sum_{\lambda'} S^{J}_{\lambda'\leftarrow\lambda}(E_c)\Phi^{+}_{E_\lambda}(R,\omega) \tag{2.6.23}$$

It also reminds us that the S-matrix element is calculated for a given value of the total angular momentum J. The method used involves calculating the flux crossing a surface located at a sufficiently large distance on the asymptotic coordinate R, so that the interactions between the two molecules are negligible. To evaluate this flux, the temporal variation of a function Θ is measured, which describes the occupation of the region beyond the asymptotic surface R. The value of R_c is chosen to be sufficiently large to guarantee asymptotic motion for all $R \geq R_c$.

$$\Theta = h(R - R_c), \tag{2.6.24}$$

where h is the Heaviside-step-function. According to the Ehrenfest theorem [197],

$$\frac{d}{dt}\langle\Psi|\Theta|\Psi\rangle = \mathrm{i}\langle\Psi|\big[H,\Theta\big]|\Psi\rangle, \tag{2.6.25}$$

One can then deduce the flux F as follows

$$F = \mathrm{i}\big[H, \Theta\big], \tag{2.6.26}$$

The function Θ can even commute with V_K and H_{int}.

$$\begin{aligned} F &= \mathrm{i}\big[T_R, \Theta\big] \\ &= \frac{-\mathrm{i}}{2\mu_R}\Big(\frac{\partial}{\partial R}\delta(R-R_c) + \delta(R-R_c)\frac{\partial}{\partial R}\Big), \end{aligned} \tag{2.6.27}$$

The S-matrix element can then be calculated as follows

$$\langle \Psi^+_{E_\lambda} | F | \Psi^+_{E_\lambda} \rangle = \sum_{\lambda'} |S^J_{\lambda' \leftarrow \lambda}(E_c)|^2 \langle \Phi^+_{E_\lambda} | F | \Phi^+_{E_\lambda} \rangle \tag{2.6.28}$$

Using the eigenfunctions and eigenvalues related to $\Phi^+_{E_\lambda}$, the S-matrix element is written as follows:

$$\langle \Psi^+_{E_\lambda} | F | \Psi^+_{E_\lambda} \rangle = (2\pi)^{-1} \sum_{\lambda'} |S^J_{\lambda' \leftarrow \lambda}(E_c)|^2 \tag{2.6.29}$$

To obtain the flux corresponding to a given final state, one can project the flux onto this state using a projector operator.

$$P_\lambda = |\zeta_\lambda\rangle\langle\zeta_\lambda|, \tag{2.6.30}$$

yielding

$$\langle \Psi^+_{E_\lambda} | P_{\lambda'} F P_{\lambda'} | \Psi^+_{E_\lambda} \rangle = (2\pi)^{-1} \sum_{\lambda'} |S^J_{\lambda' \leftarrow \lambda}(E_c)|^2 \tag{2.6.31}$$

As mentioned earlier, the Complex Absorbing Potential (CAP) can be used to determine the flux. The Hamiltonian is then modified as follows [198, 195]

$$\tilde{H} = H - \mathrm{i}W, \tag{2.6.32}$$

where $-\mathrm{i}W$ stands for the CAP. It should also be noted that the CAP is defined in such a way that the propagation is carried out with $\tilde{H}$ without altering the value of the wave function in the interaction region. The CAP, therefore, only affects the distant parts of

the wave function, allowing undisturbed propagation in the internal regions. The flux can be calculated as follows

$$\langle \Psi^+_{E_\lambda} | F | \Psi^+_{E_\lambda} \rangle = \frac{1}{(2\pi)^2 |\Delta E_c|^2} \int_{-\infty}^{+\infty} dt \int_{-\infty}^{+\infty} dt' \langle \Psi_0 | e^{\mathrm{i}(\tilde{H}^\dagger - E_c)t} F e^{\mathrm{i}(\tilde{H} - E_c)t'} | \Psi_0 \rangle, \quad (2.6.33)$$

where ΔE_c is initial distribution energy of the wave packet Ψ_0. The flux can be then expressed using equation 2.6.26 as follows

$$F = i\big[H, \Theta\big] = 2W + \tilde{H}^\dagger \Theta - \mathrm{i}\Theta\tilde{H} \quad (2.6.34)$$

Since the wave packet is limited to negative momentum of space, it cannot interact with the CAP for negative times. Therefore, the lower bounds of the integrals can be replaced by 0. It then becomes possible to inject the expression of the flux into equation 2.6.34 using the relationship given by equation 2.6.25.

$$\begin{aligned} \langle \langle \Psi^+_{E_\lambda} | F | \Psi^+_{E_\lambda} \rangle = & \frac{1}{(2\pi)^2 |\Delta E_c|^2} \int_0^{+\infty} dt \int_0^{+\infty} dt' \big[2 \langle \Psi_0 | e^{\mathrm{i}(\tilde{H}^\dagger - E_c)t} W e^{\mathrm{i}(\tilde{H} - E_c)t'} | \Psi_0 \rangle \\ & \big(\frac{d}{dt} + \frac{d}{dt'} \big) \langle \Psi_0 | e^{\mathrm{i}\left(\tilde{H}^\dagger - E_c\right)t} \Theta e^{-\mathrm{i}\left(\tilde{H} - E_c\right)t'} | \Psi_0 \rangle \big] \end{aligned} \quad (2.6.35)$$

Some terms can be removed due to the fact that $\Theta\Psi_0 = 0$ and as $t \to \infty$, $e^{-\mathrm{i}\tilde{H}t}\Psi_0 \to 0$ because the wave packet is absorbed by the CAP. One can define the time-dependent wave function as a function of Ψ_0, and with $\Psi(t) = e^{-\mathrm{i}\tilde{H}t}\Psi_0$, we can then obtain the following formula for the flux .

$$\langle \Psi^+_{E_\lambda} | F | \Psi^+_{E_\lambda} \rangle = \frac{1}{2\pi^2 |\Delta E_c|^2} \int_0^{+\infty} dt \int_0^{+\infty} dt' \langle \Psi(t) | W | \Psi(t) \rangle e^{-\mathrm{i}E_c(t-t')} \quad (2.6.36)$$

The S-matrix element can be expressed as a function of the CAP as follows

$$\sum_{\lambda'} |S^J_{\lambda' \leftarrow \lambda}(E_c)|^2 = \frac{1}{\pi |\Delta E_c|^2} \int_0^{+\infty} dt \int_0^{+\infty} dt' \langle \Psi(t) | W | \Psi(t) \rangle e^{-\mathrm{i}E_c(t-t')} \quad (2.6.37)$$

This S-matrix element can then be obtained by projecting onto a final state λ'.

$$|S^J_{\lambda' \leftarrow \lambda}(E_c)|^2 = \frac{1}{\pi |\Delta E_c|^2} \int_0^{+\infty} dt \int_0^{+\infty} \langle \Psi(t) | P_{\lambda'} W P_{\lambda'} | \Psi(t') \rangle e^{-\mathrm{i} E_c (t-t')} \tag{2.6.38}$$

By making the temporary variable change $\tau = t' - t$, we can express the S-matrix element more simply for a specific initial state as follows

$$\sum_{\lambda'} |S^J_{\lambda' \leftarrow \lambda}(E_c)|^2 = \frac{1}{\pi |\Delta E_c|^2} \int_0^{+\infty} dt \langle \Psi(t) | W | \Psi(t+\tau) \rangle e^{\mathrm{i} E_c \tau}, \tag{2.6.39}$$

and after projection, we obtain the simplified expression for the S-matrix element corresponding to the final state.

$$|S^J_{\lambda' \leftarrow \lambda}(E_c)|^2 = \frac{1}{\pi |\Delta E_c|^2} \int_0^{+\infty} dt \langle \Psi(t) | P_{\lambda'} W P_{\lambda'} | \Psi(t+\tau) \rangle e^{\mathrm{i} E_c \tau} \tag{2.6.40}$$

These elements of the S-matrix element will allow us to calculate transition probabilities and cross sections in the following sections.

2.6.3.3 Inelastic cross-section and Rate coefficient:

To define the initial state as well as the different rotational states after the collision, the Hamiltonian of the system is expressed as follows

$$\hat{H} = -\frac{\hbar^2}{2\mu_R} \frac{\partial^2}{\partial R^2} + \frac{\hbar^2}{2\mu_R} \frac{\hat{J}^2}{R^2} + \hat{H}_1 + \hat{H}_2 + \hat{V}(R, \theta_i) \tag{2.6.41}$$

where, μ_R is the reduced mass of the system, R the inter-monomers distance between, $\hat{J}$ the angular momentum operator. $\hat{H}_1$ and $\hat{H}_1$ are the Hamiltonian of the two monomers used to describe their internal structures, and $\hat{V}(R, \theta_i)$ represents the PES term used to describe the inter-monomers interactions. The relative orientations of the molecules in collisions is described by the set of angles θ_i.

The initial wave function is the product of the angular wave function and radial wave

function expressed as follows

$$\psi(R, \theta_i) = \psi(\theta_i)\chi(R) \tag{2.6.42}$$

where $\chi(R)$ is the radial distribution defined in equation 2.6.12. After the propagation, two methods can be used to determine the transition probabilities between states. These are the flux-based approach [173, 196] or the method developed by Tannor and Weeks [199]. The transition probabilities between states are given by the following expression [200, 196].

$$P^J_{i\to f}(E) = \frac{1}{4\pi^2|\Delta_i(E)|^2|\Delta_j(E)|^2}\left|\int_0^T e^{\mathrm{i}Et}C_{if}(t)dt\right|^2 = \left|S^J_{if}(E)\right|^2 \tag{2.6.43}$$

where E is the total energy of the collisional process, $S^J_{if}(E)$ is the S-matrix element, and C_{if} is the autocorrelation function defined as a function of the initial and final wave packet, ψ_i and ψ_f, respectively given as

$$C_{if}(t) = \langle\psi_i|e^{-\mathrm{i}Ht}|\psi_f\rangle \tag{2.6.44}$$

where Δ_i and Δ_f stand for the energy distribution of ψ_i and ψ_f, respectively [201, 195].

From equation 2.6.43, the transition $i \to f$ can ve rewritten as

$$(i_1, i_2) \to (f_1, f_2) \tag{2.6.45}$$

where (i_1, i_2) and (f_1, f_2) are the initial and final transition states of the two monomers.

The calculation of the inelastic cross-section is helpful in measuring the probability of a collision process between two entities, which can be an atom, a molecule, or a molecule-molecule.

For each specific value of the total angular momentum J, individual wave packet propagation simulate the collision from a given initial state (i_1, i_2) to the final state (f_1, f_2), the transition probability for any transition occurring is represented as $P^J(i_1, i_2 \to f_1, f_2)$.

By conducting these simulations for multiple J values using the Tannor and Weeks [199] method, the overall cross section can be determined by summing each contribution. The cross-section for all transitions is given by the following formula:

$$\sigma^{BF}_{i_1,i_2\to f_1,f_2}(E) = \frac{\pi\hbar^2}{2\mu_R(2j_1+1)(2j_2+1)E_{\text{coll}}}\sum_{J=0}^{J_{max}}(2J+1)P^J_{i_1,i_2\to f_1,f_2}(E), \qquad (2.6.46)$$

where E_{coll} is the collisional energy or kinetic energy of the system. This energy is expressed as $E_{\text{coll}} = E - E_{\text{int}} = E - \epsilon_1 - \epsilon_2$, with E_{int}, ϵ_1, ϵ_2 as the internal initial energy of the whole system and the initial rotational energy of each monomer.

The rate coefficient corresponds to the time average of the product of the cross section and the relative velocity of the interacting particles. It is possible to calculate the rate coefficient for each transition between states using the following formula.

$$K_{i_1,i_2\to f_1,f_2}(T) = \Big(\frac{8k_BT}{\pi\mu_R}\Big)^{\frac{1}{2}}\frac{1}{\big(k_BT\big)^{\frac{1}{2}}}\int_0^\infty \sigma^{BF}_{i_1,i_2\to f_1,f_2}(E)exp\big(\frac{-E_{\text{coll}}}{K_BT}\big)E_{E_{\text{coll}}}dE_{\text{coll}} \qquad (2.6.47)$$

where k_B is the Boltzmann constant and T the gas temperature. These calculated coefficients can also be used as inputs for astrophysical modelling as said in the introduction.

2.6.4 Methodical approach to MCTDH calculations

In this section, I will present the different steps to follow to perform an MCTDH calculation. One must remember that this calculation is only feasible if the representation of the PES in the MCTDH code accurately corresponds to the initial PES.

2.6.4.1 The discrete variable representations and SPFs:

For this section, most of equations are taken from reference ([202]). For each degree of freedom, it is essential to define the basis in which the wave function will be propagated. In order to diagonalize the kinetic energy operator in this basis, one has to select functions suitable for the nature of the problem. These functions, which are then used to define the SPFs bases, must obey the rules of orthogonality and normalization. They are defined at

specific points on a grid used for numerical calculations and are referred to as discrete variable representations (DVR). In the following, I will only focus on the functions applied to the systems studied in my thesis. To establish the elements used by the MCTDH method in the basis defined by the DVR, we consider the matrix elements defined as follow:

$$q_{jk} = \langle \_j|\hat{x}|\varphi_k\rangle \tag{2.6.48}$$

$$q_{jk}^{(1)} = \langle \varphi_j|\partial x|\varphi_k \tag{2.6.49}$$

$$q_{jk}^{(2)} = \langle \varphi_j|\partial^2 x|\varphi_k\rangle \tag{2.6.50}$$

For the R DOF, the DVR based on FFT is used as it employs plane waves as basis functions to describe the dissociation of a molecular system. Furthermore, in MCTDH, their representation respects the periodic boundary conditions of the grid, with $\varphi^{x_0} = \varphi(x_N)$. The functions φ, not to be confused with the SPFs (which are expressed in this basis), are defined from the eigenfunctions of the particle in an angular motion problem. The basis functions are represented as follows:

$$\varphi_j(x) = L^{-1/2} exp\Big(2\mathrm{i}\pi j\big(x_0 - x\big)/L\Big) \tag{2.6.51}$$

With $N = 2n + 1$, $-n \leq j \leq n$, and $L = x_N - x_0$.

To describe the θ DOF, we use DVRs based on extended Legendre functions and associated Legendre functions. The extended Legendre DVR involves the Legendre functions $P_j^K(cos(\theta))$, which are the eigenfunctions of the rotational momentum operator $\hat{j}^2$. It is mainly used to describe the angular motions of a molecule with a total angular momentum $J > 0$.

$$\varphi_{j-K+1(\theta,K)} = (-1)^K \sqrt{\frac{2j+1}{2}\frac{(j-K)!}{(j+K)!}} P_j^K(cos(\theta)) \tag{2.6.52}$$

With $K \geq 0$ and $K \leq j \leq K + N + 1$. The projection of angular momentum is given by K, and to use this DVR in the framework of MCTDH, it is necessary to combine the two modes θ and K. Similarly, the associated Legendre DVR, also known as Legendre in

two dimensions, is used for initial potentials without the need for Fourier transformation. The values of K correspond to the magnetic quantum number m.

$$\varphi_{j-m+1(\theta,m)} = (-1)^m \sqrt{\frac{2j+1}{2}\frac{(j-m)!}{(j+m)!}} P_j^m(cos(\theta)) \tag{2.6.53}$$

With $m \geq 0$, $0 \leq m \leq j$, and j restricted to $m \leq j \leq m+N+1$.

Wigner function-based DVR is used to describe the complete rotation of a polyatomic molecule using Wigner L^2-Normalized functions and defined as $D^j_{m,k}(\alpha,\beta,\gamma)$. Here, α and γ are the Euler angles representing rotation around the Space-Fixed and Body-Fixed z-axis, while β is the Euler angle between the z-axes of these two frames.

$$\varphi_{j,m,k}(\alpha,\beta,\gamma) = D^j_{m,k} = \sqrt{\frac{2j+1}{8\pi^2}} D^j_{m,k}(\alpha,\beta,\gamma) \tag{2.6.54}$$

$$D^j_{m,k}(\alpha,\beta,\gamma) = e^{-\mathrm{i}m\alpha} d^j_{m,k}(\beta) e^{-\mathrm{i}k\gamma} \tag{2.6.55}$$

The Wigner d-function is defined as $d^j_{m,k}(\beta)$.

$$d^j_{m,k}(\beta) = \langle j,m|e^{-\mathrm{i}\beta\hat{J}_Y}|j,k\rangle \tag{2.6.56}$$

In MCTDH, the current representation of these functions incorporates symmetry operations.

2.6.4.2 Number of SPFs:

The number of Single-Particle Functions (SPFs) must be determined based on the results of convergence tests. For multidimensional systems, such as those studied in my thesis. For the calculations, one can choose configurations that exhibit strong interactions, while disregarding those with negligible correlations. A more efficient approach is to use a combination scheme that selectively reduces the storage requirements of the wave function. This method optimizes the computational resources without sacrificing accuracy. I will provide a more detailed explanation of this approach in the respective chapters.

2.6.4.3 Integration scheme:

In a relaxation or propagation calculation, it is necessary to solve an ordinary differential equation, which becomes simpler when the Hamiltonian is expressed as a sum of products of low-dimensional operators, thus avoiding the calculation of voluminous integrals. Many integrators have been developed to handle the time-dependent Schrödinger equation. In the framework of the MCTDH method, several integrators can be used: for the A-coefficients , it is possible to use the short iterative Lanczos (SIL) [188] integration scheme or the Davidson (DAV) [203] scheme, while the SPF can be integrated using Bulirsch-Stoer extrapolation (BS) [204] or 8th order Runge-Kutta (RK8) [205] method. The constant mean field (CMF) approach can also be adopted. This approach involves keeping the mean field fixed over a relatively long time interval and integrating the A-coefficients and SPF with much shorter time steps. In other words, in the CMF method, computational effort is reduced by keeping the mean fields, density matrices, and Hamiltonian matrix elements constant for a certain period, instead of updating them at each integration step [204].

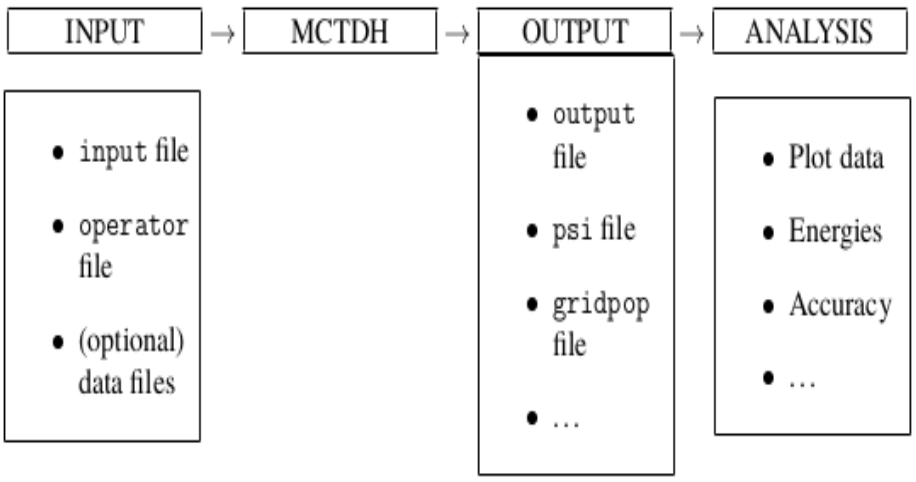

Figure 2.4: The workflow with MCTDH proceeds as follows: All parameters and settings are specified in the operator and input files. Additional data files may provide necessary information, such as the PES or the initial wave function. During the calculation, the program generates output files that can be analyzed and visualized using built-in tools or external scripts. Furthermore, tools are available to assess both the accuracy and efficiency of the calculations.

3. Rovibrational states calculations of the H_2O–HCN heterodimer

In this chapter, I will present my work on the spectroscopy of water (H_2O) molecules interacting with hydrogen cyanide (HCN) molecules in the rigid rotor approximation. Thus in the following sections, I will introduce the H_2O-HCN system, describe the Hamiltonian used for the calculations and present the results I have obtained from these studies.

3.1 H_2O-HCN system

In my thesis, the first system I investigated was the H_2O-HCN complex. I developed scripts to analyze the results from the MCTDH calculations, which will be further adapted to facilitate the analysis of results obtained for the H_2O-H_2O system. Hydrogen cyanide (HCN), a well-known hydrogen-bond-forming molecule, is also one of the most observed molecules in the ISM. Data on the interaction between water and HCN, particularly in spectroscopy and collisions, can be used to accurately determine the abundance of HCN in the interstellar medium (ISM) [138, 120]. In addition, the dissociation energy calculation of the H_2O-HCN complex is used to understand the thermal stability of molecular clusters in atmospheric chemistry. It represents the minimum energy needed to cause fragmentation, influencing chemical reactivity and cluster stability.

Initially, the H_2O-HCN system was studied using *ab initio* calculations at the Hartree-Fock level [206] and later became the subject of various microwave spectroscopic studies [207, 208, 209]. These investigations provided information on its ground-state geometry, rotational constants, and rotational transition frequencies. When I began working on this project, the only available PES in the literature was developed by Ernesto and Dubernet [210] to study the H_2O and HCN interaction in the rigid rotor approximation. At the same time a new H_2O-HCN PES [120] was developed using the Symmetry Adapted Perturbation Theory with Density Functional Theory (SAPT(DFT)) [211] method and

the autoPES [212, 213] code. The two works were done simultaneously.

The H_2O-HCN system was an ideal initial project, allowing me to deepen my understanding of spectroscopic theory while also generating valuable data for atmospheric and astronomical research. While the system is not computationally demanding, the primary goal was to accurately represent the PES for MCTDH calculations. In the following sections, the approach used to calculate the rovibrational states of this system will be described, and the presentation of the results obtained.

3.2 Coordinates and exact Hamiltonian for the H_2O-HCN system

In this section, the Hamiltonian operator used for the calculations will be described. To do this, coordinate transformations will be applied to the system, followed by the expression of the kinetic energy operator, and finally, the PES. The H_2O and HCN are labeled A and B, respectively. The body-fixed (BF) frame has its z-axis along the vector that points to the center of mass of H_2O (A) and HCN (B). The system is described by the angular coordinates defined as $\{\alpha_A, \beta_A, \gamma_A\}$, which are Euler angles for the orientation of the H_2O with respect to the BF frame, $\{\alpha_B, \beta_B\}$ are the polar angles of the HCN axis relative to the BF frame, and $\{\alpha, \beta\}$ are the polar angles for the orientation of the vector $\vec{r}_0$ with respect to the space-fixed (SF) frame, as illustrated in Figure 3.1, where r_0 is the length of the vector connecting the center of mass of H_2O (A) to that of HCN (B). From these coordinate descriptions in the body-fixed (BF) frame, where E_2 is the frame of reference described by Gatti and Iung [158], the intermonomer Hamiltonian can be expressed as follows [214].

$$\hat{H}_{int} = \hat{T}_A + \hat{T}_B \underbrace{-\frac{1}{\mu_{r_0} r_0^2}\frac{\partial}{\partial r_0} r_0^2 \frac{\partial}{\partial r_0} + \frac{1}{2\mu_{r_0} r_0^2}\left[\hat{\mathbf{J}}^{\dagger}\hat{\mathbf{J}} + (\hat{\mathbf{j}}_{\mathbf{A}} + \hat{\mathbf{j}}_{\mathbf{B}})^{\mathbf{2}} - \mathbf{2}(\hat{\mathbf{j}}_{\mathbf{A}} + \hat{\mathbf{j}}_{\mathbf{B}}).\hat{\mathbf{J}}\right]\mathbf{E_2}}_{\hat{T}_{\text{int}}} + V(r_0, \omega), \tag{3.2.1}$$

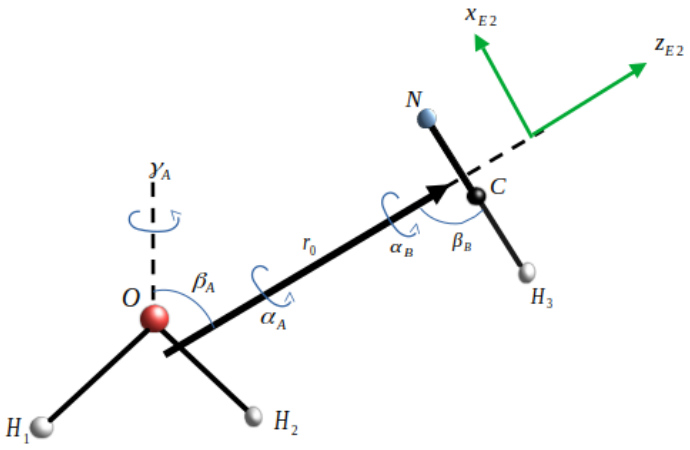

Figure 3.1: Body-fixed coordinates used to describe the H_2O-HCN system

where the reduced mass of the system is denoted by $\mu_{r_0} = \frac{m_{H_2O} \times m_{HCN}}{m_{H_2O}+m_{HCN}}$, the inter-monomer kinetic energy operator is represented by $\hat{T}_{\text{int}}$, J stands for the total angular momentum, $V(r_0, \omega)$ is the interaction potential energy surface (PES) between the monomers, where $\omega = \left\{\alpha_A - \alpha_B, \beta_A, \gamma_A, \beta_B\right\}$, and $\hat{j}_A$ and $\hat{j}_B$ are the angular momentum operators of fragments A (H_2O) and B (HCN). Here we note that the dimer PES is not influenced by the individual values of α_A and α_B, but only by their difference $\alpha_0 = \alpha_A - \alpha_B$. The kinetic energy operators (KEO) of the monomers H_2O ($\hat{T}_A$) [215] and HCN ($\hat{T}_B$) [69] are expressed as follows

$$\hat{T}_A = \frac{A}{2}(\hat{j}^2_{A,+} + \hat{j}^2_{A,-} + \hat{j}_{A,+}\hat{j}_{A,-} + \hat{j}_{A,-}\hat{j}_{A,+}) - \frac{C}{2}(\hat{j}^2_{A,+} + \hat{j}^2_{A,-} - \hat{j}_{A,+}\hat{j}_{A,-} - \hat{j}_{A,-}\hat{j}_{A,+})$$
$$Bj^2_{zBF_A}, \tag{3.2.2}$$
$$\hat{T}_B = B(\text{HCN})\hat{j}^2_B, \tag{3.2.3}$$

Here, A, B, and C represent the rotational constants with values of 27.88063 cm^{-1}, 9.2771 cm^{-1}, and 14.52177 cm^{-1}, respectively [62]. For HCN, $B = 1.4782218$ cm^{-1} [216]. To perform the calculations, the final form of the kinetic energy operator (KEO)

implemented in the MCTDH is expressed as follows

$$\begin{aligned}\hat{T} = &-\frac{1}{\mu_{r_0} r_0^2}\frac{\partial}{\partial r_0} r_0^2 + \hat{T}_A + \hat{T}_B + \frac{1}{2\mu_{r_0} r_0^2}\left(J(J+1) + \vec{j}_A^2 + \vec{j}_B^2 - 2j_{A,z}^2 - 2j_{B,z}^2\right) E_2 \\ &+ \frac{1}{2\mu_{r_0} r_0^2}\left(j_{A,+}j_{B,-} + j_{A,-}j_{B,+} - 2j_{A,z}j_{B,z}\right) E_2 \\ &+ \frac{1}{2\mu_{r_0} r_0^2}\left(C_+(J,K)(j_{A,+} + j_{B,+})\right) + \frac{1}{2\mu_{r_0} r_0^2}\left(C_-(J,K)(j_{A,-} + j_{B,-})\right) E_2, \end{aligned} \tag{3.2.4}$$

with

$$C_\pm(J,K) = \sqrt{(J(J+1) - K(K\pm 1)} \tag{3.2.5}$$

$$\hat{j}_{A(B)} = \hat{j}_{A(B),x} \pm \mathrm{i}\hat{j}_{A(B),y} \tag{3.2.6}$$

where K is the projection of J on the intermolecular axis Z_{BF}, and $\hat{j}_{A(B)\pm}$ are the corresponding creation and lowering operators of $\hat{j}_{A(B)}$. The coefficients $C_\pm(J,K)$ are obtained using the POTFIT algorithm implemented in the MCTDH package for values of J greater than zero. The same number of grid points is used along the K (angular momentum representation of the angles α and γ) in the calculations, ensuring consistency in the discretization of angular coordinates. In reduced dimensionality, the kinetic energy operator (KEO) of the H_2O can be rewritten as follows [215]

$$\hat{T}_A = \left(\frac{A+C}{2}\right)\hat{j}^2 + \left[B - \left(\frac{A+C}{2}\right)\right]\hat{j}_z^2 + \left(\frac{A-C}{4}\right)\left(\hat{j}_+^2 + \hat{j}_-^2\right) \tag{3.2.7}$$

With $\hat{j}_+ = \hat{j}_x + \mathrm{i}\hat{j}_y$ and $\hat{j}_- = \hat{j}_x - \mathrm{i}\hat{j}_y$.

The kinetic energy operator (KEO) is typically expressed in a product form, which is naturally suited for polyspherical coordinates, such as the Jacobi coordinates employed in this study. This coordinate choice ensures that the KEO maintains the necessary structure for accurate calculations. The relevant aspect of the work, however, involves the detailed description and representation of the potential energy surface (PES), which is fundamental to achieving precise results in the calculations.

3.3 The Potential Energy Surface of the H_2O-HCN complex

3.3.1 Characterization of the H_2O-HCN PES

The PES used in this work was calculated by Ernesto and Dubernet [210] using the Coupled-Cluster with Single, Double, and Perturbative Triple excitations method, and Augmented Virtual Double-Zeta basis set (AVDZ). A total of 43,000 *ab initio* points were calculated for the H_2O-HCN system, revealing two minima. The first, as shown in Figure 3.2, corresponds to the global minimum, obtained for a configuration where the hydrogen atom of HCN approaches the oxygen of the water molecule. The energy associated with this minimum is approximately -1814.51 cm^{-1} at the intermolecular distance $R = 7.16$ bohr. Compared to the global minimum reported by Vindel $et\ al.$ [120], with an energy of -1852.35 cm^{-1}, it is found that the well depth of the PES obtained in this work is higher than that obtained by Vindel $et\ al.$ [120]. This high energy value indicates that the H_2O-HCN system is very stable. The local minimum is located in a geometry where the nitrogen of HCN approaches one of the hydrogens of H_2O, as shown in Figure 3.3, at the intermolecular distance of $R = 7.0$ bohr with an energy of -1377.30 cm^{-1}. Compared to Vindel $et\ al.$ [120], who reported an energy of -1338.36 cm^{-1} for this second minimum, our result shows a lower interaction energy. These differences between the two potentials can be attributed to the different *ab initio* methods used, with CCSD(T) used in the work of Ernesto and Dubernet [210], and the SAPT(DFT) method in the calculations of Vindel $et\ al.$ [120], as well as the size of the basis sets used.

3.3.2 Representation of the PES for MCTDH calculation

When implementing the PES calculations, we were unable to use the POTFIT algorithm due to the high number of degrees of freedom in the system. POTFIT is generally more efficient for systems with less than 4 degrees of freedom, but in our case, the complexity of the PES made this approach inapplicable. To overcome this limitation, we chose to transform the analytical potential into a form that allows us to represent the PES in a

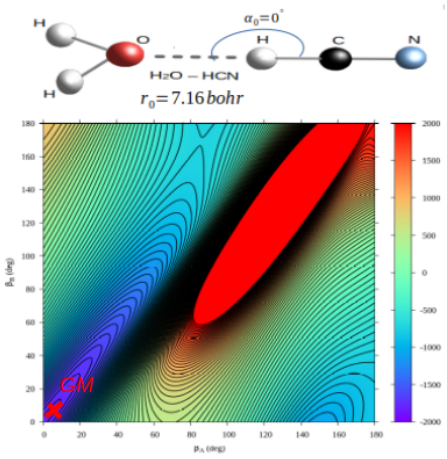

Figure 3.2: 2D PES contour plot as a function of β_A and β_B describing the H_2O-HCN system at the global minimum.

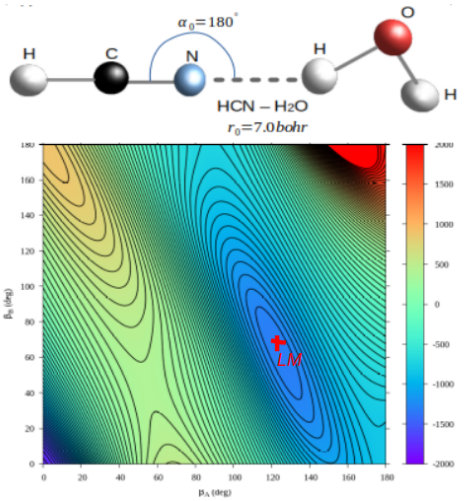

Figure 3.3: 2D PES contour plot as a function of β_A and β_B describing the H_2O-HCN system at the local minimum.

product form, with coefficients tailored for MCTDH calculations.

The transformation applied to the H_2O-HCN PES is generalizable to other systems with similar characteristics. The FORTRAN program we have written to represent this PES could be used to automatically generate potentials for the same types of systems in MCTDH format and will be made available in a GitHub repository [1]. Thus, for a new system, it is sufficient to read the ab initio data and automatically generate the new form adapted to MCTDH. This offers a significant time and precision advantage for more complex systems.

Regarding the spectroscopic calculations of the H_2O-HCN complex, I limited the study of the global minimum of the system. Specifically, I restricted the intermolecular distance r_0 to a range between 2 and 22 bohrs. This approach allowed for achieving convergence of calculations with a precision of about 10^{-8}, ensuring the reliability of the results. Since the use of POTFIT was not possible in our case, the main objective was to develop an automatic method for representing potentials of this type of systems within the framework of MCTDH.

[1] https://github.com/MolQuantDynLab-Haverford/MolQuantDynLab-Repository

The initial potential, in its multipolar form, is expressed as follows

$$V(r_0, \alpha_A, \beta_A, \gamma_A, \alpha_B, \beta_B) = \sum_{\lambda} v_\lambda(r_0) \bar{t}_\lambda(\alpha_A, \beta_A, \gamma_A, \alpha_B, \beta_B) \ , \tag{3.3.1}$$

When applying the Fourier Transform to the PES, we get the following formula

$$\tilde{V}(r_0, \alpha_A, \beta_A, \gamma_A, \alpha_B, \beta_B) = \sum_{\lambda} v_\lambda(r_0) \bar{t}_\lambda(K_{\alpha_A}, \beta_A, K_{\gamma_A}, K_{\alpha_B}, \beta_B) \ , \tag{3.3.2}$$

With $\lambda = \{l_A, m_A, l_B, l\}$, K_{α_A}, K_{γ_A}, and K_{α_B} are the momentum representations of α_A, γ_A, and α_B, respectively.

From equation 3.3.1, the indices l_A and l_B describe the anisotropic features of the interaction potential with respect to the orientations of H_2O and HCN, respectively. Figure 3.4 illustrates the first few radial expansion coefficients for the *para*-H_2O-HCN PES. As one can see in Figure 3.4, it was found that the most significant long-range interactions are the electrostatic terms, with their magnitudes decreasing in a specific order. In the following discussions, for further simplification, let's assume that $R = r_0$. At a distance of $R = 20$ bohr, the value of the water dipole-HCN dipole v_{1012} is approximately -240 cm^{-1}, while at $R = 40$ bohr, it decreases to around 31 cm^{-1}, which is still significant. The dipole-dipole interaction between water and HCN v_{1012} decreases in order of magnitude of $1/R^3$. Similarly, the dipole-quadrupole interaction between water and HCN v_{2213} and another dipole-dipole term v_{1023} decrease in $1/R^4$. Other terms, which decrease with $1/R^5$, have comparable magnitudes at $R = 30$ bohr, such as the dipole-octopole interaction v_{1034}, a quadrupole-quadrupole term v_{2224}, and the octopole-dipole interactions (v_{3014} and v_{3214}). Another quadrupole-quadrupole term v_{2024} also decreases as $1/R^5$ but is an order of magnitude smaller. Upon further investigation, it was observed that some of these coefficients include small induction effects, though these contributions remain negligible at large distances. The minimum of the isotropic term, v_{0000}, is found to be -1587.26 cm^{-1} at a distance of $R = 7.472$ bohr.

I have implemented the potential in MCTDH in two ways. The first approach is to lin-

Table 3.1: The first important $v_{l_A m_A l_B l}$ expansion coefficients of the H_2O-HCN PES. R and $v_{l_A m_A l_B l}$ are given in bohr and Hartree (Ha), respectively.

R	v_{0000}	v_{1012}	v_{1023}	v_{1034}	v_{2213}	v_{2224}	v_{3014}	v_{3214}
2	4.81E+00	-3.52E-01	2.78E-01	-2.21E-01	-2.51E-01	2.17E-01	8.16E-02	-1.51E-01
3	1.73E+00	-2.26E-01	1.73E-01	-1.38E-01	-1.59E-01	1.34E-01	5.08E-02	-9.41E-02
4	6.03E-01	-1.42E-01	1.02E-01	-8.22E-02	-9.75E-02	7.86E-02	3.01E-02	-5.58E-02
5	1.87E-01	-8.62E-02	5.52E-02	-4.49E-02	-5.63E-02	4.14E-02	1.63E-02	-3.02E-02
6	3.43E-02	-4.84E-02	2.36E-02	-1.98E-02	-2.88E-02	1.64E-02	7.02E-03	-1.30E-02
7	-5.95E-03	-2.71E-02	8.15E-03	-7.18E-03	-1.39E-02	4.90E-03	2.40E-03	-4.44E-03
8	-6.16E-03	-1.75E-02	3.95E-03	-3.31E-03	-7.97E-03	2.27E-03	1.07E-03	-1.97E-03
9	-3.42E-03	-1.22E-02	2.37E-03	-1.78E-03	-4.99E-03	1.29E-03	5.71E-04	-1.06E-03
10	-1.77E-03	-8.90E-03	1.56E-03	-1.05E-03	-3.28E-03	7.79E-04	3.37E-04	-6.23E-04
11	-9.48E-04	-6.69E-03	1.07E-03	-6.51E-04	-2.24E-03	4.91E-04	2.10E-04	-3.89E-04
12	-5.37E-04	-5.10E-03	7.63E-04	-4.21E-04	-1.58E-03	3.23E-04	1.36E-04	-2.56E-04
13	-3.19E-04	-4.01E-03	5.56E-04	-2.83E-04	-1.15E-03	2.16E-04	9.12E-05	-1.72E-04
14	-1.98E-04	-3.21E-03	4.14E-04	-1.95E-04	-8.52E-04	1.50E-04	6.29E-05	-1.19E-04
15	-1.27E-04	-2.61E-03	3.15E-04	-1.38E-04	-6.46E-04	1.06E-04	4.45E-05	-8.44E-05
16	-8.51E-05	-2.15E-03	2.44E-04	-1.00E-04	-5.00E-04	7.69E-05	3.24E-05	-6.12E-05
17	-5.82E-05	-1.80E-03	1.91E-04	-7.40E-05	-3.92E-04	5.68E-05	2.40E-05	-4.52E-05
18	-4.08E-05	-1.51E-03	1.52E-04	-5.56E-05	-3.12E-04	4.28E-05	1.81E-05	-3.40E-05
19	-2.91E-05	-1.29E-03	1.23E-04	-4.24E-05	-2.51E-04	3.26E-05	1.38E-05	-2.59E-05
20	-2.12E-05	-1.10E-03	9.99E-05	-3.29E-05	-2.05E-04	2.53E-05	1.07E-05	-2.01E-05
21	-1.57E-05	-9.52E-04	8.22E-05	-2.57E-05	-1.69E-04	1.98E-05	8.39E-06	-1.57E-05
22	-1.18E-05	-8.28E-04	6.83E-05	-2.04E-05	-1.40E-04	1.57E-05	6.65E-06	-1.25E-05
23	-9.00E-06	-7.25E-04	5.71E-05	-1.63E-05	-1.17E-04	1.26E-05	5.32E-06	-9.99E-06
24	-6.95E-06	-6.38E-04	4.82E-05	-1.32E-05	-9.88E-05	1.02E-05	4.30E-06	-8.08E-06
25	-5.41E-06	-5.64E-04	4.10E-05	-1.08E-05	-8.39E-05	8.30E-06	3.51E-06	-6.59E-06
26	-4.27E-06	-5.02E-04	3.50E-05	-8.85E-06	-7.17E-05	6.82E-06	2.88E-06	-5.42E-06
27	-3.39E-06	-4.48E-04	3.01E-05	-7.32E-06	-6.16E-05	5.64E-06	2.39E-06	-4.48E-06
28	-2.72E-06	-4.02E-04	2.60E-05	-6.11E-06	-5.33E-05	4.71E-06	1.99E-06	-3.74E-06
29	-2.21E-06	-3.62E-04	2.27E-05	-5.15E-06	-4.65E-05	3.97E-06	1.68E-06	-3.15E-06
30	-1.79E-06	-3.27E-04	1.98E-05	-4.33E-06	-4.05E-05	3.34E-06	1.41E-06	-2.65E-06
31	-1.47E-06	-2.96E-04	1.73E-05	-3.67E-06	-3.55E-05	2.83E-06	1.20E-06	-2.25E-06
32	-1.21E-06	-2.69E-04	1.53E-05	-3.13E-06	-3.13E-05	2.42E-06	1.02E-06	-1.92E-06
33	-1.01E-06	-2.45E-04	1.35E-05	-2.69E-06	-2.76E-05	2.07E-06	8.75E-07	-1.64E-06
34	-8.39E-07	-2.24E-04	1.20E-05	-2.31E-06	-2.45E-05	1.79E-06	7.54E-07	-1.42E-06
35	-7.04E-07	-2.06E-04	1.07E-05	-2.00E-06	-2.18E-05	1.55E-06	6.52E-07	-1.23E-06
36	-5.94E-07	-1.89E-04	9.53E-06	-1.74E-06	-1.95E-05	1.34E-06	5.67E-07	-1.06E-06
37	-5.03E-07	-1.74E-04	8.54E-06	-1.52E-06	-1.75E-05	1.17E-06	4.94E-07	-9.28E-07
38	-4.28E-07	-1.61E-04	7.68E-06	-1.33E-06	-1.57E-05	1.03E-06	4.32E-07	-8.12E-07
39	-3.66E-07	-1.49E-04	6.92E-06	-1.16E-06	-1.42E-05	9.01E-07	3.80E-07	-7.13E-07
40	-3.14E-07	-1.38E-04	6.25E-06	-1.03E-06	-1.28E-05	7.94E-07	3.34E-07	-6.28E-07

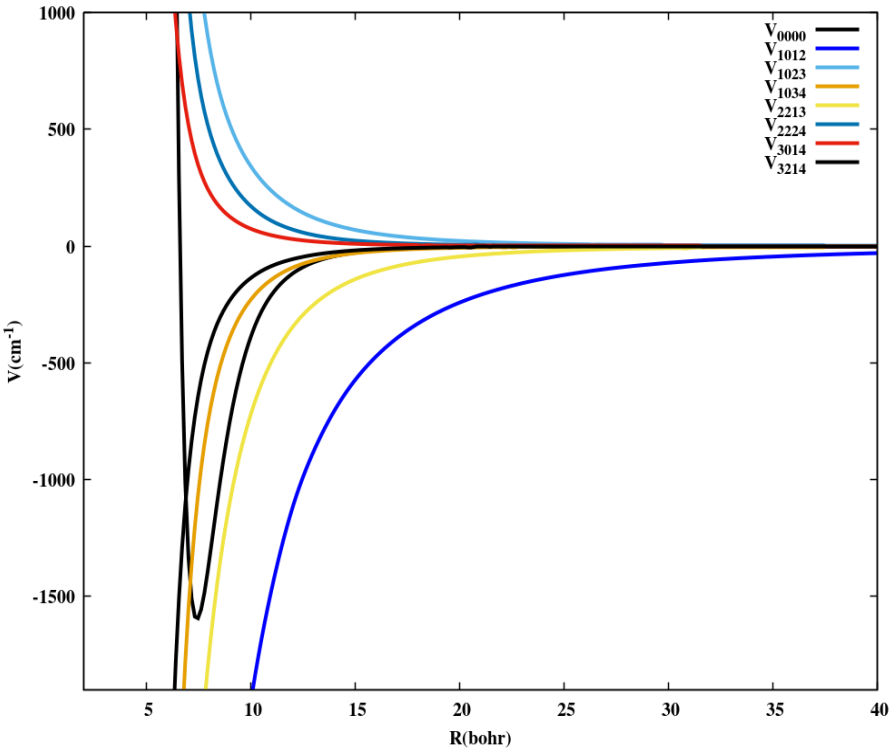

Figure 3.4: Plots of the first radial expansion coefficients $v_{l_A m_A l_B l}$ of the multipolar PES of the H_2O-HCN system.

Table 3.2: Comparison of the first bound states using the exponential and Fourier Transform form of the PESs for the SPFs 10/100/60

Energy	Exponential form	Fourier Transform form
E_0	-1457.281	-1457.281
E_1	-1442.898	-1442.898
E_2	-1442.898	-1442.898
E_3	-1399.824	-1399.824

earize the PES formula, where the potential V is expressed as a product. This method generates approximately 9569 lines of potential using 445 expansion coefficients. The second approach applies Fourier transformation to the PES, reducing the number of lines to around 6147 for the same number of coefficients. Mathematically, the MCTDH code has to do more work to read and process the potential lines in the linearized form. When calculating the ground state to determine the global minimum of the potential by propagating a single wave packet, the first approach took about 9 hours to converge, while the Fourier-transform version converged in 4 hours with the same results as shown in Ta-

ble 3.2. This demonstrates the advantage of using the Fourier transform of the potential for better efficiency in calculations.

3.4 Parameters used for the calculations

The rovibrational states calculations were carried out using the improved relaxation method, specifically the block improved relaxation approach, as detailed in the theoretical section. The input files for the calculations include the operator file, which contains the Hamiltonian and all physical constants, the Natpot folder, which holds the radial expansion coefficients, and the input file, which specifies the calculation parameters. I used the PES transformed by the Fourier transform because of the very short calculation time.

For the calculations, the basis wave function was chosen as follows

$$\Psi(r_0, \alpha_A, \beta_A, \gamma_A) = \Psi_A(\alpha_A, \beta_A, \gamma_A)\Psi_B(\alpha_B, \beta_B)\chi(R) \tag{3.4.1}$$

where Ψ_A and Ψ_B are the initial wave functions of the H_2O and HCN. $\chi(R)$ is the radial distribution used to describe the intermolecular distance.

The choice of the DVR influences the accuracy and convergence of results. In these calculations, the goal is to correctly describe the low-energy states of a quantum system by solving the Schrödinger equation, especially for complex systems like H_2O-HCN clusters. A well-chosen DVR can capture the details of the potential, ensure good localization of wave functions, and accelerate the convergence of energy levels. The relaxation is performed using the following DVRs.

- The FFT DVR is used to describe the intermonomer distance, with 96 grid points ranging from 2 to 22 bohr, with 20 SPFs.
- The Wigner DVR is used for β_A with 12 grid points ranging from 0 to π with 100 SPFs.
- The associated Legendre (Kleg) DVR is used to describe the β_B primitive basis,

with 24 grid points ranging from 0 to π with 60 SPFs.

- α_A,γ_A, and α_B are described by their corresponding momentum representation K_{α_A} with 23 grid points ranging from -11 to 11, K_{γ_A} with 11 grid points ranging from -5 to 5, and K_{α_B} with 11 grid points ranging from -5 to 5

It has been found that a relatively small number of basic functions is sufficient, but the default integrator parameters need to be adjusted to achieve accurate relaxation of the wave function. We can note that default parameter such as the integrators and schemes can result in a final energy lower than that of the ground state E_0. So, some tests have to be done to check which integrator can be appropriate for better convergence. The algorithm converges quickly when propagating four wave packets on an appropriate energy scale, but it becomes challenging to converge at higher energy values. By default, the integrator used for the SPF is the Bulirsch-Stoer (BS) [204] with an accuracy of 10^{-6}, but it deviates from the exact value $E = -1457.281$ cm^{-1} by about 0.004 cm^{-1}, which is a significant error for quantum chemistry calculations, but the results can be further improved by using a different integrator. More accurate results were obtained using 8th-order Runge-Kutta (RK) integrators for the SPF and Davidson (rDAV) for the A-vector (especially for real Hamiltonian) with an accuracy of 10^{-8}. We also followed the two convergence steps by increasing the size of the primitive basis and the number of SPFs to improve the accuracy of the results. Calculations converged with 45,000 SPFs, but for better accuracy in excited levels, we opted for 120,000 SPFs. Finally, the Constant Mean Field (CMF) integration scheme with a step size of 1.0 and a tolerance of 10^{-7} was used.

INTEGRATOR-SECTION	INTEGRATOR-SECTION
CMF= 1.0, 1d-7	CMF= 1.0, 1d-7
BS/spf = 1d-6, 0.01	RK8/spf = 1d-9, 0.01
rDAV/A = 800, 1d-8	rDAV/A = 800, 1d-8
END-INTEGRATOR-SECTION	END-INTEGRATOR-SECTION

3.5 Results and discussions

As mentioned earlier, the rovibrational calculations using the Ernesto and Dubernet [210] potential were submitted before those of Vindel $et\ al.$ [120]. That is why some parameters such as the rotational constants were not the same for better comparison in our article (Tajouo $et\ al.$ [217]). In this section, the results obtained are compared to those of Vindel $et\ al.$ [120], as well as to the available experimental data.

3.5.1 The bound states calculations and characterization

At low energy with $J = 0$, the calculated binding energy is -1457.281 cm^{-1}, with a zero-point energy (ZPE) of 357.2 cm^{-1}. In contrast, Vindel $et\ al.$ [120] reported values of -1488.342 cm^{-1} and 364.64 cm^{-1} for binding energy and ZPE, respectively. Our computed binding energy is slightly higher, whereas the ZPE is slightly lower. These differences are attributed to variations in computational methodologies, as previously discussed. The ZPE is calculated using the formula $ZPE = D_0 - D_e$, where D_0 is the ground state energy (first binding energy determined in the MCTDH by setting the system's reference energy to 0 cm^{-1}) and D_e is the well depth of the PES. Table 3.3 presents, for each bound state, the expected values of the parameters $< R >$, $< \beta_A >$, and $< \theta_B >$. The expectation values of the polar angles are calculated using the expression $< angle_j >= cos^{-1}(angle_j)$, where $< angle_j >$ corresponds to the expectation value of the $angle_j$ for a given state. It is found that for the ground state, $< \beta_B >$ is $25.21°$ and $< \theta_B >$ is $171.05°$. The values calculated in Vindel $et\ al.$ [120] are $27.942°$ and $170.13°$. This implies that the molecular axis of HCN is closely aligned with the intermolecular axis of the H_2O-HCN system, with a deviation angle of $8.95°$ and $10°$ in Vindel $et\ al.$ [120]. In microwave spectroscopy of the H_2O-HCN dimer, the orientation of the HCN axis relative to the intermolecular axis is described by the complementary angle of θ_B. These experimental values are 10.16° [209] and 9.4° [207], respectively, and correspond very well to our complementary angle of $8.95°$ in the ground state compared to 9.87° in Vindel $et\ al.$ [120].

Table 3.3: Calculated bound states for H_2O-HCN. The parameters $< R >$ and ΔR are given in bohr; $< \beta_A >$, $\Delta\beta_A$, $< \theta_B >$, and $\Delta\theta_B$ are in degrees and are defined in the text.

N	parity	Energy(cm^{-1})	$< r_0 >$	Δr_0	$< \beta_A >$	$\Delta\beta_A$	$< \theta_B >$	$\Delta\theta_B$
0	+	-1457.281	7.1343	0.2045	25.210	13.693	171.050	4.394
1	+	-1363.804	7.0980	0.2073	28.940	13.590	167.046	5.254
2	-	-1346.292	7.1191	0.2073	31.959	16.730	167.567	5.220
3	+	-1327.215	7.2260	0.3571	25.823	13.928	170.478	4.921
4	+	-1285.608	7.1390	0.2073	34.320	16.134	170.163	4.893
5	-	-1284.047	7.0860	0.2288	31.827	15.355	162.468	7.293
6	+	-1239.668	7.1618	0.3588	30.171	14.043	165.780	6.228
7	+	-1232.440	7.0838	0.2102	36.531	16.346	164.330	5.517
8	-	-1224.844	7.1694	0.3558	30.286	15.131	165.694	6.142
9	+	-1219.591	7.2085	0.3623	32.205	16.925	166.880	5.660

The deviation of the H_2O molecule from the C_{2v} planar geometry of the complex is quantified by the angle β_A, which describes the out-of-plane orientation of H_2O. This angle depends on the magnitude of the average vibrations. In these calculations, by definition, the polar angle is between 0 and 180° and can only take positive values. Even for a flat equilibrium geometry where $\beta_A = 0°$, the expected value of $< \beta_A >$ will always be positive and non-zero. According to Table 3.3, the calculated value of $< \beta_A >$ for the ground state is $25.210°$ comparing to $27.94°$ in Vindel $et\ al.$ [120], reflecting the significant amplitude of the out-of-plane vibrational orientation. This result matches with the spectroscopic value of 20° reported in Reference [207]. However, Reference [209] reports a value of 50.9° based on a microwave spectroscopic study. This higher value is attributed to the large-amplitude out-of-plane vibration of H_2O in the H_2O-HCN complex. However, the method used for this averaging in their work is not clearly specified.

In the case of the variation of the intermolecular distance in the ground state, our calculation estimates $< r_0 >= 7.134$ bohr in Table 3.3, compared to 7.135 bohr in

Vindel $et\ al.$ [120]. The values obtained using the two PESs are in excellent agreement with the intermonomer center-of-mass distances measured by microwave spectroscopy, which are 7.123 and 7.137 bohr in References [209] and [207], respectively. The calculations of the average positions of the bound states show that the results obtained in this work are close to those reported in Vindel $et\ al.$ [120], which can be explained by the use of different methods used to calculate the PESs and rotational constants. Regarding comparisons with experimental results, the data obtained with the two potentials show good agreement.

3.5.2 The rovibrational states

MCTDH does not yet have internal tools dedicated to the treatment of rovibrational states, which requires manual processing of results after each step of improved relaxation. The calculations are performed by initially propagating four wave packets. Each obtained wave function is then used as the initial wave function for a new propagation, this time with a single wave packet. The primitive basis and the SPF maintain the same parameters, while taking into account the type of relaxation used: for propagating multiple wave packets, the MCTDH keyword **relaxation=0** is used, while for a single wave packet, **relaxation=lock** is defined.

For $J = 0$, the rovibrational states must have a projection $K = 0$ of J. This is enforced by ensuring that the average values of the moments associated with the angles α_A and α_B satisfy the relation $< k_{\alpha_A} > + < k_{\alpha_B} >= 0$. Similarly, for $J = 1$, the projections must satisfy $< k_{\alpha_A} > + < k_{\alpha_B} >= 0, 1$, and for $K = 0, 1$, the rovibrational levels correspond to the symmetries Σ and Π. The rovibrational characters $j_{k_a k_c}$ are determined as follows: the initial states of H_2O are expressed as a linear combination of Wigner-D matrices, in the simplified form $j_{k_a k_c}$, where j represents the rotational angular momentum, and k_a and k_c are the projections on the body-fixed (BF) z-axis. Each rotational state can be denoted as $|jkm\rangle$, where m is the projection of j on the BF z-axis and k is its projection

on the SF z-axis. Thus, the rotational states of H_2O are written as follows

$$|jkm\rangle = \sum_{m_1=-j}^{j} C_{m_1 m} |j, k, m\rangle \tag{3.5.1}$$

with $m_1 = k_a - k_c$, m_1 ranging from $-j$ to j.

For each evaluation, it is necessary to determine the rotational states taking into account their degeneracy, which is $2j + 1$. For example, for $j = 0$, the rotational state of H_2O is $|0, 0, 0\rangle$ and the eigenvalue is 0. For $j = 1$, there are three rotational states. The states for $j = 2$ and $j = 3$ were calculated using an external FORTRAN script. To determine the characters $j_{k_a k_c}$, the rovibrational wave function is projected onto the rotational states of H_2O, and these characters are obtained by selecting the projection of the rovibrational state onto the corresponding rotational state of H_2O. If the rovibrational wave function is Ψ, its projection onto the rotational state of H_2O is $p_i = \Psi|\hat{P}_i|\Psi\rangle$ and $\hat{P}_i = |j_{kakc}, m\rangle\langle j_{kakc}, m|$ is the projector on each rotational state $|j_{kakc}, m\rangle$. The corresponding j_{kakc} for each rovibrational state is obtained by choosing the largest magnitude after the summation of each contribution of the projection of $|j_{kakc}, m\rangle$.

The calculations of the rovibrational states for the H_2O-HCN complex are reported in Tables 3.4-3.6, corresponding to total angular momentum J ranging from 0 to 2. Table 3.4 presents the vibrational energy levels where the calculated energies are compared to those obtained using another method. In this Table 3.4, comparisons are made with other calculations using another PES developed for the same system. Energies are relative to the ground state at -1457.281 cm^{-1} and are given in cm^{-1}.. These include the ground state, HCN libration, H_2O wagging, $O--C$ stretching, H_2O torsion, and H_2O rocking. Each of these vibrational modes reflects specific molecular motions within the complex:

- Ground state: Represents the lowest energy level of the system, where no vibrational excitation occurs with $< r_0 >= 7.1343$ bohr.

- HCN libration: A rotational oscillation of the HCN molecule within the complex, which is influenced by its interaction with the H_2O molecule with an energy of

93.477 cm^{-1} and $< r_0 >= 7.0980$ bohr compared to the value of 94.632 cm^{-1} in Vindel $et\ al.$ [120]

- H_2O wagging: Describes the oscillatory motion of the water molecule as its hydrogen atoms move up and down, also referred to as the water inversion mode with an energy of 110.989 cm^{-1} compared to the value of 112.514 cm^{-1} in Vindel $et\ al.$ [120].

- O−−C stretching: Corresponds to the stretching vibration between the oxygen of H_2O and the carbon of HCN, which involves the periodic elongation and contraction of the O−−C bond with an energy of 130.065 cm^{-1} compared to the value of 128.65 cm^{-1} in Vindel $et\ al.$ [120].

- H_2O torsion: Refers to the twisting motion of the water molecule, where its atoms rotate around the molecular z-axis with an $\alpha_0 = \alpha_A - \alpha_B$. The harmonic frequency corresponds to the energy of 171.673 cm^{-1} and 174.288 cm^{-1} in Vindel $et\ al.$ [120].

- H_2O rocking: This mode involves the rocking motion of the water molecule, where the entire molecule moves back and forth like a pendulum with an energy of 173.234 cm^{-1} compared to the value of 178.238 cm^{-1} in Vindel $et\ al.$ [120].

The variations in intermolecular distances $< r_0 >$ and Δr_0 increase significantly with the number of excited states. In the ground state, these values are 7.1343 and 0.2045 bohrs compared to 7.135 and 0.2050 bohrs in Vindel $et\ al.$ [120], respectively, while they reach 7.2260 and 0.3571 bohr compared to 7.226 and 0.360 bohr in Vindel $et\ al.$ [120] for the first vibrational excited state. In comparison, the expectation values of angles $< \beta_A >$ and $< \theta_B >$ remain almost unchanged compared to those of the ground state. This indicates that the complex undergoes significant stretching upon excitation. In comparison to the Vindel $et\ al.$ [120] results, the calculated values in this work are slightly lower

These values correspond to the harmonic frequencies of the system, indicating the energy associated with each vibrational mode. We observe a slight difference between the harmonic frequencies calculated from the two potentials. Indeed, each potential describes the interactions between H_2O and HCN molecules differently, which influences the char-

acteristics of the vibrational states of the complex. These variations, although minor, can have an impact on the energy levels.

Tables 3.5 and 3.6 present the rovibrational energy levels for $J = 1, 2$. We can also note here that there are differences in the calculations, which can probably be explained by the different values of the rotational constants used in the two works. The rotational constants used in this work are identical to those used in previous studies by Wang and Carrington [62], as well as Ndengué *et al.* [69], on the H_2O-H_2 complex. These references ensure some consistency in the comparison of results, although the slight variations observed may be related to differences in the representation of potential energy surfaces or the calculation methods used for rovibrational states. These differences can also be explained by the relatively low number of SPFs used, especially as energy increases. Indeed, as one moves away from the ground states towards higher energy levels, a larger number of SPFs is needed to properly capture the complexity of the rovibrational states of the system.

Table 3.4: Table: Low energy rovibrational levels of para and *ortho*-H_2O-HCN for $J = 0$.

p/o-H_2O	Assignment	MCTDH	Vindel *et al.* [120]
p	$\Sigma(1_{11})$	0.000	0.00
o	$\Sigma(1_{01})$	93.477	94.631
o	$\Sigma(1_{01})$	110.989	112.514
p	$\Sigma(1_{11})$	130.066	128.65
o	$\Sigma(2_{21})$	171.673	174.288
p	$\Sigma(1_{11})$	173.234	178.238
o	$\Sigma(1_{01})$	217.613	217.665
p	$\Sigma(2_{11})$	224.841	227.084
p	$\Sigma(2_{11})$	229.862	232.162
o	$\Sigma(1_{01})$	237.690	273.827
p	$\Sigma(1_{11})$	253.893	251.131
o	$\Sigma(2_{12})$	254.397	256.959
o	$\Sigma(2_{12})$	260.083	263.109

Table 3.5: Same as Table 3.4 for $J = 1$.

p/o-H_2O	Assignment	MCTDH	Vindel *et al.* [120]
p	$\Sigma(1_{11})$	0.205	0.203
o	$\Sigma(1_{01})$	14.595	14.594
o	$\Sigma(1_{01})$	14.595	14.595
p	$\Sigma(1_{11})$	90.031	91.098
p	$\Sigma(1_{11})$	90.032	91.099
p	$\Sigma(1_{11})$	93.684	94.631
o	$\Sigma(1_{01})$	111.194	112.514
o	$\Sigma(1_{01})$	130.267	
p	$\Pi(1_{11})$	143.018	144.325
o	$\Pi(1_{01})$	144.518	144.325
o	$\Sigma(2_{21})$	171.877	
p	$\Sigma(1_{11})$	173.442	174.288
p	$\Pi(1_{11})$	214.898	214.694
o	$\Sigma(1_{01})$	217.817	217.664

Table 3.6: Same as Table 3.4 for $J = 2$.

p/o-H_2O	Assignment	MCTDH	Vindel *et al.* [120]
p	$\Sigma(1_{11})$	0.611	0.609
o	$\Sigma(1_{01})$	15.001	14.999
o	$\Sigma(1_{01})$	15.003	15.002
o	$\Delta(1_{10})$	58.101	58.102

3.5.3 Microwave transitions frequencies and rotational constants

The comparison between experimental and theoretical results for the H_2O-HCN complex is presented in Table 3.7. The rotational energy levels obtained from the calculations are used to determine the microwave rotational transition frequencies. For comparison, experimental values reported by Fillery-Travis *et al.* [209], as well as theoretical values from Vindel *et al.* [120], are included. The computed microwave rotational transition frequencies show excellent agreement with the experimental measurements. However, a slight discrepancy between the results of this work and those of Vindel *et al.* [120] can be observed. This difference might stem from the SAPT (DFT) [120] and CCSD(T) [210] used or possibly from variations in the rotational constants used in this work.

Table 3.8 provides the ground-state rotational constants A, B, and C for the H_2O-HCN

complex, based on 5D-PES calculations within the rigid rotor approximation for the $J = 1$ rovibrational states. A comparison of these constants with experimental values and those from Vindel $et\ al.$ [120] reveals good overall agreement. The values of B and C are quite close, indicating that the H_2O-HCN complex behaves as a nearly prolate symmetric top.

Table 3.7: Calculated Microwave transition frequencies (cm^{-1}) for H_2O-HCN. rel. er.=relative error

Transition	MCTDH(cal)	Vindel [120](theo)	exp [209]	% rel. er.(exp-cal)	% rel. er.(exp-theo)
$1_{01} \leftarrow 0_{00}$	0.2046	0.2031	0.2034	0.59	0.14
$2_{02} \leftarrow 1_{01}$	0.4079	0.4062	0.4068	0.27	0.14
$2_{11} \leftarrow 1_{10}$	0.4091	0.4069	0.4075	0.39	0.14
$2_{12} \leftarrow 1_{11}$	0.4078	0.4052	0.4058	0.49	0.14
$3_{03} \leftarrow 2_{02}$	0.6138		0.6102	0.59	
$3_{12} \leftarrow 2_{11}$	0.6136		0.6113	0.38	
$3_{13} \leftarrow 2_{12}$	0.6131		0.6088	0.71	

Table 3.8: Calculated rotational constants (in GHZ) for the intermolecular ground states of H_2O-HCN using MCTDH and compared with the previous theoretical(theo) and experimental(exp) results.

Rot. Constant	MCTDH(cal)	Vindel [120](theo)	exp [209]	%(exp-cal)	%(exp-theo)
A	434.528	434.492			
B	3.059	3.057	3.062	0.62	0.16
C	3.043	3.032	3.036	0.23	0.13

Our results are summarized in the following publication.

PCCP

PAPER

View Article Online
View Journal | View Issue

Cite this: *Phys. Chem. Chem. Phys.*, 2023, **25**, 31813

Rovibrational states calculations of the H_2O–HCN heterodimer with the multiconfiguration time dependent Hartree method†

Hervé Tajouo Tela,[a] Ernesto Quintas-Sánchez,[b] Marie-Lise Dubernet,[c] Yohann Scribano,[d] Richard Dawes,[b] Fabien Gatti[e] and Steve Ndengué *[af]

Received 7th July 2023,
Accepted 1st November 2023

DOI: 10.1039/d3cp03225f

rsc.li/pccp

Water and hydrogen cyanide are two of the most common species in space and the atmosphere with the ability of binding to form dimers such as H_2O–HCN. In the literature, while calculations characterizing various properties of the H_2O–HCN cluster (equilibrium distance, vibrational frequencies and rotational constants) have been done in the past, extensive calculations of the rovibrational states of this system using a reliable quantum dynamical approach have yet to be reported. In this work, we intend to mend that by performing the first calculation of the rovibrational states of the H_2O–HCN van der Waals complex on a recently developed potential energy surface. We use the block improved relaxation procedure implemented in the Heidelberg MultiConfiguration Time-Dependent Hartree (MCTDH) package to compute the states of the H_2O–HCN isomer, from which we extract the transition frequencies and rotational constants of the complex. We further adapt an approach first suggested by Wang and Carrington—and supported here by analysis routines of the Heidelberg MCTDH package—to properly characterize the computed rovibrational states. The subsequent assignment of rovibrational states was done by theoretical analysis and visual inspection of the wavefunctions. Our simulations provide a Zero Point Energy (ZPE) and intermolecular vibrational frequencies in good agreement with past *ab initio* calculations. The transition frequencies and rotational constants obtained from our simulations match well with the available experimental data. This work has the broad aim to propose the MCTDH approach as a reliable option to compute and characterize rovibrational states of van der Waals complexes such as the current one.

1 Introduction

Water (H_2O) and hydrogen cyanide (HCN) are common components of planetary and interstellar environments,[1–3] contributing significantly to their rich chemistry. For instance, H_2O is the most abundant molecule in cometary atmospheres and HCN is amongst the few dozen molecules that have been observed around comets. Furthermore, hydrogen bonding is a fundamental phenomenon in chemistry, and its importance has been widely recognized in various fields of study, including atmospheric chemistry, biological processes, catalytic reactions, and materials science.[4–7] The HCN molecule is scientifically fascinating for multiple reasons. It is a highly anharmonic system that possesses a wide range of vibrational states, which combined with its triatomic nature, makes it a convenient model-system for the accurate study of predissociation and to develop/test theoretical methodologies that can be applied to more complex systems.[8,9] The H_2O–HCN is a relevant complex in astrophysics,[9,10] composed of two common molecules in planetary environments and comets.[1,2] In the Insterstellar Medium (ISM), H_2O is also one of the most abundant molecules after CO and H_2.

The interaction between water and hydrogen cyanide has been extensively studied,[11–16] with a special interest in the theoretical investigation of its structure and spectroscopy. This interaction leads to two different isomers. In one, HCN acts as the proton donor ($H_2O\cdots HCN$), and in the other one HCN acts as the proton acceptor ($HCN\cdots H_2O$), as shown in Fig. 1, with

[a] *ICTP-East African Institute for Fundamental Research, University of Rwanda, Kigali, Rwanda. E-mail: sndengue@eaifr.org*
[b] *Department of Chemistry, Missouri University of Science and Technology, 65409 Rolla, Missouri, USA*
[c] *LERMA, Observatoire de Paris, PSL Research University, CNRS, Sorbonne University, UPMC Univ Paris 06, 75014 Paris, France*
[d] *Laboratoire Univers et Particules de Montpellier, UMR-CNRS 5299, Université de Montpellier, Place Eugène Bataillon, 34095 Montpellier, France*
[e] *Institut de Sciences Moleculaires d'Orsay, UMR 8214, Université Paris-Sud – Université Paris-Saclay, 91405 Orsay, France*
[f] *Department of Physics, Trinity College, 06106 Hartford, Connecticut, USA*

† Electronic supplementary information (ESI) available. See DOI: https://doi.org/10.1039/d3cp03225f

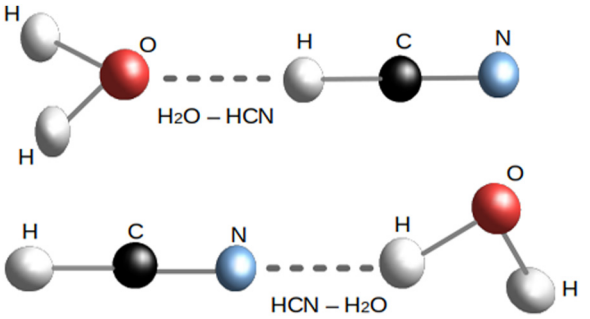

Fig. 1 Structures of H_2O–HCN (corresponding to the global minimum) and HCN–H_2O (corresponding to the secondary minimum) isomers.

the $H_2O\cdots HCN$ isomer being the more stable.[17–19] Moreover, the isomerization reaction between water and hydrogen cyanide has been studied (using high-level *ab initio* calculations[20,21] and microwave spectroscopy[22,23]) as well as for its isotopes[11] (using the pulsed-nuzzle technique, Fourier-transform microwave spectroscopy and a modified Balle/Flygare Fourier-transform microwave spectrometer associated with a sample source pulsed supersonic nozzle). While numerous works in the past two decades have surveyed (some even in full dimensionality) the rovibrational states of water containing heterodimers with linear molecules of astrophysical relevance (such as H_2O–H_2,[24–26] H_2O–CO,[27–32] H_2O–HF,[33–35] H_2O–CO_2[36] and H_2O–HCl,[37–39] just to name a few) there is to our knowledge no published report of rovibrational states calculations for the H_2O–HCN system, either in full dimensionality nor even in the rigid rotor approximation. Not even after the publication of a new state-of-the-art five-dimensional potential energy surface (PES) of H_2O–HCN by Quintas-Sánchez and Dubernet[15] (referred to as the QSD PES later in the text); which, despite being built primarily for astrophysical simulations, turn out—as we will show here—to be quite reliable for spectroscopic studies as well.

We present in this work the first calculations of the low-lying rovibrational states for the H_2O–HCN complex, obtained using the MultiConfiguration Time-Dependent Hartree (MCTDH) method. The paper is organized as follows. In the next section, we describe the methodology and computational procedure followed for the MCTDH calculations. Following that, in another section, we present and discuss our results. Finally, we summarize our work and discuss future avenues of research for this system and others.

2 Computational procedure

2.1 Rovibrational states calculations with MCTDH

The rovibrational spectrum of the H_2O–HCN cluster is studied using the MCTDH algorithm.[40–43] MCTDH is a time-dependent method in which each degree of freedom is associated with a small number of orbitals (or single-particle functions, SPFs) which, through their time dependence, allow an efficient description of the molecular dynamical processes. The total MCTDH wave function is expanded in Hartree products, that is,

$$\begin{aligned}\Psi(Q_1,\ldots,Q_f,t) &= \sum_{j_1=1}^{n_1}\cdots\sum_{j_f=1}^{n_f} A_{j_1\cdots j_f}(t)\prod_{\kappa=1}^{f}\varphi_{j_\kappa}^{(\kappa)}(Q_\kappa,t)\\ &= \sum_{\Lambda} A_\Lambda \Phi_\Lambda,\end{aligned} \tag{1}$$

where f is the number of degrees of freedom (DOF) of the system, $Q_1,\ldots,Q_f$ are the nuclear coordinates, $A_\Lambda \equiv A_{j_1\cdots j_f}$ denotes the MCTDH expansion coefficients, and $\phi_{j_\kappa}^{(\kappa)}(Q_\kappa,t)$ are the n_κ SPFs associated with each degree of freedom κ (*i.e.*, they form a time dependent variable basis along κ). The subsequent equations of motion for the coefficients and SPFs are derived after substituting the wave function *ansatz* into the time-dependent Schrödinger equation. To solve the equations of motion, the κ SPFs are represented on a (fixed) primitive basis or discrete variable representation (DVR)-grid[44–46] of N_κ points:

$$\phi_{j_\kappa}^{(\kappa)}(Q_\kappa,t) = \sum_{i_\kappa=1}^{N_\kappa} c_{i_\kappa j_\kappa}^{(\kappa)}(t)\chi_{i_\kappa}^{(\kappa)}(Q_\kappa), \tag{2}$$

where ideally the n_κ of eqn (1) is such that $n_\kappa \ll N_\kappa$. Thus, the MCTDH method propagates the wave function on a small, time-dependent, variationally optimized basis set of single-particle functions, which in turn are defined on a fixed time-independent primitive basis set.

The MCTDH algorithm is more efficient when the Hamiltonian operator is written as a sum of products (SOP) of single-particle operators. The Kinetic Energy Operator (KEO) can easily be expressed in the required form when using polyspherical coordinates, such as the Jacobi coordinates used in this work. We followed the subsystem KEO derivation presented by Gatti and Iung,[47] which was used in some of our previous work to describe an asymmetric rotor–atom collision[48] and an asymmetric rotor–diatom collision and spectroscopy.[26,49] In the specific case of dimers, this separation of subsystem is similar to the formulation for dimers given in the seminal work by Brocks *et al.*[50] As we did in our previous MCTDH calculations,[51] we do not work in the Body-Fixed (BF) frame but in the E_2

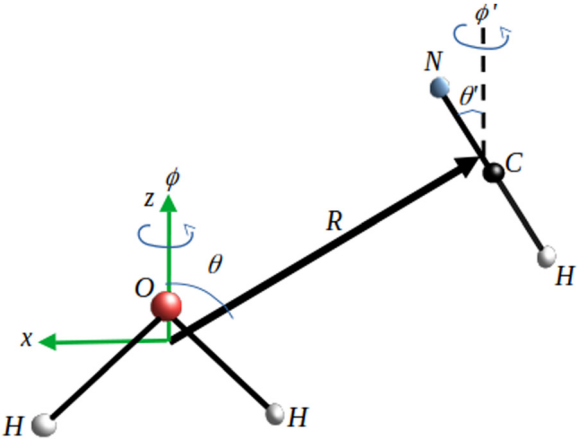

Fig. 2 Definition of the dimer BF coordinates system used in ref. 15 to represent the PES of the H_2O–HCN system.

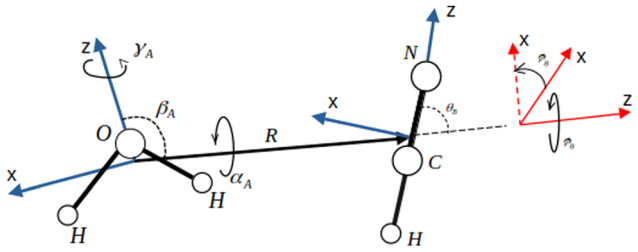

Fig. 3 Definition of the H_2O–HCN in the rigid rotor approximation and coordinates system used to compute the rovibrational states. The red solid frame is the E_2 frame.

frame,[26,47] which is obtained by rotation of the two first Euler angles of the SF frame (*cf.* Fig. 2 and 3). This representation leads to a decoupling of the modes of each monomer and is particularly useful for inelastic calculations with the MCTDH approach.[49] The KEO in the E_2 frame can be expressed as

$$\begin{aligned} 2\hat{T} &= -\frac{1}{\mu}\frac{\partial^2}{\partial R^2} + 2\hat{T}_A + 2\hat{T}_B \\ &\quad + \frac{1}{\mu R^2}\left(\vec{J}^\dagger\vec{J} + (\vec{L}_A + \vec{L}_B)^2 - 2(\vec{L}_A + \vec{L}_B)\vec{J}\right)_{E_2}, \end{aligned} \tag{3}$$

where μ is the reduced mass of the H_2O–HCN cluster, and the A and B subscripts refer to the H_2O and HCN fragments respectively. The rigid rotor Hamiltonian of the H_2O molecule is expressed as[52,53]

$$\begin{aligned} \hat{T}_A &= \frac{A}{2}\left(L_{A,+}{}^2 + L_{A,-}{}^2 + L_{A,+}L_{A,-} + L_{A,-}L_{A,+}\right) \\ &\quad - \frac{C}{2}\left(L_{A,+}{}^2 + L_{A,-}{}^2 - L_{A,+}L_{A,-} - L_{A,-}L_{A,+}\right) \\ &\quad + BL_{z^{BF}{}_A}{}^2, \end{aligned} \tag{4}$$

with the H_2O rotational constants: A = 27.88063 cm^{-1}, B = 9.27771 cm^{-1} and C = 14.52177 cm^{-1}.[54] The rigid rotor kinetic energy of the HCN fragment can be written simply as $\hat{T}_B = B_{HCN}\vec{L}_B{}^2$, with the rotational constant B_{HCN} = 1.4782218 cm^{-1}.[55,56] The reduced mass used for the H_2O–HCN system was μ = 10.805547045 a.m.u.

The final form of the KEO as implemented in the MCTDH code is then

$$\begin{aligned} 2\hat{T} &= -\frac{1}{\mu}\frac{\partial^2}{\partial R^2} + 2\hat{T}_A + 2\hat{T}_B \\ &\quad + \frac{1}{\mu R^2}\left(J(J+1) + \vec{L}_A{}^2 + \vec{L}_B{}^2 - 2L_{A,z}{}^2 - 2L_{B,z}{}^2\right) \\ &\quad + \frac{1}{\mu R^2}\left(L_{A,+}L_{B,-} + L_{A,-}L_{B,+} - 2L_{A,z}L_{B,z}\right) \\ &\quad + \frac{1}{\mu R^2}\left(C_+(J,K)(L_{A,+} + L_{B,+})\right) \\ &\quad + \frac{1}{\mu R^2}\left(C_-(J,K)(L_{A,-} + L_{B,-})\right), \end{aligned} \tag{5}$$

with

$$C_\pm(J,K) = \sqrt{(J(J+1) - K(K\pm 1)}. \tag{6}$$

2.2 The potential energy surface

The potential energy operator, just as the KEO, also needs to be expressed in a sums of products form. Usually, for systems of the appropriate dimension (<6) for which the PES is not expressed in the product-form already, there exists an efficient fitting procedure (Potfit,[57,58] implemented in the MCTDH package[59]) to obtain the appropriate representation. For potentials in even higher dimensionality, a MultiGrid Potfit,[60] a Multi-Layer Potfit,[61] or even more recently, a Monte-Carlo implementation of the Canonical Polyadic Decomposition (CPD)[62] for MCTDH are now available to transform general potentials into a product form. However, some of these implementations can lead to a prohibitive number of terms in the potential expansion—and thus slow down computations—while for others the handling of the system's symmetries becomes problematic—and thus may restrict, or poorly represent, the whole range of the potential for this type of application. In this study, just as we did in our previous work for H_2O–H_2,[26] we overcome this problem by taking advantage of the fact that the potential is already represented in a multipolar form[15] and that we only have to make a transformation to re-express it in coordinates more suitable for the MCTDH calculations.

The PES from ref. 15 is originally expressed as:

$$V(R,\theta,\varphi,\theta',\varphi') = \sum_i v_i(R)\bar{t}_i(\theta,\varphi,\theta',\varphi'), \tag{7}$$

with $i = \{l_A, m_A, l_B, l\}$, and

$$\begin{aligned} \bar{t}_i(\theta,\varphi,\theta',\varphi') &= \frac{1}{2\pi}\alpha_{l_A,m_A}\sum_{r_1=-l_A}^{l_A}\sum_{r_2=-l_B}^{l_B}\beta_{i,r_1}\begin{pmatrix} l_A & l_B & l \\ r_1 & r_2 & r \end{pmatrix} \\ &\quad \times P_{l_B}^{r_2}(\cos\theta')P_l^r(\cos\theta)\cos(r_2\varphi' + r\varphi), \end{aligned} \tag{8}$$

where the expression in large brackets is a Wigner 3-*j* symbol, and the factors α_{l_A,m_A} and β_{i,r_1} are given by:

$$\alpha_{l_A,m_A} = \frac{\sqrt{2l_A+1}}{\sqrt{2+2\delta_{m_A,0}}}, \tag{9}$$

and

$$\beta_{i,r_1} = \frac{1}{2\pi}\left(\delta_{m_A,r_1} + (-1)^{l_A+m_A+l_B+l}\delta_{-m_A,r_1}\right). \tag{10}$$

Indices r_1, r_2, and r are dependent through $r = -(r_1 + r_2)$. The maximum order of the terms involved in the expansion are determined by l_A = 7, l_B = 12, m_A = 4, and l = 18 (with $m_A \geq 0$, and l_A and $l_A + l_B + l$ always being even because of symmetry considerations) resulting in a total of 445 one-dimensional $v_i(R)$ terms in eqn (7). The angles (θ,φ) and (θ',φ') represent respectively the collisional direction and the HCN fragment orientation in the BF frame, as represented in Fig. 2. As can be seen in the figure, the BF of the original PES is defined such that its origin is the center of mass of the H_2O molecule, the *z*-axis is its C_2 axis, with the positive *z* in the direction of the

O atom and the *xz* plane being the plane containing the H_2O molecule.

Fig. 4 shows a two-dimensional cut of the QSD PES as a function of R and θ (the other three angular coordinates are fixed at their corresponding values for the global minimum: $\varphi = 0^\circ$, $\theta' = 0^\circ$, and $\varphi' = 0^\circ$). Notice that the global minimum of the potential—corresponding to the $H_2O\cdots HCN$ isomer—is located at the bottom of the figure ($\theta = 0^\circ$ and $R = 7.162$ Å), with a well depth of 1814.51 cm^{-1}. A secondary minimum (not shown in the figure) corresponding to the $HCN\cdots H_2O$ isomer, is located at $\theta = 119.61^\circ$, $\varphi = 0^\circ$, $\theta' = 74.49^\circ$, $\varphi' = 180^\circ$ and $R = 7.004$ Å, with a well depth of 1377.30 cm^{-1}.

In the MCTDH implementation, the dynamics of this system in the E_2 frame is described by six coordinates: the fragments' separation R and five angles (α_A, β_A, γ_A, θ_B and φ_B), as shown in Fig. 3. The origin of the E_2 frame is the center of mass of H_2O, as it was the case for the BF frame. The z-axis is in the direction of $\vec{R}$, the vector connecting the centers of mass of the two molecules (*cf.* Fig. 3). The three Euler angles (α_A, β_A, γ_A) determine the orientation of the H_2O molecule in our E_2 frame, while the other two spherical angles (θ_B and φ_B) define the orientation of the HCN molecule.

As van der Avoird and Nesbitt pointed out,[24] there are two ways to transform the PES coordinates from the BF Frame to the E_2 Frame. In the first approach, the coordinates are related according to $\theta = \beta_A$; $\phi = \pi - \gamma_A$; and θ', ϕ' can be expressed in terms of α_A, β_A, γ_A, θ_B, ϕ_B with the use of an inverse Euler rotation matrix;[24] then, the PES in the appropriate frame can be numerically generated. This procedure, used by Wang and Carrington,[25] is not convenient for this work as it would require building a new SOP expansion of the PES after the surface is numerically transformed. We should point out that our BF and E_2 Frames correspond respectively to the Molecule Fixed (MF) and the Dimer Fixed (DF) Frames described in the work of Wang and Carrington. The second approach, which is the one we used, relates the coefficients of the multipolar expansion in both frames[24] and thus allows to generate the PES in the E_2 Frame directly in a SOP form. The correctness of the new multipolar expansion in the E_2 frame can be conveniently verified by comparing the new PES values with the corresponding ones generated using the original PES. This approach saves a significant amount of time and allows more flexibility in the calculations. It is worth noticing that this transformation was already tested and checked in our previous work on H_2O–H_2,[26] which used a multipolar PES constructed with the same type of coordinates as the ones used by Quintas-Sánchez and Dubernet.[15]

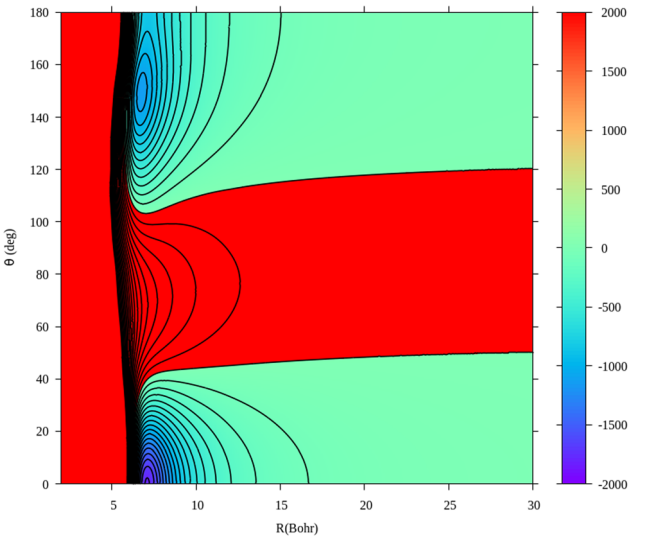

Fig. 4 2D cut of the PES. The figure shows the global minimum (De = 1814.51 cm^{-1}) which is the $H_2O\cdots HCN$ isomer.

2.3 Details of the computations

The rovibrational bound states of the H_2O–HCN complex are obtained with the block improved relaxation method[42,63] implemented in the Heidelberg MCTDH package.[59] The block improved relaxation is derived from the improved relaxation method,[64,65] a MCSCF approach where the SPFs are optimized by relaxation[66] (propagation in negative imaginary time) but the coefficients vector (*A*-vector) is determined by diagonalization of the Hamiltonian matrix evaluated in the set of present SPFs using the Davidson algorithm.[67] MCTDH is, thus, used here as a time-independent method, where however the optimized basis functions are obtained by relaxation, a time dependent approach. The working equations of the improved relaxation and block improved relaxation have already been extensively described elsewhere[42,64,65] and do not need to be repeated here.

The primitive basis, its range, and the number of SPFs used for the calculations of the rovibrational states are summarized in Table 1. We performed all the calculations reported in this work using the block improved relaxation method—proceeding in blocks of three states, starting from the ground state and progressing to highly excited states. The relaxation time for a converged calculation with a block of three wavefunctions took approximately 72 hours of computational time using 16 processors on a Linux Cluster. For the evaluation of levels with $J > 0$, one could start the calculations from the previously converged results corresponding to $J - 1$, and thus save a

Table 1 Parameters of the primitive basis used for the rovibrational calculations of H_2O–HCN. FFT stands for the Fast Fourier Transform. Wigner stands for the Wigner DVR. KLeg is the extended Legendre DVR. *K* stands for the momentum representation of a set of angles: the first and third Euler angles α_A and γ_A of H_2O, and the second spherical angle ϕ_B of HCN, both monomers in the rigid rotor approximation. The units for distance and angle are Bohrs and radians respectively. We additionally would like to stress that the range of γ_A, α_A and ϕ_B are actually the ranges of their respective momentum representation k_γ, k_α and k_ϕ respectively

Coordinate	Primitive basis	Number of points	Range	Size of SPF basis
R	FFT	96	2.0–22.0	10–20
β_A	Wigner	12	0–π	20–100
γ_A	K	23	−11,11	
α_A	K	11	−5,5	
θ_B	KLeg	24	0–π	40–60
ϕ_B	K	11	−5,5	

significant amount of computational time to reach convergence. To describe the orientation of the H_2O and the HCN fragments in the E_2 frame, a primitive basis composed of Fast Fourier Transform (FFT) functions for the intermolecular distance R, was coupled with a Wigner-DVR basis for β_A, and a two-dimensional extended Legendre-K DVR (replacing ϕ_B by k_ϕ), while α_A and γ_A are replaced by their momentum representation k_α and k_γ. For testing purposes, we also ran ($J = 0$) calculations with the angular primitive basis composed of the Wigner-DVR basis and a two-dimensional Legendre DVR. The (Wigner, K, K) and (KLeg, K) DVRs are thus replaced in these tests by their counterparts the (Wigner, Exp, Exp) and (PLeg, Exp) DVRs, where KLeg and PLeg are respectively the extended Legendre DVR and two dimensional Legendre DVR. As mentioned in our previous work,[26] while calculations in real space coordinates basis at $J = 0$ may be slightly faster than calculations in real and momentum basis, we used the real and momentum basis because it is the only one that allows $J > 0$ calculations with the MCTDH description of our chosen frame and operators.

After transforming the PES from eqn (7) to the E_2 frame, we can write

$$V(R,\beta_A,\gamma_A,\alpha_A,\theta_B,\varphi_B) = \sum_{\substack{r_\beta,r_\gamma \\ r_\alpha,r_\theta}} \tilde{V}_{\substack{r_\beta,r_\gamma \\ r_\alpha,r_\theta}}(R) f_{\substack{r_\beta,r_\gamma \\ r_\alpha,r_\theta}}(\omega_A,\omega_B), \quad (11)$$

where

$$f_{\substack{r_\beta,r_\gamma \\ r_\alpha,r_\theta}}(\omega_A,\omega_B) = D^{(r_\beta)}_{r_\alpha r_\gamma}(\alpha_A,\beta_A,\gamma_A)^* C_{r_\theta,-r_\alpha}(\theta_B,\varphi_B), \quad (12)$$

with $D^{(r_\beta)}_{r_\alpha r_\gamma}(\alpha_A,\beta_A,\gamma_A)$ and $C_{r_\theta,-r_\alpha}(\theta_B,\phi_B)$ being respectively the Wigner D-matrix and the Racah normalized spherical harmonics. The action of the potential on the wavefunction can then be obtained using k_α, k_γ and k_ϕ to express the angles α_A, γ_A, and ϕ_B. In the following, we drop the indices A and B for simplicity.

$$\hat{V}\Psi(R,\beta,k_\gamma,k_\alpha,\theta,k_\varphi) = \sum_{\substack{r_\beta,r_\gamma \\ r_\alpha,r_\theta}} \bar{V}_{\substack{r_\beta,r_\gamma \\ r_\alpha,r_\theta}}(R,\beta,k_\gamma,k_\alpha,\theta,k_\varphi) \times \Psi(R,\beta,k_\gamma - r_\gamma, k_\alpha - r_\alpha,\theta,k_\varphi + r_\alpha). \quad (13)$$

We selected the primitive basis set by testing the convergence of the low-lying energy levels for various choices of the DOF parameters. The ones reported in Table 1 yield convergence of the results to within 0.02 cm^{-1} or less for the low-lying states. Also, the number of SPFs was increased in the calculations from a relatively small number for the lower levels to significantly larger values for the excited states: this grows quickly because of the deep well of the potential and the rapidly growing density of states with increasing energy.

A point of emphasis to ease the reading of this manuscript: in the following sections, J,K will relate to the rotation of the dimer, while j,k will be associated to the rotation of the H_2O monomer.

The Wigner-DVR can be implemented in two forms in MCTDH. In one, the 3 Euler angles can be used as they are defined to characterize each of the degrees of Freedom of the Wigner-DVR. In the other, the α and γ angles could be Fourier Transformed into the K component used in the calculations. This approach is also used with the Extended Legendre DVR implemented in MCTDH where the azimuthal angle can be Fourier Transformed and limited to values smaller than the expected size of the primitive basis: which is what was done here.

2.4 Symmetry and assignment of states

The current implementation of the Wigner-DVR in the MCTDH package does not allow even/odd symmetry differentiation while performing the calculations using a direct product basis. Hence, it was not possible to selectively compute (ro)vibrational states that have a specific symmetry with respect to the H_2O fragment axis. Nevertheless, using the computational procedure described above we are able to obtain a large number of states (some real and some fictitious) which can be challenging to assign directly. In previous calculations of this type of cluster, such as the H_2O–H_2 calculations performed by van der Avoird and Nesbitt,[24] or Wang and Carrington,[25] the primitive basis was constrained such that K, the projection of the total angular momentum, satisfies: $K = m_A + m_B$. Wang and Carrington proposed a method to characterize the rovibrational states according to the abundance of the character of the rigid rotor rotational state of H_2O in the wavefunction: that is, characterizing it along the most abundant $j_{k_a k_c}$, where k_a and k_c are the projections of the total angular momentum J on the inertial axis in the prolate and oblate limits.

In this work, we are able to go beyond the analysis we performed previously on a similar system[26] (H_2O–H_2) to do a characterization in a similar fashion as Wang and Carrington.[25] First, as we did in our previous work on H_2O–H_2, the Σ, Π, ... characters of the wavefunction can be extracted after the MCTDH calculation by looking at the output file of a single state calculation. Here, by summing the average values of the α and ϕ DOFs (which correspond to the m_A and m_B used by Wang and Carrington), we can determine K as $K = \langle\alpha\rangle + \langle\phi\rangle$. This approach not only makes it possible to determine K but also turns out to filter physical states from fictitious ones; since we are using a direct basis with no constraints on the basis functions, the computational procedure is free to generate for instance for $J = 0$, states having a projection $K > 0$, which is not physical. By applying the $K = \langle\alpha\rangle + \langle\phi\rangle$ criterion, we can discard all the nonphysical states from the results. In Table 3, we show the lowest 8 states from a block improved relaxation calculation, where 6 of the 8 are nonphysical.

The H_2O character ($j_{k_a k_c}$) of the rovibrational state was obtained by projection of the rovibrational wavefunction onto the rotational states of H_2O. The specific $j_{k_a k_c}$ character presented in Tables 4–7 was assigned by selecting the largest projection of the rovibrational state to the H_2O rotational states considered. The projection of the rovibrational state $|\Psi\rangle$ is obtained from the relation $p_i = \langle\Psi|\hat{P}_i|\Psi\rangle$, where the projector $\hat{P}_i$ onto a rovibrational state $|j_{k_a k_c},m\rangle$ writes $\hat{P}_i = |j_{k_a k_c},m\rangle\langle j_{k_a k_c},m|$. The contributions of each projection $|j_{k_a k_c},m\rangle$ are then summed to obtain the contribution of the $|j_{k_a k_c}\rangle$ rotational state to the

wavefunction. Additional details on this derivation are provided in the Appendix.

3 Results and discussion

The primary motivation of this work is the lack of availability in the literature of work reporting calculations of rovibrational states of the H_2O–HCN complex with only a couple of exceptions. We also independently performed here *ab initio* calculations at a higher level of theory (CCSD(T)-F12) to serve as a basis of comparison for the rovibrational state ($J = 0$) calculations.

3.1 Comparison with harmonic frequencies

A limited number of published results on the vibrational states of H_2O–HCN are available in the literature. So far, only harmonic frequencies[14,68] have been reported for this system and some of its isotopologues/isotopomers. This limits the validation of our new results. Nevertheless, in Table 2 we compare the previously reported harmonic frequencies obtained by Heikkilä *et al.*[14] (2nd order Møller–Plesset perturbation theory (MP2) with 6-311++G(2d,2p)) and Tshehla and Anthony[68] (MP2 with 6-31G** split-valence polarized basis set) with our new CCSD(T)-F12b/VTZ-F12 harmonic frequencies and the full variational vibrational frequencies ($J = 0$) obtained from MCTDH using the QSD PES.

The four different approaches compared in the table exhibit significant, but not drastic, variations between each of the three sets of harmonic frequencies as well as with the full MCTDH calculations. Of course harmonic frequencies are notoriously inaccurate for low frequency modes corresponding to large amplitude motion. This particular complex is somewhat more tightly bound with its rather large well depth, so the comparison is still sensible. Of the three harmonic calculations, the CCSD(T)-F12 method employed in our new calculations is most similar to that underlying the QSD PES, yet especially for certain modes there are significant differences between those harmonic frequencies and the more complete MCTDH results.

The MCTDH rovibrational calculations reflect the quality of the electronic structure calculations (CCSD(T) with counterpoise correction for basis set superposition error) and fitting quality of the QSD PES. The significant variation observed, most notably for the HCN libration and H_2O torsion modes, is not surprising given the different methods employed, but points to the valuable contribution that an experimental measurement could make.

The assignment of the nodal excitation of the lowest vibrational states is straightforward and can be done by analysis and visual inspection of the vibrational wavefunctions. However, it becomes more difficult with increasing energy as the modes become mixed and the coordinate system is no longer ideal[25] for their visual assignment.

Table 2 Harmonic and variational intermolecular frequencies of H_2O–HCN. Heikkilä are the results from Heikkilä *et al.*[14] (MP2 with 6-311++G(2d,2p)), Tshehla are the results from Tshehla and Anthony[68] (MP2 with 6-31G** split-valence polarized basis set), Harm are our new CCSD(T)-F12b/VTZ-F12 *ab initio* harmonic frequencies, and MCTDH corresponds to the results of this work—obtained on the QSD PES at $J = 0$. All energies are in cm^{-1}

Mode	Heikkilä	Tshehla	Harm	MCTDH
ν_1 (HCN libration)	98.9	57.2	72.7	93.4
ν_2 (H_2O wagging)	101.6	110.0	84.6	110.9
ν_3 (O···C stretch)	139.9	133.8	121.2	130.0
ν_4 (H_2O torsion)	144.6	222.4	147.8	171.6
ν_5 (H_2O rocking)	243.1	255.0	239.1	237.6
ZPE*	364.1	389.2	332.7	357.2

3.2 Rovibrational states and rotational constants

The rovibrational states of the H_2O–HCN cluster for $J = 0,\ldots,3$ are computed using the quantum mechanical method described above. The convergence of an MCTDH calculation is tested with respect to both bases: the primitive basis and the SPF basis. In this study, we first performed a series of calculations for $J = 0$, varying the SPFs basis sizes to determine the required size to reach convergence. Then, using that SPF basis, we modified the primitive basis to determine an appropriate basis that ensured a converged calculation while balancing computational cost. The primitive basis reported in Table 1 is the one finally selected, and all the results presented in this work were obtained using that basis. Finally, to ensure consistency, we once again vary the SPF basis to ensure that the vibrational levels do not vary significantly. The results of these last convergence tests are presented in Table 3, where we show the convergence of the ground state and the first two excited states with increasing SPFs basis size. As already mentioned, MCTDH calculations are likely to produce real and fictitious states: the states with energy E_1, E_2, E_3, E_4, E_5, and E_6 are six examples of those spurious states coming directly from MCTDH calculations that we filter out from our results using the analysis procedure described before. By systematically testing the convergence of our results with different basis sizes, we were able to ensure that our calculations are accurate and reliable.

Despite some limitations of the current implementation of the MCTDH method in the Heidelberg MCTDH package (*i.e.*, lack of symmetry of the Wigner-DVR), important information can be obtained from the calculations of Tables 4–7 using various analysis procedures. First, the primitive basis selected for the calculation connects the average value of the angular modes α and ϕ to m_A and m_B respectively, which is necessary to define $K = m_A + m_B$. Thus by simply checking the output file from the MCTDH calculation, the major character (Σ,Π,...) of the eigenstates can be extracted. Tables 4–7 show the energy levels of H_2O–HCN reported relative to the 5D ground state energy at $-1457.281\ cm^{-1}$. In the tables, the energy levels are labeled with the values of K, the projection of the total angular momentum on the z-axis of the system, with $K = 0$, $K = 1$, $K = 2$, and $K = 3$ corresponding to Σ, Π, Δ, and Φ states respectively.

Second, the 'weight' and 'assignment' columns are based on the magnitude of the contribution of each $j_{k_a k_c}$ to the total wavefunction as referenced in the work of Wang and Carrington.[25] A more detailed description of how this procedure has been applied in this context is provided in the Appendix. For this work, we evaluated the weights for the $J = 0,\ldots,3$ rotational states and neglected the others. As such,

Table 3 Convergence of the ground state rovibrational energy (cm^{-1}) of H_2O–HCN for J = 0. In the table, the first column represents the SPF basis, where $a_1/a_2/a_3$ stands for the number of SPF along the first mode R (after extensive testing along the R mode, we determined that the mode achieves convergence with an SPF value of 8. However, in order to ensure a higher level of accuracy, we have opted to set the SPF value to 10), the second combined mode Wigner/K/K, and the third combined mode KLeg/K, as suggested in Table 1. The energy E_0 is the ground state energy of this system and E_7 is the first excited state. E_1, E_2, E_3, E_4, E_5, and E_6 are nonphysical energy levels that are filtered out from our results

	Energy							
SPF	E_0	E_1	E_2	E_3	E_4	E_5	E_6	E_7
10/60/40	−1457.280	*−1442.897*	*−1442.897*	*−1399.824*	*−1399.824*	*−1367.465*	*−1367.464*	−1363.799
10/70/40	−1457.280	*−1442.898*	*−1442.898*	*−1399.824*	*−1399.824*	*−1367.466*	*−1367.466*	−1363.797
10/80/40	−1457.280	*−1442.898*	*−1442.898*	*−1399.825*	*−1399.825*	*−1367.467*	*−1367.467*	−1363.803
10/90/40	−1457.281	*−1442.898*	*−1442.898*	*−1399.825*	*−1399.825*	*−1367.467*	*−1367.467*	−1363.803
10/100/40	−1457.281	*−1442.898*	*−1442.898*	*−1399.825*	*−1399.825*	*−1367.467*	*−1367.467*	−1363.804
10/60/50	−1457.280	*−1442.897*	*−1442.897*	*−1399.823*	*−1399.823*	*−1367.464*	*−1367.464*	−1363.799
10/70/50	−1457.280	*−1442.898*	*−1442.898*	*−1399.825*	*−1399.825*	*−1367.466*	*−1367.465*	−1363.801
10/80/50	−1457.280	*−1442.898*	*−1442.898*	*−1399.825*	*−1399.825*	*−1367.467*	*−1367.467*	−1363.802
10/90/50	−1457.281	*−1442.898*	*−1442.898*	*−1399.825*	*−1399.825*	*−1367.467*	*−1367.467*	−1363.803
10/100/50	−1457.281	*−1442.898*	*−1442.898*	*−1399.825*	*−1399.825*	*−1367.467*	*−1367.467*	−1363.804
10/60/60	−1457.280	*−1442.897*	*−1442.897*	*−1399.824*	*−1399.823*	*−1367.464*	*−1367.464*	−1363.798
10/70/60	−1457.280	*−1442.898*	*−1442.898*	*−1399.824*	*−1399.824*	*−1367.466*	*−1367.466*	−1363.802
10/80/60	−1457.280	*−1442.898*	*−1442.898*	*−1399.824*	*−1399.824*	*−1367.467*	*−1367.467*	−1363.802
10/90/60	−1457.281	*−1442.898*	*−1442.898*	*−1399.825*	*−1399.825*	*−1367.467*	*−1367.467*	−1363.804
10/100/60	−1457.281	*−1442.898*	*−1442.898*	*−1399.825*	*−1399.825*	*−1367.467*	*−1367.467*	−1363.804

Table 4 Low energy rovibrational levels of H_2O–HCN for J = 0. The definition of weight and cumulative weight (cum. wgt.) is given in the text. p/o-H_2O specifies the *para*/*ortho*-H_2O character of the rovibrational states. Energies are relative to the ground state at −1457.281 cm^{-1} and are given in cm^{-1}. The weights and cumulative weights are dimensionless

p/o-H_2O	Assignment	Energy	Weight	Cum. wgt.
p	$\Sigma(1_{11})$	0.000	0.343	0.934
o	$\Sigma(1_{01})$	93.477	0.224	0.861
o	$\Sigma(1_{01})$	110.989	0.198	0.894
p	$\Sigma(1_{11})$	130.066	0.343	0.913
o	$\Sigma(2_{21})$	171.673	0.328	0.861
p	$\Sigma(1_{11})$	173.234	0.276	0.849
o	$\Sigma(1_{01})$	217.613	0.225	0.856
p	$\Sigma(2_{11})$	224.841	0.253	0.793
p	$\Sigma(2_{11})$	229.862	0.234	0.835
o	$\Sigma(1_{01})$	237.690	0.204	0.898
p	$\Sigma(1_{11})$	253.893	0.341	0.913
o	$\Sigma(2_{12})$	254.397	0.212	0.687
o	$\Sigma(2_{12})$	260.083	0.220	0.755

Table 5 Same as Table 4 for J = 1

p/o-H_2O	Assignment	Energy	Weight	Cum. wgt.
p	$\Sigma(1_{11})$	0.205	0.343	0.912
o	$\Sigma(1_{01})$	14.595	0.243	0.899
o	$\Sigma(1_{01})$	14.595	0.243	0.854
p	$\Sigma(1_{11})$	90.031	0.309	0.878
p	$\Sigma(1_{11})$	90.032	0.309	0.878
p	$\Sigma(1_{11})$	93.684	0.309	0.879
o	$\Sigma(1_{01})$	111.194	0.198	0.894
o	$\Sigma(1_{01})$	130.267	0.224	0.856
p	$\Pi(1_{11})$	143.018	0.343	0.913
o	$\Pi(1_{01})$	144.518	0.245	0.900
o	$\Sigma(2_{21})$	171.877	0.328	0.765
p	$\Sigma(1_{11})$	173.442	0.276	0.825
p	$\Pi(1_{11})$	214.898	0.307	0.884
o	$\Sigma(1_{01})$	217.817	0.225	0.856
p	$\Sigma(2_{11})$	225.049	0.253	0.807
p	$\Sigma(2_{11})$	230.101	0.234	0.830
o	$\Sigma(1_{01})$	237.891	0.204	0.898
p	$\Sigma(1_{11})$	254.090	0.341	0.913
o	$\Sigma(2_{12})$	254.601	0.212	0.687
p	$\Pi(1_{11})$	255.658	0.250	0.839
o	$\Sigma(2_{12})$	260.290	0.220	0.752

the 'Cumulative Weight' that is obtained only sums the contributions of all the partial weights contributions from J = 0,...,3. As the cumulative weight is often above 75% and the individual weight is usually near or above 20%, the rotational state assignment is quite reliable assuming that higher rotational states have a negligible contribution to that specific wavefunction. However, while we attempt to associate a major H_2O rotational character to the rovibrational wavefunctions, it is worth pointing out that for several of these states the contribution of a specific H_2O rotational state was just marginally higher than others, and it is actually more likely that two or three H_2O rotational states contribute to the character of a specific rovibrational state rather than just a single state.

Third, we can also specify the *para*/*ortho*-H_2O parity of the rovibrational state by assessing the major character obtained in the 'assignment' column. In fact, the overlaps of the rovibrational wavefunctions are only non-zero for *para*/*ortho* states according to the character of the most dominant H_2O rotational states. This specific aspect supports the idea that states from different rotational symmetries (*para*/*ortho*) do not mix in the generation of rovibrational states of the cluster (at least at low energies as displayed here) and thus the implementation of symmetry on the Wigner-DVR in MCTDH, allowing to separate *para* from *ortho* H_2O states in the calculations would definitely help in reducing the cost of the calculations while producing yet accurate results.

One current limitation that we experience in our setup is the inability to implement the inversion symmetry in the MCTDH

Table 6 Same as Table 4 for $J = 2$

p/o-H_2O	Assignment	Energy	Weight	Cum. wgt.
p	$\Sigma(1_{11})$	0.611	0.343	0.912
o	$\Sigma(1_{01})$	15.001	0.243	0.899
o	$\Sigma(1_{01})$	15.003	0.243	0.856
o	$\Delta(1_{10})$	58.101	0.246	0.845
p	$\Sigma(1_{11})$	90.441	0.309	0.883
p	$\Sigma(1_{11})$	90.442	0.309	0.883
o	$\Sigma(1_{01})$	94.095	0.224	0.861
o	$\Sigma(1_{01})$	111.602	0.198	0.888
p	$\Sigma(1_{11})$	130.666	0.343	0.913
o	$\Sigma(1_{01})$	144.919	0.245	0.900
o	$\Sigma(1_{01})$	172.254	0.328	0.861
p	$\Sigma(1_{11})$	173.854	0.276	0.857
p	$\Pi(1_{11})$	215.308	0.307	0.884
o	$\Sigma(1_{01})$	218.223	0.225	0.865
p	$\Sigma(2_{11})$	225.467	0.252	0.803
p	$\Sigma(2_{11})$	230.535	0.234	0.831
p	$\Delta(2_{11})$	236.557	0.244	0.810
o	$\Sigma(1_{01})$	238.292	0.204	0.898
p	$\Sigma(1_{11})$	254.482	0.341	0.913
o	$\Sigma(2_{12})$	255.008	0.212	0.686
p	$\Pi(1_{11})$	256.082	0.251	0.838
o	$\Sigma(2_{12})$	260.701	0.220	0.753

Table 7 Same as Table 4 for $J = 3$

p/o-H_2O	Assignment	Energy	Weight	Cum. wgt.
p	$\Sigma(1_{11})$	1.215	0.343	0.911
o	$\Sigma(1_{01})$	15.608	0.243	0.899
o	$\Sigma(1_{01})$	15.613	0.243	0.915
p	$\Delta(2_{11})$	58.711	0.285	0.849
p	$\Sigma(1_{11})$	91.055	0.309	0.883
p	$\Sigma(1_{11})$	91.060	0.309	0.883
o	$\Sigma(1_{01})$	94.711	0.224	0.860
o	$\Sigma(1_{01})$	112.215	0.198	0.894
p	$\Sigma(1_{11})$	131.264	0.343	0.913
o	$\Sigma(1_{01})$	145.513	0.245	0.901
p	$\Gamma(1_{01})$	155.500	0.261	0.814
o	$\Sigma(1_{10})$	172.812	0.210	0.860
p	$\Sigma(1_{11})$	174.473	0.276	0.853
p	$\Pi(1_{11})$	215.909	0.307	0.884
o	$\Sigma(1_{01})$	218.882	0.225	0.865
p	$\Sigma(1_{11})$	226.081	0.256	0.805
p	$\Sigma(2_{11})$	231.128	0.234	0.830
p	$\Delta(2_{11})$	237.172	0.245	0.810
o	$\Sigma(1_{01})$	238.959	0.204	0.898
p	$\Sigma(1_{11})$	255.067	0.341	0.913
o	$\Sigma(2_{12})$	255.618	0.212	0.686
p	$\Pi(1_{11})$	256.704	0.251	0.838
o	$\Gamma(3_{12})$	261.059	0.336	0.710
o	$\Sigma(2_{12})$	261.316	0.220	0.753

code unlike other authors such as Wang and Carrington.[25] The global structure of the MCTDH code requires a particular attention and care in the selection of subroutines that would need to be modified to properly integrate the symmetries. This type of project, which is quite significant and is being planned, is also very important as it should enhance the ability of the Heidelberg MCTDH package in dealing with the type of problems and systems that we investigate here.

The calculation and assignment of the rovibrational energy levels allows us to compute the rotational transition frequencies, from which we deduce the rotational constants of the rigid rotor H_2O–HCN system. The rovibrational energy levels of a molecular system can be described by a set of quantum numbers, which represent the rotational and vibrational states of the molecule. In the rigid rotor approximation, H_2O–HCN is an asymmetric rotor whose rotational states can be described using $j_{K_aK_c}$, where K_a and K_c are specified as above for H_2O. Thus, our calculations at $J = 0$ will provide for instance the 0_{00} state (along with various vibrational excitations), while the calculations at $J = 1$ will provide the 1_{01}, 1_{11} and 1_{10} states (with various rovibrational excitations). Although there are currently no experimental rovibrational energy levels available for comparison with the theoretical values, there are some experimental measurements of other spectroscopic properties—such as the rotational constants and transition frequencies—that can be used to assess the accuracy of the theoretical model and provide a mean to validate our results. The theoretical transition frequencies we obtain from our calculations are reported in Table 8 and are in excellent agreement with the observed values by Fillery *et al.*,[22] the largest error being 0.71%.

In Table 9, calculated rotational constants are determined from the $J = 1, \cdots, 3$ levels. A number of approaches can be used to reasonably estimate the rotational constants of a molecular system from the rovibrational states—such as fitting an expansion with several coefficients. Usually, a first-order approximation which links the rotational energy levels of an asymmetric top for the total angular momentum $J = 1$ ($1_{01} = B + C$, $1_{10} = A + B$ and $1_{11} = A + C$) with $A \neq B \neq C$ is applied. However, in this case this procedure leads to a degeneracy of B and C, because of the near degeneracy of the 2nd and 3rd state obtained in Table 5 at the precision displayed. The values of A, B and C obtained in this case are respectively 434.473 GHz, 3.067 GHz and 3.065 GHz. Here we supplemented these calculations, with the first order approximation of the rotational constants for $J = 2$ and $J = 3$. For $J = 2$ we obtain for A, B and C

Table 8 Selected rotational $j_{K_aK_c}$ transition frequencies of H_2O–HCN, energy units are in cm^{-1}

Transition	MCTDH	Experiment[22]	% error
$1_{01} \leftarrow 0_{00}$	0.2046	0.2034	0.59
$2_{02} \leftarrow 1_{01}$	0.4079	0.4068	0.27
$2_{11} \leftarrow 1_{10}$	0.4091	0.4075	0.39
$2_{12} \leftarrow 1_{11}$	0.4078	0.4058	0.49
$3_{03} \leftarrow 2_{02}$	0.6138	0.6102	0.59
$3_{12} \leftarrow 2_{11}$	0.6136	0.6113	0.38
$3_{13} \leftarrow 2_{12}$	0.6131	0.6088	0.71

Table 9 Calculated rotational constants of H_2O–HCN using MCTDH and compared with the previous theoretical(theo) and experimental (exp) results, units in GHZ. With (Theo1) (CCSD(T)) level of theory,[15] (Theo2) MP2/aug-cc-pVTZ level of theory,[12] (Theo3) MP2/6-311++G(2df,2p) level of theory,[17] (Theo4) MP2/6-311++G(2df,2p) level of theory,[13] (Theo5) MP2/aug-cc-pVDZ level of theory,[19] (Exp1),[22] and (Exp2)[11]

	MCTDH	Theo1	Theo2	Theo3	Theo4	Theo5	Exp1	Exp2
A	434.528	423.753	583.647	402.514	401.031	429.98		
B	3.059	3.073	3.183	3.046	3.046	3.04	3.062	3.046
C	3.043	3.051	3.159	3.026	3.027	3.01	3.037	3.020

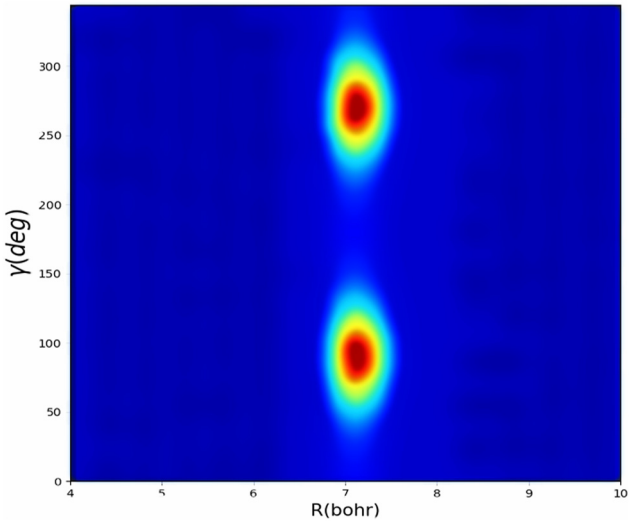

Fig. 5 Wavefunction cut (R, γ) of H_2O–HCN at E = 93.477 cm^{-1}.

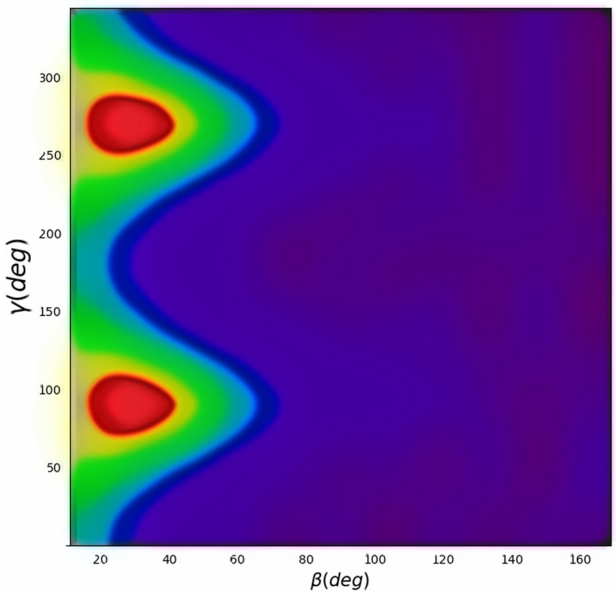

Fig. 6 Wavefunction cut (β, γ) of H_2O–HCN at E = 110.90 cm^{-1}.

434.501 GHz, 3.061 GHz and 3.040 GHz. And for J = 3, 434.610 GHz, 3.047 GHz and 3.024 GHz. The values reported in Table 9 is an average for A, B and C of these values.

The comparison of these numerical results with experimentally determined values and also previous calculations shows the quality of the PES in describing the interactions and provides some confidence in its reliability for collisional dynamics.

We further investigated the rovibrational energy levels of the H_2O–HCN by examining the wavefunctions associated with each level. These wavefunctions can provide relevant information about the molecular structure and behavior of the heterodimer, the type of motion associated with each vibrational

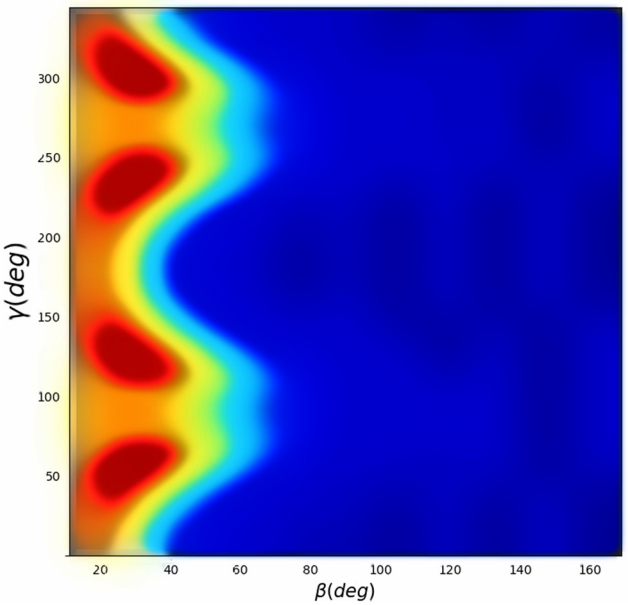

Fig. 7 Wavefunction cut (β, γ) of H_2O–HCN at E = 130.0 cm^{-1}.

mode, and even the deviation of the progression from the normal mode to local mode behavior. Table 2 summarizes the character of motion associated with the various vibrational modes of H_2O–HCN. Fig. 5 describes the mode ν_1, which is the librational motion of the HCN molecule with respect to the H_2O molecule. The libration mode involves the oscillation of the HCN molecule around the γ axis that is perpendicular to the H_2O–HCN bonding axis corresponding to *ortho*-H_2O–HCN Σ state (K = 0) J = 0 at the equilibrium position where the wavefunction has a maximum located at R = 7.096 Bohr. In Fig. 6 we also have the *ortho*-H_2O–HCN state assigned to the mode ν_2 which describes the wagging motion of the water molecule with respect to the HCN molecule and its plot represents pivoting of the water molecule around its O–H bonding axis of *ortho*-H_2O–HCN Σ state. For J = 0, the angular plot at R = 7.096 Bohr in Fig. 7 shows the mode ν_3 corresponding to the O$\cdots$C stretch of the wavefunction of *para*-H_2O–HCN state localized near the global minimum, with the plot describing the stretching or contracting of the bond between the O-atom of the water molecule and C-atom of the HCN molecule. Fig. 8 and 9 show the most excited states localized at the global and secondary minima, with both the same assignment Σ which is the H_2O rocking mode corresponding to the *para*-H_2O–HCN and *ortho*-H_2O–HCN states respectively.

4 Conclusion

This paper describes the calculation of low-lying rovibrational states of the H_2O–HCN heterodimer in the rigid rotor approximation using the potential energy surface developed by Quintas-Sánchez and Dubernet[15] and the MCTDH method for values of the total angular momentum quantum number J between 0 and 3. The rovibrational states have been reported

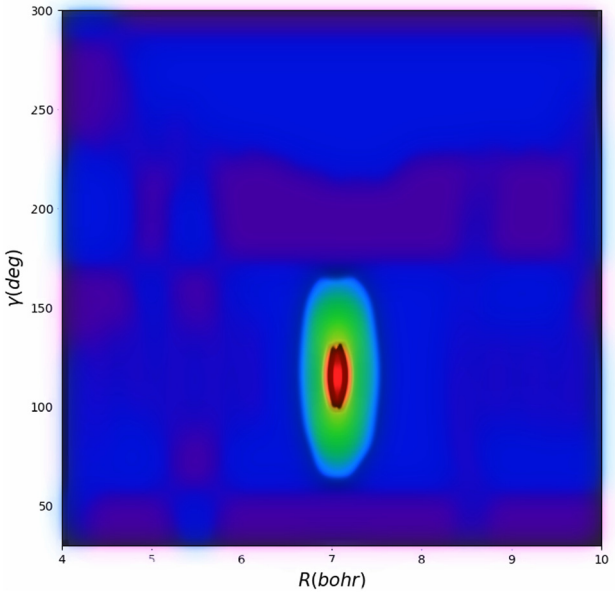

Fig. 8 Wavefunction cut (R, γ) of H_2O–HCN at E = 224.841 cm^{-1}.

with considerable detail assigning the *para*/*ortho* (*p*/*o*) nature of H_2O for each total angular momentum with a computational approach similar to the one previously used by us[26] for the rovibrational states of H_2O–H_2. While the calculation for the specific H_2O–HCN complex is new and we believe deserves to be highlighted here, one of the main ideas of this paper is to present the MCTDH method and code as a reliable tool to perform this type of calculation more routinely: that is spectroscopic calculations involving molecular dimers. Methodologically, we went beyond what was presented in our previous work on H_2O–H_2 by presenting an extensive set of tools that are either already available in the MCTDH code, or that could be implemented with minimal effort, which could be used to perform a deep analysis of the rovibrational states of a variety of systems and extract their character and symmetry in addition to the transition frequencies, rotational constants, and wavefunction visualization. This is particularly useful as there is available an open source tool (the MCTDH code) that allows the community to study various systems that are relevant to the astrophysics and atmospheric chemistry communities. These are presented as alternatives to other approaches such as those by Carrington *et al.*[69,70] and Bačić *et al.*[36,71,72] Those approaches are efficient for this type of application, as has been demonstrated previously. Here, we are highlighting capabilities, versatility, and open access of the MCTDH package.

The results presented here show a very good agreement with transition frequencies and rotational constants observed experimentally. However, the lack of experimental rovibrational energies is an opportunity for this system.

In future work, we plan to survey some isotopologues of this system such as D_2O–HCN, which could be relevant for astrophysical applications. Experimental results for isotopically substituted clusters have already been reported. Gutowsky *et al.*[11] have observed the rotational transition frequencies of the water and hydrogen cyanide dimer using a modified Balle/Flygare Fourier transform microwave spectrometer associated with a sample source pulsed supersonic nozzle. It will be interesting to assess those results in the light of our present calculations. Finally, in the spirit of the work we initiated on H_2O–H_2, we plan to produce converged quantum scattering cross-sections using the MCTDH method which we proved before to be robust enough[49] for this type of study.

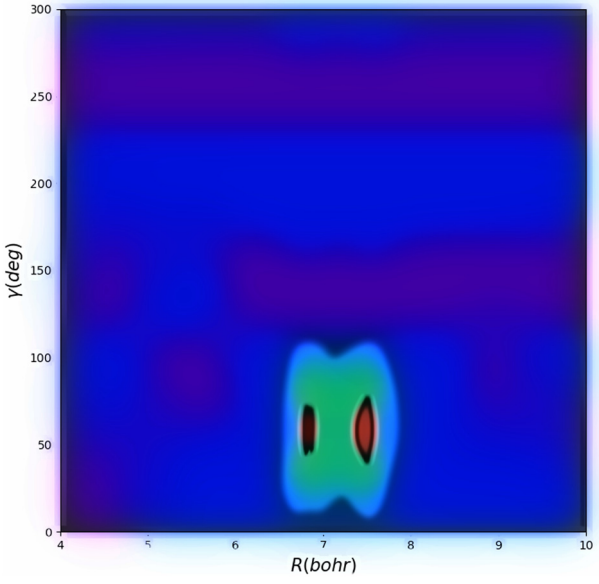

Fig. 9 Wavefunction cut (R, γ) of H_2O–HCN at E = 237.690 cm^{-1}.

Author contributions

Hervé Tajouo Tela performed the rovibrational calculations, analyzed the results, and contributed to the writing of the manuscript. Ernesto Quintas-Sánchez and Marie-Lise Dubernet computed the PES used for these calculations and contributed to the writing of the manuscript. Yohann Scribano, Fabien Gatti, and Richard Dawes contributed to the analysis of the results and the writing of the manuscript. Steve Ndengué conceptualized and designed the work and contributed to the analysis of the results; he also contributed to the writing of the manuscript.

Conflicts of interest

There is no conflict of interest for this work.

Appendix

The basis on which each rovibrational state is computed can be written as a sum of the individual basis functions multiplied by

some coefficients,[25,30]

$$|\Psi\rangle = \sum_{j_A k_A m_A,\mu} C_{j_A k_A m_A,\mu} | j_A, k_A, m_A\rangle |\mu\rangle \quad (14)$$

where $\mu = \{j_B(m_B); JKM; n_0\}$ and n_0 labels the radial basis functions. The coefficients discussed in the context of the wave function determine the contribution of each basis function to the overall wave function and depend on the specific rovibrational state of the system.

The rotational wavefunction of an asymmetric top H_2O molecule can be described by $|j_A,k_A,m_A;K_a,K_c\rangle$ with j_A as the total angular momentum, k_A as the projection of the total angular momentum j_A along the principal axis of rotation, m_A, the eigenvalue of j_A onto the laboratory frame (body-fixed Z-axis)[49]

One can re-expand eqn (14) as

$$|\Psi\rangle = \sum_{j_A K_a K_c m_A,\mu} C_{j_A K_a K_c m_A,\mu} |j_A, m_A, K_a, K_c\rangle |\mu\rangle \quad (15)$$

The expansion coefficients $C_{j_A K_a K_c m_A,\mu}$ from eqn (15),

$$C_{j_A K_a K_c m_A,\mu} = \sum_{k_A} C_{j_A k_A m_A,\mu} \alpha^{(j_A m_A)}_{k_A,K_a K_c} \quad (16)$$

The coefficients $\alpha^{(j_A m_A)}_{k_A,K_a K_c}$ described in eqn (16) can be obtained by diagonalizing the rotational Hamiltonian of the water monomer in the $|j_A,k_A,m_A\rangle$ basis.

$$| j_A, m_A, K_a, K_c\rangle = \sum_{k_A} \alpha^{j_A m_A}_{k_A,K_a K_c} | j_A, k_A, m_A\rangle \quad (17)$$

$|j_A,k_A,m_A\rangle$ is the Wigner-D matrix describing the rotation of the molecule from the principal axis frame to the laboratory frame. The contribution of each state $|j_{K_a K_c}\rangle$ form eqn (17) is given by

$$\zeta_{j_A K_a K_c,\mu} = \sum_{\mu} \sum_{m_A} C_{j_A K_a K_c m_A,\mu}{}^2 \quad (18)$$

We assign the $|j_{K_a K_c}\rangle$ based on the highest magnitude of $\zeta_{j_A K_a K_c,\mu}$. The H_2O nature is *para* H_2O with $(-1)^{(K_a-K_c)} = +1$ and *ortho* H_2O with $(-1)^{(K_a-K_c)} = -1$.

Acknowledgements

The authors would like to acknowledge the support from CINECA for the computational time allocated to ICTP-EAIFR. R. D. and E. Q. S. are supported by the U.S. Department of Energy (Award DE-SC0019740). H. T. T. acknowledges the financial support from the Office of External Activities of the Abdus Salam International Centre for Theoretical Physics: (PhD fellowship No. AF-16/20-04)/ICTP-OEA.

Notes and references

1 M. Festou, H. Rickman and R. West, *Astron. Astrophys. Rev.*, 1993, **5**, 37–163.
2 J. Crovisier, N. Biver, D. Bockelée-Morvan and P. Colom, *Planet. Space Sci.*, 2009, **57**, 1162–1174.
3 P. Gerakines, M. Moore and R. Hudson, *Icarus*, 2004, **170**, 202–213.
4 D. A. Smith, *Modeling the hydrogen bond*, ACS Publications, 1994.
5 S. Scheiner*et al.*, *Hydrogen bonding: a theoretical perspective*, Oxford University Press on Demand, 1997.
6 S. J. Grabowski, *Hydrogen bonding: new insights*, Springer, 2006, vol. 3.
7 D. Hadzi, *Theoretical treatments of hydrogen bonding*, John Wiley & Sons, Chichester, New York, Weinheim, Brisbane, Singapore, Toronto, 1997.
8 E. Muchová, V. Špirko, P. Hobza and D. Nachtigallová, *Phys. Chem. Chem. Phys.*, 2006, **8**, 4866–4873.
9 Q. Li, X. Wang, J. Cheng, W. Li, B. Gong and J. Sun, *Int. J. Quantum Chem.*, 2009, **109**, 1396–1402.
10 S. Liebman, R. Pesce-Rodriguez and C. Matthews, *Adv. Space Res.*, 1995, **15**, 71–80.
11 H. Gutowsky, T. Germann, J. Augspurger and C. Dykstra, *J. Chem. Phys.*, 1992, **96**, 5808–5816.
12 T. Malaspina, E. Fileti, J. Riveros and S. Canuto, *J. Phys. Chem. A*, 2006, **110**, 10303–10308.
13 R. Rivelino and S. Canuto, *J. Phys. Chem. A*, 2001, **105**, 11260–11265.
14 A. Heikkilä, M. Pettersson, J. Lundell, L. Khriachtchev and M. Räsänen, *J. Phys. Chem. A*, 1999, **103**, 2945–2951.
15 E. L. Quintás-Sanchez and M.-L. Dubernet, *Phys. Chem. Chem. Phys.*, 2017, **19**, 6849–6860.
16 M.-L. Dubernet and E. Quintas-Sánchez, *Mol. Astrophys.*, 2019, **16**, 100046.
17 R. Rivelino and S. Canuto, *Chem. Phys. Lett.*, 2000, **322**, 207–212.
18 L. Turi and J. Dannenberg, *J. Phys. Chem.*, 1993, **97**, 7899–7909.
19 E. E. Fileti, R. Rivelino and S. Canuto, *J. Phys. B: At., Mol. Opt. Phys.*, 2003, **36**, 399.
20 A. Hinchliffe, *J. Mol. Struct.*, 1986, **136**, 193–199.
21 R. Rivelino, *Int. J. Quantum Chem.*, 2011, **111**, 1256–1269.
22 A. Fillery-Travis, A. Legon and L. Willoughby, *Proc. R. Soc. London, Ser. A*, 1984, 405–423.
23 A. J. Fillery-Travis, A. Legon and L. Willoughby, *Chem. Phys. Lett.*, 1983, **98**, 369–372.
24 A. van der Avoird and D. Nesbitt, *J. Chem. Phys.*, 2011, **134**, 044314.
25 X.-G. Wang and T. Carrington Jr., *J. Chem. Phys.*, 2011, **134**, 044313.
26 S. A. Ndengué, Y. Scribano, D. M. Benoit, F. Gatti and R. Dawes, *Chem. Phys. Lett.*, 2019, **715**, 347–353.
27 J. Lundell, *J. Phys. Chem.*, 1995, **99**, 14290–14300.
28 Š. Budzák, P. Carbonniere, M. Medved' and I. Černušák, *Mol. Phys.*, 2014, **112**, 3225–3236.
29 A. Barclay, A. van der Avoird, A. McKellar and N. Moazzen-Ahmadi, *Phys. Chem. Chem. Phys.*, 2019, **21**, 14911–14922.
30 P. M. Felker and Z. Bačić, *J. Chem. Phys.*, 2020, **153**, 074107.
31 P. M. Felker and Z. Bačić, *J. Phys. Chem. A*, 2021, **125**, 980.
32 Y. Liu and J. Li, *Phys. Chem. Chem. Phys.*, 2019, **21**, 24101–24111.

33 Z. Kisiel, A. C. Legon and D. Millen, *Proc. R. Soc. London, Ser. A*, 1982, **381**, 419–442.
34 J. Loreau, Y. N. Kalugina, A. Faure, A. van Der Avoird and F. Lique, *J. Chem. Phys.*, 2020, **153**, 214301.
35 D. Viglaska, X.-G. Wang, T. Carrington Jr. and D. P. Tew, *J. Mol. Spectrosc.*, 2022, **384**, 111587.
36 P. M. Felker and Z. Bačić, *J. Chem. Phys.*, 2022, **156**, 064301.
37 Y. Liu, J. Li, P. M. Felker and Z. Bačić, *Phys. Chem. Chem. Phys.*, 2021, **23**, 7101–7114.
38 P. M. Felker and Z. Bačić, *Chin. J. Chem. Phys.*, 2021, **34**, 728–740.
39 M. Masia, H. Forbert and D. Marx, *J. Phys. Chem. A*, 2007, **111**, 12181–12191.
40 H.-D. Meyer, U. Manthe and L. S. Cederbaum, *Chem. Phys. Lett.*, 1990, **165**, 73–78.
41 U. Manthe, H.-D. Meyer and L. S. Cederbaum, *J. Chem. Phys.*, 1992, **97**, 3199–3213.
42 *Multidimensional Quantum Dynamics: MCTDH Theory and Applications*, ed. H. D. Meyer, F. Gatti and G. A. Worth, Wiley-VCH, Weinheim, 2009.
43 M. H. Beck, A. Jäckle, G. A. Worth and H. D. Meyer, *Phys. Rep.*, 2000, **324**, 1–105.
44 Z. Bačić and J. C. Light, *J. Chem. Phys.*, 1986, **85**, 4594.
45 Z. Bačić and J. C. Light, *J. Chem. Phys.*, 1987, **86**, 3065.
46 J. C. Light and T. Carrington Jr., *Adv. Chem. Phys.*, 2000, **114**, 263–310.
47 F. Gatti and C. Iung, *Phys. Rep.*, 2009, **484**, 1–69.
48 S. Ndengué, R. Dawes, F. Gatti and H. D. Meyer, *Chem. Phys. Lett.*, 2017, **668**, 42.
49 S. Ndengué, Y. Scribano, F. Gatti and R. Dawes, *J. Chem. Phys.*, 2019, **151**, 134301.
50 G. Brocks, A. V. D. Avoird, B. T. Sutcliffe and J. Tennyson, *Mol. Phys.*, 1983, **50**, 1025.
51 S. A. Ndengue, R. Dawes and F. Gatti, *J. Phys. Chem. A*, 2015, **119**, 7712.
52 C. Leforestier, *J. Chem. Phys.*, 1994, **101**, 7357–7363.
53 D. Hou, Y.-T. Ma, X.-L. Zhang and H. Li, *J. Chem. Phys.*, 2016, **144**, 014301.
54 F. C. DeLucia, P. Helminger and W. H. Kirchhoff, *J. Phys. Chem. Ref. Data*, 1974, **3**, 211–219.
55 A. G. Maki, W. B. Olson and R. L. Sams, *J. Mol. Spectrosc.*, 1970, **36**, 433–447.
56 O. Denis-Alpizar, T. Stoecklin, P. Halvick and M.-L. Dubernet, *J. Chem. Phys.*, 2013, **139**, 034304.
57 A. Jäckle and H. D. Meyer, *J. Chem. Phys.*, 1996, **104**, 7974–7984.
58 A. Jäckle and H. D. Meyer, *J. Chem. Phys.*, 1998, **109**, 3772–3779.
59 G. Worth, M. Beck, A. Jäckle and H. D. Meyer, The MCTDH Package, Version 8.2, (2000), University of Heidelberg, Heidelberg, Germany. H.-D. Meyer, Version 8.3 (2002), Version 8.4 (2007), O. Vendrell and H.-D. Meyer, Version 8.5 (2011), 2007, see **https://mctdh.uni-hd.de**.
60 M. Schröder and H.-D. Meyer, *J. Chem. Phys.*, 2017, **147**, 064105.
61 F. Otto, *J. Chem. Phys.*, 2014, **140**, 014106.
62 M. Schröder, *J. Chem. Phys.*, 2020, **152**, 024108.
63 L. J. Doriol, F. Gatti, C. Iung and H.-D. Meyer, *J. Chem. Phys.*, 2008, **129**, 224109.
64 H. D. Meyer and G. A. Worth, *Theor. Chem. Acc.*, 2003, **109**, 251–267.
65 H. D. Meyer, F. L. Quéré, C. Léonard and F. Gatti, *Chem. Phys.*, 2006, **329**, 179–192.
66 R. Kosloff and H. Tal-Ezer, *Chem. Phys. Lett.*, 1986, **127**, 223–230.
67 E. Davidson, *J. Comput. Phys.*, 1975, **17**, 87.
68 T. M. Tshehla and T. Anthony Ford, *S. Afr. J. Chem.*, 1995, **48**, 127–134.
69 X. Wang and T. Carrington Jr., *J. Chem. Phys.*, 2008, **129**, 234102.
70 X. Wang and T. Carrington Jr., *J. Chem. Phys.*, 2023, **158**, 084107.
71 P. M. Felker and Z. Bačić, *J. Chem. Phys.*, 2022, **157**, 194103.
72 P. M. Felker and Z. Bačić, *J. Chem. Phys.*, 2023, **158**, 234109.

3.6 Conclusion

The main goal of this work was to calculate the spectroscopic properties of the vdW H_2O-HCN system in the rigid rotor approximation and analyze them. To do that, an improved FORTRAN routine used to automate the representation of the PES of the H_2O-H_2 [69] system has been applied here since it was not possible to represent the PES using the POTFIT algorithm. We are particularly pleased with this new approved technique as it offers a streamlined solution for researchers using MCTDH to study this system. The bound states and rovibrational states were calculated for the values of the total angular momentum quantum number J from 0 to 2 as well as the microwave rotational transition frequencies and rotational constants. A comparison of the results obtained to those of the group of Vindel $et\ al.$ [120], which were carried out with another potential developed for the same system. The calculated ground state binding energy is -1457.281 cm^{-1} and -1488.342 cm^{-1} in Vindel $et\ al.$ [120], with the rotational constants A, B, and C being 434.528, 3.059, and 3.043 GHz, respectively, compared to 434.492, 3.057, and 3.032 reported by Vindel $et\ al.$ [120]. Our results show slight differences, which can be explained by the calculation methods used. Compared to experimental values, both methods are in good agreement, demonstrating the accuracy of the potentials used. Rovibrational calculations provide precise spectroscopic data (microwave frequencies and intensities of transitions) necessary to model and predict the interactions of these molecules with solar or infrared radiation, playing a role in the energy and chemical balances of atmospheres [218, 120, 207]. Another major contribution of this work lies in the use of MCTDH for the detailed analysis of rovibrational states. This method not only allows for accurate calculation of the energy states but also predicts the distribution of weights associated with each state, providing a deep understanding of their structure and dynamics. Developed scripts are used to accurately analyze these states in $j_{k_a k_c}$ performed with the MCTDH method. These scripts are designed to be applicable to similar systems and will allow for a detailed analysis of the obtained results. They will be made available in our GitHub repositories [2] providing an accessible resource for the scientific community to

[2] https://github.com/MolQuantDynLab-Haverford/MolQuantDynLab-Repository

facilitate the reproduction and extension of our studies on complex molecular systems.

4. The rovibrational states calculations and collisional dynamics of the rigid $(H_2O)_2$ Dimer

4.1 Introduction

The water dimer ($(H_2O)_2$) has been intensively studied for its contribution to many fields of science [219, 220]. Due to its higher concentration in the Earth's atmosphere [221, 222], it is also the main subject of studies related to atmospheric processes [223], such as water continuum absorption [224] and chemical reactions [111]. The main source of information on the water dimer come from its experimental spectroscopic measurements, and to understand these measurements, a potential energy surface describing the interaction between water monomers has to be performed.

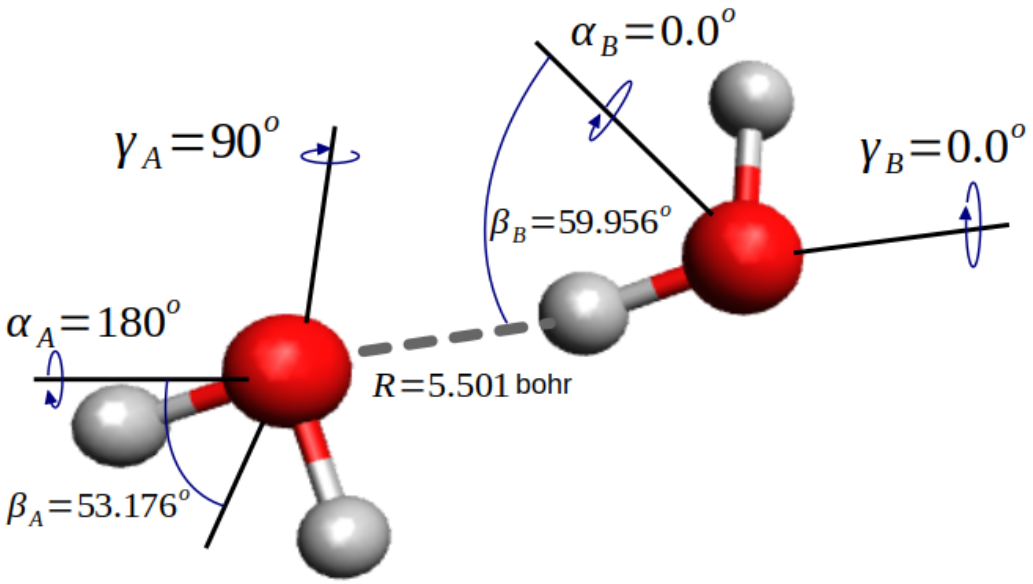

Figure 4.1: Structure of the Water dimer equilibrium. The first monomer in the figure is a proton acceptor, and the second is a proton donor.

In this chapter, the calculations of the rovibrational states and collisional dynamics of the

water dimer will be presented. The Hamiltonian of the rigid $(H_2O)_2$ will be discussed, along with the procedure used to represent the PES in the correct form and its implementation in the MCTDH code. The chapter will also outline the difficulties encountered, both analytical and numerical, as well as the methods used to resolve them. Finally, the results obtained during this work will be presented.

4.2 Representation of the Hamiltonian for the water dimer

The two monomers are labeled A and B, respectively. The system is defined by intramolecular coordinates (interatomic distances and bond angles), which describe the rotations from an axis of each monomer fixed at their equilibrium positions (R_{OH}=0.9579 and $\langle HOH = 104.5°$) [118], as well as by intermolecular coordinates $\omega_x = (\alpha_x, \beta_x, \gamma_x)$, $x \in \{A, B\}$ are the Euler angles , characterizing the relative movements between the monomers as shown in Figure 4.1. The coordinate system used to describe the motion of water dimer molecules is as follows: two sets of Euler angles (α_A, β_A, γ_A) and (α_B, β_B, γ_B) are used to describe the orientations of each monomer with respect to the body-fixed (BF) frame. The polar angles (α, β) are the coordinates of the vector $\vec{R}$ connecting the centers of mass of monomers G_A and G_B with respect to the space-fixed (SF) frame. The BF frame z-axis of the system is aligned with the vector $\vec{R}$. In this frame, we embedded a distance *R* (which is the distance between the centers of mass of the two monomers) along the BF z-axis. This BF frame is equivalent to the E_2 frame of Gatti and co-workers [165] and Ndengué and co-workers [69]. The BF frame follows the definition by Brocks $et\ al.$ [214].

For the asymmetric tops, the Hamiltonian in the body-fixed (BF) is derived using the

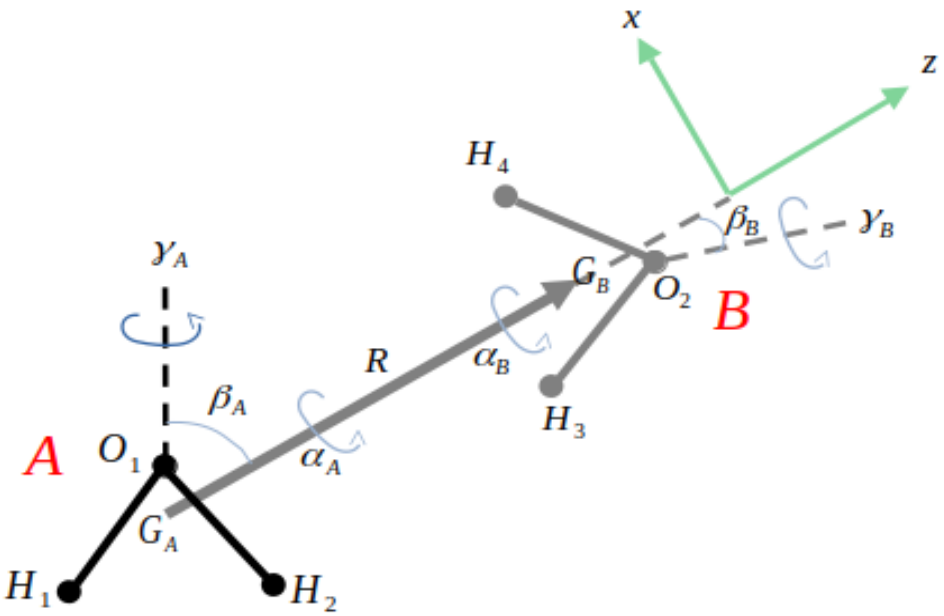

Figure 4.2: Body-fixed coordinates for $(H_2O)_2$ in the rigid rotor approximation.

approximation employed by Brocks *et al.* [214] and is expressed as follows:

$$\hat{H} = \hat{T}^{A}_{\text{rot}} + \hat{T}^{B}_{\text{rot}} + \frac{1}{2\mu_{AB}R^2}\left[-\frac{\partial}{\partial R}R^2\frac{\partial}{\partial R} + \hat{J}^2 + \hat{J}^{\dagger}\hat{J} + (\hat{j}_A + \hat{j}_B)^2 - 2(\hat{j}_A + \hat{j}_B).\hat{J}\right]E_2 + V(R, \omega_A, \omega_B), \tag{4.2.1}$$

where $\omega_A = (\alpha_A, \beta_A, \gamma_A)$ and $\omega_B = (\alpha_B, \beta_B, \gamma_B)$ are the Euler angles that specify the orientation of monomers; $\hat{T}^{A}_{\text{rot}}$ and $\hat{T}^{B}_{\text{rot}}$ are the Kinetic Energy Operators (KEO) of the monomers A and B; R stands for the center of mass (COM) between the monomers; the operator $\hat{J}$ is the total angular momentum, $\hat{j}_A$ and $\hat{j}_B$ are the angular momenta of each fragment A and B, and μ_{AB} is the dimer reduced mass. The quantity $V(R, \omega_A, \omega_B)$ is the PES.

The KEO of a water monomer is given by:

$$\hat{T}^{x}_{\text{rot}} = \frac{A_x}{2}(\hat{j}^2_{x,+} + \hat{j}^2_{x,-} + \hat{j}_{x,+}\hat{j}_{x,-} + \hat{j}_{x,-}\hat{j}_{x,+}) - \frac{C_x}{2}(\hat{j}^2_{x,+} + \hat{j}^2_{x,-} - \hat{j}_{x,+}\hat{j}_{x,-} - \hat{j}_{x,-}\hat{j}_{x,+})$$
$$B_x j^2_{zBF_x}, \tag{4.2.2}$$

where A_x, B_x, and C_x are the rotational constants and x can be A or B. The body-fixed superscript implies that the set of (x, y, z) refers to the components of j_x along the principal axes of monomers A and B, respectively [119]. To perform the calculations, the final form of the KEO implemented in the MCTDH is expressed as follows

$$\begin{aligned} 2\hat{T} = &-\frac{1}{2\mu_{AB}R^2}\frac{\partial^2}{\partial R^2} + 2\hat{T}^{A}_{\text{rot}} + 2\hat{T}^{B}_{\text{rot}} + \frac{1}{\mu_{AB}R^2}\left(J(J+1) + \vec{j}^2_A + \vec{j}^2_B - 2j^2_{A,z} - 2j^2_{B,z}\right)E_2 \\ &+ \frac{1}{\mu_{AB}R^2}\left(j_{A,+}j_{B,-} + j_{A,-}j_{B,+} - 2j_{A,z}j_{B,z}\right)E_2 \\ &+ \frac{1}{\mu_{AB}R^2}\left(C_+(J,K)(j_{A,+} + j_{B,+})\right) + \frac{1}{\mu_{AB}R^2}\left(C_-(J,K)(j_{A,-} + j_{B,-})\right)E_2, \end{aligned} \tag{4.2.3}$$

with

$$C_{\pm}(J,K) = \sqrt{(J(J+1) - K(K\pm 1)} \tag{4.2.4}$$
$$\hat{j}_{A(B)} = \hat{j}_{A(B),x} \pm \mathrm{i}\hat{j}_{A(B),y} \tag{4.2.5}$$

Same as in the H_2O-HCN system, in the reduced dimensionality, the KEO of the H_2O can be rewritten as follows [214, 215]

$$\hat{T}^{x}_{\text{rot}} = \left(\frac{A_x + C_x}{2}\right)\hat{j}^2 + \left[B - \left(\frac{A_x + C_x}{2}\right)\right]\hat{j}^2_{zBF} + \left(\frac{A_x - A_x}{4}\right)\left(\hat{j}^2_+ + \hat{j}^2_-\right) \tag{4.2.6}$$

With $\hat{j}_{A(B),+} = \hat{j}_x + \mathrm{i}\hat{j}_y$ and $\hat{j}_{A(B)-} = \hat{j}_x - \mathrm{i}\hat{j}_y$.

With the H_2O rotational constants: $A_x = 27.8806$ cm^{-1}, $B_x = 14.5216$ cm^{-1} and $C_x = 9.2778$ cm^{-1} [63, 62], with the mass of hydrogen=1.007825035 AMU and the mass of oxygen=15.99491463 AMU [63].

4.3 Theoretical intermolecular potential energy surface

In this section, I will present the ab initio CCpol-8s and multipolar potential energy surfaces used and the reasons for choosing the multipolar PES. Let's briefly introduce the PESs available for the water dimer. The high-quality potentials have been constructed due to the importance of the water dimer, and a recent review provides a good summary [225]. Among the PESs calculated to describe the water dimer, the most accurate rigid monomer is called the Coupled-Cluster polarized CCpol-8s [118] with eight-shell basis set. Another potential energy surface, called Symmetry Adapted Perturbation Theory-5st (SAPT-5st) with six DOF, has also been found interesting for calculating the spectroscopic properties of the water dimer and has been extensively studied [78].

4.3.1 The Ab initio CCpol-8s Potential Energy Surface

The rigid rotor CCpol-8s PES used in this work was constructed in 2008 [118]. It is an extension of the CC-pol water pair potential developed in 2007 [226] and has been successfully used in simulation to predict the spectrum of the water dimer. To obtain this PES, the intermolecular interaction between water monomers from the coupled cluster calculations of the CCpol [226] water pair potential has been fitted using 2510 geometry points and was already benchmarked with the experimental data [227]. This new form that includes eight sites is referred to as CCpol-8s. They used the functional form expressed as follows

$$V(A,B) = \sum_{a\in A, b\in B} u_{ab}(r_{ab}) + V_2^{\text{ind}}(A,B) \tag{4.3.1}$$

$$u_{ab}(r_{ab}) = \underbrace{f_1(\delta_1^{ab}, r_{ab})\frac{q_a q_b}{r_{ab}}}_{1} + \underbrace{exp(-\beta_{ab} r_{ab}) \sum_{m=0}^{3} C_m^{ab} r_{ab}^m}_{2} + \underbrace{\sum_{n=6,8,10} f_n(\delta_n^{ab}, r_{ab})\frac{C_n^{ab}}{r_{ab}^n}}_{3} \tag{4.3.2}$$

where $V_2^{\text{ind}}(A,B)$ represents the induction interaction between monomers A and B, and

u_{ab} are site-site potentials depending on distance r_{ab} between sites. In equation 4.3.1, The first term (1) stands for the electrostatic energy, adjusted by an attenuation function to avoid short-distance divergences. The second term (2) is the repulsive component of the potential, which decreases exponentially with the distance between the r_{ab} monomers A and B. The third term describes the dispersion energy, also modified by an attenuation function to ensure correct asymptotic behavior of the two-body term. The free parameters δ_n^{ab}, C_n^{ab}, and β_{ab} were determined from the same *ab initio* calculated points above, while the attenuation functions $f_n(r, \delta_n^{ab})$ are used to adjust the long-range terms, taking into account the overlaps of the electronic functions expressed as follows.

$$f_n(r, \delta^{ab}) = 1 - exp^{-\delta_r^{ab}} \sum_{j=0}^{n} \frac{(\delta_r^{ab})^j}{j!} \tag{4.3.3}$$

This *ab initio* potential is defined in terms of the Euler angles $\omega_x(\alpha_x, \beta_x, \gamma_x)$ x=A,B·, with respect to the body-fixed (BF) frame. The two monomers are connected by a vector $\vec{R}$ connecting their centers of mass, which undergoes a rotation described by the polar angles (α, β) with respect to the space-fixed (SF) frame. The dimer geometry depends on the angles α_A and α_B only through the difference $\alpha = \alpha_B - \alpha_A$. Thus, the potential actually depends on the inter-monomer distance R and five angles.

The *ab initio* CCpol-8s PES used in the work was provided in the supplementary material of reference [118]. The equilibrium position of the *ab initio* CCpol-8s is found to be at: *R*=5.5 bohr, $(\alpha_A, \beta_A, \gamma_A) = (0°, 118.956°, 0°)$, and $(\alpha_B, \beta_B, \gamma_B) = (-180°, 124.879°, 270°)$, and the global minimum at $De = -1785.15$ cm^{-1} [118], obtained using an optimized steepest descent method and compared to the experimental value $De = -1748.775$ cm^{-1} [227].

Figures 4.3, 4.4, and 4.5 show one- and two-dimensional contour plots of the potential energy surface *ab initio*. In Figure 4.3, the α, β, and γ coordinates of each monomer have been fixed at values close to the equilibrium position of the surface. In Figure 4.4, the coordinates in both directions R and γ_A; and γ_A and γ_B in Figure 4.5 vary while

the others are fixed at values close to the equilibrium values of the surface represented. The figures show the global minimum at -1785.15. For Figures 4.4 and 4.5 showing the surface in two directions, we observed a very large barrier between the equivalent equilibrium positions of the potential.

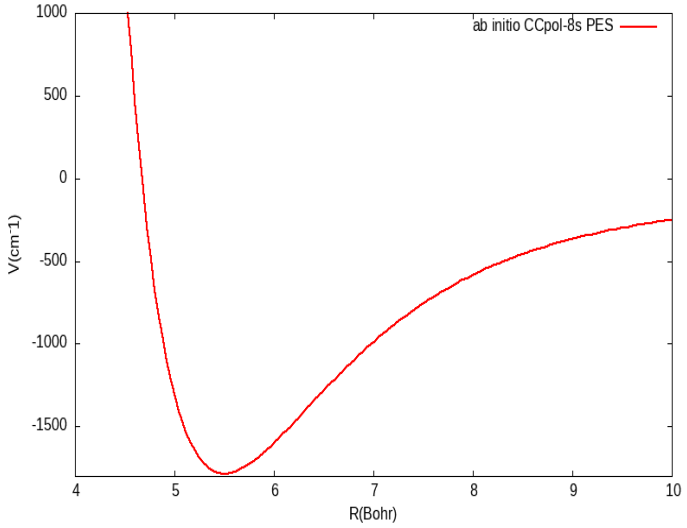

Figure 4.3: 1D cut of the *ab initio* PES. The angles are fixed at their equilibrium values. The figure shows the global minimum at R=5.5 bohr (De=$-1785.15\ cm^{-1}$ for $(H_2O)_2$ dimer).

4.3.2 Representation of the PES in MCTDH: Fit and Potfit

Similar to the KEO, the potential energy operator must be expressed as a SOP form. There is an effective algorithm called POTFIT [173, 192, 193] implemented in the MCTDH package for low-dimensional systems that are not yet in the SOP form. The POTFIT algorithm requires storing the PES on a direct product primitive grid, which becomes challenging for systems with 6 DOFs. Unfortunately, *ab initio* PESs often do not conform to SPFs, especially in coordinates suitable for quantum dynamics calculations. Various Potfit procedures have been proposed to convert such PESs into the product form, such as MultiGrid [228], Multi-Layer [229], and Monte Carlo [230]. These methods are available to convert a general potential into a SOP form. We decided to implement the analytical PES, it resulted in a large number of Hamiltonian terms, which slowed down calculations implemented in the MCTDH code, and the MCTDH code was unable to compile. Faced

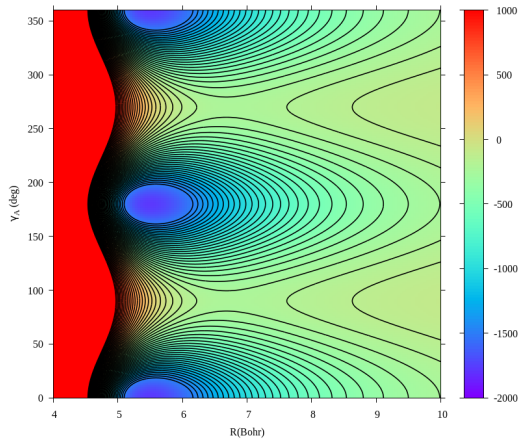

Figure 4.4: 2D contour plot of the *ab initio* PES as a function of R and γ_A, while the other angles are fixed at their equilibrium values. The figure shows the global minimum (De=-1785.15 cm^{-1} for the $(H_2O)_2$ dimer)

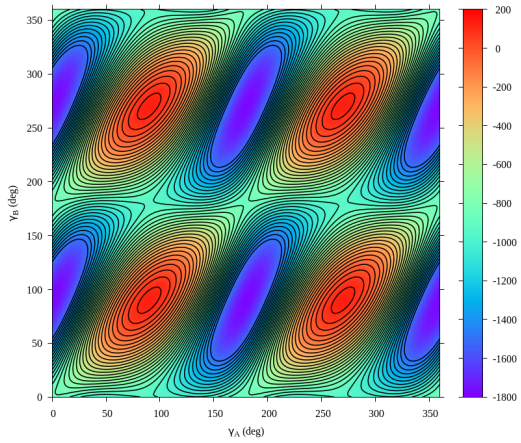

Figure 4.5: 2D contour plot of the *ab initio* PES. γ_A and γ_B are varying while the other angles are fixed at their equilibrium values. The figure shows the global minimum (De=-1785.15 cm^{-1} for $(H_2O)_2$ dimer).

with these challenges, we have developed a stronger alternative method for representing the potential energy surface by reducing the terms used in its SOP form.

Our PES and KEO are expressed in Jacobi coordinates. This choice is appropriate for describing the rotations and intermolecular vibrations of the water dimer. In most cases, the KEO is already in this product form, and what we have to do is to transform the PES. In the POTFIT algorithm, each degree of freedom requires a primitive basis on a defined grid size and a maximum number of SPFs to accurately represent the PES. For a large-dimensional system like the water dimer, there will be numerous functions, making it difficult to express the potential in the SOP form due to POTFIT's limitation on the size of the primitive basis it can handle. The multipolar expansion of the CCpol-8s PES is expressed as follows:

$$V(R,\omega_A,\omega_B) = \sum_{\{\Lambda\}} v_{\{\Lambda\}}(R) A_{\{\nu\}}(\omega_A,\omega_B), \tag{4.3.4}$$

Where

$$A_{\{\nu\}}(\omega_A,\omega_B) = \sum_{\substack{M_A \\ (M_B=-M_A)}} (-1)^{L_A+L_B+L} \begin{pmatrix} L_A & L_B & L \\ M_A & M_B & M \end{pmatrix} \times D^{L_A}_{M_A K_A}(\omega_A)^* D^{L_B}_{M_B K_B}(\omega_B)^*, \tag{4.3.5}$$

with $\Lambda = (L_A, K_A, L_B, K_B, L)$ and $\nu = (L_A, K_A, M_A, L_B, K_B, M_B, L)$. In the body-fixed frame $M = M_A + M_B = 0$. Therefore, $M_B = -M_A$.

This multipolar PES consists of a set of Wigner functions [231] $D^{L_A}_{M_A K_A}(\alpha_A, \beta_A, \gamma_A)^*$ and $D^{L_B}_{-M_A K_B}(\alpha_B, \beta_B, \gamma_B)^*$ for the description of the rotations of the monomers A and B, the values of L_{Amax} and L_{Bmax} have been increased for convergence tests.

$$D^l_{mk}(\alpha,\beta,\gamma)^* = (-1)^{m-k} D^l_{-m-k}(\alpha,\beta,\gamma), \tag{4.3.6}$$

$$D^l_{mk}(\alpha,\beta,\gamma) = e^{-\mathrm{i}\alpha m} d^l_{mk}(\beta) e^{-\mathrm{i}\gamma k}, \tag{4.3.7}$$

where $d^l_{mk}(\beta)$ is the Wigner d-function.

In this case, the L_{Amax} and the L_{Bmax} are capped at a maximum total angular momentum value of 8. The factor in large brackets in equation 4.3.5 is the Wigner 3-*j* symbol multiplied by Wigner functions for the overall water dimer with quantum numbers L_A and L_B, the total angular momentum of each monomer A and B, M_A and M_B, the projection of each total angular momentum on a space-fixed z-axis, K_A and K_B, the projection of M_A and M_B on the water dimer z-axis. One can notice that L_A, L_B, M_A, and M_B are exact quantum numbers.

$$0 \leq L_A \leq L_{\text{Amax}}; 0 \leq L_B \leq L_{\text{Bmax}}; -L_A \leq K_A \leq L_A; -L_B \leq K_B \leq L_B;$$
$$|L_A - L_B| \leq L \leq L_A + L_B;$$
$$0 \leq M_A \leq L_A; 0 \leq \alpha \leq 360^\circ; 0 \leq \beta \leq 180^\circ; 0 \leq \gamma \leq 360^\circ, \quad (4.3.8)$$

The radial expansion coefficients are calculated at each distance *R* employing Gauss-Legendre quadrature in (β_A, β_B) and Gauss-Chebyshev quadrature in (γ_A, γ_B), with $\alpha = \alpha_A - \alpha_B$ for the purpose of working in the body-fixed frame.

To achieve good convergence of the computed expansion coefficients $v_{\{\Lambda\}}(R)$, we used the maximum value of quadrature points equal to (18,12,18,12,12) for each angle $(\beta_A, \gamma_A, \beta_B, \gamma_B, \alpha)$, respectively. The radial expansion coefficients $v_{\{\Lambda\}}(R)$ can be determined by projecting the PES $V(R, \omega_A, \omega_B)$ onto the basis angular potential $A_{\{\nu\}}(\omega_A, \omega_B)$.

The $v_{\{\Lambda\}}(R)$ expansions of the PES are calculated using the following expression [119]:

$$\begin{aligned} v_\Lambda(R) =& \frac{(2L_A+1)(2L_B+1)(2L+1)}{64\pi^4} \times \int d\omega_A d\omega_B A_\nu(\omega_A, \omega_B) V(R, \omega_A, \omega_B) \quad (4.3.9) \\ =& \frac{(2L_A+1)(2L_B+1)(2L+1)}{64\pi^4} \sum_{M_A} (-1)^{L_A+L_B+L} \\ & \times \begin{pmatrix} L_A & L_B & L \\ M_A & -M_A & 0 \end{pmatrix} \int D^{L_A}_{M_A K_A}(\omega_A)^* D^{L_B}_{-M_A K_B}(\omega_B)^* \\ & \times V(R, \omega_A, \omega_B) d\omega_A d\omega_B, \end{aligned}$$

where $d\omega_X = sin\beta_X d\alpha_X d\beta_X d\gamma_X$. One of the Euler rotational angles, either α_A or α_B, can be set to zero and omitted from the integration. $V(R, \alpha_A, \beta_A, \gamma_A, \alpha_B, \beta_B, \gamma_B) = V(R, 0, \beta_A, \gamma_A, \alpha, \beta_B, \gamma_B)$. With $\alpha = \alpha_B - \alpha_A$

Equation 4.3.9 can become:

$$v_\Lambda(R) = \frac{(2L_A+1)(2L_B+1)(2L+1)}{64\pi^4} \sum_{M_A} (-1)^{L_A+L_B+L} \begin{pmatrix} L_A & L_B & L \\ M_A & -M_A & 0 \end{pmatrix} \quad (4.3.10)$$
$$\times 2\pi \int_0^{2\pi} d\alpha \int_0^{\pi} sin\beta_A \, d\beta_A \int_0^{2\pi} d\gamma_A \int_0^{\pi} sin\beta_B \, d\beta_B \int_0^{2\pi} d\gamma_B$$
$$\times V(R, 0, \beta_A, \gamma_A, \alpha, \beta_B, \gamma_B) A_\nu(\omega_A, \omega_B),$$

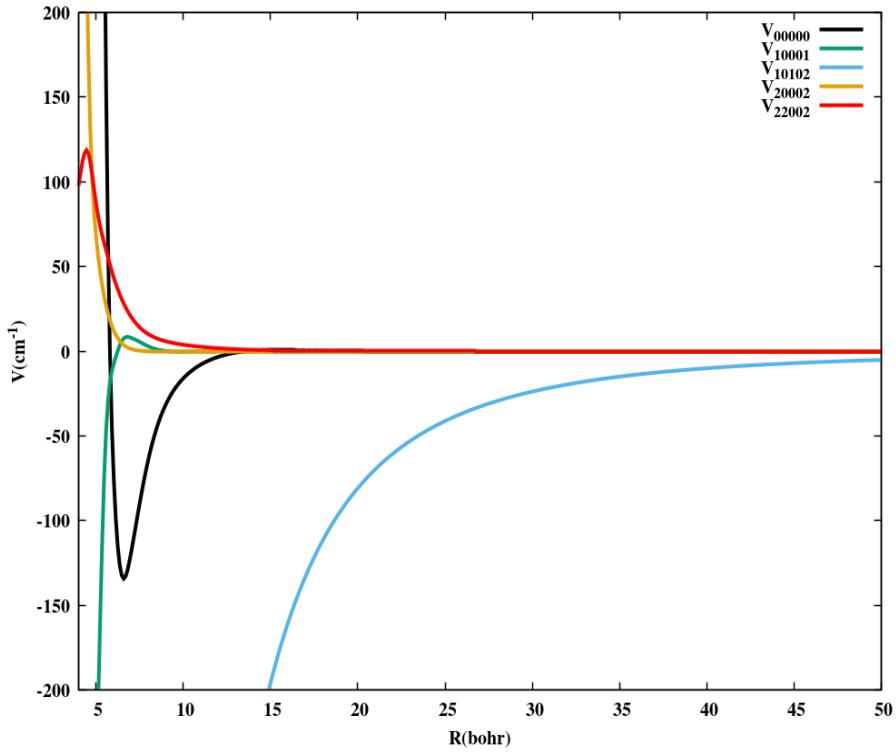

Figure 4.6: Expansion coefficients, as a function of the interatomic distance, for the multipolar PES represented in equation 4.3.9, are shown.

The calculation of integrals presented significant challenges, especially in terms of numerical aspects, as it was necessary to perform pre-computations for angular functions, which were then stored as binary files. This helped reduce the memory storage in subsequent steps. Each integration was then carried out by retrieving the R distance values from these binary files. For a typical integration, I estimated a calculation time of approximately 194 days to obtain all 8037 expansion coefficients. These integrals were computed on a high-performance computing cluster utilizing 32 processors. The calculation of the

coefficients required approximately 93 days of continuous processing time, highlighting the computational intensity of the task due to the complexity of the integrals involved. The routine developed for calculating these coefficients is broadly applicable to all van der Waals systems within the rigid rotor approximation. This general applicability holds as long as the ab initio potential is adapted to the specific system and suitable basis functions are selected.

In Figure 4.6, the main coefficients expansion of the PES are represented, identified by five indices: These terms are indicated with the indices (L_A,K_A,L_B,K_B,L). It is useful to recall that K_A and K_B are even numbers, while L_A and L_B obey the condition $|L_A - L_B| < L < L_A + L_B$. The dipole-dipole interaction term corresponds to the case $L_A = L_B = 1$ (with $L = 2$ and $K_A = K_B = 0$), giving it the label 10102 [53]. It is observed that this term is negative and of high amplitude, with a value of approximately -41 cm^{-1} at a distance of $R = 25$ bohr. Even at a higher distance of $R = 35$ bohr, it remains significant, around -15 cm^{-1}. Upon verification, I have confirmed that the dipole-dipole interaction term follows the expected asymptotic behavior of a dipole-dipole interaction, $v_{10102} \approx \frac{1}{R^3}$. It is also noteworthy that Figure 4.6 reveals that the amplitude of v_{10102} exceeds that of the isotropic term v_{00000} over the entire range of considered distances R. The well depth of v_{00000} is approximately -134 cm^{-1}, with a minimum located at a distance close to 6.55 bohr.

Other notable terms of dipole-dipole ($L_A = 1$) or quadrupolar ($L_A = 2$) type are also represented in Figure 4.6. Although these terms are less important than v_{10102}, they decrease faster as the intermolecular distance increases. However, some of them reach a magnitude comparable to that of the elastic term v_{00000}, highlighting that the PES is anisotropic even at long-range distances.

4.3.3 Reduction of the analytical multipolar PES

The original formula of the analytic potential, expressed using Wigner functions, is a complex potential. However, in the framework of the MCTDH method, it is not possible

to represent a potential in complex form. Therefore, it was necessary to reformulate the potential by exploiting the different symmetry operations related to the rotations of the Euler angles for the water dimer. In this section, we will present in detail these symmetry operations and their impact on the potential and the associated expansion coefficients. This analysis will help us understand how symmetry can simplify the potential and make it possible to integrate it into MCTDH.

In 1977 [64], the theoretical spectroscopy performed by Dyke showed that the water dimer belongs to symmetry group G_{16}, and that some of these symmetries are equivalent. Eight distinct symmetry operations belong to the G_8 symmetry group.

The rigid water dimer possesses several symmetry operations that affect the expansion coefficients. One can notice that the potential energy surface $V(R, \omega_A, \omega_B)$ remains invariant under all symmetry operations and the expansion coefficients $v_{\{\Lambda\}}(R)$ must also remain invariant. We obtained the following symmetry conditions [64]: This operation

- Identity operation

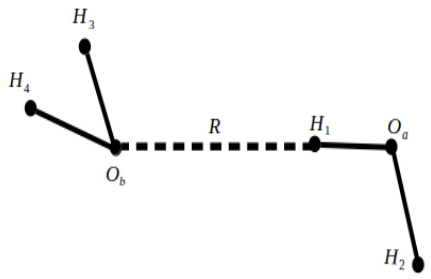

- Inversion operation

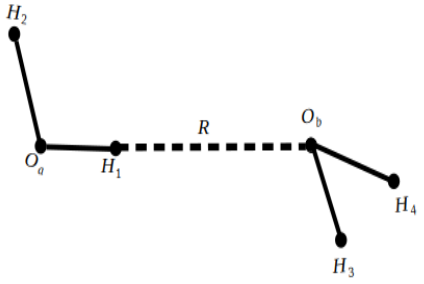

transforms changes the Euler angles as follows:

$$\begin{aligned} \omega_A(\alpha_A, \beta_A, \gamma_A) &= \omega_A(\pi + \alpha_A, \pi - \beta_A, \pi - \gamma_A), \\ \omega_B(\alpha_B, \beta_B, \gamma_B) &= \omega_B(\pi + \alpha_B, \pi - \beta_B, \pi - \gamma_B), \end{aligned} \tag{4.3.11}$$

and

$$V(R, \alpha_A, \beta_A, \gamma_A, \alpha_B, \beta_B, \gamma_B) = V(R, \pi + \alpha_A, \pi - \beta_A, \pi - \gamma_A, \pi + \alpha_B, \pi - \beta_B, \pi - \gamma_B) \tag{4.3.12}$$

As consequence, the expansion coefficients are obtained as follows:

$$v_{L_A K_A L_B K_B L}(R) = (-1)^{L_A+L_B+L} v_{L_A -K_A L_B -K_B L}(R) \tag{4.3.13}$$

- Identity operation

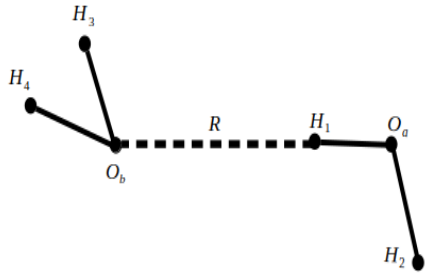

- Permutation operation

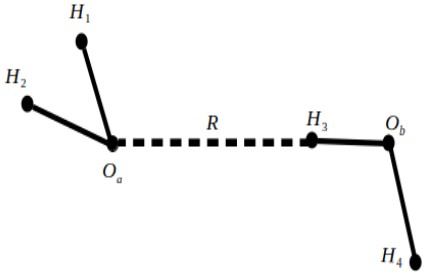

This operation changes the positions of each monomer; i.e, the Euler angles are given as follows:

$$\begin{aligned} \omega_A(\alpha_A, \beta_A, \gamma_A) &= \omega_B(\alpha_A, \beta_A, \gamma_A), \\ \omega_B(\alpha_B, \beta_B, \gamma_B) &= \omega_A(\alpha_B, \beta_B, \gamma_B), \end{aligned} \tag{4.3.14}$$

and

$$V(R, \alpha_A, \beta_A, \gamma_A, \alpha_B, \beta_B, \gamma_B) = V(R, \alpha_B, \beta_B, \gamma_B, \alpha_A, \beta_A, \gamma_A) \tag{4.3.15}$$

As consequence, the expansion coefficients are obtained as follows

$$v_{L_A K_A L_B K_B L}(R) = (-1)^{L_A+L_B} v_{L_B K_B L_A K_A L}(R) \tag{4.3.16}$$

This operation is the rotation of one water monomer with axis trough its oxygen atom. It changes the Euler angles as follows

$$\begin{aligned} \omega_A(\alpha_A, \beta_A, \gamma_A) &= \omega_B(\alpha_A, \beta_A, \gamma_A + \pi), \\ \omega_B(\alpha_B, \beta_B, \gamma_B) &= \omega_A(\alpha_B, \beta_B, \gamma_B), \end{aligned} \tag{4.3.17}$$

- Identity operation

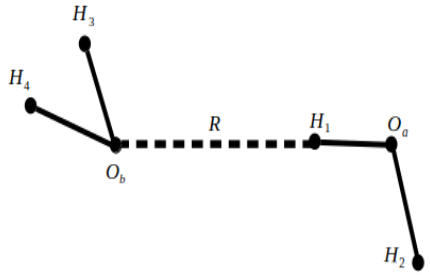

- $C_{2\nu}$ symmetry of the water molecule:

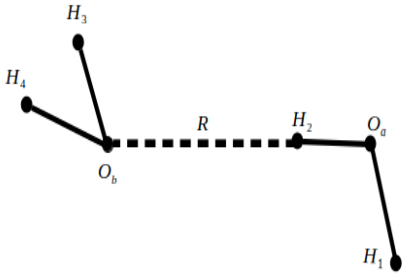

and

$$V(R,\alpha_A,\beta_A,\gamma_A,\alpha_B,\beta_B,\gamma_B) = V(R,,\alpha_A,\beta_A,\gamma_A+\pi,\alpha_B,\beta_B,\gamma_B) \tag{4.3.18}$$

as consequence, the expansion coefficients are obtained as follows

$$v_{L_AK_AL_BK_BL}(R) = (-1)^{K_A} v_{L_AK_AL_BK_BL}(R) \tag{4.3.19}$$

$$v_{L_AK_AL_BK_BL}(R) = (-1)^{K_B} v_{L_AK_AL_BK_BL}(R) \tag{4.3.20}$$

Equations 4.3.18 and 4.3.19 mean that the expansion coefficients can be written as follows

$$v_{L_AK_AL_BK_BL}(R) = 0, \tag{4.3.21}$$

when the values of K_A and/or K_B are odd.

Combining these symmetry conditions, we can find that the PES can be rewritten as follows:

$$
\begin{aligned}
V(R,\omega_A,\omega_B) = & \sum_{L_A L_B L} \sum_{M_A=0}^{L_A} \sum_{K_A=0}^{L_A} \sum_{K_B=0}^{L_B} (-1)^{L_A+L_B+L} \begin{pmatrix} L_B & L_A & L \\ M_A & -M_A & 0 \end{pmatrix} \\
& \times \frac{2}{\left(1+\delta_{M_A 0}\right)\left(1+\delta_{K_A 0}\right)\left(1+\delta_{K_B 0}\right)} \\
& \times \Bigg[\Bigg[v_{L_A K_A L_B K_B L}(R) \Bigg(cos\left(M_A\left(\alpha_A-\alpha_B\right)+K_A\gamma_A+K_B\gamma_B\right) d^{L_A}_{M_A K_A}(\beta_A) d^{L_B}_{-M_A K_B}(\beta_B) \\
& + (-1)^{L_A+L_B+L} cos\left(M_A\left(\alpha_A-\alpha_B\right)-K_A\gamma_A-K_B\gamma_B\right) d^{L_A}_{M_A -K_A}(\beta_A) d^{L_B}_{-M_A -K_B}(\beta_B) \Bigg) \\
& + v_{L_A K_A L_B -K_B L}(R) \Bigg(cos\left(M_A\left(\alpha_A-\alpha_B\right)+K_A\gamma_A-K_B\gamma_B\right) d^{L_A}_{M_A K_A}(\beta_A) d^{L_B}_{-M_A -K_B}(\beta_B) \\
& + (-1)^{L_A+L_B+L} cos\left(M_A\left(\alpha_A-\alpha_B\right)-K_A\gamma_A+K_B\gamma_B\right) d^{L_A}_{M_A -K_A}(\beta_A) d^{L_B}_{-M_A K_B}(\beta_B) \Bigg) \Bigg] \Bigg]
\end{aligned}
\tag{4.3.22}
$$

The analytical expression shown above (equation 4.3.22) of the multipolar PES in the reduced form is presented with more details in the appendix.

Table 4.1: Five important $v_{L_AK_AL_BK_BL}$ expansion coefficients of the water dimer PES. R and $v_{L_AK_AL_BK_BL}$ given in bohr and Hartree (Ha) respectively.

R	v_{00000}	v_{10001}	v_{10102}	v_{20002}	v_{22002}
4	5.60E-02	-3.43E-04	-6.87E-02	7.55E-03	2.02E-03
4.25	3.33E-02	-1.75E-04	-5.25E-02	3.50E-03	8.68E-04
4.5	1.94E-02	-6.59E-05	-4.11E-02	1.60E-03	3.80E-04
4.75	1.09E-02	-4.43E-05	-3.29E-02	7.37E-04	1.70E-04
5	5.76E-03	-4.29E-05	-2.69E-02	3.48E-04	7.81E-05
5.25	2.78E-03	-3.90E-05	-2.24E-02	1.74E-04	3.84E-05
5.5	1.08E-03	-3.22E-05	-1.90E-02	9.40E-05	2.08E-05
5.75	1.51E-04	-2.55E-05	-1.63E-02	5.57E-05	1.25E-05
6	-3.26E-04	-2.06E-05	-1.41E-02	3.54E-05	8.10E-06
6.25	-5.41E-04	-1.73E-05	-1.23E-02	2.36E-05	5.51E-06
6.5	-6.07E-04	-1.52E-05	-1.09E-02	1.61E-05	3.83E-06
6.75	-5.95E-04	-1.39E-05	-9.67E-03	1.11E-05	2.68E-06
7	-5.44E-04	-1.28E-05	-8.64E-03	7.68E-06	1.89E-06
7.25	-4.77E-04	-1.17E-05	-7.76E-03	5.40E-06	1.34E-06
7.5	-4.09E-04	-1.06E-05	-7.00E-03	3.86E-06	9.74E-07
7.75	-3.46E-04	-9.32E-06	-6.34E-03	2.82E-06	7.24E-07
8	-2.90E-04	-7.95E-06	-5.76E-03	2.12E-06	5.54E-07
8.25	-2.43E-04	-6.53E-06	-5.25E-03	1.64E-06	4.36E-07
8.5	-2.03E-04	-5.11E-06	-4.80E-03	1.30E-06	3.53E-07
8.75	-1.70E-04	-3.76E-06	-4.41E-03	1.05E-06	2.91E-07
9	-1.43E-04	-2.52E-06	-4.06E-03	8.63E-07	2.43E-07
9.25	-1.20E-04	-1.43E-06	-3.74E-03	7.15E-07	2.04E-07
9.5	-1.02E-04	-5.04E-07	-3.46E-03	5.96E-07	1.72E-07
9.75	-8.62E-05	2.54E-07	-3.21E-03	4.96E-07	1.45E-07
10	-7.29E-05	8.47E-07	-2.98E-03	4.13E-07	1.22E-07
10.25	-6.16E-05	1.29E-06	-2.78E-03	3.42E-07	1.02E-07
10.5	-5.19E-05	1.60E-06	-2.59E-03	2.83E-07	8.48E-08
10.75	-4.35E-05	1.79E-06	-2.42E-03	2.33E-07	7.02E-08
11	-3.61E-05	1.89E-06	-2.26E-03	1.91E-07	5.79E-08
11.25	-2.98E-05	1.92E-06	-2.12E-03	1.56E-07	4.75E-08
11.5	-2.42E-05	1.88E-06	-1.99E-03	1.27E-07	3.88E-08
11.75	-1.95E-05	1.81E-06	-1.87E-03	1.03E-07	3.16E-08
12	-1.53E-05	1.71E-06	-1.75E-03	8.36E-08	2.56E-08

4.4 The Equilibrium Positions of $(H_2O)_2$ Rigid Multipolar PES

The equilibrium position of the multipolar potential in equation 4.3.22 is calculated using the Steepest descent method by increasing the value of the total angular momentum L_{Amax} and L_{Bmax}. Our results are summarized in Table 4.2, showing agreement between the values obtained using the exact *ab initio* CCpol-8s potential and the value obtained by Wang and Carrington [63].

Table 4.2: The equilibrium position of the multipolar PES when increasing the values of L_{Amax} and L_{Bmax}

$L_{\text{Amax}}/L_{\text{Bmax}}$	α_A	β_A	γ_A	α_B	β_B	γ_B	R_e(Bohr)	$D_e(cm^{-1})$
0	0	117.55	-0.47	50	-0.47	122.70	6.56	-133.78
1	-0.47	0	-0.43	49.6	0	122.74	5.531	-1322.34
2	0	55.86	-90	0	-90	0	5.45	-1922.71
3	0	72.58	0	-180	107.41	180	4.54	-2592.3
4	0	125.83	0	-180	163.99	270	5.55	-1673.51
5	0	120.33	0	-180	131.34	270	5.445	-1838.08
6	0	65.775	90	-180	63.321	0	5.455	-1803.09
7	0	54.737	90	-180	60.356	0	5.529	-1763.2
8	0	53.176	90	-180	59.956	0	5.501	-1789.59
Ref. [63]	0	54.36	90	-180	60.05	0	5.508	-1785.66
Ref. [118]	0	61.04	0	-180	55.12	90	5.5	-1785
Exp. [118]								-1748.775± 24.482

4.4.1 Comparison of the ab initio and multipolar PESs

The convergence of the expansion coefficients was tested by increasing the value of the angular momentum of the multipolar potential for each monomer. Figure 4.7 shows that starting from a total angular momentum value of 6 for each monomer, the calculations exhibit good convergence with respect to the *ab initio* potential displayed in Figure 4.8. This is further supported by the root mean square error (RMSE) of the multipolar potential with respect to the *ab initio* potential as shown in Table 4.3 at high energies (when the two monomers are very close) and at low energies (when the two monomers are very distant).

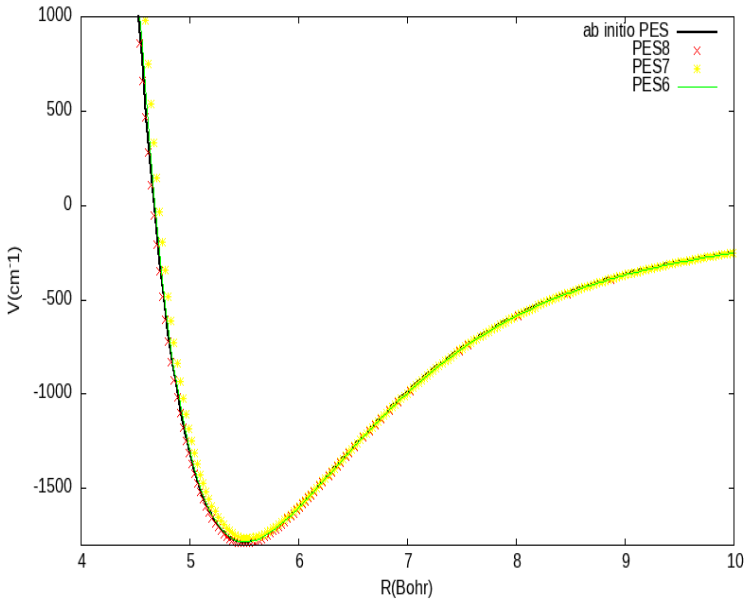

Figure 4.7: Convergence of the PES as a function of the intermolecular distance R. The other coordinates are fixed at the equilibrium positions. The figure shows the global minimum for $L_{Amax} = L_{Bmax} = 6, 7, 8$.

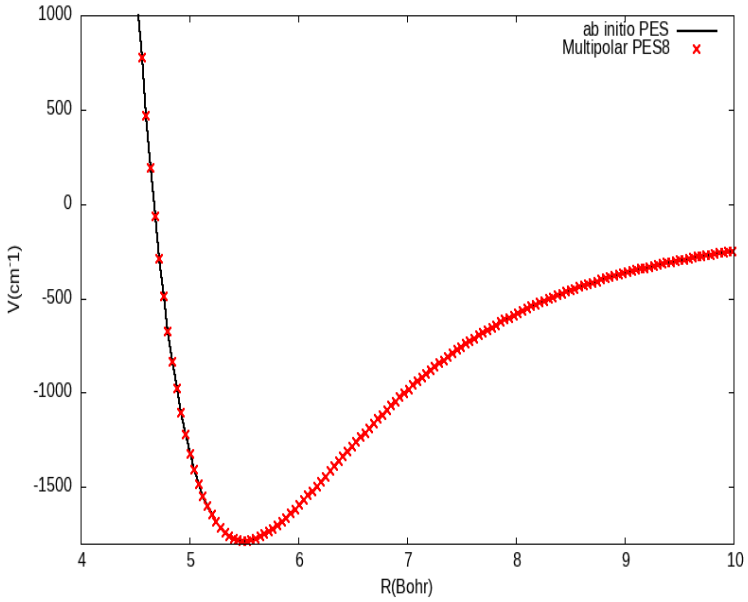

Figure 4.8: 1D cut of the *ab initio* PES and multipolar PES at $L_{Amax} = L_{Bmax} = 8$. R varies while the other coordinates are fixed at the equilibrium positions. The figure shows the global minimum (De$=-1785.15$ cm^{-1} for *ab initio* and -1789.59 cm^{-1} for the multipolar PES $(H_2O)_2$ dimer).

Figures 4.9 and 4.10 show the approximation of the multipolar potential to the *ab initio* PES at large intermolecular distances. We also observed a weak representation of the

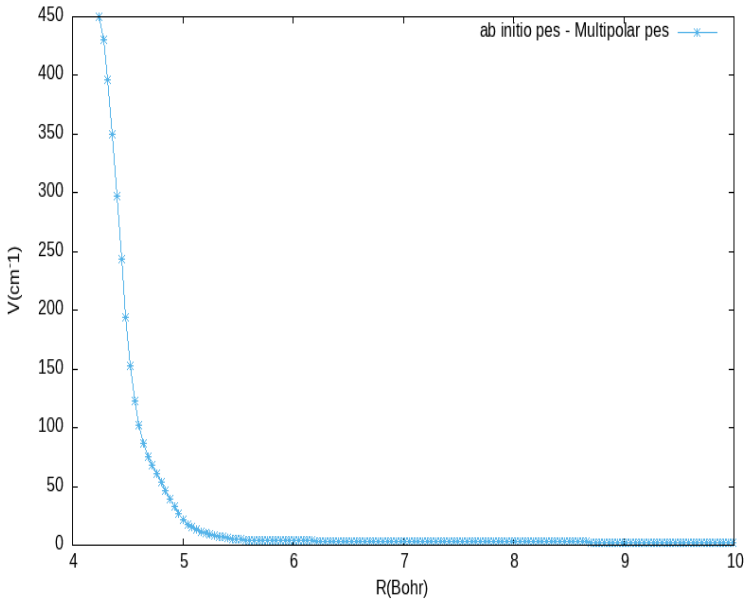

Figure 4.9: Error between the *ab initio* PES and multipolar PES for $L_{Amax} = L_{Bmax} = 8$.

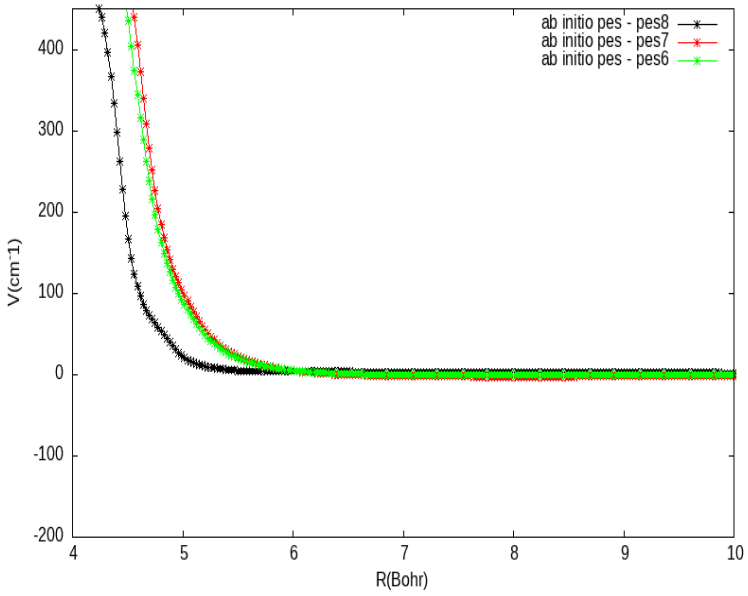

Figure 4.10: Error of the multipolar PES for $L_A max$=$L_B max$=6,7,8 with respect to the *ab initio* PES.

potential at short distances. Figures 4.11 and 4.12 show that the two-dimensional contour plots are visually identical, demonstrating an accurate transformation of the analytical multipolar potential ready to be implemented in the MCTDH package. We also remind you that the coordinate values set are close to the equilibrium values of the surface represented.

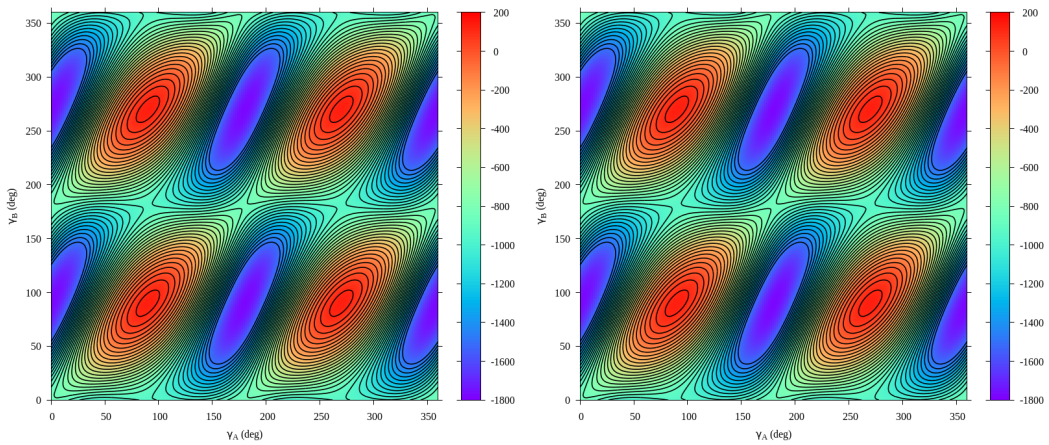

(a) (b)

Figure 4.11: 2D contour plots of the potential of H_2O-H_2O as a function of γ_A and γ_B. The other coordinates are fixed at the equilibrium positions. Figure 4.11a shows the *ab initio* PES, and Figure 4.11b shows the multipolar PES. The figures show the global minimum of -1785.15 cm^{-1} and -1789.59 cm^{-1}, respectively

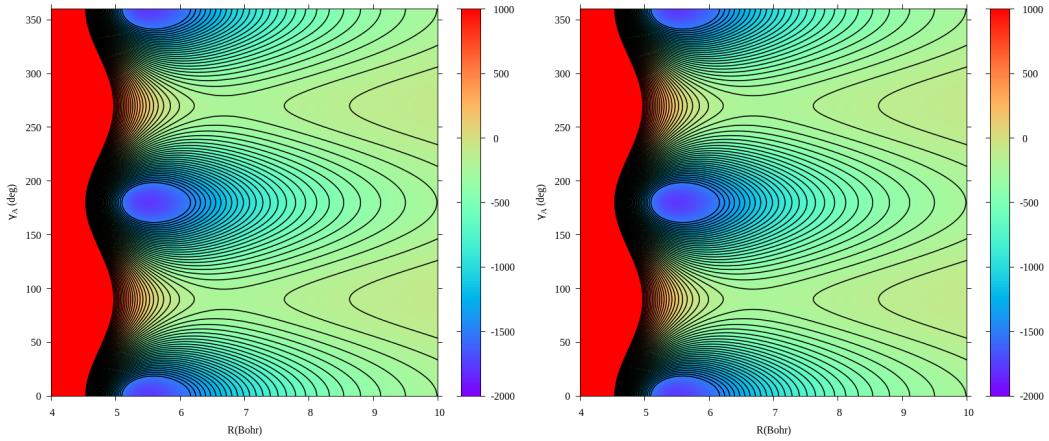

(a) (b)

Figure 4.12: 2D contour plot of the potential of $(H_2O)_2$ as a function of R and γ_A. The other coordinates are fixed at the equilibrium positions. Figure 4.12a shows the *ab initio* PES, and Figure 4.12b shows the multipolar PES. The figures display the global minimum of -1785.15 cm^{-1} and -1789.59 cm^{-1}, respectively

Table 4.3: The RMSE of the multipolar potential with respect to the *ab initio* potential. E_+ is for positive values of the potential and V_- for negative values

L_{Amax}/L_{Bmax}	E_+	$V_- < 0$
6	627.518	56.644
7	567.824	42.63
8	189.543	12.001

Table 4.3 shows that the potential is better represented at higher distances with a low RMSE value. This RMSE is displayed in Figure 4.14a. For the energies greater than or equal to zero, i.e., at the lower intermolecular distances, the RMSE is 627.518, 567.824, and 189.543 cm^{-1} for the values of L_{Amax}/L_{Bmax} 6, 7, and 8, respectively. For the energies less than zero, i.e., at higher intermolecular distances, the RMSE values are 56.644, 42.63, and 12.001 cm^{-1} for the values of L_{Amax}/L_{Bmax} 6, 7, and 8, respectively. One can find that the PES is well described at the higher intermolecular distances than at lower distances.

After running several numerical tests to ensure the correct expression of the multipolar PES, the implementation of the PES in the MCTDH code is carried out. This is achieved through a FORTRAN routine that generates the PES in the sum-of-products form. One of the methods for verifying the correctness of the implementation is to compare the contour plots of the implemented PES with the analytical potential using the same geometry points. A comparison of the two-dimensional contour plots of the multipolar potential and that implemented in the MCTDH code is shown in Figure 4.13.

Figures 4.13a and 4.13b show that the 2D contour plots of the analytical multipolar PES and that implemented in the MCTDH are visually identical. We also remind you that the coordinate values set are close to the equilibrium values of the surface represented. We can notice that the representations of the two-dimensional contour plots of the potential energy surface are the tests to ensure that it is well implemented in the MCTDH because this step is the main node of the calculations.

The exponential form of the PES is advantageous because it allows us to accurately check its representation in the MCTDH with respect to all angular orientations, but it cannot be

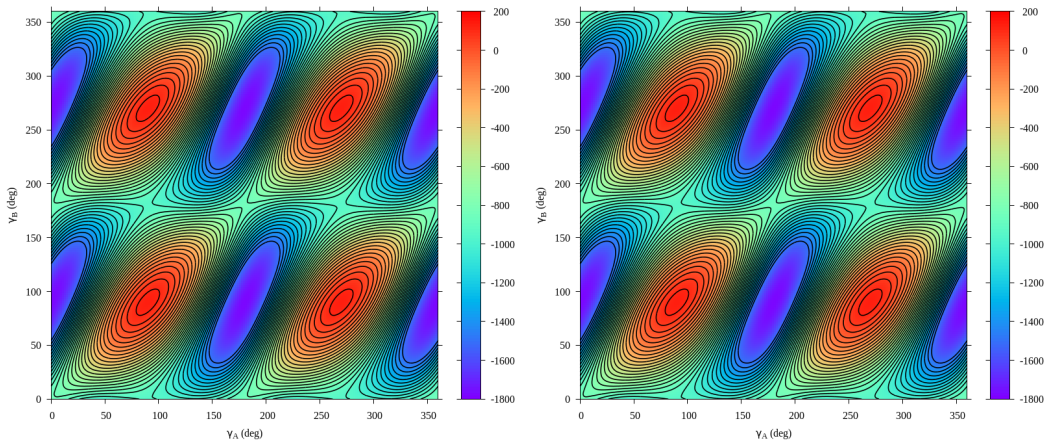

(a) (b)

Figure 4.13: Comparison of the 2D contour plots of the analytical PES in Figure 4.13a and the PES implemented in MCTDH in Figure 4.13b for $(H_2O)_2$ as a function of γ_A and γ_B.

used to perform calculations for a total angular momentum greater than zero ($J_{\text{tot}} > 0$) because this approach is not yet implemented in the MCTDH package. To solve this problem, we opted for a Fourier transformation (FT) of some angles the potential. In the Wigner functions, the angles α_A, γ_A, α_B, and γ_B can be Fourier Transformed into the K component (projection of the total angular momentum) used in the calculation. Each angle is replaced by its momentum representation k_{α_A}, k_{γ_A}, k_{α_B}, and k_{γ_B}.

In the following, the PES can be given as:

$$\hat{V}(R, k_{\alpha_A}, \beta_A, k_{\gamma_A}; k_{\alpha_B}, \beta_B, k_{\gamma_B}) = \sum_{\{\Lambda\}} v_{\{\Lambda\}}(R) \hat{A}_{\{\nu\}}(k_{\alpha_A}, \beta_A, k_{\gamma_A}; k_{\alpha_B}, \beta_B, k_{\gamma_B}), \quad (4.4.1)$$

In the MCTDH code, the kinetic energy operator and the potential energy surface are written line by line. In cases like the water dimer, the number of potential terms can exceed the computational limits of MCTDH, complicating the calculations. To address this issue, we have opted to numerically reduce the sum-of-products (SOP) terms of the potential energy surface (PES), ensuring that each expansion coefficient corresponds uniquely to a specific combination of Wigner functions. However, after factorization, the

number of expansion coefficients increases while the number of lines in the PES decreases. It has been observed that MCTDH takes more time to open and read the factorized files containing the new expansion coefficients. The factorization is done to reduce the number of lines of the Hamiltonian implemented in the MCTDH code because a high number of lines prevents the code from compiling. With the reduced multipolar PES, considering a case with L_{Amax}=L_{Bmax}=8 and using the exponential form of the PES, initially, there are 8037 expansion coefficients with 572658 lines of the potential energy surface. After factorization, the number of expansion coefficients reduced to 48969, corresponding to 48969 lines of the PES. The advantage of this factorization is that it enables us to represent the potential energy surface (PES) up to values of L_{Amax}=L_{Bmax}=8, which was not feasible with the unfactorized PES. There is a reduction in calculation time using the factorized potential, which is more advantageous for systems with a small number of degrees of freedom. The factorized potential significantly reduces calculation time, making it especially advantageous for systems with a large number of degrees of freedom (DOF). As shown in Table 4.4, we conducted test calculations for L_{Amax}=L_{Bmax}=8 using 32 processors, progressively increasing the number of single-particle functions (SPFs). The results demonstrate that the factorization procedure applied to the PES yields faster computations compared to calculations with the unfactorized PES. Because symmetries

Table 4.4: Computational time of the ground state at L_{Amax}=L_{Bmax}=8. The time is given in hour.

SPFs	Time (Unfactorized PES)	Time (Factorized PES)
10/10/10	210	80
10/20/20	260	120
10/30/30	430	160

are not yet implemented for the Wigner functions, the relaxation time to converge a ground state calculation for a number of SPFs 10/30/30 (10 for R, 30 for α and γ, 30 for β) took approximately 4 weeks. Note that each set of degrees of freedom in the Wigner functions is represented in combined modes in the SPFs section as follows

sbasis-section

$$R = 10$$

$$\beta_A, \gamma_A, \alpha_A = 30$$

$$\beta_B, \gamma_B, \alpha_B = 30$$

end-sbasis-section

We can notice that the advantage of using the factorization of the PES allows us to reduce the lines and run the calculations with a higher size of the Hamiltonian in less computational time. Tables 4.5 and 4.6 show the reduction of the size of the multipolar PES. We find that it is more advantageous to use the Fourier Transform form with fewer potential terms

Table 4.5: Factorization of the multipolar PES in the exponential form

L_{Amax}/L_{Bmax}	Unfactorized PES	Factorized PES
6	117463 lines	12993 lines
7	258110 lines	25240 lines
8	564515 lines	48969 lines

Table 4.6: Factorization of the multipolar potential energy surface in the Fourier Transform form.

L_{Amax}/L_{Bmax}	Unfactorized PES	Factorized PES
6	37618 lines	4599 lines
7	80346 lines	8568 lines
8	170755 lines	15993 lines

The mathematical formulation of this factorization of the PES can be given as follows:

$$V(R, \omega_A, \omega_B) = \sum_{\{\Lambda\}} v^i_{\{\Lambda\}}(R) A_{\{\nu\}}(\omega_A, \omega_B), \tag{4.4.2}$$

The new analytical formula for the PES is expressed as follows

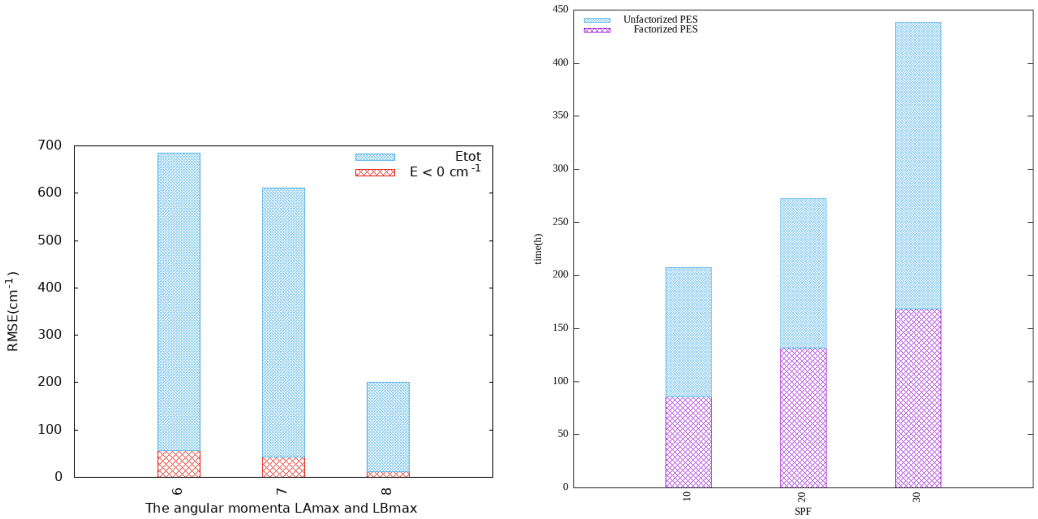

(a) (b)

Figure 4.14: Variation of the RMSE is shown in Figure 4.14a, and the computational time using the factorized and unfactorized PESs is shown in Figure 4.14b.

$$V(R,\omega_A,\omega_B)=\sum_{\{\Lambda\}}P^k_{\{\Lambda\}}(R)A_{\{\nu\}}(\omega_A,\omega_B), \tag{4.4.3}$$

where the new radial expansion coefficients $P^k_{\{\Lambda\}}(R)$ and the angular functions $A_{\{\nu\}}(\omega_A,\omega_B)$ are unique, i from 4.4.2 and k from 4.4.3 are such that $k>i$.

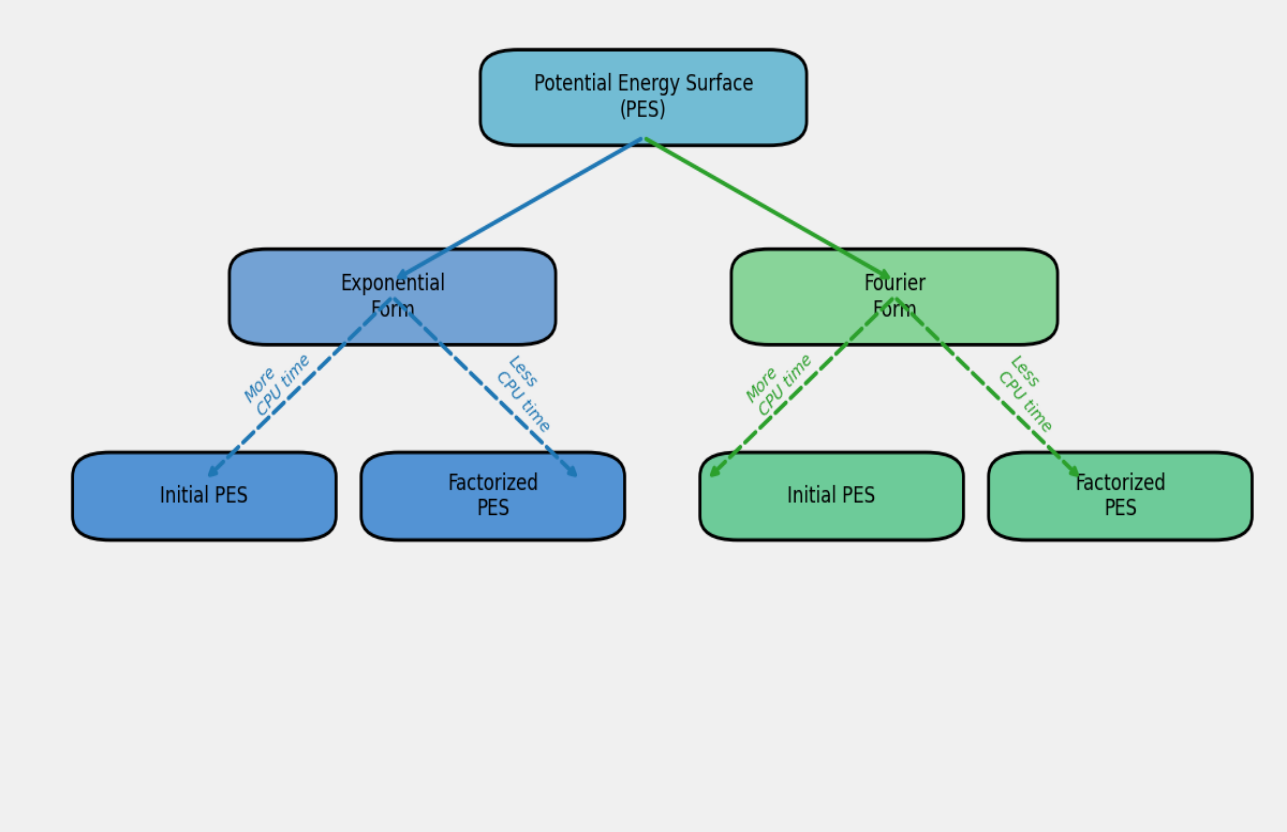

Figure 4.15: The two different forms (Exponential and Fourier) and the process of factorization to optimize computational efficiency in MCTDH calculations

Figure 4.15 shows a brief description of the two distinct approaches for representing the PES in the MCTDH calculations: the Exponential and Fourier forms. Both forms begin with the initial PES but diverge in terms of computational demands and efficiency. The Exponential form requires more CPU time when using the initial PES, but through factorization, it becomes more efficient, reducing computational time. Similarly, the Fourier form can also start with the initial PES, but the factorization of this form allows for a more efficient representation, significantly decreasing CPU time.

4.5 Rovibrational states calculations with MCTDH

In this section, we introduce the primitive basis chosen for the improved relaxation method, tailored to optimize the computational efficiency.

- FFT stands for the Fast Fourier Transform (FFT) functions in *R* mode [148].
- K stands for the momentum representation corresponding to the Fourier Transform of the angles α and γ [69]. The units for distance and angle are bohrs and radians, respectively.
- Wigner stands for the Wigner DVR [215].

One can also note that the two primitive bases are presented to show the reader the two possible approaches for performing the calculations. Table 4.7 presents the primitive base used for the initial potential, while Table 4.8 shows the primitive base after applying the Fourier transformation. It is also worth noting that this transformation affects the kinetic energy operator. Calculations performed with the base from Table 4.7 offer the advantage of representing the wave function taking into account the entire dimer geometry, whereas in Table 4.8, only the angles β_A and β_B can be represented,but it can still be used to perform calculations for total angular momentum $J > 0$. For the final calculations, I used the Fourier transform form, which implies that the parameters of the primitive base from Table 4.8 were adopted.

Table 4.7: Parameters used for the relaxation calculations. CMF is the Constant Mean Field integrator scheme, RK8 is the Runge-Kutta procedure of order 8, and DAV is the Davidson integrator.

Coordinates	Primitive basis	Number of points	Range	The size of the SPFs
R	FFT	32	4 - 10	8-10
β_A	Wigner	11	0–π	10–100
γ_A	Exp	21	0–2π	10–100
α_A	Exp	21	0–2π	10–100
β_B	Wigner	11	0–π	10-100
γ_B	Exp	21	0–2π	10–100
α_B	Exp	21	0–2π	10–100
Integrator	Scheme	A-vector	SPF	
Type	CMF	DAV	RK8	
Time step	1	0.01	800	
Accuracy	10^{-6}	10^{-9}	10^{-9}	

Using the Fourier Transform of the PES:

Table 4.8: Parameters used for the relaxation calculations of $(H_2O)_2$.

Coordinate	Primitive Basis	Number of Points	Range	Size of SPF basis
R	FFT	32	4–10	8–10
β_A	Wigner	11	0–π	10–100
γ_A	K	21	-10,10	
α_A	K	21	-10,10	
β_B	Wigner	11	0–π	10–100
γ_B	K	21	-10,10	
α_B	K	21	-10,10	
Integrator	Scheme	A-vector	SPF	
Type	CMF	DAV	RK8	
Time step	1.0	0.01	800	
Accuracy	10^{-6}	10^{-9}	10^{-9}	

Tables 4.7 and 4.8 contain the parameters used to calculate rovibrational states. Table 4.7 shows the parameters used for the initial potential, and Table 4.8 shows the parameters for the Fourier transform. Both forms of potential give the same results, with the only difference being that calculations are quicker with the parameters in Table 4.8.

I performed several convergence tests to determine the values of excited rovibrational states for $J = 0$. It was found that the calculations did not reach sufficient convergence unless the number of SPFs was significantly increased, which also increased the calculation time, requiring several days to obtain stable results. The goal was to observe the behavior of energy level splittings, but this phenomenon did not manifest due to convergence issues. These tests are summarized in tables 4.9 and 4.10. In general, I expected to see energy levels appearing in pairs. The only viable solution to achieve a reasonable calculation time was to opt for convergence with a single wave packet.

Table 4.9: Convergence of vibrational levels for 8 wave packets with a primitive basis of 48/21/11/11/21/11/11

SPF	10/10/10	10/20/20	10/30/30	10/40/40	10/50/50	Teory [63]	Exp [118]
ZPE	1055.345	1070.222	1078.193	1086.002	1088.688	1094.225	1093.54
E_0	0.000	0.000	0.000	0.000	0.000	0.000	0.000
E_1	4.431	2.488	0.013	1.121	0.029	0.4342	0.651
E_2	4.445	3.507	1.463	5.389	14.034	0.7824	0.752
E_3	5.602	4.580	1.475	6.752	14.321	12.4505	11.18
E_4	11.818	11.864	11.561	16.54	15.313	12.8253	
E_5	28.780	12.795	11.597	16.581	15.313	13.1144	
E_6	30.927	13.197	15.181	17.00	15.366	60.6737	
E_7	31.024	25.208	15.22	17.021	15.366	63.3903	

Table 4.10: Convergence of vibrational levels for 4 wave packets with a primitive basis of 48/21/11/11/21/11/11

SPF	10/10/10	10/20/20	10/30/30	10/40/40	10/50/50	Teory [63]	Exp [118]
ZPE	1062.923	1084.688	1089.616	1090.248	1091.144	1094.225	1093.54
E_0	0.000	0.000	0.000	0.000	0.000	0.000	0.000
E_1	0.092	12.223	16.411	5.780	4.923	0.4342	0.651
E_2	12.476	18.337	17.070	16.434	15.673	0.7824	0.752
E_3	12.648	18.337	17.162	16.435	15.574	12.4505	11.18

In Tables 4.9 and 4.10, the primitive basis 48/21/11/11/21/11/11 is associated to the numbers of grid points of each degree of freedom $(R/\alpha_A/\beta_A/\gamma_A/\alpha_B/\beta_B/\gamma_B)$ and the 10/50/50 is associated the numbers of the SPFs for each degree of freedom in combined modes, that is, $R = 10, (\alpha_A, \beta_A, \gamma_A) = 50, and (\alpha_B, \beta_B, \gamma_B) = 50$

4.6 Comparison of the Zero-Point Energy (ZPE)

. Due to challenges in achieving convergence with calculations of rovibrational states for the water dimer, despite employing a factorized potential with fewer Hamiltonian terms, we opted to focus solely on computing the zero-point energy. This was accomplished by expanding the size of the primitive basis and increasing the number of single-particle functions (SPFs). The results of these calculations were then compared to those obtained using the same PES [118, 63, 116] and are reported in Table 4.11. In this table, the first column represents the SPF basis, where $a_1/a_2/a_3$ stands for the number of SPF along the first mode R (After extensive testing along the R mode). The parameter a_1 represents the number of SPFs associated with R, while a_2 and a_3 correspond to the numbers of SPFs for the Euler angles of each monomer in combined modes.

Table 4.11: The convergence of the ground state energy with the number of the SPFs for the primitive basis (32/11/21) and (48/11/21) for $J = 0$. ZPE is the Zero-Point Energy (ZPE). Units in cm^{-1}.

Primitive Basis	(32/11/21)	(48/11/21)
	ZPE	ZPE
10/50/50	1092.142	1092.154
10/60/60	1093.862	1093.873
10/70/70	1093.926	1093.936
10/80/80	1093.976	1093.979
10/90/90	1093.993	1093.996
10/100/100	1094.003	1094.004
Ref. [63]	1094.225	1094.225
Ref. [118]	1093.54	1093.54
Ref. [116]	1094	1094

Figure 4.16 shows the probability density of the ground-state wave function as a function of the coordinates R and the angle γ_B, fixed at values close to the equilibrium values of the represented surface. The wave function is localized at the global minimum, which is observed by exploring all the other minima. The discrepancy between these positions arises from the low energy barrier that separates the equivalent global minima. When the energy increases, the function has difficulty exploring all eight potential wells and

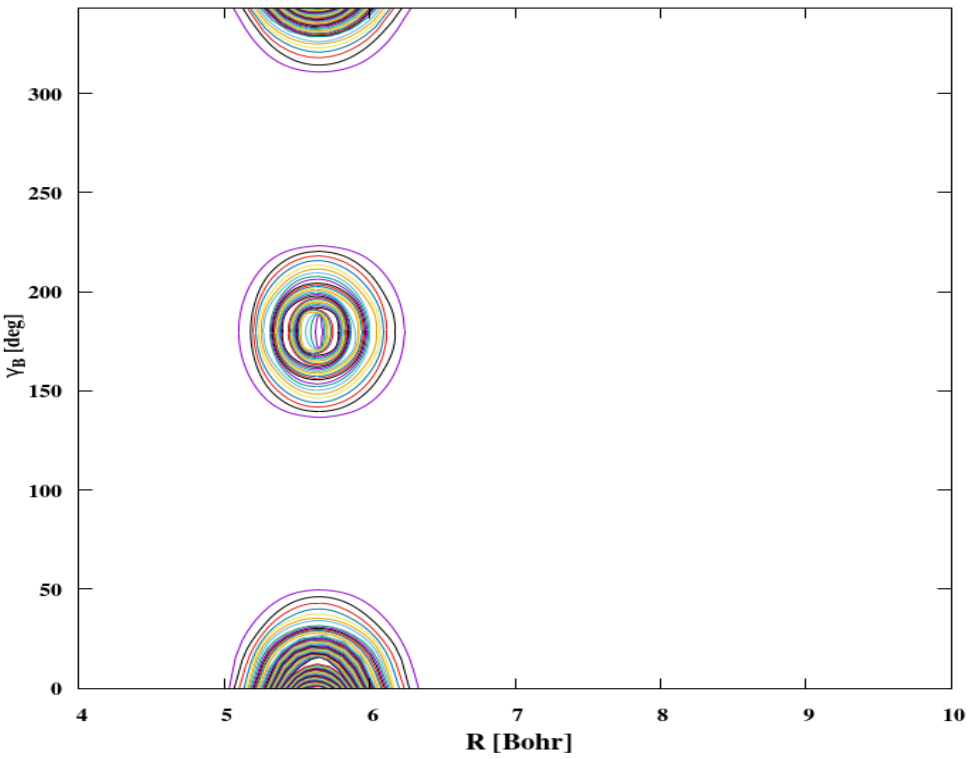

Figure 4.16: Wavefunction of the ground state energy level of the water dimer as a function of R and γ_B.

located at the equilibrium position at R=5.5 bohr. This also highlights the importance of tunneling between rovibrational states of the water dimer.

4.7 Discussion of the Zero Point Energy of the $(H_2O)_2$

We used the CCpol-8s PES version from the SI of reference [118]. In Table 4.11, we compare our zero-point energy with those obtained previously using the same *ab initio* PES in the rigid rotator approximation. As mentioned before, the size of the primitive basis and the number of SPFs contribute to the convergence of the calculations, and these effects can be seen in Table 4.11. Despite some limitations in the current implementation of the MCTDH method within the Heidelberg MCTDH package, such as the lack of symmetry in the Wigner-DVR functions, we managed to extract valuable information regarding the

ground state energy of our system. Throughout our work, we attempted to converge our calculations by employing a maximum of 10000 SPFs with a zero-point energy of 1094 cm^{-1}, where the results were approximately the same for two sets of primitive bases (32/11/21) and (48/11/21). The results obtained by Wang and Carrington [63] using the Lanczos method, Cencek $et\ al.$ [118] using the Coupled Cluster method, and Leforestier $et\ al.$ [116] using the Symmetry-Adapted Lanczos method were 1094.225, 1094.54, and 1094 cm^{-1}, respectively, using the *ab initio* CCpol-8s PES. In comparison with our results, we found that MCTDH, despite using the multipolar PES, is able to calculate the binding energy of the water dimer. Moreover, as shown in Table 4.11, the ZPE converges slowly, with a maximum error of 0.001 cm^{-1} between the two sets of primitive bases. We can say that the main source of a slight difference between our results and those of other authors is due to the different rotational constants used.

4.8 Collisional dynamics of $H_2O + H_2O$ system

After successfully testing the representation of the PES by performing rovibrational state calculations on the rigid rotor water dimer, we initiated the inelastic collisional calculations using the MCTDH method. As stated in the introduction, the water molecule is one of the most abundant and important molecules in the interstellar medium. Collisional data from two water molecules are used in the analysis of data from star-forming regions [232]. Inelastic collisions between two water molecules, $H_2O + H_2O$, play a role in the transfer of collisional energies in environments such as the atmosphere of icy planets [233], cometary comae [234], and the atmosphere of water-rich exoplanets [235]. Inelastic collision studies on this system have already been carried out.

Describing the collision between H_2O molecules is challenging in quantum mechanics because both molecules have to be considered as asymmetric top rotors. This complexity results in a very large number of quantum states for the entire $H_2O + H_2O$ system. Earlier studies were performed using the MQCT to model rotational collisions between $H_2O + H_2O$. This method (MQCT) approximates the translational motion of the water molecules

responsible for scattering classically using the average trajectory approach, while their internal motions, such as rotations and vibrations, are treated quantum mechanically [53, 236]. However, there is not yet a method able to treat this system in the full quantum approach. Performing the inelastic collision of this system could be a benchmark using the MCTDH approach and allows us to learn more about collision theory, especially for large molecules, and obtain new databases such as the rate coefficients that are suitable for astronomical and astrophysical applications. In the following, we will present the steps we have followed to try to perform these inelastic collision calculations and the difficulties encountered.

4.8.1 Perfoming calculations

To perform the scattering calculations, we used the same PES as describes in the spectroscopic calculations. By using the multipolar expression of the PES with the same transformation, we can extend the PES to any radial distance for an accurate description of the low-energy regions of the cross section. For the purpose of calculations, as we are working in the momentum representation for the degrees of freedom γ and α , we replace the angles γ_A, α_A, γ_B, and α_B of each monomer with their momentum representations m_1, k_1, m_2, and k_2.

The scattering calculations with the MCTDH code begin with the construction of the initial wave function. Since the monomers are rigid rotors, the initial wave function is considered as the product of the rotational state of each monomer and a Gaussian function along the dissociative radial coordinate R, which describes the distance between the centers of mass. The Gaussian parameters are chosen to cover the entire energy range of the system, with a negative momentum. Thus, the initial wave function can be expressed as follows:

$$\begin{aligned}\Psi_i(R, \beta_A, m_1, k_1, \beta_B, m_2, K_2) &= \Psi_i(\beta_A, m_1, k_1, \beta_B, m_2, k_2)\chi(R) \\ &= \psi_{i,1}(\beta_A, m_1, k_1)\psi_{i,2}(\beta_B, m_2, k_2)\chi(R), \quad (4.8.1)\end{aligned}$$

where Ψ_i is the production of the initial rotational states of each monomer H_2O ($\psi_{i,1}$) and H_2O ($\psi_{i,2}$).

After constructing the initial wave function, we proceeded to determine the CAP parameters. As described in the theoretical section, the intensity of the CAP is determined using the plcap program, implemented in the MCTDH package. The length of the CAP was selected at 40 bohr, its strength is 3.732×10^{-8}, and its order 4.

We have thus defined the primitive basis as well as the SPF bases for the calculations. Table 4.12 presents the primitive bases and the number of SPFs used for wave packet propagation. A primitive basis using the Fast Fourier Transform (FFT) function was selected to model the intermolecular distance R, in combination with the Wigner-DVR method to represent the orientation of the two monomers in the E_2 reference frame.

Table 4.12: Primitive basis and SPFs used for the wavepacket propagation.

Coordonate	Primitive basis	Number of points	Range	Size of the SPFs basis
R	FFT	192	4.0–40	10–50
β_A	Wigner	6	0–5	10–50
m_1	K	11	-5 to 5	
k_1	K	11	-5 to 5	
β_B	Wigner	6	0–5	10–50
m_2	K	11	-5 to 5	
k_2	K	11	-5 to 5	

4.8.2 Convergence of the calculations

The convergence of MCTDH calculations relies on several factors: the primitive basis, the SPF basis, the propagation interval, the CAP intensity, and the propagation duration. In this study, the number of DVR points for the radial degree of freedom was adjusted to ensure sufficient density over the considered interval. In the following sections, detailed convergence tests were rigorously performed, and the results will be presented progressively at each stage of the calculations.

Convergence with the radial dissociative coordinate range

To establish the integration interval at $J_{tot} = 0$, we performed two separate calculations. The first one covered R ranging from 4 to 50 bohr, with 192 grid points. The second one considered R from 4 to 60 bohr, with 388 grid points. In each calculation, the position of the CAP was adjusted without changing the density of points. For all tests, we opted for a total of 1000 SPFs ($n_R \times n_{\beta_A} \times n_{\beta_B} = 10 \times 10 \times 10$). As anticipated, widening the grid and shifting the CAP did not lead to an improvement in the calculation results.

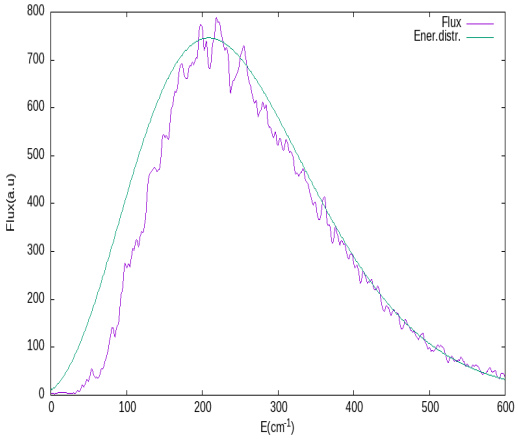

(a) Flux as a function of energy for SPF basis size 50.

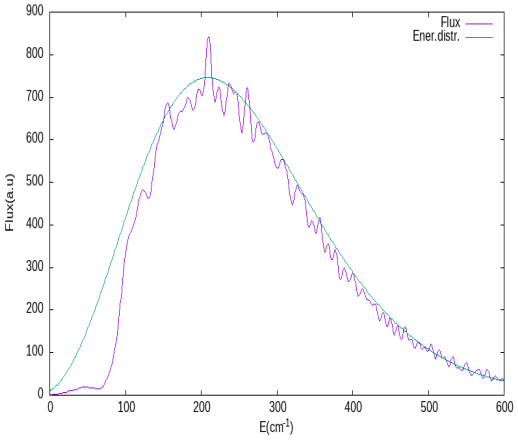

(b) Flux as a function of energy for SPF basis size 60.

Figure 4.17: Flux as a function of energy for different sizes of the SPF basis at J_{tot}=0. "Ener. distr." represents the energy distribution for the system.

Figure 4.17 illustrates the flux calculations performed using 32 processors for an energy range between 0 and 400 cm^{-1}. These two calculations took 25 and 28 days, respectively, for a propagation of 10000 fs. In terms of memory usage, the wave function in each calculation occupies approximately 1.5 GB, which is important for determining the transition probability. As shown in the figures, modeling collisions at low energy poses a particular challenge. We chose a Gaussian wavepacket centered at 42 bohrs with a width of 1.3 a.u. and an initial momentum space of -4.5 a.u., where the negative sign indicates that the wavepacket is directed toward the interaction region. In the second calculation, the Gaussian is centered at 52 bohrs with a width of 1.0 a.u., and the initial momentum is again -4.5 a.u.

The total values of incoming and outgoing flux were not satisfactory with the increase in

the primitive basis. The goal was to obtain very close values for these two values of the flux, as well as to have the flux curve converging towards that of the energy distribution function. However, these results were not achieved, indicating that the base used does not allow for an accurate description of the evolution of energy flux. For the modes R ranging from 4 to 50 bohr, with 192 grid points, the values of the flux were given as follows

$$0.792686285 \text{ (total outgoing flux)}$$
$$0.979222171 \text{ (total incoming flux)},$$

and

$$0.802686285 \text{ (total outgoing flux)}$$
$$0.989222171 \text{ (total incoming flux)},$$

for the modes R ranging from 4 to 60 bohr, with 388 grid points. The total outgoing flux should be 1, if there is only one channel and no operators/projectors are applied. This difficulty persists despite these adjustments, suggesting that other factors, such as the symmetries of Wigner functions, may limit the accuracy of the low-energy description by impacting the wave function. when the calculations

Convergence with the SPFs

One of the main advantages of the MCTDH method lies in its variational nature. However, while the primitive basis is fixed for a given calculation, it is necessary to determine an appropriate SPF basis to improve the results by increasing its size. The convergence of the SPF basis can be evaluated in two ways. The first method involves performing several calculations by increasing the number of SPFs and observing the convergence of the transition probability. In scattering calculations, once we achieve convergence with the primitive basis set, we can proceed to refine the convergence of the Single Particle Functions (SPFs). This step-by-step approach ensures that the primitive basis accurately represents the system's fundamental states, allowing the SPFs to capture finer details in the scattering process for more precise results. The second method is to examine the

natural populations of the weakly populated SPFs during propagation and ensure that they remain below a specified tolerance. In our calculations, we obtained values on the order of 10^{-2} and 10^{-3}, which are insufficient to guarantee the accuracy of the results. Figures 4.18a and 4.18b of Figure 4.18 show the population of 25,000 SPFs as a function of time for $J_{tot} = 0$. From these figures, it is evident that the calculations require a large number of SPFs to achieve convergence.In the limit where the number of Single Particle Functions (SPFs) matches the number of primitive basis functions, we achieve a numerically exact calculation. At this exact level, the total flux can be accurately approximated by the energy distribution of the propagated wave function. This ensures that the energy distribution effectively reflects the true dynamics of the system, providing a reliable representation of the scattering process. We use the program **plnat** implemented in the MCTDH package to plot the natural population of the SPFs. A challenge with these collisional calculations is that each propagation requires approximately 16.5 GB of memory to store the wave function and takes around 60 days for propagation. This significant computational cost makes the process slow and memory-intensive. The supercomputer does not have to shut down during the propagation to avoid distorting the propagation time step and creating errors in transition probability calculations. In this case, you just need to submit a new calculation. In figures 4.18a and 4.18b, one can be observed that increasing the number of SPFs does not improve the convergence of the basis compared to the R mode. The convergence following this mode reaches a value of 2.047×10^{-2} for an SPF configuration of $50/50/50$ and 9.047×10^{-3} for $60/60/60$. These values are insufficient to ensure robust convergence, which is necessary before moving on to propagation calculations for angular moments $J > 0$.

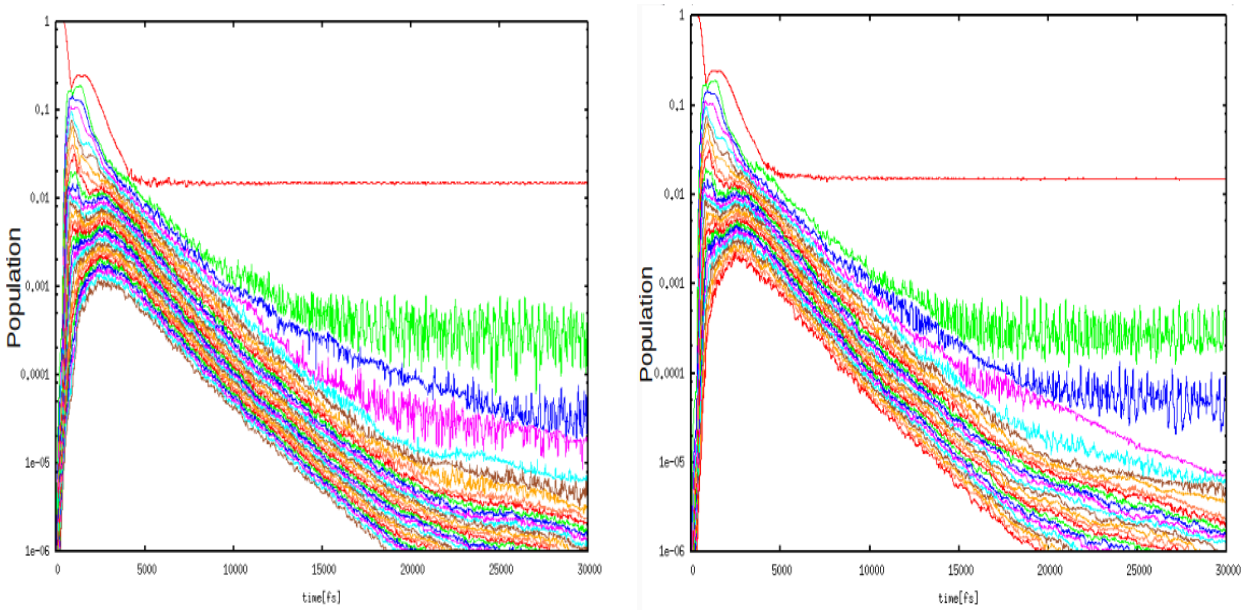

(a) (b)

Figure 4.18: Population of the SPF as a function of time for $J_{tot} = 0$.

4.9 Conclusion

The main goal of this work was to study the rovibrational states and collisional dynamics of the water dimer. To achieve this, I began by outlining the procedures involving symmetry operations to transform the potential energy surfaces (PESs) of the water dimer into a suitable form for conducting MCTDH calculations. The primary objective was to map out the potential energy surface for this system using the MCTDH code. Through meticulous calculations involving the convergence of both primitive and single-particle function (SPF) bases, I successfully determined the zero-point energy (ZPE). These computations provided valuable insights into the challenges and limitations associated with the MCTDH methodology. The ZPE was reported with respect to the number of SPFs, and the results presented here show good agreement with previous literature. Additionally, I presented the initial stages of scattering calculations for two water molecules. While full convergence has not been achieved yet, as shown in Figure 4.17, there is a noticeable difference between the energy distribution function and the flux energy. During wave packet propagation, it is crucial to monitor the calculations closely to prevent unexpected interruptions that could lead to energy loss from the wave function, affecting the accuracy

of the propagation time interval. This disruption would directly impact the calculation of probabilities and cross sections, but the technical issue has been addressed in newer versions of the MCTDH package. I also plan to replicate these calculations using the ML-MCTDH (Multi-Layer Multi-Configuration Time-Dependent Hartree) [237, 238] method by expressing the time-dependent primitive basis functions as a linear combination of multiple layers of time-independent primitive bases. All routines and scripts developed in the course of this work will be made publicly available in a dedicated GitHub repository [1].

[1] https://github.com/MolQuantDynLab-Haverford/MolQuantDynLab-Repository

5. PES and Rovibrational states calculations of the N_2O-CO vdW complex

In this chapter, the spectroscopic properties of the van der Waals N_2O-CO clusters using a newly calculated *ab initio* PES in the rigid rotor approximation will be presented. As one can read in the introduction, CO and N_2O have been long-standing interest molecules in the atmosphere. The N_2O-CO complex can be seen as an ideal system for exploring intermolecular van der Waals interactions in atmospheric chemistry. Understanding the physical and chemical properties of these greenhouse molecules, along with their intermolecular interactions, provides valuable insights for atmospheric and environmental sciences, as well as for applications in industry. These insights deepen our knowledge of molecular behavior in atmospheric conditions, aiding in the modeling of climate processes, the study of environmental impacts, and the development of industrial technologies involving greenhouse gases. However, the N_2O-CO system is relatively new within the MCTDH community, since its potential could not be directly implemented in the standard MCTDH code. As a result, it became essential to propose an alternative method for representing this type of potential. In comparison to the calculations done on the H_2O-HCN system, the N_2O-CO system has a significantly larger reduced mass. This increased reduced mass makes the computational process much harder to converge. This is similar to the challenges faced with the $CO-CO$ [60] system, as recently reported in the literature. To the best of our knowledge, only one published Potential Energy Surface (PES) of Jiang [145] currently exists in the literature with rovibrational state calculations for the N_2O-CO system. Therefore, constructing a new PES provides valuable data for comparison and further evaluation of existing results. In this work, we have developed an *ab initio* PES to gain deeper insights into the structure and dynamics of the N_2O-CO complex. The accuracy of the new PES is evaluated by comparing the theoretical ro-

tational transition frequencies with experimental measurements, allowing us to assess its precision in representing the molecular interactions of this system. In the following sections, the Hamiltonian as well as its kinetic energy operator and the PES for the N_2O-CO system will be discussed. Then the results obtained from this work will be presented comparing to those from a different potential (PES of Jiang [145]) constructed for the study of the same system and with experimental measurements [3].

5.1 Interaction Hamiltonian for the N_2O-CO system

The N_2O and CO monomers are assumed to be in their ground vibrational state and are approximated as linear rigid rotors with N-N, N-O, and C-O bond lengths fixed at their average values, that is, (r_{NN}=1.127 Å and r_{NO}=1.185 Å) [239] and r_{CO}=1.1615 Å [240] as shown in Figure 5.1 where the two linear rigid monomers are labeled as (a) and (b). Their relative geometry is described using the Jacobi coordinate system $\left\{R, \theta_1, \theta_2, \phi\right\}$. Here, R represents the distance between the center of mass of N_2O and CO. The angles θ_1 and θ_2 denote the polar angles, which describe the orientation of the molecular axes of N_2O and CO, respectively, relative to the vector $\vec{R}$, with $R = ||\vec{R}||$. The ϕ is the out-of-plane torsional angle, capturing the rotation of the monomers around the R axis as shown in Figure 5.1.

The rovibrational Hamiltonian for the van der Waals N_2O-CO complex in the Born-Oppenheimer approximation has been used for other type of calculations before [119, 241] and written in the Jacobi coordinates as follows

$$\hat{H} = \hat{T}_a^{rot} + \hat{T}_b^{rot} + \hat{T}_{ab}^{int} + \hat{V}_{int}(R, \theta_1, \theta_2, \phi) \tag{5.1.1}$$

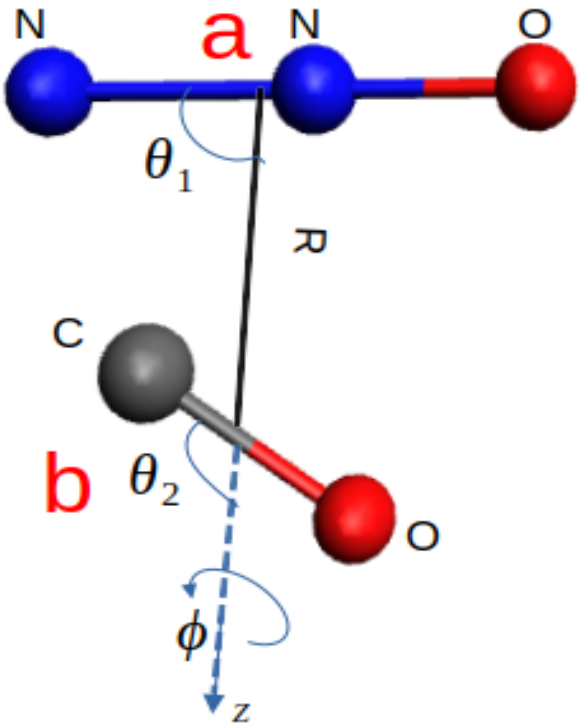

Figure 5.1: Jacobi coordinates for the N_2O-CO complex. The angle ϕ is the out-of-plane torsional angle.

The terms in the Hamiltonian can be defined as follows

$$\hat{T}_{ab}^{int} = \frac{1}{2\mu_{ab}}\Big[\frac{\partial^2}{\partial R^2} + \frac{(\hat{J} - \hat{j}_a - \hat{j}_b)^2}{R^2}\Big] \tag{5.1.2}$$

$$\hat{T}_{a}^{rot} = A_a \hat{j}_a^2 \tag{5.1.3}$$

$$\hat{T}_{b}^{rot} = B_b \hat{j}_b^2 \tag{5.1.4}$$

Here $\hat{T}_{ab}^{int}$ is the internal KEO of the system, $\hat{T}_{x=a,b}^{rot}$ are the rotational KEO of each mononomer, μ_{ab} is the reduced mass of the system, R is the intermolecular distance between the center of mass, B_a and B_b are the rotational constants of N_2O and CO, respectively and $\hat{V}_{int}(R, \theta_1, \theta_2, \phi)$ is the inter-monomer PES used to describe the intermolecular interaction between N_2O and CO. The total kinetic energy operator implemented in the

MCTDH code is expressed as follows [201]

$$\begin{aligned} 2\hat{T} = &-\frac{1}{\mu_{ab}}\frac{\partial^2}{\partial R^2} + (2B_a + \frac{1}{\mu_{ab}R^2})\hat{j}_a^2 + (2B_b + \frac{1}{\mu_{ab}R^2})\hat{j}_b^2 \\ &+ \frac{1}{\mu_{ab}R^2}(\hat{j}_{a+}\hat{j}_{b-} + \hat{j}_{a-}\hat{j}_{b+} + J(J+1) - 2k_a^2 - 2k_b^2 - 2k_ak_b) \\ &- \frac{C_+(J,k_a+k_b)}{\mu_{ab}R^2}\left(\hat{j}_{a+} + \hat{j}_{b+}\right) - \frac{C_-(J,k_a+k_b)}{\mu_{ab}R^2}\left(\hat{j}_{a-} + \hat{j}_{b-}\right) \end{aligned} \tag{5.1.5}$$

Where

$$\hat{j}_a^2 = -\frac{1}{\sin\theta_1}\frac{\partial}{\partial\theta_1}\sin\theta_1\frac{\partial}{\partial\theta_1} + \frac{k_a}{\sin^2\theta_1}, \tag{5.1.6}$$

$$\hat{j}_b^2 = -\frac{1}{\sin\theta_2}\frac{\partial}{\partial\theta_2}\sin\theta_2\frac{\partial}{\partial\theta_2} + \frac{k_b}{\sin^2\theta_2} \tag{5.1.7}$$

and

$$\hat{j}_{a\pm} = \pm\frac{\partial}{\partial\theta_1} - k_a\cot\theta_1, \tag{5.1.8}$$

$$\hat{j}_{b\pm} = \pm\frac{\partial}{\partial\theta_2} - k_b\cot\theta_2, \tag{5.1.9}$$

with

$$C_\pm(J,K) = \sqrt{(J(J+1) - K(K\pm1)}. \tag{5.1.10}$$

With an additional shift $k \to k \pm 1$ in equations (5.1.8) and (5.1.9) to lower or raise the magnetic quantum number. In equation (5.1.5), J is the total angular momentum, and K its projection on internuclear z-axis of the system. $\hat{j}_a$ and $\hat{j}_b$ refer to the angular momenta of the monomers N_2O and CO; k_a and k_b are the projections of the monomers's angular momenta on the body-fixed (BF) frame.

We used the masses of the N_2O-CO as follows: 1.0 AMU for H, 12.0 AMU for C, 15.99491461959 AMU for O and 14.0030740048 AMU for N, and the rotational constants are $B_a = 0.419011\ cm^{-1}$ and $B_b = 1.922528\ cm^{-1}$ [242, 60]. The potential $V(R,\theta_1,\theta_2,\phi)$ needs to be implemented in the MCTDH package in order to run simulations.

5.2 N_2O-CO Potential

The potential energy surface (PES) used in the calculation was calculated in Richard Dawes' group at Missouri CST using the Coupled-Cluster with Single, Double, and Perturbative Triple excitations [CCSD(T)]-F12b level [243, 244]. The calculations were performed with the CVnZ-F12 [245, 243] basis set. The recently developed PES by Jiang [145] used the [CCSD(T)]-F12a [246, 247] level with the aug-cc-pVTZ basis set [248, 249] and included 30,000 randomly selected *ab initio* points. We found that the PES exhibits two minima, corresponding to different stable configurations of the N_2O-CO complex. These minima represent local energy troughs where the system is most stable, and they provide insight into the preferred geometries and interaction potentials of the complex as shown in Figure 5.1. The interaction potential, $V(R,\theta_1,\theta_2,\phi)$ was calculated using the following expression [250]

$$V(R,\theta_1,\theta_2,\phi) = E_{\mathrm{N_2O-CO}}(R,\theta_1,\theta_2,\phi) - E_{\mathrm{N_2O}}(R,\theta_1,\theta_2,\phi) - E_{\mathrm{CO}}(R,\theta_1,\theta_2,\phi) \quad (5.2.1)$$

Where $E_{\mathrm{N_2O-CO}}(R,\theta_1,\theta_2,\phi)$ is the total electron energy of the whole system, and $E_{\mathrm{N_2O}}(R,\theta_1,\theta_2,\phi)$ and $E_{\mathrm{CO}}(R,\theta_1,\theta_2,\phi)$ are the electronic energies of monomer N_2O and CO, respectively.

To derive analytical representation of the N_2O-CO *ab initio* PES we use contracted normalized bispherical harmonics [251] (Equation 5.2.2) as follows:

$$V(R,\theta_1,\theta_2,\phi) = \sum_{l_a l_b l} v_{l_a l_b l}(R) A_{l_a l_b}(\theta_1,\theta_2,\phi), \quad (5.2.2)$$

where the basis functions $A_{l_a l_b}(\theta_1,\theta_2,\phi)$ are written as

$$A_{l_a l_b l}(\theta_1,\theta_2,\phi) = \sum_{m_a=0}^{\min(l_a,l_b)} \gamma_i \frac{\epsilon i}{(1+\delta_{m_a})} \begin{pmatrix} l_a & l_b & l \\ m_a & -m_a & 0 \end{pmatrix} \times P_{l_a m_a}(\theta_1) \times P_{l_b m_a}(\theta_2) cos(m_a \phi), \quad (5.2.3)$$

with

$$\gamma_i = 2(-1)^{m_a}(\frac{2l_a+1}{2\pi})\frac{1}{\sqrt{4\pi}}(-1)^{(l_a+l_b)}, \tag{5.2.4}$$

and

$$\epsilon_i = \frac{\sqrt{(2l_a+1)(l_b+1)}}{2}\sqrt{\frac{(l_a-m_a)!(l_b-m_a)!}{(l_a+m_a)!(l_b+m_a)!}}, \tag{5.2.5}$$

where, P_{lm} is an associated Legendre polynomial and $\langle \cdots | \cdots \rangle$ is a Clebsh-Gordan coefficient. The angles ϕ can be decoupled in order to describe each monomer such as $\phi = (\phi_a - \phi_b)$. The rotational motion of N_2O and CO are l_a and l_b respectively. The expression in large brackets is a Wigner 3-*j* symbol matrix, and $l = |l_a - l_b|, ..., l_a + l_b$.

The global minimum was identified in a configuration where the carbon atom of the CO molecule is directed toward the moiety of the N_2O molecule, with an energy of approximately -409.57 cm^{-1} and an intermolecular separation of 7.17 bohr. When compared to the global minimum reported by Jiang $et\ al.$ [145], which had an energy of -411.58 cm^{-1}, the potential well calculated in this study is slightly higher. A second minimum was found in a geometry where the oxygen atom of the CO molecule approaches the moiety of the N_2O molecule. It should be noted that the configuration considered in the study by Jiang $et\ al.$ [145] corresponds to the $CO-N_2O$ system. The distance between the oxygen of CO and the N_2O was determined to be 6.65 bohr, with an energy of -306.71 cm^{-1}. This differs from Jiang $et\ al.$ [145] second minimum, where the energy was reported as -302.00 cm^{-1}, showing that our calculated interaction energy is slightly lower. These discrepancies between the two potential energy surfaces may stem from differences in the ab initio methods employed in the calculations.

Table 5.1: Equilibrium position of the N_2O-CO for the first PES

		R(bohr)	$\theta_1(\circ)$	$\theta_2(\circ)$	$\phi(\circ)$	V(cm^{-1})
This work	Global min	7.17	82.36	12.67	0	409.57
This work	Local min	6.55	82.03	154.6	180	302.00
Jiang *et al.* [145]	Global min	7.23	82.7	167.8	0.00	411.58
Jiang *et al.* [145]	Local min	6.55	82.1	25.4	180	308.68

5.3 Representation of the potential energy surface

As the MCTDH method dictates, to make a calculation, the potential must be in the SOP form. While adding code for a new PES into the MCTDH program package is generally straightforward, there are cases where it is preferable to use an existing PES routine to generate a related PES. In such cases, we can reduce the PES's dimensionality by creating an effective potential, which is derived from the full-dimensional PES by averaging over specific Degrees of Freedom (DOFs) and then applying a Fourier transform on the angular DOFs. This can be achieved using the projection program.

The projection program takes a potential $V(q_1, \cdots, q_m)$ from an existing PES routine and removes selected DOFs $(q_1, \cdots, q_p)$ by integrating over them with specific projection functions $\chi_k(q_k)$ as shown in equation 5.3.1. This process produces a reduced $(m-p)$-dimensional projected potential.

$$V_{\text{proj}}(q_{p+1}, \cdots, q_m) = \int dq_1 \cdots dq_p \chi_1(q_1) \cdots \chi_p(q_p) V(q_1, \cdots, q_m), \tag{5.3.1}$$

Numerically, this is done by evaluating both the PES and the projection functions on DVR grid points $x_{\alpha_k}^{(k)}$ and using DVR weights $\omega\alpha_k{}^{(k)}$ as shown in equation 5.3.2.

$$V_{\text{proj}}(x_{\alpha_{p+1}}^{p+1}, \cdots, x_{\alpha_m}^{m}) = \sum_{\alpha_1} \cdots \sum_{\alpha_p} \omega_{\alpha_1}^{(1)} \chi_1(x_{\alpha_1}^{(1)}) \cdots \omega_{\alpha_p}^{(p)} \chi_p(x_{\alpha_p}^{(p)}) V(x_{\alpha_1}^{(1)}, \cdots, x_{\alpha_m}^{(m)}) \tag{5.3.2}$$

The program stores the resulting projected potential V_{proj} as a **vpot** file, which can then be processed through a subsequent POTFIT run.

During the projection process, the first p DOFs are removed, allowing any DVR basis to be chosen for these DOFs. However, the remaining $(m-p)$ DOFs must use a DVR basis that matches the one required for the later POTFIT step.

This projecting method was used by Gatti [162] to simulate the inelastic collision of *para*-H_2 and *para*-H_2, and by Ndengue [60] to compute the inelastic cross sections of the rigid rotor CO−CO system using the E_2 reference in the rigid rotor approximation and it is repeated in this work for the N_2O−CO PES.

Table 5.2 contains the parameters used for the projection run, POTFIT and the rovibrational states calculations. Table 5.2 also presents the integrators and integration scheme use for the relaxation process. For the polar angles θ_1 and θ_2, we employed the extended Legendre DVR, while K represents the conjugate momenta associated with the two torsional angles ϕ_1 and ϕ_1 .

Table 5.2: Parameters used for the rovibrational calculations of N_2O−CO. FFT stands for the Fast Fourier Transform DVR, KLeg is the extended Legendre DVR, K stands for the momentum representation of the ϕ_1 and ϕ_2. The units for distance and angle are bohrs and radians respectively. CMF is the Constant Mean Field integrator scheme, RK8 is the Runge-Kutta procedure of order 8, and DAV is the Davidson integrator.

Coordinate	Primitive Basis	Number of Points	Range	Size of SPF basis
R	FFT	96	5.0–12.0	8–10
θ_1	KLeg	51	0–π	10–90
ϕ_1	K	25	-12,12	
θ_2	KLeg	45	0–π	10–60
ϕ_2	K	23	-11,11	
Integrator	Scheme	A-vector	SPF	
Type	CMF	DAV	RK8	
Time step	0.25	0.1	800	
Accuracy	10^{-6}	10^{-7}	10^{-7}	

The DVRs used during the projection step must be consistent with those applied in the subsequent POTFIT procedure and quantum calculations to ensure accuracy. However, an exception can be made for the torsional angles ϕ_1 and ϕ_2, where the DVR grid can be adjusted specifically within the POTFIT algorithm without affecting the overall consistency

of the calculations.

The PES in equation 5.2.2 is given in the rigid rotor approximation as follows:

$$V(R, \theta_1, \theta_2, \varphi_1^{BF}) \tag{5.3.3}$$

with $\varphi_1^{BF} = \phi_1 - \phi_2$.

The PES used is fitted with the POTFIT procedure after replacing φ_1^{BF} by a momentum variable Ω

$$\tilde{V}_\Omega(R, \theta_1, \theta_2, \varphi_1^{BF}) = (2\pi)^{-1} \int_0^{2\pi} e^{-\imath\Omega\varphi_1^{BF}} V(R, \theta_1, \theta_2, \varphi_1^{BF})\, d\varphi_1^{BF} \tag{5.3.4}$$

or

$$\begin{aligned} V(R, \theta_1, \theta_2, \varphi_1^{BF}) &= \sum_\Omega \tilde{V}_\Omega(R, \theta_1, \theta_2) \times e^{\imath\Omega\varphi_1^{BF}} \\ &= \sum_\Omega \tilde{V}_\Omega(R, \theta_1, \theta_2) \times e^{\imath\Omega\phi_1^{E_2}} e^{-\imath\Omega\phi_2^{E_2}} \end{aligned} \tag{5.3.5}$$

because $\varphi_1^{BF} = \phi_1^{E_2} - \phi_2^{E_2}$ as shown in Figure 5.2. The action of the potential on the wave function then writes

$$\begin{aligned} &(\tilde{V}\Psi)(R, \theta_1, k_1, \theta_2, k_2) \\ &= \sum_\Omega \tilde{V}_\Omega(R, \theta_1, k_1, \theta_2, k_2) \times \Psi(R, \theta_1, k_1 - \Omega, \theta_2, k_2 + \Omega) \end{aligned} \tag{5.3.6}$$

The best representation of the potential was achieved by making projections for positive Ω values, ranging from 0 to 14. Several convergence tests were carried out according to the Ω value and already at 4, our calculations converged and for good accuracy on the calculation, we considered the values of $\Omega = 0, ..., 7$. Like we do for MCTDH calculation,

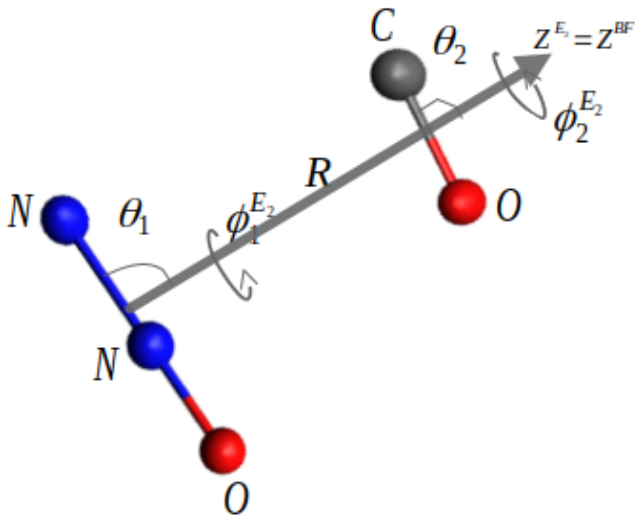

Figure 5.2: Jacobi Coordinate system used to represent the PES implemented in the MCTDH.

we conducted convergence tests on the primitive basis and the SPFs basis. One of the issue with this projecting method is that if it is necessary to change this primitive basis chosen for a calculation, another projection calculation will need to be redone. The initial potential is expressed in Jacobi coordinates (R,θ_1, θ_2,φ_1^{BF})) and a Fourier transform is applied to have the potential in the appropriate by adjusting the function $\tilde{V}_\Omega(R,\theta_1,\theta_2)$, for $\Omega = 0,...,7$ and using the POTFIT algorithm. Table 5.2 presents the primitive basis with the mean error in the projection of potential of 0.3644 cm^{-1}. The errors obtained during the sum of product fit of the PES are $\tilde{V}_\Omega(R,\theta_1,\theta_2)$ (mev), the weights $\Omega = 0,...,7$ are 0.0125 , 0.0128, 0.0062, 0.0035, 0.0023, 0.0013, 0.0013, and 0.0008 meV. In Figures 5.3: Figures 5.3a- 5.3c illustrate the contour lines of the natural potential adjusted by the POTFIT algorithm at the value of $\Omega = 0$, as well as the projected potential. These visualizations allow for a visual comparison of the quality of the fit between the two potentials. The obtained fit has a maximum error of 10^{-7} cm^{-1} and the RMSE of 0.1536 cm^{-1}, indicating a very high agreement between the adjusted potential and the projected potential. The colored areas in Figure 5.3c highlight where the fitting error is most significant. These regions correspond to locations in the variable space where the PES exhibits less regularity, making the fitting more complex.

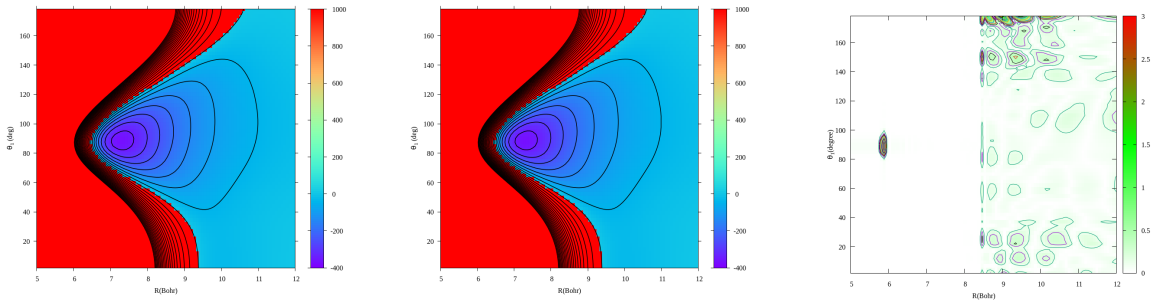

(a) (b) (c)

Figure 5.3: Contour plots for $\Omega = 0$ at $\theta_2 = 12.67°$: Figure 5.3a is the natural PES, Figure 5.3b is the projected PES, and Figure 5.3c is the absolute error between the natural PES and projected PES.

5.4 Rovibrational state energy levels

This section focuses on the results obtained by applying the MCTDH method to study the rovibrational states of the N_2O-CO system with a potential represented using the projection method. The rovibrational energy levels are calculated for the values of the total angular momentum J from 0 to 3. We first present the calculations of the vibrational states by setting the total angular momentum value to 0. We proceeded with calculations by propagating four wave packets, and for a given primitive basis and SPF as shown in Table 5.2, the calculation takes approximately 4 days. One of the main factors contributing to the very high computation time is the large dimension of the basis functions used in this work. As shown in Table 5.2, the size of the basis for θ_1 and θ_2 required for convergence is 51 and 45, respectively. The rovibrational states are reported in Tables 5.4–5.6 compared with the available results in the literature. For these calculations, most of the recorded states are indeed non-physical. These states arise from the relaxation of constraints imposed on the calculations and are not due to the block-improved relaxation method. Therefore, if calculations using other methods also relax constraints as we did here, one should expect to observe the same non-physical states. The physical states output from the rovibrational calculations obey several constraints, including $K = m_A + m_B \leq J$. Since this constraint cannot be enforced in the MCTDH calculation as Wang and Carrington [62] could do, we are generating states that obey all constraints except

that specific one. Consequently, we obtain states that violate that constraint and the known physics of the problem, which are labeled as non-physical states. This is the same procedure used for the H_2O-HCN work, where the characters Σ, Π, ... of the wave function are determined and extracted after performing a propagation of a single wave packet once the calculation is completed.

The ground state energy for the $J = 0$ state of the N_2O-CO complex is found to be -297.367 cm^{-1} in this work. When compared to the value reported by Jiang $et\ al.$ [145], which was -299.6052 cm^{-1}, the energy calculated here is slightly higher. The zero-point energy (ZPE) obtained in this study is approximately 112.203 cm^{-1}. In comparison with the work of Jiang [145], the reported ZPE is 111.973 cm^{-1}, making the ZPE calculated in this work slightly lower. These differences in both the bound state energy and the ZPE could be attributed to the different computational methods employed in the two studies. According to reference [252], the vibrational states are classified into modes of in-plane disrotation, out-of-plane torsion, dissociation, and in-plane conrotation. In Table 5.3 the first intermolecular excited state corresponds to the in-plane disrotation mode, with a frequency of 24.8734 cm^{-1}, as calculated in this study. This is in good agreement with the value of 24.9488 cm^{-1} reported by Jiang $et\ al.$ [145], indicating that our PES provides a reliable prediction of bound states. The second excited state is associated with the out-of-plane torsion mode, for which this work predicts a frequency of 40.9548 cm^{-1}, closely matching the 40.898 cm^{-1} value reported by Jiang $et\ al.$ [145]. The third excited state, characterized by two nodes in the θ_1 coordinate of the wave function, can be interpreted as the second excitation of the in-plane disrotation mode, with a frequency approximately twice that of the first in-plane disrotation. The fourth excited state corresponds to the dissociation mode, with a frequency of 52.8774 cm^{-1}, compared to the 52.6551 cm^{-1} reported by Jiang $et\ al.$ [145]. The first in-plane conrotation mode occurs at the sixth intermolecular excited state, yielding a frequency of 66.45 cm^{-1}, which is consistent with the 66.5211 cm^{-1} reported by Jiang $et\ al.$ [145]. At higher excitation levels, the vibrational modes may become highly mixed, making mode assignment more challenging.

We further extended the calculations to determine the rovibrational levels for $J = 0, 1, 2, 3,$

Table 5.3: Harmonic and variational intermolecular frequencies reported by Jiang [145] and the MCTDH results correspond to those obtained in this work at $J = 0$. All energies are in cm^{-1}.

Mode	MCTDH	Jiang [145]
ν_1 (disrotation mode)	24.8734	24.9488
ν_2 (torsion mode)	40.9548	40.898
ν_3 (dissociation mode)	52.8774	52.6551
ν_4 (conrotation mode)	66.450	66.5211
ZPE*	112.203	111.973

as presented in Tables 5.4– 5.7. The results show a strong agreement between the values obtained in this study and those reported by Jiang $et\ al.$ [145]. The rovibrational energy levels of the N_2O-CO complex are characterized using the asymmetric top quantum numbers $J_{K_aK_b}$, where J represents the total angular momentum of the system, and k_a and k_b denote the projections of J onto the a- and c-axes in the principal axes of inertia.

Table 5.4: The N_2O-CO vibrational energy levels for $J = 0$. With the ZPE=112.203 cm, energies are relative to the dissociation energy -297.367 cm^{-1}. The units are given in cm^{-1}.

N	**Assignment**	**MCTDH**	Theo [145]
0	$\Sigma(K=0)$	0.00	0.00
1	$\Sigma(K=0)$	24.8734	24.9488
2	$\Sigma(K=0)$	40.9548	40.9000
3	$\Sigma(K=0)$	49.1829	49.1858
4	$\Sigma(K=0)$	52.7670	52.6551
5	$\Sigma(K=0)$	65.5236	65.5027
6	$\Sigma(K=0)$	66.4500	66.5211
7	$\Sigma(K=0)$	72.3879	72.3886
8	$\Sigma(K=0)$	72.8325	72.8527
9	$\Sigma(K=0)$	78.4051	78.5800

Table 5.5: Same as Table 5.4 for $J = 1$.

J$_{k_ak_c}$	**Assignment**	**This work**	Theory [145]
1_{01}	$\Sigma(K=0)$	0.1192	0.1190
1_{11}	$\Sigma(K=0)$	0.4846	0.4839
1_{10}	$\Sigma(K=0)$	0.4932	0.4925

Table 5.6: Same as Table 5.4 for $J = 2$.

$J_{k_a k_c}$	Assignment	This work	Theory [145]
2_{02}	$\Sigma(K=0)$	0.3574	0.3570
2_{12}	$\Sigma(K=0)$	0.7143	0.7133
2_{11}	$\Sigma(K=0)$	0.7402	0.7391
2_{21}	$\Gamma(K=2)$	1.8366	1.8343
2_{20}	$\Gamma(K=2)$	1.8368	1.8344

Table 5.7: Same as Table 5.4 for $J = 3$.

$J_{k_a k_c}$	Assignment	This work	Theory [145]
3_{03}	$\Sigma(K=0)$	0.7143	0.7135
3_{13}	$\Sigma(K=0)$	1.0587	1.0573
3_{12}	$\Sigma(K=0)$	1.1105	1.1090
3_{22}	$\Gamma(K=2)$	2.1939	2.1911
3_{21}	$\Gamma(K=2)$	2.1946	2.1919
3_{31}	$\Delta(K=3)$	4.0426	4.0374
3_{30}	$\Delta(K=3)$	4.0425	4.0374
3_{22}	$\Delta(K=3)$	6.6058	–
3_{21}	$\Delta(K=3)$	6.6069	—

5.5 Transition frequencies and Rotational constants

In this section, 25 pure rotational transitions for the N_2O-CO complex in its ground state are summarized in Table 5.8, which also includes the deviations from the values reported by Jiang $et\ al.$ [145] as well as the observed rotational transition frequencies. As shown in Table 5.8, the calculated microwave transition frequencies closely match both theoretical and experimental data. The deviations calculated for the transitions observed [3] in this work are around 0.0005 cm^{-1}. When compared to the deviations reported by Jiang $et\ al.$ [145], which are in the range of 0.0004 cm^{-1}, it is evident that the potentials derived in this work provide a reliable basis for calculating transition frequencies.

We extracted the rotational constants from the transition frequencies using the formulas from ref. [253]: $1_{01} = B + C$, $1_{11} = A + C$, and $1_{10} = A + B$

Table 5.8: Rotational $j_{K_aK_c}$ transition frequencies of N_2O-CO; (Exp) [3]. The unit is given in cm^{-1}.

Transition	This work (Cal)	Theo [145]	Exp [3]	Cal - Exp	Theo - Exp
$1_{11} \leftarrow 0_{00}$	0.48463	0.4839	0.4842	0.00043	-0.0003
$1_{10} \leftarrow 1_{01}$	0.374086	0.3734	0.3738	0.000286	-0.0004
$2_{02} \leftarrow 1_{01}$	0.238213	0.2379	0.238	0.000213	-0.0001
$2_{12} \leftarrow 1_{11}$	0.229679	0.2294	0.2295	0.000179	-0.0001
$2_{11} \leftarrow 1_{10}$	0.246954	0.2467	0.2468	0.000154	-0.0001
$2_{12} \leftarrow 1_01$	0.595124	0.5942	0.5946	0.000524	-0.0004
$2_{11} \leftarrow 2_02$	0.382827	0.3822	0.3825	0.000327	-0.0003
$3_{03} \leftarrow 2_{02}$	0.356927	0.3565	0.3566	0.000327	-0.0001
$3_{13} \leftarrow 2_{12}$	0.344413	0.344	0.3441	0.000313	-0.0001
$3_{12} \leftarrow 2_{11}$	0.370318	0.3699	0.3700	0.000318	-0.0001
$3_{12} \leftarrow 3_{03}$	0.396218	0.3955	0.3959	0.000318	-0.0004
$3_{22} \leftarrow 2_{21}$	0.357385	0.3568	0.3569	0.000485	-0.0001
$3_{21} \leftarrow 2_{20}$	0.357994	0.3574	0.3575	0.000494	-0.0001
$3_{22} \leftarrow 4_{13}$	0.589858	0.5891	0.589	0.000858	0.0001
$4_{04} \leftarrow 3_{03}$	0.47517	0.4746	0.4748	0.00037	-0.0002
$4_{14} \leftarrow 3_{13}$	0.459019	0.4585	0.4586	0.000419	-0.0001
$4_{13} \leftarrow 3_{12}$	0.493537	0.4929	0.4931	0.000437	-0.0002
$4_{23} \leftarrow 3_{22}$	0.476186	0.4756	0.4758	0.000386	-0.0002
$4_{22} \leftarrow 3_{21}$	0.477686	0.4771	0.4772	0.000486	-0.0001
$4_{13} \leftarrow 4_{04}$	0.414585	0.4139	0.4142	0.000385	-0.0003
$5_{05} \leftarrow 4_{04}$	0.592794	0.5921	0.5923	0.000494	-0.0002
$5_{15} \leftarrow 4_{14}$	0.573467	0.5728	0.5730	0.000467	-0.0002
$5_{14} \leftarrow 4_{13}$	0.616583	0.6158	0.6161	0.000483	-0.0003
$5_{05} \leftarrow 4_{14}$	0.264548	0.2644	0.2643	0.000248	0.0001
$5_{14} \leftarrow 5_{05}$	0.438374	0.4376	0.4380	0.000374	-0.0004

The asymmetry of the N_2O-CO system was determined by calculating the asymmetry parameter k defined as $k = (\frac{A-C-2B}{C-A})$, which was found to be $k = -0.9534$. This indicates that the system can be considered a near-asymmetric prolate top, as the parameter is close to -1. The results show strong agreement between the values calculated in this work, those reported by Jiang $et\ al.$ [145], and experimental data. The close match between the predicted transition frequencies and rotational constants with the observed [3] values and the data from Jiang $et\ al.$ [145]. demonstrates that the potential energy surface (PES) used in this study for the N_2O-CO system is highly accurate.

The information on the dynamics of the N_2O-CO complex generally comes from the

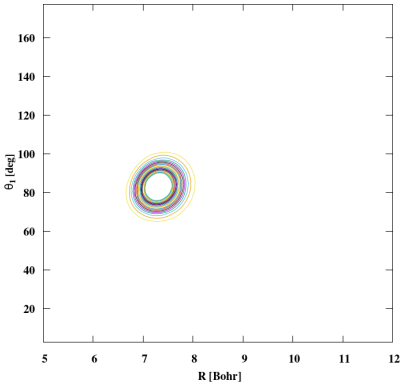

Figure 5.4: Probability densities plot as a function of $(R,\ \theta_1)$ of N_2O-CO at $E = 0.0$ cm^{-1}

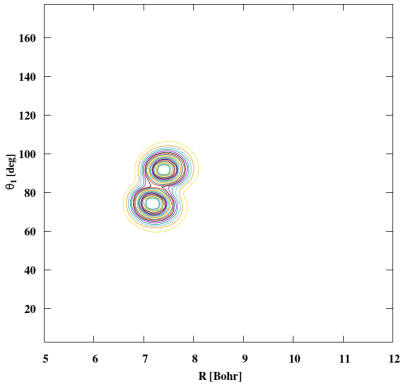

Figure 5.5: Probability densities plot as a function of $(R,\ \theta_1)$ of N_2O-CO at $E = 24.8734$ cm^{-1}

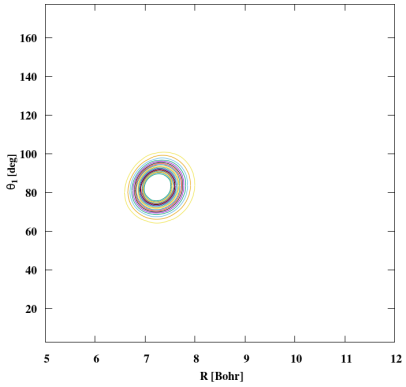

Figure 5.6: Probability densities plot as a function of $(R,\ \theta_1)$ of N_2O-CO at $E = 40.9548$ cm^{-1}

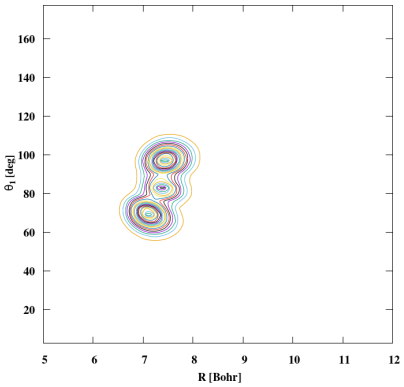

Figure 5.7: Probability densities plot as function of $(R,\ \theta_1)$ of N_2O-CO at $E = 49.1825$ cm^{-1}

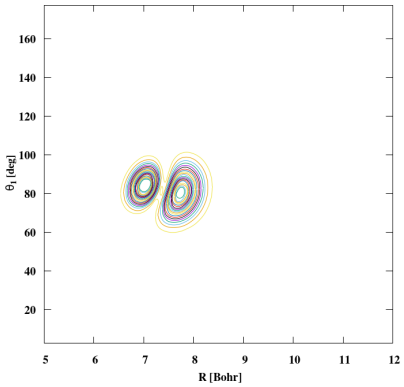

Figure 5.8: Probability densities plot as a function of $(R,\ \theta_1)$ of N_2O-CO at $E = 52.8774$ cm^{-1}

Table 5.9: Calculated rotational constants of N_2O-CO using MCTDH, compared with previous theoretical (theo) and experimental (exp) results. The units are given in cm^{-1}.

Rot. Const.	This work (Cal)	Theo [145]	Exp [3]	Cal - Exp	Theo - Exp
A	0.4293	0.4287	0.4290	0.0003	-0.0001
B	0.0639	0.0638	0.0638	0.0001	0.0000
C	0.0552	0.0552	0.0552	0.0000	0.0000

behavior of the probability density of the wave function of each vibrational level. To better analyze these levels, the cuts of these densities along the intermolecular distance R and the angle θ_1 have been displayed. For the ground state (5.4), it is generally nodeless, reflecting the localization of the wave function at the global minimum. For the first excitation corresponding to the second excited state, in the coordinate ϕ, (5.6) shows no nodes along the other three directions. The wave function cuts for the first and third excited states exhibit one and two nodes in θ_1, respectively, as shown in Figures 5.5 and 5.7. The wave function for the third excited state extends over a slightly larger range of the coordinate θ_1. In Figure 5.8, the plot of the wave function of the fourth excited state reveals a clear node along the R direction. I find that several wave functions are localized around the global minimum, which is due to the depth of the potential existing between the two minima, which is around -196 cm^{-1}.

5.6 Conclusion

In this work, the main goal was to represent the potential energy surface of the N_2O-CO system in the MCTDH package to carry out calculations of the spectroscopic properties. I used the projection method implemented in MCTDH to represent the PES for N_2O-CO, which is not in the form of a product. I calculated the rovibrational states, transition frequencies, and rotational constants. The results I have obtained are in good agreement with the theoretical results reported by Jiang $et\ al.$ [145], who used a new PES for the same system and experimental data available in the literature. This demonstrates that the PES used in this work is highly accurate and can effectively describe the spectrum of the N_2O-CO system. The potential, implemented by the projection method, requires

a large basis to ensure optimal accuracy. While the MCTDH method has previously been employed to calculate the rovibrational states of various molecular clusters, this study presents the first application of the MCTDH approach specifically geared towards generating a database of spectroscopic properties of these clusters that are directly relevant to atmospheric chemistry. This new application provides a foundation for future research directions. Moving forward, we intend to extend this approach to additional molecular systems and to refine several aspects of the current work. For instance, the present study focuses solely on the rovibrational states in proximity to the global minimum (C-bound configuration). In future work, we aim to compute the rovibrational states of an O-bound configuration by reorienting the CO moiety, thereby exploring the local minimum. Another important extension will be to expand the range of intermolecular distances analyzed here, enabling the study of collisional dynamics between N_2O and CO at large distances for astronomical and astrophysical applications.

6. Conclusion and Perspectives

During this thesis work, we addressed several questions related to the quantum dynamics of van der Waals molecular clusters. A presentation of the different concepts necessary for the study of such systems allowed us, first of all, to describe the various approaches to represent the potential energy surface in the MCTDH code. Then, the examination of the MCTDH wave packet propagation method highlighted the advantages that time-dependent methods bring to numerical calculations, especially for the accuracy and efficiency of the dynamic treatment of these systems. The purpose was to use the potential energy surfaces representation to compute the rovibrational state energy levels and start a preliminary stage of collisional dynamics calculations using the MultiConfiguration Time-Dependent Hartree (MCTDH) method [172, 173, 174, 148].

From a methodological point of view, significant progress was made during this thesis regarding the representation of potential energy surfaces for systems with a large number of degrees of freedom, as well as spectroscopic and collision calculations. Several molecular clusters were studied in this work to assess of seeing the capabilities and limitations of the MCTDH code in bridging the gap between the traditional POTFIT method of surface implementation for small systems and those for large systems. Additionally, we have provided the astrochemical and astrophysical community with a substantial database. Now, we will provide a summary of every project presented in this work.

- $\mathbf{H_2O-HCN}$ cluster: An accurate description of this cluster is key to better understanding the phenomenon of HCN isomerization in cometary atmospheres. The algorithm we have developed to automatically generate the potential of this type of system represents a major contribution to the MCTDH community. This tool will automate the process of generating potentials, optimizing the time and resources required for the study of multi-degree-of-freedom systems, and facilitating the application of the MCTDH method to a wider variety of complex systems. We have determined the spectroscopic properties for the H_2O-HCN system using the MCTDH code. The 5D rigid rotor multipolar potential energy surface constructed

by Ernesto and Dubernet [210] has been used and implemented in the MCTDH code. The rovibrational states of *para*-H_2O-HCN and *ortho*-H_2O-HCN have been calculated and analyzed with a newer script to determine the $j_{k_a k_c}$ states. We determined the transition frequencies and the rotational constants. The results obtained were in good agreement with the previous theoretical [120] work with another PES for H_2O-HCN and experimental data [209].

- $\mathbf{H_2O-H_2O}$ cluster: Water is commonly detected in numerous media, including the Earth's atmosphere and the interstellar medium, making it a highly significant system. For such a system, spectroscopic data will be important for analyses conducted through observations. In order to compute the rovibrational states of the water dimer, an approach for representing the rigid rotor CCpol-8s [118] (6D) PES in the MCTDH package was developed. The accuracy of the results obtained was in good agreement with the data available in the literature [63]. Collisional calculations of two water molecules using the potential in its factorized form have also been initiated by introducing some preliminary steps, and the difficulties encountered in achieving convergence have been identified. An increase in the number of SPFs is necessary to achieve convergence, but this poses a challenge as increasing the number of SPFs results in significant memory usage to store the wave function. We have considered using the ML-MCTDH method, although its immediate application is limited to the ground state. However, this approach would first be explored to assess the extent to which calculations can converge.

- $\mathbf{N_2O-CO}$ cluster: This system is significant due to the role of CO as a greenhouse gas and N_2O as a substance that contributes to ozone layer depletion in the stratosphere. A new 4D-PES has been developed to investigate the spectroscopic properties of this system. One challenge we faced is the large size of the primitive basis, which makes the calculations costly due to the projection algorithm used to represent this potential and determine the rotational states, transition frequencies, and rotational constants. Our results closely match the theoretical [145] and experimental data [3] found in the literature. The calculations are intended for use in

astrophysical and atmospheric applications.

The work outlined in this thesis opens up many perspectives for the future.

Building on previous work, we will study the collisions of the H_2O-HCN system by extending the intermolecular distance and calculating the rovibrational states of all its isotopologues. Since we already have a coordinate transformation code and the potential energy surface is available, we will only need to configure the parameters for the scattering calculations.

Another focus of this work will be implementing symmetry of Wigner functions, calculating the rovibrational states of the water dimer beyond the ground state and for angular momentum values greater than zero. Subsequently, we will compute the spectra of the water dimer using the dipole moment under the rigid rotor approximation. Additionally, we will develop a new strategy for implementing the potential energy surface in the MCTDH framework.

Other future objectives include the calculation of the rovibrational states of the N_2O-CO isotopologues and the collision calculations of N_2O-CO. The calculations of the rovibrational states of the isotopologues will be computationally efficient, as we already possess the converged calculations for N_2O-CO. This will allow us to simply read and refine these existing results.

Another future direction of this work will involve calculating rovibrational states and cross sections of the PO^+-H_2 system for non-zero angular momentum values of H_2 ($j = 0$). This will be done using both the 4D and 2D potentials developed by François Lique's group at the University of Rennes, France, which have not been published yet. The spectroscopic calculations will be used to assess the accuracy of this PES representation in collision calculations. We have already conducted calculations of rovibrational states and compared the results with those obtained from another code, as experimental data are not yet available. Additionally, ongoing tests are being conducted on cross sections, and some data are already available in the literature for comparison.

It is essential to provide an overview of the application of MCTDH to small molecular systems. For systems with fewer than four degrees of freedom, the implementation of the potential in MCTDH is typically straightforward, particularly when the traditional POTFIT algorithm is used to obtain an exact potential. These studies are often conducted on a compact basis set, as demonstrated by my initial parallel investigation of the H_2He^+ system at the beginning of my thesis.

Appendix

Transformation of the CCpol-8s multipolar potential energy surface In this section, we describe all the steps involved in transforming the multipolar potential energy surface of the water dimer. The water dimer possesses several symmetry operations which can be used to reduce the multipolar PES. For each symmetry operation, we present the changes in the Euler angles and their impact on the multipolar potential formula.

- The first symmetry operation is the $C_{2\nu}$:

This operation transforms the angles describing each monomer as follows: $\omega_A(\alpha_A, \beta_A, \gamma_A) = \omega_A(\alpha_A, \beta_A, \gamma_A + \pi)$; $\omega_B(\alpha_B, \beta_B, \gamma_B) = \omega_B(\alpha_B, \beta_B, \gamma_B + \pi)$; $\omega(\alpha, \beta)$

In the space-fixed frame, the polar angles $\omega(\alpha, \beta)$ are for the overall rotation of the system with respect to the z-axis.

$$V(R, \omega_A, \omega_B, \omega) = \sum_{\{\Lambda\}} v_{\{\Lambda\}}(R) A_{\{\Lambda\}}(\omega_A, \omega_B, \omega), \tag{.0.1}$$

$$A_\Lambda(\omega_A, \omega_B, \omega) = \sum_{M_A, M_B, M} (-1)^{L_A+L_B+L} \begin{pmatrix} L_A & L_B & L \\ M_A & M_B & M \end{pmatrix} \times D^{L_A}_{M_A K_A}(\omega_A)^* D^{L_B}_{M_B K_B}(\omega_B)^* C^L_M(\alpha, \beta) \tag{.0.2}$$

Here one can switch from space-fixed to body-fixed.

$$
\begin{aligned}
V(R,\omega_A,\omega_B,\omega) = &\sum_{\Lambda} \nu_\Lambda(R) \sum_{M_A,M_B,M} (-1)^{L_A+L_B+L} \begin{pmatrix} L_A & L_B & L \\ M_A & M_B & M \end{pmatrix} \\
&\times D^{L_A}_{M_A K_A}(\alpha_A,\beta_A,\gamma_A)^* D^{L_B}_{M_B K_B}(\alpha_B,\beta_B,\gamma_B+\pi)^* C^L_M(\alpha,\beta) \\
&= \sum_{\Lambda} \nu_\Lambda(R)(-1)^{K_B} \sum_{M_A,M_B,M} (-1)^{L_A+L_B+L} \begin{pmatrix} L_A & L_B & L \\ M_A & M_B & M \\ & & \end{pmatrix} \\
&\times D^{L_A}_{M_A K_A}(\alpha_A,\beta_A,\gamma_A)^* D^{L_B}_{M_B K_B}(\alpha_B,\beta_B,\gamma_B)^* C^L_M(\alpha,\beta)
\end{aligned}
$$

$$
\begin{aligned}
V(R,\omega_A,\omega_B,\omega) = &\sum_{\{\Lambda\}} v_{\{\Lambda\}}(R) \sum_{M_A,M_B,M} (-1)^{L_A+L_B+L} \begin{pmatrix} L_A & L_B & L \\ M_A & M_B & M \end{pmatrix} \\
&\times D^{L_A}_{M_A K_A}(\alpha_A,\beta_A,\pi+\gamma_A)^* D^{L_B}_{M_B K_B}(\alpha_B,\beta_B,\gamma_B)^* C^L_M(\alpha,\beta) \\
&= \sum_{\{\Lambda\}} v_{\{\Lambda\}}(R)(-1)^{K_A} \sum_{M_A,M_B,M} (-1)^{L_A+L_B+L} \begin{pmatrix} L_A & L_B & L \\ M_A & M_B & M \end{pmatrix} \\
&\times D^{L_A}_{M_A K_A}(\alpha_A,\beta_A,\gamma_A)^* D^{L_B}_{M_B K_B}(\alpha_B,\beta_B,\gamma_B)^* C^L_M(\alpha,\beta) \qquad (.0.4)
\end{aligned}
$$

The potential remains the same, so in body-fixed frame, $(\alpha,\beta) = (0,0)$ and $M = M_A + M_B = 0$, $M_B = -M_A$, $C^L_M(0,0) = \delta_M 0$. So the only worked case is $M = 0$. When we include the transformation of these angles in equation .0.1, we obtain the following equations:

$$
\begin{aligned}
V(R,\omega_A,\omega_B) = &\sum_{\{\Lambda\}} v_{\{\Lambda\}}(R)(-1)^{K_B} \sum_{M_A} (-1)^{L_A+L_B+L} \begin{pmatrix} L_A & L_B & L \\ M_A & -M_A & 0 \end{pmatrix} \\
&\times D^{L_A}_{M_A K_A}(\alpha_A,\beta_A,\gamma_A)^* D^{L_B}_{-M_A K_B}(\alpha_B,\beta_B,\gamma_B)^* \qquad (.0.5)
\end{aligned}
$$

$$V(R,\omega_A,\omega_B) = \sum_{\{\Lambda\}} v_{\{\Lambda\}}(R)(-1)^{K_A} \sum_{M_A} (-1)^{L_A+L_B+L} \begin{pmatrix} L_A & L_B & L \\ M_A & -M_A & 0 \end{pmatrix} \times D^{L_A}_{M_A K_A}(\alpha_A,\beta_A,\gamma_A)^* D^{L_B}_{-M_A K_B}(\alpha_B,\beta_B,\gamma_B)^* \quad (.0.6)$$

The equations obtained by applying $C_{2\nu}$ symmetry to the potential are as follows:

$$\begin{aligned} v_{\{\Lambda\}}(R) &= (-1)^{K_A} v_{\{\Lambda\}}(R), \\ v_{\{\Lambda\}}(R) &= (-1)^{K_B} v_{\{\Lambda\}}(R) \end{aligned} \quad (.0.7)$$

From eqs. .0.7,

$$v_{\{\Lambda\}}(R) = 0, \quad (.0.8)$$

if K_A and/or K_B odd

- The second symmetry operation is the inversion:

This inversion changes the Euler angles as follows:

$$\begin{aligned} \omega_A(\alpha_A,\beta_A,\gamma_A) &= \omega_A(\pi+\alpha_A,\pi-\beta_A,\pi-\gamma_A), \\ \omega_B(\alpha_B,\beta_B,\gamma_B) &= \omega_B(\pi+\alpha_B,\pi-\beta_B,\pi-\gamma_B), \\ \omega(\alpha,\beta) &= \omega(\pi+\alpha,\pi-\beta), \end{aligned} \quad (.0.9)$$

From equation .0.1

$$V(R,\omega_A,\omega_B) = \sum_{\{\Lambda\}} v_{L_A,-K_A,L_B,-K_B,L}(R)(-1)^{L_A+L_B+L} \sum_{M_A} (-1)^{L_A+L_B+L} \begin{pmatrix} L_A & L_B & L \\ M_A & -M_A & 0 \end{pmatrix} \times D^{L_A}_{M_A-K_A}(\alpha_A,\beta_A,\gamma_A)^* D^{L_B}_{-M_A-K_B}(\alpha_B,\beta_B,\gamma_B)^* \quad (.0.10)$$

After applying this symmetry operation, we obtain the following equation:

$$v_{L_A,K_A,L_B,K_B,L}(R) = (-1)^{L_A+L_B+L} v_{L_A,K_A,L_B,K_B,L}(R), \tag{.0.11}$$

- The third symmetry operation is the permutation:

This symmetry operation changes the Euler angles as follows:

$$\begin{aligned} &\omega_A(\alpha_A,\beta_A,\gamma_A) = \omega_B(\alpha_A,\beta_A,\gamma_A), \\ &\omega_B(\alpha_B,\beta_B,\gamma_B) = \omega_A(\alpha_B,\beta_B,\gamma_B), \\ &\omega(\pi+\alpha,\pi-\beta), \end{aligned} \tag{.0.12}$$

Including the angles in equation .0.1, we obtain

$$\begin{aligned} V(R,\omega_A,\omega_B) = &\sum_{\{\Lambda\}} v_{\{\Lambda\}}(R) \sum_{M_A} (-1)^{L_A+L_B+L} \begin{pmatrix} L_B & L_A & L \\ -M_A & M_A & 0 \end{pmatrix} \\ &\times D^{L_A}_{M_A K_A}(\alpha_B,\beta_B,\gamma_B)^* D^{L_B}_{-M_A K_B}(\alpha_A,\beta_A,\gamma_A)^* \\ &= \sum_{\{\Lambda\}} v_{L_B,K_B,L_A,K_A,L}(R)(-1)^{L_A+L_B} \sum_{M_A} (-1)^{L_A+L_B+L} \begin{pmatrix} L_A & L_B & L \\ M_A & -M_A & 0 \end{pmatrix} \\ &\times D^{L_A}_{M_A K_A}(\alpha_B,\beta_B,\gamma_B)^* D^{L_B}_{-M_A K_B}(\alpha_A,\beta_A,\gamma_A)^* \end{aligned} \tag{.0.13}$$

The expansion coefficient can be expressed as follows:

$$v_{L_A,K_A,L_B,K_B,L}(R) = (-1)^{L_A+L_B} v_{L_B,K_B,L_A,K_A,L}(R) \tag{.0.14}$$

Note that I have used the symmetry of Wigner functions.

- Symmetry operation of the Wigner d-functions and matrix *3j*-symbol.

$$d^l_{mk}(\beta) = (-1)^{m-k} d^l_{-m-k}(\beta) = (-1)^{m-k} d^l_{km}(\beta) \tag{.0.15}$$

$$\begin{pmatrix} L_A & L_B & L \\ M_A & -M_A & 0 \end{pmatrix} = (-1)^{L_A+L_B+L} \begin{pmatrix} L_B & L_A & L \\ M_A & -M_A & 0 \end{pmatrix} = (-1)^{L_A+L_B+L} \begin{pmatrix} L_A & L_B & L \\ -M_A & M_A & 0 \end{pmatrix} \tag{.0.16}$$

In the body-fixed coordinates:

$$V(R,\omega_A,\omega_B) = \sum_{\{\Lambda\}} v_{\{\Lambda\}}(R) \sum_{M_A} (-1)^{L_A+L_B+L} \begin{pmatrix} L_B & L_A & L \\ M_A & -M_A & 0 \end{pmatrix} \times D^{L_A}_{M_A K_A}(\omega_A)^* D^{L_B}_{-M_A K_B}(\omega_B)^* \tag{.0.17}$$

$$\begin{pmatrix} L_B & L_A & L \\ 0 & 0 & 0 \end{pmatrix} \neq 0 \tag{.0.18}$$

if $L_A + L_B + L$ even and as shown above,

$$v_{L_A,K_A,L_B,K_B,L}(R) = (-1)^{L_A+L_B+L} v_{L_A,K_A,L_B,K_B,L}(R) \tag{.0.19}$$

Combining these symmetry conditions, one can find that the PES can be re-written as follows:

$$
\begin{aligned}
V(R,\omega_A,\omega_B) = & \sum_{L_A L_B L} \sum_{M_A=0}^{L_A} \sum_{K_A=0}^{L_A} \sum_{K_B=0}^{L_B} (-1)^{L_A+L_B+L} \begin{pmatrix} L_B & L_A & L \\ M_A & -M_A & 0 \end{pmatrix} \\
& \times \frac{2}{\big(1+\delta_{M_A 0}\big)\big(1+\delta_{K_A 0}\big)\big(1+\delta_{K_B 0}\big)} \\
& \times \Bigg[\Bigg[v_{L_A K_A L_B K_B L}(R) \Bigg(cos\big(M_A\big(\alpha_A-\alpha_B\big)+K_A\gamma_A+K_B\gamma_B\big) d^{L_A}_{M_A K_A}(\beta_A) d^{L_B}_{-M_A K_B}(\beta_B) \\
& + (-1)^{L_A+L_B+L} cos\big(M_A\big(\alpha_A-\alpha_B\big)-K_A\gamma_A-K_B\gamma_B\big) d^{L_A}_{M_A -K_A}(\beta_A) d^{L_B}_{-M_A -K_B}(\beta_B) \Bigg) \\
& + v_{L_A K_A L_B -K_B L}(R) \Bigg(cos\big(M_A\big(\alpha_A-\alpha_B\big)+K_A\gamma_A-K_B\gamma_B\big) d^{L_A}_{M_A K_A}(\beta_A) d^{L_B}_{-M_A -K_B}(\beta_B) \\
& + (-1)^{L_A+L_B+L} cos\big(M_A\big(\alpha_A-\alpha_B\big)-K_A\gamma_A+K_B\gamma_B\big) d^{L_A}_{M_A -K_A}(\beta_A) d^{L_B}_{-M_A K_B}(\beta_B) \Bigg) \Bigg] \Bigg]
\end{aligned}
\tag{.0.20}
$$

References

[1] Fred Goesmann, Helmut Rosenbauer, J-H Bredehöft, M Cabane, P Ehrenfreund, T Gautier, C Giri, H Krüger, A Mc-Dermott, S McKenna-Lawlor, et al. The first mass spectrometry measurements of cosac after touchdown on comet 67p/churyumov-gerasimenko. *Science*, 349, 2015.

[2] Walter Gordy and Robert I Cook. Microwave molecular spectra. *(No Title)*, 1984.

[3] Yunjie Xu, Wolfgang Ja, et al. Rotational spectroscopic investigation of the weak interaction between CO and N_2O. *Journal of molecular spectroscopy*, 197(2):244–253, 1999.

[4] Website. http://www-ssg.sr.unh.edu/ism/what1.html. Accessed: 28.06.2024.

[5] AGGM Tielens. The molecular universe. *Reviews of Modern Physics*, 85(3):1021–1081, 2013.

[6] JG Calvert. The chemistry of the atmosphere and its perturbations through human activities. *Pure and applied chemistry*, 69(1):1–12, 1997.

[7] MJ Illán-Gómez, E Raymundo-Pinero, A Garcıa-Garcıa, A Linares-Solano, and C Salinas-Martınez de Lecea. Catalytic NOx reduction by carbon supporting metals. *Applied Catalysis B: Environmental*, 20(4):267–275, 1999.

[8] Enzo Gallori. Astrochemistry and the origin of genetic material. *Rendiconti Lincei*, 22:113–118, 2011.

[9] Alexander Dalgarno. A serendipitous journey. *Annu. Rev. Astron. Astrophys.*, 46(1):1–20, 2008.

[10] Michaël De Becker. Astrochemistry: the issue of molecular complexity in astrophysical environments. *arXiv preprint arXiv:1305.6243*, 2013.

[11] Floris van der Tak. Radiative transfer and molecular data for astrochemistry. *Proceedings of the International Astronomical Union*, 7(S280):449–460, 2011.

[12] Ewine F Van Dishoeck. Astrochemistry: overview and challenges. *Proceedings of the International Astronomical Union*, 13(S332):3–22, 2017.

[13] Satoshi Yamamoto. Introduction to astrochemistry. *Editorial: Springer*, 614, 2017.

[14] James Lequeux. *The interstellar medium*. Springer Science & Business Media, 2004.

[15] David A Williams. Gas and dust in the interstellar medium. In *Journal of Physics: Conference Series*, volume 6, page 1. IOP Publishing, 2005.

[16] John C Brandt and Robert D Chapman. *Introduction to comets*. Cambridge University Press, 2004.

[17] Nicolas Thomas. Light curves, orbits, and reservoirs. In *An Introduction to Comets*, pages 1–26. Springer, 2020.

[18] Martin Rubin, Kathrin Altwegg, Jean-Jacques Berthelier, Michael R Combi, Johan De Keyser, Stephen A Fuselier, Tamas I Gombosi, Murthy S Gudipati, Nora Hänni, Kristina A Kipfer, et al. Volatiles in the H_2O and CO_2 ices of comet 67p/churyumov–gerasimenko. *Monthly Notices of the Royal Astronomical Society*, 526(3):4209–4233, 2023.

[19] Anita L Cochran, Anny-Chantal Levasseur-Regourd, Martin Cordiner, Edith Hadamcik, Jérémie Lasue, Adeline Gicquel, David G Schleicher, Steven B Charnley, Michael J Mumma, Lucas Paganini, et al. The composition of comets. *Space Science Reviews*, 197:9–46, 2015.

[20] Nicolas Biver and Dominique Bockelée-Morvan. Complex organic molecules in comets from remote-sensing observations at millimeter wavelengths. *ACS Earth and Space Chemistry*, 3(8):1550–1555, 2019.

[21] D Despois, N Biver, D Bockelée-Morvan, and J Crovisier. Observations of molecules in comets. *Proceedings of the International Astronomical Union*, 1(S231):469–478, 2005.

[22] Robin T Garrod. Simulations of ice chemistry in cometary nuclei. *The Astrophysical Journal*, 884(1):69, 2019.

[23] Jesse C Mcnichol and Richard Gordon. Are we from outer space? a critical review of the panspermia hypothesis. *Genesis-In The Beginning: Precursors of Life, Chemical Models and Early Biological Evolution*, pages 591–619, 2012.

[24] David Tepfer. The origin of life, panspermia and a proposal to seed the universe. *Plant Science*, 175(6):756–760, 2008.

[25] Joseph L Kirschvink and Benjamin P Weiss. Mars, panspermia, and the origin of life: where did it all begin. *Palaeontologia electronica*, 4(2):8–15, 2002.

[26] Andrew McKellar. Evidence for the molecular origin of some hitherto unidentified interstellar lines. *Publications of the Astronomical Society of the Pacific*, 52(307):187–192, 1940.

[27] Walter Sydney Adams. What lies between the stars. *Publications of the Astronomical Society of the Pacific, Vol. 53, No. 312, p. 73*, 53:73, 1941.

[28] AE Douglas and GERHARD Herzberg. Note on ch^{+} in interstellar space and in the laboratory. *Astrophysical Journal, vol. 94, p. 381*, 94:381, 1941.

[29] Charles H Townes. 16. microwave and radio-frequency resonance lines of interest to radio astronomy. In *Symposium-International Astronomical Union*, volume 4, pages 92–103. Cambridge University Press, 1957.

[30] Sander Weinreb, Alan H Barrett, M Littleton Meeks, and John C Henry. Radio observations of oh in the interstellar medium. In *A Source Book in Astronomy and Astrophysics, 1900–1975*, pages 666–670. Harvard University Press, 1979.

[31] AC Cheung, David M Rank, CH Townes, Douglas D Thornton, and WJ Welch. Detection of NH_3 molecules in the interstellar medium by their microwave emission. *Physical Review Letters*, 21(25):1701, 1968.

[32] Christian P Endres, Stephan Schlemmer, Peter Schilke, Jürgen Stutzki, and Holger SP Müller. The cologne database for molecular spectroscopy, cdms, in the virtual atomic and molecular data centre, vamdc. *Journal of Molecular Spectroscopy*, 327:95–104, 2016.

[33] Nicolas Biver, Neil Dello Russo, Cyrielle Opitom, and Martin Rubin. Chemistry of comet atmospheres. *arXiv preprint arXiv:2207.04800*, 2022.

[34] M-L Dubernet, MH Alexander, YA Ba, N Balakrishnan, Christian Balança, C Ceccarelli, J Cernicharo, F Daniel, F Dayou, M Doronin, et al. Basecol2012: A collisional database repository and web service within the virtual atomic and molecular data centre (vamdc). *Astronomy & Astrophysics*, 553:A50, 2013.

[35] Nikku Madhusudhan. Atmospheric retrieval of exoplanets. *arXiv preprint arXiv:1808.04824*, 2018.

[36] Ryan C Fortenberry. Quantum astrochemical spectroscopy. *International Journal of Quantum Chemistry*, 117(2):81–91, 2017.

[37] Axel Weiss, F Walter, and NZ Scoville. The spectral energy distribution of co lines in m 82. *Astronomy & Astrophysics*, 438(2):533–544, 2005.

[38] M López-Puertas, G Zaragoza, MÁ López-Valverde, and FW Taylor. Non local thermodynamic equilibrium (lte) atmospheric limb emission at 4.6 μm: 2. an analysis of the daytime wideband radiances as measured by uars improved stratospheric and mesospheric sounder. *Journal of Geophysical Research: Atmospheres*, 103(D7):8515–8530, 1998.

[39] Evelyne Roueff and François Lique. Molecular excitation in the interstellar medium: Recent advances in collisional, radiative, and chemical processes. *Chemical reviews*,

113(12):8906–8938, 2013.

[40] A van der Avoird and DJ Nesbitt. Rovibrational states of the h_2o-h_2 complex: An ab initio calculation. *J. Chem. Phys.*, 134(4):044314, 2011.

[41] A Faure and E Josselin. Collisional excitation of water in warm astrophysical media-i. rate coefficients for rovibrationally excited states. *Astronomy & Astrophysics*, 492(1):257–264, 2008.

[42] Paul McGuire and Donald J Kouri. Quantum mechanical close coupling approach to molecular collisions. jz-conserving coupled states approximation. *The Journal of Chemical Physics*, 60(6):2488–2499, 1974.

[43] R Goldflam, S Green, and D_J Kouri. Infinite order sudden approximation for rotational energy transfer in gaseous mixtures. *The Journal of Chemical Physics*, 67(9):4149–4161, 1977.

[44] A Faure, N Crimier, C Ceccarelli, P Valiron, L Wiesenfeld, and ML Dubernet. Quasi-classical rate coefficient calculations for the rotational (de) excitation of H_2O by H_2. *Astronomy & Astrophysics*, 472(3):1029–1035, 2007.

[45] Dmitri Babikov and Alexander Semenov. Recent advances in development and applications of the mixed quantum/classical theory for inelastic scattering. *The Journal of Physical Chemistry A*, 120(3):319–331, 2016.

[46] Alexander Semenov and Dmitri Babikov. Accurate calculations of rotationally inelastic scattering cross sections using mixed quantum/classical theory. *The Journal of Physical Chemistry Letters*, 5(2):275–278, 2014.

[47] Alexander Semenov and Dmitri Babikov. Mixed quantum/classical calculations of total and differential elastic and rotationally inelastic scattering cross sections for light and heavy reduced masses in a broad range of collision energies. *The Journal of Chemical Physics*, 140(4), 2014.

[48] Dulat Bostan, Bikramaditya Mandal, Carolin Joy, Michał Żółtowski, François Lique, Jérôme Loreau, Ernesto Quintas-Sánchez, Adrian Batista-Planas, Richard Dawes, and Dmitri Babikov. Mixed quantum/classical calculations of rotationally inelastic scattering in the co + co system: a comparison with fully quantum results. *Physical Chemistry Chemical Physics*, 26(8):6627–6637, 2024.

[49] Alexander Semenov and Dmitri Babikov. Inelastic scattering of identical molecules within framework of the mixed quantum/classical theory: application to rotational excitations in $H_2 + H_2$. *The Journal of Physical Chemistry A*, 120(22):3861–3866, 2016.

[50] Alexander Semenov, Marie-Lise Dubernet, and Dmitri Babikov. Mixed quantum/classical theory for inelastic scattering of asymmetric-top-rotor+ atom in the body-fixed reference frame and application to the H_2O + He system. *The Journal of Chemical Physics*, 141(11), 2014.

[51] Mikhail Ivanov, Marie-Lise Dubernet, and Dmitri Babikov. Rotational quenching of H_2O by he: Mixed quantum/classical theory and comparison with quantum results. *The Journal of Chemical Physics*, 140(13), 2014.

[52] Carolin Joy, Dulat Bostan, Bikramaditya Mandal, and Dmitri Babikov. Rate coefficients for rotational state-to-state transitions in $H_2O + H_2$ collisions as predicted by mixed quantum/classical theory (mqct). *arXiv preprint arXiv:2408.13339*, 2024.

[53] Alexander Semenov and Dmitri Babikov. Mqct. i. inelastic scattering of two asymmetric-top rotors with application to $H_2O + H_2O$. *The Journal of Physical Chemistry A*, 121(26):4855–4867, 2017.

[54] Ad van der Avoird and David J Nesbitt. Rovibrational states of the H_2O--H_2 complex: An ab initio calculation. *The Journal of Chemical Physics*, 134(4), 2011.

[55] Thierry Stoecklin, Otoniel Denis-Alpizar, Alexandre Clergerie, Philippe Halvick, Alexandre Faure, and Yohann Scribano. Rigid-bender close-coupling treatment of

the inelastic collisions of H_2O with *para*-H_2. *The Journal of Physical Chemistry A*, 123(27):5704–5712, 2019.

[56] Yu N Kalugina, A Faure, A van Der Avoird, K Walker, and François Lique. Interaction of H_2O with CO: potential energy surface, bound states and scattering calculations. *Physical Chemistry Chemical Physics*, 20(8):5469–5477, 2018.

[57] AJ Barclay, A van der Avoird, ARW McKellar, and N Moazzen-Ahmadi. The water–carbon monoxide dimer: new infrared spectra, ab initio rovibrational energy level calculations, and an interesting in-termolecular mode. *Physical Chemistry Chemical Physics*, 21(27):14911–14922, 2019.

[58] A Faure, François Lique, and J Loreau. The effect of $CO-H_2O$ collisions in the rotational excitation of cometary co. *Monthly Notices of the Royal Astronomical Society*, 493(1):776–782, 2020.

[59] Jérôme Loreau, Yulia N Kalugina, Alexandre Faure, Ad van Der Avoird, and François Lique. Potential energy surface and bound states of the H_2O-HF complex. *The Journal of Chemical Physics*, 153(21), 2020.

[60] Steve A Ndengue, Richard Dawes, and Fabien Gatti. Rotational excitations in $CO--CO$ collisions at low temperature: Time-independent and multiconfigurational time-dependent hartree calculations. *The Journal of Physical Chemistry A*, 119(28):7712–7723, 2015.

[61] HD Meyer. Version 8.3 (2002), version 8.4 (2007). *See http://mctdh. uni-hd. de*, 2000.

[62] Xiao-Gang Wang and Tucker Carrington. Theoretical study of the rovibrational spectrum of H_2O--H_2. *The Journal of Chemical Physics*, 134(4), 2011.

[63] Xiao-Gang Wang and Tucker Carrington. Using monomer vibrational wavefunctions to compute numerically exact (12d) rovibrational levels of water dimer. *The Journal of Chemical Physics*, 148(7), 2018.

[64] TR Dyke. Km mack and js muenter. *J. Chem. Phys*, 66:498, 1977.

[65] KM Evenson, DA Jennings, and FR Petersen. Tunable far-infrared spectroscopy. *Applied physics letters*, 44(6):576–578, 1984.

[66] RC Cohen, Kerry L Busarow, KB Laughlin, Geoffrey A Blake, M Havenith, Yuan-Tseh Lee, and RJ Saykally. Tunable far infrared laser spectroscopy of van der waals bonds: Vibration–rotation–tunneling spectra of Ar− −H_2O. *The Journal of chemical physics*, 89(8):4494–4504, 1988.

[67] EN Karyakin, Gerald T Fraser, Francis J Lovas, RD Suenram, and M Fujitake. Donor–acceptor interchange tunneling in hdo–doh and the higher energy hdo–hod isotopomer. *The Journal of chemical physics*, 102(3):1114–1121, 1995.

[68] M Born and JR Oppenheimer. Ann. phys. *Ann. Phys*, 84:457, 1927.

[69] Steve A Ndengué, Yohann Scribano, David M Benoit, Fabien Gatti, and Richard Dawes. Intermolecular rovibrational bound states of $h_2o - h_2$ dimer from a multi-configuration time dependent hartree approach. *Chemical Physics Letters*, 715:347–353, 2019.

[70] Dominika Viglaska, Xiao-Gang Wang, Tucker Carrington Jr, and David P Tew. Computational study of the rovibrational spectrum of H_2O-HF. *Journal of Molecular Spectroscopy*, 384:111587, 2022.

[71] Peter M Felker and Zlatko Bačić. Intermolecular rovibrational states of the H_2O-CO_2 and D_2O-CO_2 van der waals complexes. *The Journal of Chemical Physics*, 156(6), 2022.

[72] Yang Liu, Jun Li, Peter M Felker, and Zlatko Bačić. $HCl-H_2O$ dimer: an accurate full-dimensional potential energy surface and fully coupled quantum calculations of intra-and intermolecular vibrational states and frequency shifts. *Physical Chemistry Chemical Physics*, 23(12):7101–7114, 2021.

[73] Peter M Felker and Zlatko Bačić. Intra-and intermolecular rovibrational states of $HCl-H_2O$ and $DCl-H_2O$ dimers from full-dimensional and fully coupled quantum calculations. *Chinese Journal of Chemical Physics*, 34(6):728–740, 2021.

[74] Marco Masia, Harald Forbert, and Dominik Marx. Connecting structure to infrared spectra of molecular and autodissociated hcl- water aggregates. *The Journal of Physical Chemistry A*, 111(49):12181–12191, 2007.

[75] Xiao-Gang Wang and Tucker Carrington. Using nondirect product wigner d basis functions and the symmetry-adapted lanczos algorithm to compute the rovibrational spectrum of CH_4-H_2O. *The Journal of Chemical Physics*, 154(12), 2021.

[76] Alberto Martín Santa Daría, Gustavo Avila, and Edit Mátyus. Performance of a black-box-type rovibrational method in comparison with a tailor-made approach: Case study for the methane–water dimer. *The Journal of Chemical Physics*, 154(22), 2021.

[77] Emil Vogt and Henrik G Kjaergaard. Vibrational spectroscopy of the water dimer at jet-cooled and atmospheric temperatures. *Annual Review of Physical Chemistry*, 73:209–231, 2022.

[78] GC Groenenboom, PES Wormer, A Van Der Avoird, EM Mas, R Bukowski, and K Szalewicz. Water pair potential of near spectroscopic accuracy. ii. vibration–rotation–tunneling levels of the water dimer. *The Journal of Chemical Physics*, 113(16):6702–6715, 2000.

[79] Peter M Felker and Zlatko Bačić. Weakly bound molecular dimers: Intramolecular vibrational fundamentals, overtones, and tunneling splittings from full-dimensional quantum calculations using compact contracted bases of intramolecular and low-energy rigid-monomer intermolecular eigenstates. *The Journal of Chemical Physics*, 151(2), 2019.

[80] Peter M Felker and Zlatko Bačić. Noncovalently bound molecular complexes beyond diatom–diatom systems: full-dimensional, fully coupled quantum calculations of rovibrational states. *Physical Chemistry Chemical Physics*, 24(40):24655–24676, 2022.

[81] Peter M Felker, Yang Liu, Jun Li, and Zlatko Bačić. DCl−H_2O, HCl−D_2O, and DCl−D_2O dimers: Inter-and intramolecular vibrational states and frequency shifts from fully coupled quantum calculations on a full-dimensional neural network potential energy surface. *The Journal of Physical Chemistry A*, 125(29):6437–6449, 2021.

[82] Peter M Felker and Zlatko Bačić. H_2O−CO and D_2O−CO complexes: Intra-and intermolecular rovibrational states from full-dimensional and fully coupled quantum calculations. *The Journal of Chemical Physics*, 153(7), 2020.

[83] Peter M Felker and Zlatko Bačić. HDO – CO complex: D-bonded and h-bonded isomers and intra-and intermolecular rovibrational states from full-dimensional and fully coupled quantum calculations. *The Journal of Physical Chemistry A*, 125(4):980–989, 2021.

[84] Peter M Felker and Zlatko Bačić. Benzene–H_2O and benzene–hdo: Fully coupled nine-dimensional quantum calculations of flexible H_2O/hdo intramolecular vibrational excitations and intermolecular states of the dimers, and their infrared and raman spectra using compact bases. *The Journal of Chemical Physics*, 152(12), 2020.

[85] Xiao-Gang Wang and Tucker Carrington. Computing excited oh stretch states of water dimer in 12d using contracted intermolecular and intramolecular basis functions. *The Journal of Chemical Physics*, 158(8), 2023.

[86] Xiao-Yu Liu and Chong Qi. Pairdiag: An exact diagonalization program for solving general pairing hamiltonians. *Computer Physics Communications*, 259:107349, 2021.

[87] Zlatko Bačić. Fully coupled six-dimensional calculations of rovibrational eigenstates of floppy four-atom molecules. *Computer physics communications*, 128(1-2):46–54, 2000.

[88] Jacek Kłos and François Lique. Cold molecular collisions: quantum scattering calculations and their relevance in astrophysical applications. 2017.

[89] Michal Zoltowski. *Collisional excitation of astrophysical molecules induced by H_2O and CO molecules*. PhD thesis, Normandie Université, 2023.

[90] AV Nesterenok and DA Varshalovich. H_2O maser pumping: The effect of quasi-resonance energy transfer in collisions between h_2 and h_2o molecules. *Astronomy Letters*, 40:425–434, 2014.

[91] MR Lerate, JA Yates, MJ Barlow, S Viti, and BM Swinyard. Chemical and radiative transfer modelling of the iso-lws fabry-perot spectra of orion-kl water lines. *Monthly Notices of the Royal Astronomical Society*, 406(4):2445–2451, 2010.

[92] F Daniel, JR Goicoechea, J Cernicharo, M-L Dubernet, and A Faure. Influence of collisional rate coefficients on water vapour excitation. *Astronomy & Astrophysics*, 547:A81, 2012.

[93] Jiří Čížek. On the correlation problem in atomic and molecular systems. calculation of wavefunction components in ursell-type expansion using quantum-field theoretical methods. *The Journal of Chemical Physics*, 45(11):4256–4266, 1966.

[94] Michal Żóltowski, François Lique, Agata Karska, and Piotr S Żuchowski. Rotational excitation of highly excited H_2O by H_2. *Monthly Notices of the Royal Astronomical Society*, 502(4):5356–5361, 2021.

[95] Michał Żółtowski, Jérôme Loreau, and François Lique. Collisional energy transfer in the $CO--CO$ system. *Physical Chemistry Chemical Physics*, 24(19):11910–11918, 2022.

[96] MS Pindzola, F Robicheaux, SD Loch, JC Berengut, T Topcu, J Colgan, M Foster, DC Griffin, CP Ballance, DR Schultz, et al. The time-dependent close-coupling method for atomic and molecular collision processes. *Journal of Physics B: Atomic, Molecular and Optical Physics*, 40(7):R39, 2007.

[97] Astrid Bergeat, Alexandre Faure, Sebastien B Morales, Audrey Moudens, and Christian Naulin. Low-energy water–hydrogen inelastic collisions. *The Journal of Physical Chemistry A*, 124(2):259–264, 2019.

[98] A Faure, M Zoltowski, L Wiesenfeld, F Lique, and A Bergeat. The rotational excitation of the water isotopologues by molecular hydrogen. *Monthly Notices of the Royal Astronomical Society*, page stad3037, 2023.

[99] Fabien Daniel, M-L Dubernet, and Alain Grosjean. Rotational excitation of 45 levels of ortho/para-h_2o by excited ortho/para-h_2 from 5 k to 1500 k: state-to-state, effective, and thermalized rate coefficients. *Astronomy & Astrophysics*, 536:A76, 2011.

[100] Jérôme Loreau, A Faure, and F Lique. Scattering of CO with H_2O: Statistical and classical alternatives to close-coupling calculations. *The Journal of Chemical Physics*, 148(24), 2018.

[101] Jérôme Loreau, François Lique, and Alexandre Faure. An efficient statistical method to compute molecular collisional rate coefficients. *The Astrophysical Journal Letters*, 853(1):L5, 2018.

[102] Steve Ndengué, Yohann Scribano, Fabien Gatti, and Richard Dawes. State-to-state inelastic rotational cross sections in five-atom systems with the multiconfiguration time dependent hartree method. *The Journal of Chemical Physics*, 151(13), 2019.

[103] Alexander Semenov and Dmitri Babikov. Mixed quantum/classical approach for description of molecular collisions in astrophysical environments. *The Journal of Physical Chemistry Letters*, 6(10):1854–1858, 2015.

[104] Alexander Semenov, Mikhail Ivanov, and Dmitri Babikov. Ro-vibrational quenching of CO (v= 1) by he impact in a broad range of temperatures: A benchmark study using mixed quantum/classical inelastic scattering theory. *The Journal of Chemical Physics*, 139(7), 2013.

[105] Nezha Bouhafs and François Lique. Collisional excitation of nh (x3σ-) by ne: Potential energy surface, scattering calculations, and comparison with experiments. *The Journal of chemical physics*, 143(18), 2015.

[106] AC Cheung, David M Rank, CH Townes, Douglas D Thornton, and WJz Welch. Detection of water in interstellar regions by its microwave radiation. *Nature*, 221(5181):626–628, 1969.

[107] Vincent Kotwicki. Water in the universe. *Hydrological sciences journal*, 36(1):49–66, 1991.

[108] https://lweb.cfa.harvard.edu/swas/.

[109] http://www.iso.vilspa.esa.es/.

[110] Josep M Anglada and Albert Solé. Impact of the water dimer on the atmospheric reactivity of carbonyl oxides. *Physical Chemistry Chemical Physics*, 18(26):17698–17712, 2016.

[111] JE Headrick and V Vaida. Significance of water complexes in the atmosphere. *Physics and Chemistry of the Earth, Part C: Solar, Terrestrial & Planetary Science*, 26(7):479–486, 2001.

[112] Philip Ball. Water and life: seeking the solution. *Nature*, 436(7054):1084–1086, 2005.

[113] Philip Ball. Water, water, everywhere? *Nature*, 427(6969):19–20, 2004.

[114] P Ehrenfreund, WA Schutte, YC Minh, and EF van Dishoek. Astrochemistry: From molecular clouds to planetary systems. In *IAU Symp*, volume 197, pages 135–46,

2000.

[115] A Bergeat, Sébastien B Morales, Christian Naulin, Laurent Wiesenfeld, and A Faure. Probing low-energy resonances in water-hydrogen inelastic collisions. *Physical Review Letters*, 125(14):143402, 2020.

[116] Claude Leforestier, Krzysztof Szalewicz, and Ad van Der Avoird. Spectra of water dimer from a new ab initio potential with flexible monomers. *The Journal of chemical physics*, 137(1), 2012.

[117] SC Althorpe and DC Clary. A new method for calculating the rovibrational states of polyatomics with application to water dimer. *The Journal of chemical physics*, 102(11):4390–4399, 1995.

[118] Wojciech Cencek, Krzysztof Szalewicz, Claude Leforestier, Rob van Harrevelt, and Ad van der Avoird. An accurate analytic representation of the water pair potential. *Physical Chemistry Chemical Physics*, 10(32):4716–4731, 2008.

[119] Ad van der Avoird, Paul ES Wormer, and Robert Moszynski. From intermolecular potentials to the spectra of van der waals molecules, and vice versa. *Chemical Reviews*, 94(7):1931–1974, 1994.

[120] Patricia Vindel-Zandbergen, Dariusz Kędziera, Michał Żółtowski, Jacek Kłos, Piotr Żuchowski, Peter M Felker, François Lique, and Zlatko Bačić. H_2O-HCN complex: A new potential energy surface and intermolecular rovibrational states from rigorous quantum calculations. *The Journal of Chemical Physics*, 159(17), 2023.

[121] Lewis E Snyder and David Buhl. Observations of radio emission from interstellar hydrogen cyanide. *Astrophysical Journal, vol. 163, p. L47*, 163:L47, 1971.

[122] WF Huebner, LE Snyder, and D Buhl. Hcn radio emission from comet kohoutek (1973f). *Icarus*, 23(4):580–584, 1974.

[123] F Peter Schloerb, Wayne M Kinzel, Daryl A Swade, and William M Irvine. Hcn production from comet halley. *Astrophysical Journal, Part 2-Letters to the Editor (ISSN 0004-637X), vol. 310, Nov. 1, 1986, p. L55-L60. Research supported by the US-France Cooperative Science Program.*, 310:L55–L60, 1986.

[124] D Despois, J Crovisier, D Bockelée-Morvan, E Gerard, and J Schraml. Observations of hydrogen cyanide in comet halley. *Astronomy and Astrophysics (ISSN 0004-6361), vol. 160, no. 2, May 1986, p. L11, L12.*, 160:L11, 1986.

[125] Feng Tian, JF Kasting, and K Zahnle. Revisiting hcn formation in earth's early atmosphere. *Earth and Planetary Science Letters*, 308(3-4):417–423, 2011.

[126] Paul B Rimmer and Sarah Rugheimer. Hydrogen cyanide in nitrogen-rich atmospheres of rocky exoplanets. *Icarus*, 329:124–131, 2019.

[127] DC Lis, J Keene, K Young, TG Phillips, D Bockelée-Morvan, J Crovisier, P Schilke, PF Goldsmith, and EA Bergin. Spectroscopic observations of comet c/1996 b2 (hyakutake) with the caltech submillimeter observatory. *Icarus*, 130(2):355–372, 1997.

[128] BE Turner, L Pirogov, and YC Minh. The physics and chemistry of small translucent molecular clouds. viii. hcn and hnc. *The Astrophysical Journal*, 483(1):235, 1997.

[129] J Hatchell, TJ Millar, and SD Rodgers. The dcn/hcn abundance ratio in hot molecular cores. *Astronomy and Astrophysics, v. 332, p. 695-702 (1998)*, 332:695–702, 1998.

[130] J Cernicharo, MJ Barlow, E Gonzalez-Alfonso, P Cox, PE Clegg, QR Nguyen, A Omont, M Guelin, XW Liu, RJ Sylvester, et al. The iso/lws far infrared spectrum of irc+ 10 216. *Astronomy and Astrophysics*, 315:L201–L204, 1996.

[131] JP Pérez-Beaupuits, Susanne Aalto, and H Gerebro. Hnc, hcn and cn in seyfert galaxies. *Astronomy & Astrophysics*, 476(1):177–192, 2007.

[132] Michel Guélin, P Salomé, Roberto Neri, S García-Burillo, J Graciá-Carpio, José Cernicharo, Pierre Cox, P Planesas, PM Solomon, Linda J Tacconi, et al. Detection of hnc and tentative detection of cn at z= 3.9. *Astronomy & Astrophysics*, 462(3):L45–L48, 2007.

[133] Georg Ch Mellau, Brenda P Winnewisser, and Manfred Winnewisser. Near infrared emission spectrum of hcn. *Journal of Molecular Spectroscopy*, 249(1):23–42, 2008.

[134] Javier R Goicoechea, M Etxaluze, J Cernicharo, M Gerin, DA Neufeld, A Contursi, TA Bell, M De Luca, P Encrenaz, N Indriolo, et al. Herschel* far-infrared spectroscopy of the galactic center. hot molecular gas: Shocks versus radiation near sgr a. *The Astrophysical Journal Letters*, 769(1):L13, 2013.

[135] J Cernicharo, F Daniel, A Castro-Carrizo, M Agundez, N Marcelino, C Joblin, JR Goicoechea, and M Guélin. Unveiling the dust nucleation zone of irc+ 10216 with alma. *The Astrophysical journal letters*, 778(2):L25, 2013.

[136] F Combes, S García-Burillo, V Casasola, L Hunt, M Krips, AJ Baker, F Boone, A Eckart, I Marquez, R Neri, et al. Alma observations of feeding and feedback in nearby seyfert galaxies: an agn-driven outflow in ngc 1433. *Astronomy & Astrophysics*, 558:A124, 2013.

[137] Takuma Izumi, Kotaro Kohno, Sergio Martín, Daniel Espada, Nanase Harada, Satoki Matsushita, Pei-Ying Hsieh, Jean L Turner, David S Meier, Eva Schinnerer, et al. Submillimeter alma observations of the dense gas in the low-luminosity type-1 active nucleus of ngc1097. *Publications of the Astronomical Society of Japan*, 65(5):100–100, 2013.

[138] N Biver, D Bockelée-Morvan, J Crovisier, Aa Sandqvist, J Boissier, DC Lis, M Cordiner, BP Bonev, N Dello Russo, R Moreno, et al. Coma composition of comet 67p/churyumov-gerasimenko from radio-wave spectroscopy. *Astronomy & Astrophysics*, 672:A170, 2023.

[139] John S Daniel and Susan Solomon. On the climate forcing of carbon monoxide. *Journal of Geophysical Research: Atmospheres*, 103(D11):13249–13260, 1998.

[140] Shuo Liu, Shuangxi Fang, Miao Liang, Qianli Ma, and Zhaozhong Feng. Study on co data filtering approaches based on observations at two background stations in china. *Science of the total environment*, 691:675–684, 2019.

[141] RAVISHANKARA AR. Nitrous oxide (N_2O): the dominant ozone-depleting substance emitted in the 21st century. *Science*, 326:123–125, 2009.

[142] Eric Herbst. Molecular ions in interstellar reaction networks. In *Journal of Physics: Conference Series*, volume 4, page 17. IOP Publishing, 2005.

[143] DCB Whittet and WW Duley. Carbon monoxide frosts in the interstellar medium. *The Astronomy and Astrophysics Review*, 2:167–189, 1991.

[144] Paul H Krupenie. The band spectrum of carbon monoxide. 1966.

[145] Xuedan Jiang, Li Liu, Yang Peng, and Hua Zhu. A new ab initio potential energy surface and rovibrational spectra for the CO–N_2O complex. *The Journal of Physical Chemistry A*, 2024.

[146] Thomas M Dame, Dap Hartmann, and P Thaddeus. The milky way in molecular clouds: a new complete co survey. *The Astrophysical Journal*, 547(2):792, 2001.

[147] RW Wilson, KB Jefferts, and AA Penzias. Carbon monoxide in the orion nebula. *Astrophysical Journal, vol. 161, p. L43*, 161:L43, 1970.

[148] Hans-Dieter Meyer, Fabien Gatti, and Graham A Worth. *Multidimensional quantum dynamics: MCTDH theory and applications*. John Wiley & Sons, 2009.

[149] H-D Meyer, Uwe Manthe, and Lorenz S Cederbaum. The multi-configurational time-dependent hartree approach. *Chemical Physics Letters*, 165(1):73–78, 1990.

[150] Anna Kaczmarek-Kedziera et al. Remarks on wave function theory and methods. In *Handbook of computational chemistry*, pages 123–171. Springer, 2017.

[151] Benjamin LASORNE. Nonadiabatic dynamics. 2019.

[152] John Zeng Hui Zhang. *Theory and application of quantum molecular dynamics*. World Scientific, 1998.

[153] R Islampour and M Gharibi. The molecular hamiltonian with two-rotational-angle embedding. *Molecular Physics*, 105(4):343–357, 2007.

[154] Matthew J Bramley and Nicholas C Handy. Efficient calculation of rovibrational eigenstates of sequentially bonded four-atom molecules. *The Journal of chemical physics*, 98(2):1378–1397, 1993.

[155] R Islampour, M Gharibi, and M Miralinaghi. The molecular hamiltonian in jacobi coordinates. *Molecular Physics*, 104(12):1879–1890, 2006.

[156] Russell T Pack and Gregory A Parker. Quantum reactive scattering in three dimensions using hyperspherical (aph) coordinates. iii. small θ behavior and corrigenda. *The Journal of Chemical Physics*, 90(7):3511–3519, 1989.

[157] Fabien Gatti. *Approche vectorielle des Hamiltoniens moléculaires, Application au spectre rovibrationnel excité de l'Ammoniac*. PhD thesis, Ph. D. Thesis, Université Montpellier, 1999.

[158] Fabien Gatti and Christophe Iung. Exact and constrained kinetic energy operators for polyatomic molecules: The polyspherical approach. *Physics Reports*, 484(1-2):1–69, 2009.

[159] Christophe Iung, Fabien Gatti, Alexandra Viel, and Xavier Chapuisat. Vector parametrization of the n-atom problem in quantum mechanics with non-orthogonal coordinates. *Physical Chemistry Chemical Physics*, 1(15):3377–3385, 1999.

[160] LC Biedenharn. Jd louck angular momentum in quantum physics addison-wesley, 1981.

[161] Duncan Bossion. *Théories et simulations de collisions moléculaires réactives pour la chimie primordiale*. PhD thesis, Université Montpellier, 2019.

[162] Fabien Gatti, Christophe Iung, Michel Menou, Yves Justum, André Nauts, and Xavier Chapuisat. Vector parametrization of the n-atom problem in quantum mechanics. i. jacobi vectors. *The Journal of chemical physics*, 108(21):8804–8820, 1998.

[163] Johann Scribano. *Etude théorique du dimère de l'eau $(H_2O)_2$ et de son rôle dans l'atmosphère*. PhD thesis, 2006.

[164] Keyvan Sadri, David Lauvergnat, Fabien Gatti, and Hans-Dieter Meyer. Rovibrational spectroscopy using a kinetic energy operator in eckart frame and the multiconfiguration time-dependent hartree (mctdh) approach. *The Journal of Chemical Physics*, 141(11), 2014.

[165] Fabien Gatti. Vector parametrization of the n-atom problem in quantum mechanics. iii. separation into two subsystems: Application to NH_3. *The Journal of chemical physics*, 111(16):7225–7235, 1999.

[166] Peter W Atkins and Ronald S Friedman. *Molecular quantum mechanics*. Oxford University Press, USA, 2011.

[167] Ira N Levine, Daryle H Busch, and Harrison Shull. *Quantum chemistry*, volume 6. Pearson Prentice Hall Upper Saddle River, NJ, 2009.

[168] Aaron James Barclay. Mid infrared investigations of van der waals complexes of atmospheric molecules (water, co, CO_2, N_2). 2022.

[169] André Nauts and Fabien Gatti. Unusual commutation relations in physics. *American Journal of Physics*, 78(12):1365–1375, 2010.

[170] Colin N Banwell and Elaine M McCash. *Fundamentals of molecular spectroscopy*. Indian Edition, 2017.

[171] Philip R Bunker and Per Jensen. *Molecular symmetry and spectroscopy*, volume 46853. NRC research press, 2006.

[172] Uwe Manthe, H-D Meyer, and Lorenz S Cederbaum. Wave-packet dynamics within the multiconfiguration hartree framework: General aspects and application to nocl. *The Journal of chemical physics*, 97(5):3199–3213, 1992.

[173] Michael H Beck, Andreas Jäckle, Graham A Worth, and H-D Meyer. The multiconfiguration time-dependent hartree (mctdh) method: a highly efficient algorithm for propagating wavepackets. *Physics reports*, 324(1):1–105, 2000.

[174] Hans-Dieter Meyer and Graham A Worth. Quantum molecular dynamics: propagating wavepackets and density operators using the multiconfiguration time-dependent hartree method. *Theoretical Chemistry Accounts*, 109:251–267, 2003.

[175] Edward A McCullough Jr and Robert E Wyatt. Quantum dynamics of the collinear (h, H_2) reaction. *The Journal of Chemical Physics*, 51(3):1253–1254, 1969.

[176] Edward A McCullough Jr and Robert E Wyatt. Dynamics of the collinear H^+H_2 reaction. i. probability density and flux. *The Journal of Chemical Physics*, 54(8):3578–3591, 1971.

[177] AD McLachlan. A variational solution of the time-dependent schrodinger equation. *Molecular Physics*, 8(1):39–44, 1964.

[178] Takeo Matsubara. A new approach to quantum-statistical mechanics. *Progress of theoretical physics*, 14(4):351–378, 1955.

[179] JC Light, IP Hamilton, and JV Lill. Generalized discrete variable approximation in quantum mechanics. *The Journal of chemical physics*, 82(3):1400–1409, 1985.

[180] John C Light. Discrete variable representations in quantum dynamics. In *Time-dependent quantum molecular dynamics*, pages 185–199. Springer, 1992.

[181] John C Light and Tucker Carrington Jr. Discrete-variable representations and their utilization. *Advances in Chemical Physics*, 114:263–310, 2000.

[182] JV Lill, Gregory A Parker, and John C Light. The discrete variable–finite basis approach to quantum scattering. *The Journal of chemical physics*, 85(2):900–910, 1986.

[183] S Carter and NC Handy. A variational method for the calculation of ro-vibronic levels of any orbitally degenerate (renner-teller) triatomic molecule. *Molecular Physics*, 52(6):1367–1391, 1984.

[184] Paul AM Dirac. Note on exchange phenomena in the thomas atom. In *Mathematical proceedings of the Cambridge philosophical society*, volume 26, pages 376–385. Cambridge University Press, 1930.

[185] Fabien Gatti, Benjamin Lasorne, Hans-Dieter Meyer, and André Nauts. *Applications of quantum dynamics in chemistry*, volume 98. Springer, 2017.

[186] Hans-Dieter Meyer. Introduction to mctdh. *Lecture Notes*, 2011.

[187] Christopher W Murray, Stephen C Racine, and Ernest R Davidson. Improved algorithms for the lowest few eigenvalues and associated eigenvectors of large matrices. *Journal of Computational Physics*, 103(2):382–389, 1992.

[188] Tae Jun Park and JC Light. Unitary quantum time evolution by iterative lanczos reduction. *The Journal of chemical physics*, 85(10):5870–5876, 1986.

[189] Ronnie Kosloff and H Tal-Ezer. A direct relaxation method for calculating eigenfunctions and eigenvalues of the schrödinger equation on a grid. *Chemical Physics Letters*, 127(3):223–230, 1986.

[190] Hans-Dieter Meyer, Frédéric Le Quéré, Céline Léonard, and Fabien Gatti. Calculation and selective population of vibrational levels with the multiconfiguration time-dependent hartree (mctdh) algorithm. *Chemical physics*, 329(1-3):179–192, 2006.

[191] Loïc Joubert Doriol, Fabien Gatti, Christophe Iung, and Hans-Dieter Meyer. Computation of vibrational energy levels and eigenstates of fluoroform using the multiconfiguration time-dependent hartree method. *The Journal of chemical physics*, 129(22), 2008.

[192] A Jäckle and H-D Meyer. Product representation of potential energy surfaces. *The Journal of chemical physics*, 104(20):7974–7984, 1996.

[193] A Jäckle and H-D Meyer. Product representation of potential energy surfaces. ii. *The Journal of chemical physics*, 109(10):3772–3779, 1998.

[194] UV Riss and H-D Meyer. Calculation of resonance energies and widths using the complex absorbing potential method. *Journal of Physics B: Atomic, Molecular and Optical Physics*, 26(23):4503, 1993.

[195] A Jäckle and H-D Meyer. Calculation of $H + H_2$ and $H + D_2$ reaction probabilities within the multiconfiguration time-dependent hartree approach employing an adiabatic correction scheme. *The Journal of chemical physics*, 109(7):2614–2623, 1998.

[196] Tamar Seideman and William H Miller. Calculation of the cumulative reaction probability via a discrete variable representation with absorbing boundary conditions. *The Journal of chemical physics*, 96(6):4412–4422, 1992.

[197] Gero Friesecke and Mario Koppen. On the ehrenfest theorem of quantum mechanics. *Journal of mathematical physics*, 50(8), 2009.

[198] A Jäckle and H-D Meyer. Time-dependent calculation of reactive flux employing complex absorbing potentials: General aspects and application within the multicon-

figuration time-dependent hartree wave approach. *The Journal of chemical physics*, 105(16):6778–6786, 1996.

[199] David J Tannor and David E Weeks. Wave packet correlation function formulation of scattering theory: The quantum analog of classical s-matrix theory. *The Journal of chemical physics*, 98(5):3884–3893, 1993.

[200] Aditya N Panda, Frank Otto, Fabien Gatti, and Hans-Dieter Meyer. Rovibrational energy transfer in ortho-H_2+ para-H_2 collisions. *The Journal of chemical physics*, 127(11), 2007.

[201] Fabien Gatti, Frank Otto, Suren Sukiasyan, and Hans-Dieter Meyer. Rotational excitation cross sections of para-H_2 + para-H_2 collisions. a full-dimensional wave-packet propagation study using an exact form of the kinetic energy. *The Journal of chemical physics*, 123(17):1743311, 2005.

[202] GA Worth, MH Beck, A Jäckle, HD Meyer, F Otto, M Brill, and O Vendrell. The heidelberg mctdh package: A set of programs for multi-dimensional quantum dynamics. *User's Guide, Version*, 8, 2000.

[203] Markus Schröder, Daniel Peláez, and Hans-Dieter Meyer. Numerical studies of the tunneling splitting of malonaldehyde and the eigenstates of hydrated hydroxide anion using mctdh. In *High Performance Computing in Science and Engineering '13: Transactions of the High Performance Computing Center, Stuttgart (HLRS) 2013*, pages 201–218. Springer, 2013.

[204] Michael H Beck and H-D Meyer. An efficient and robust integration scheme for the equations of motion of the multiconfiguration time-dependent hartree (mctdh) method. *Zeitschrift für Physik D Atoms, Molecules and Clusters*, 42:113–129, 1997.

[205] Hans-Dieter Meyer. Studying molecular quantum dynamics with the multiconfiguration time-dependent hartree method. *Wiley Interdisciplinary Reviews: Computational Molecular Science*, 2(2):351–374, 2012.

[206] Alan Hinchliffe. Ab initio study of the hydrogen-bonded complexes NH_3-HCN, PH_3-HCN, AsH_3-HCN, H_2O-HCN, H_2S-HCN and $H_2Se-HCN$. *Journal of Molecular Structure: THEOCHEM*, 136(1-2):193–199, 1986.

[207] HS Gutowsky, Timothy Clark Germann, JD Augspurger, and CE Dykstra. Structure and dynamics of the $H_2O--HCN$ dimer. *The Journal of chemical physics*, 96(8):5808–5816, 1992.

[208] Annette J Fillery-Travis, AC Legon, and LC Willoughby. Characterisation by rotational spectroscopy of a hydrogen-bonded dimer formed between H_2O and hcn. *Chemical Physics Letters*, 98(4):369–372, 1983.

[209] AJ Fillery-Travis, AC Legon, and LC Willoughby. Rotational spectrum and properties of the hydrogen-bonded heterodimer H_2O-HCN from pulsed-nozzle, fourier-transform microwave spectroscopy. *Proceedings of the Royal Society of London. Series A, Mathematical and Physical Sciences*, pages 405–423, 1984.

[210] Ernesto Quintas Sánchez and Marie-Lise Dubernet. Theoretical study of hcn–water interaction: five dimensional potential energy surfaces. *Physical Chemistry Chemical Physics*, 19(9):6849–6860, 2017.

[211] Alston J Misquitta, Rafał Podeszwa, Bogumił Jeziorski, and Krzysztof Szalewicz. Intermolecular potentials based on symmetry-adapted perturbation theory with dispersion energies from time-dependent density-functional calculations. *The Journal of chemical physics*, 123(21), 2005.

[212] Michael P Metz and Krzysztof Szalewicz. A statistically guided grid generation method and its application to intermolecular potential energy surfaces. *The Journal of Chemical Physics*, 152(13), 2020.

[213] Michael P Metz, Konrad Piszczatowski, and Krzysztof Szalewicz. Automatic generation of intermolecular potential energy surfaces. *Journal of Chemical Theory and Computation*, 12(12):5895–5919, 2016.

[214] G Brocks, A Van Der Avoird, BT Sutcliffe, and J Tennyson. Quantum dynamics of non-rigid systems comprising two polyatomic fragments. *Molecular Physics*, 50(5):1025–1043, 1983.

[215] Claude Leforestier. Grid method for the wigner functions. application to the van der waals system $Ar--H_2O$. *The Journal of chemical physics*, 101(9):7357–7363, 1994.

[216] Arthur G Maki, Wm Bruce Olson, and Robert L Sams. Hcn rotational-vibrational energy levels and intensity anomalies determined from infrared measurements. *Journal of Molecular Spectroscopy*, 36(3):433–447, 1970.

[217] Hervé Tajouo Tela, Ernesto Quintas-Sánchez, Marie-Lise Dubernet, Yohann Scribano, Richard Dawes, Fabien Gatti, and Steve Ndengué. Rovibrational states calculations of the H_2O-HCN heterodimer with the multiconfiguration time dependent hartree method. *Physical Chemistry Chemical Physics*, 25(46):31813–31824, 2023.

[218] Ryan C Fortenberry and Timothy J Lee. Vibrational and rovibrational spectroscopy applied to astrochemistry. *Vibrational Dynamics of Molecules*, 1, 2022.

[219] Gerald T Fraser. $(H_2O)_2$: spectroscopy, structure and dynamics. *International Reviews in Physical Chemistry*, 10(2):189–206, 1991.

[220] A Grosjean, M-L Dubernet, and C Ceccarelli. Collisional excitation rates of H_2O with H_2-ii. rotational excitation with *ortho*-H_2 at very low temperature and application to cold molecular clouds. *Astronomy & Astrophysics*, 408(3):1197–1203, 2003.

[221] K Pfeilsticker, A Lotter, C Peters, and H Bosch. Atmospheric detection of water dimers via near-infrared absorption. *Science*, 300(5628):2078–2080, 2003.

[222] Nir Goldman, Claude Leforestier, and RJ Saykally. Water dimers in the atmosphere ii: results from the vrt (asp-w) iii potential surface. *The Journal of Physical Chemistry A*, 108(5):787–794, 2004.

[223] Nir Goldman, Raymond S Fellers, Claude Leforestier, and Richard J Saykally. Water dimers in the atmosphere: Equilibrium constant for water dimerization from the vrt (asp-w) potential surface. *The Journal of Physical Chemistry A*, 105(3):515–519, 2001.

[224] Yohann Scribano and Claude Leforestier. Contribution of water dimer absorption to the millimeter and far infrared atmospheric water continuum. *The Journal of chemical physics*, 126(23), 2007.

[225] Piotr Jankowski, Garold Murdachaew, Robert Bukowski, Omololu Akin-Ojo, Claude Leforestier, and Krzysztof Szalewicz. Ab initio water pair potential with flexible monomers. *The Journal of Physical Chemistry A*, 119(12):2940–2964, 2015.

[226] Robert Bukowski, Krzysztof Szalewicz, Gerrit C Groenenboom, and Ad Van der Avoird. Predictions of the properties of water from first principles. *Science*, 315(5816):1249–1252, 2007.

[227] Eric M Mas, Robert Bukowski, Krzysztof Szalewicz, Gerrit C Groenenboom, Paul ES Wormer, and Ad van der Avoird. Water pair potential of near spectroscopic accuracy. i. analysis of potential surface and virial coefficients. *The Journal of Chemical Physics*, 113(16):6687–6701, 2000.

[228] Daniel Peláez and Hans-Dieter Meyer. The multigrid potfit (mgpf) method: Grid representations of potentials for quantum dynamics of large systems. *The Journal of Chemical Physics*, 138(1), 2013.

[229] Markus Schröder and Hans-Dieter Meyer. Transforming high-dimensional potential energy surfaces into sum-of-products form using monte carlo methods. *The Journal of Chemical Physics*, 147(6), 2017.

[230] Frank Otto. Multi-layer potfit: An accurate potential representation for efficient high-dimensional quantum dynamics. *The Journal of Chemical Physics*, 140(1), 2014.

[231] Dmitriĭ Varshalovich. *Quantum theory of angular momentum*.

[232] A Faure, Pierre Hily-Blant, C Rist, G Pineau des Forêts, A Matthews, and DR Flower. The ortho-to-para ratio of water in interstellar clouds. *Monthly Notices of the Royal Astronomical Society*, 487(3):3392–3403, 2019.

[233] Audrey Vorburger, Shahab Fatemi, André Galli, Lucas Liuzzo, Andrew R Poppe, and Peter Wurz. 3d monte-carlo simulation of ganymede's water exosphere. *Icarus*, 375:114810, 2022.

[234] Martin Andrew Cordiner, IM Coulson, E Garcia-Berrios, C Qi, François Lique, M Zołtowski, M de Val-Borro, Y-J Kuan, W-H Ip, S Mairs, et al. A sublime 3d model for cometary coma emission: the hypervolatile-rich comet c/2016 r2 (panstarrs). *The Astrophysical Journal*, 929(1):38, 2022.

[235] A García Muñoz, A Asensio Ramos, and A Faure. NIte modelling of water-rich exoplanet atmospheres. cooling and heating rates. *Icarus*, 415:116080, 2024.

[236] Bikramaditya Mandal, Carolin Joy, Dulat Bostan, Alexander Eng, and Dmitri Babikov. Adiabatic trajectory approximation: A new general method in the toolbox of mixed quantum/classical theory for collisional energy transfer. *The Journal of Physical Chemistry Letters*, 14(3):817–824, 2023.

[237] Haobin Wang and Michael Thoss. Multilayer formulation of the multiconfiguration time-dependent hartree theory. *The Journal of chemical physics*, 119(3):1289–1299, 2003.

[238] Haobin Wang. Multilayer multiconfiguration time-dependent hartree theory. *The Journal of Physical Chemistry A*, 119(29):7951–7965, 2015.

[239] J-L Teffo and A Chedin. Internuclear potential and equilibrium structure of the nitrous oxide molecule from rovibrational data. *Journal of Molecular Spectroscopy*, 135(2):389–409, 1989.

[240] Guosen Yan, Minghui Yang, and Daiqian Xie. Ab initio potential energy surface and rovibrational spectra of $He--CO_2$. *The Journal of chemical physics*, 109(23):10284–10292, 1998.

[241] John ZH Zhang, Jiqiong Dai, and Wei Zhu. Development of accurate quantum dynamical methods for tetraatomic reactions. *The Journal of Physical Chemistry A*, 101(15):2746–2754, 1997.

[242] Matsuo Kobayashi and Isao Suzuki. Sextic force field of nitrous oxide. *Journal of Molecular Spectroscopy*, 125(1):24–42, 1987.

[243] Richard Dawes, Xiao-Gang Wang, and Tucker Carrington Jr. Co dimer: New potential energy surface and rovibrational calculations. *The Journal of Physical Chemistry A*, 117(32):7612–7630, 2013.

[244] David Feller and Kirk A Peterson. An expanded calibration study of the explicitly correlated ccsd (t)-f12b method using large basis set standard ccsd (t) atomization energies. *The Journal of chemical physics*, 139(8), 2013.

[245] Nitai Sylvetsky and Jan ML Martin. Probing the basis set limit for thermochemical contributions of inner-shell correlation: balance of core-core and core-valence contributions. *Molecular Physics*, 117(9-12):1078–1087, 2019.

[246] Thomas B Adler, Gerald Knizia, and Hans-Joachim Werner. A simple and efficient ccsd (t)-f12 approximation. *The Journal of chemical physics*, 127(22), 2007.

[247] Katrina M de Lange and Joseph R Lane. Explicit correlation and intermolecular interactions: Investigating carbon dioxide complexes with the ccsd (t)-f12 method. *The Journal of Chemical Physics*, 134(3), 2011.

[248] David E Woon and Thom H Dunning Jr. Gaussian basis sets for use in correlated molecular calculations. iii. the atoms aluminum through argon. *The Journal of chemical physics*, 98(2):1358–1371, 1993.

[249] Thom H Dunning Jr. Gaussian basis sets for use in correlated molecular calculations. i. the atoms boron through neon and hydrogen. *The Journal of chemical physics*, 90(2):1007–1023, 1989.

[250] Samuel F Boys and FJMP Bernardi. The calculation of small molecular interactions by the differences of separate total energies. some procedures with reduced errors. *Molecular physics*, 19(4):553–566, 1970.

[251] Sheldon Green. Rotational excitation in H_2--H_2 collisions: Close-coupling calculations. *The Journal of Chemical Physics*, 62(6):2271–2277, 1975.

[252] M Dehghany, Mahin Afshari, Z Abusara, and N Moazzen-Ahmadi. Nonpolar nitrous oxide dimer: fundamentals of the mixed $^{14}N_2O--^{15}N_2O$ dimer and new combination bands of $(^{14}N_2O)_2$ and $(^{15}N_2O)_2$ involving the b u intermolecular bend. *Physical Chemistry Chemical Physics*, 11(35):7585–7588, 2009.

[253] Eduardo Castro-Juárez, Xiao-Gang Wang, Tucker Carrington, Ernesto Quintas-Sánchez, and Richard Dawes. Computational study of the ro-vibrational spectrum of $CO--CO_2$. *The Journal of chemical physics*, 151(8), 2019.